# CHERENKOV RELATED BACKGROUNDS IN THE DARKSIDE-50 EXPERIMENT

#### XIN XIANG

A DISSERTATION

PRESENTED TO THE FACULTY

OF PRINCETON UNIVERSITY

IN CANDIDACY FOR THE DEGREE

OF DOCTOR OF PHILOSOPHY

RECOMMENDED FOR ACCEPTANCE

BY THE DEPARTMENT OF

PHYSICS

ADVISER: CRISTIANO GALBIATI

September 2018

© Copyright by Xin Xiang, 2018.

All rights reserved.

#### Abstract

Weakly Interacting Massive Particles (WIMPs) remain the most popular dark matter candidate as of 2018. DarkSide-50 is a dark matter direct detection experiment at Gran Sasso National Laboratory in Italy. The primary mission of DarkSide-50 is to detect the nuclear recoil signals created by WIMPs scattering off Argon nuclei in a background-free operation.

While DarkSide-50 had demonstrated various background suppression techniques toward the background-free operation, Cherenkov radiation in coincidence with LAr scintillation remains the most severe background. In this work, I will first describe the discovery of this troublesome background in a non-blind analysis, followed by detailed background characterizations in a GEANT4-based Monte Carlo simulation. I will take you through various benchmarks of the background study, from tuning the Cherenkov related optics, to building data-driven F90 and S2 models, to exploring the analysis cuts, and finally to validating the background predictions in a recently published blind analysis. The study of Cherenkov background turns out to be crucial to establishing the background-free liquid argon technology in the field.

#### Acknowledgements

For the past five years, my quest to the Ph.D. has been a journey with ups and downs. This dissertation would not have been possible with the support of the many. I would like to give a special shout-out to the people and the organizations who deserve the credit.

Firstly I would like to express my sincere gratitude to my advisor Prof. Cristiano Galbiati for the financial support of my study, for his patience, motivation, and setting an example of high standards. His guidance helped me in all the time of research and writing of this thesis.

I was very fortunate to work with Prof. Peter Meyers, a kind mentor who has been a tireless source of guidance on my professional development. Peter played a critical role in this work. I would like to especially thank him for spending countless hours with me to discuss the details of the G4DS optics. I am absolutely amazed by his ability to keep track of the analysis details at all time.

I have benefited a lot from interacting with many of my collaborators. Dr. Masayuki Wada is a human encyclopedia of ROOT, and DarkArt. He was the go-to guy regarding pretty much any technical aspects of the DarkSide-50 analysis. The amount of time and effort he has dedicated to the data processing is essential for the success of me and the rest of the analysis team. I really appreciate Dr. Graham Giovanetti for his careful proof-reading of this dissertation, including this particular sentence. I had been working closely with Guangyong Koh on the electronic recoil background for two and half years. The team was able to fast forward the blind analysis because of his hard work. Hats off to him. The 3D event display by Chris Stanford has been extremely useful for me to inspect baffling events one by one. I would also like to thank him for being a good office mate for three years, and for his fashion advice such as maintaining a good hairstyle. Shawn Westerdale has a unique sense of humor which I enjoy a lot. I would like to thank him for the collaboration on the cosmogenic neutron analysis, and for introducing me to the GEANT4 framework. Many other collaborators deserve a note. I would like to thank Alden Fan for his knowledge on DarkArt. Paolo Agnes

for his knowledge on G4DS, Chengliang Zhu for sharing his experience on the optics tuning, Tessa Johnson for the collaboration on the Cherenkov analysis, Hao Qian for his work on the neutron veto efficiency, Jason Brosky for his work on xy algorithm, Xinran Li for the work on the elelctron diffusion, Erin Edikin for her work on the NR acceptances, Luca Pagani for his work on the energy variables, Huajie Cao for his work on the SCENE experiment, and Pablo Mosteiro for sharing his stories during my first year at Princeton. The list of collaborators is too long to name everyone, but I appreciate the things I learned from you.

The DarkSide-50 detectors were remarkably stable for the past five years. I would like to give the credit to the pioneers who assembled the detectors carefully, and the operation team for the prompt actions in face of occasional crisis.

Outside of my collaborators I've made a group of colorful friends whose existence really enriched my graduate school experience. Suerfu for being a good house-mate and sharing his knowledge on the subject of neutrino physics, CMB, and hardware. Farzan Beroz, Jos Ferreira, and Alex Tarr for sharing the passion of pumping iron. Yuntao Bai for the dinner conversations of his HEP theory research stuff, which I mostly pretended to understand. Mallika, Tom, Wudi, Peter, Sid, and Will for the prelim exam preparation.

I would like to acknowledge the physics department of Princeton University for the funding of the first year fellowship, the travel reimbursement, and many semesters of teaching assistant.

The last but not the least, I would like to thank my parents and other family members for their unconditional support. I cannot thank them enough for their continuous encouragement to always follow my passion for physics throughout this journey.

To my parents.

## Contents

	Abst	tract .		iii
	Ackı	nowledg	gements	iv
	List	of Tabl	les	xiii
	List	of Figu	ires	xiv
1	Intr	oducti	ion	1
	1.1	Cosmo	ological Evidence	1
		1.1.1	Galactic Rotation Curve	1
		1.1.2	CMB	2
		1.1.3	Bullet Cluster	3
		1.1.4	A Galaxy Lacking Dark Matter	3
	1.2	WIME	P Dark Matter	5
		1.2.1	The "WIMP miracle"	5
		1.2.2	Vanilla WIMPs	7
	1.3	Direct	Detection	8
		1.3.1	Event Rate	8
		1.3.2	Cross-section	10
		1.3.3	Detection of Electronic Recoils	12
		1.3.4	Annual Modulation	13
2	The	. Dark	Sido-50 Experiment	15

	2.1	Operati	ional Timeline	15
	2.2	Dual-pl	hase TPC	16
		2.2.1	LAr Scintillation	17
		2.2.2	Location Reconstruction	19
		2.2.3	Background Discrimination	20
		2.2.4	Signal Corrections	22
		2.2.5	Reconstructing the Recoil Energy	23
	2.3	Underg	round Argon	24
	2.4	Neutro	n Veto	25
		2.4.1	Liquid Scintillator Vessel	26
		2.4.2	Signal Formation	26
	2.5	Water (	Cherenkov Veto	28
	2.6	Data P	rocessing Software	28
3	The	First A	Analysis with the UAr	31
3	<b>The</b> 3.1		Analysis with the UAr -day Campaign	<b>31</b> 31
3		The 70-	·	
3	3.1	The 70-	-day Campaign	31
3	3.1 3.2	The 70-Data Se	-day Campaign	31 33
3	3.1 3.2	The 70-Data Set The And 3.3.1	-day Campaign	31 33 34
3	3.1 3.2	The 70-Data Set The And 3.3.1 3.3.2	-day Campaign	31 33 34 34
3	3.1 3.2	The 70-Data See The Am 3.3.1 3.3.2 3.3.3	-day Campaign	31 33 34 34 35
3	3.1 3.2 3.3	The 70- Data Se The An 3.3.1 3.3.2 3.3.3 Main R	-day Campaign	31 33 34 34 35 36
3	3.1 3.2 3.3	The 70-Data Set The Am 3.3.1 3.3.2 3.3.3 Main R 3.4.1	-day Campaign	31 33 34 34 35 36 37
3	3.1 3.2 3.3	The 70-Data Set The Am 3.3.1 3.3.2 3.3.3 Main R 3.4.1 3.4.2	-day Campaign	31 33 34 35 36 37 37
3	3.1 3.2 3.3	The 70- Data Se The An 3.3.1 3.3.2 3.3.3 Main R 3.4.1 3.4.2 3.4.3	-day Campaign election and Validation  nalysis Cuts  Quality Cuts  TPC Analysis Cuts  Veto Cuts  tesults  ER Backgrounds  Observing a F90 Shoulder	31 33 34 34 35 36 37 37
3	3.1 3.2 3.3	The 70- Data Se The An 3.3.1 3.3.2 3.3.3 Main R 3.4.1 3.4.2 3.4.3 3.4.4	-day Campaign election and Validation nalysis Cuts  Quality Cuts  TPC Analysis Cuts  Veto Cuts  ER Backgrounds  Observing a F90 Shoulder  Designing the WIMP Box	31 33 34 34 35 36 37 37 38 39

		3.5.1	Beyond the Ar-39 Endpoint	44
		3.5.2	Further Analysis on the Excess	46
		3.5.3	The Necessity for a PTFE Cherenkov Model	47
4	The	Cher	enkov Simulation	50
	4.1	Introd	luction	50
		4.1.1	The Mechanism	51
		4.1.2	Influence on the Discrimination	55
	4.2	Pure (	Cherenkov Events	56
		4.2.1	Event Selection	56
		4.2.2	Comparing to Na-22 Data	58
	4.3	Model	ling the Cherenkov Radiation in G4DS	60
		4.3.1	The Physics	60
		4.3.2	Sources of Radioactivity	62
		4.3.3	Optics of PTFE	65
		4.3.4	Optics of Fused Silica	69
		4.3.5	Other Relevant Optics	70
		4.3.6	Cherenkov Related Optics Tuning	75
		4.3.7	Modeling the PMT Geometry	86
		4.3.8	Systematics of the Cherenkov Response in G4DS	87
	4.4	Buildi	ing a Compound Model for ER Backgrounds	90
		4.4.1	Overview	90
		4.4.2	Clustering Deposits into Scatters	91
		4.4.3	Calculating S1 from the Energy	93
		4.4.4	Data-driven F90 Modeling	95
		4.4.5	Modeling S1 Prompt Maximum Fraction	96
		4.4.6	Data-driven S2 Modeling	97
		447	Modeling the Number of Pulses	100

		4.4.8	Modeling the Drift Time	102
		4.4.9	Modeling S1 Pulse Finder Efficiency	102
		4.4.10	Modeling the Veto Prompt Charge	103
	4.5	The M	Iodel Results	105
		4.5.1	The Characteristics of ER Backgrounds	105
		4.5.2	Decomposing the Radioactive Sources	106
5	Tho	Blind	Analysis	108
J			iew	
	5.1			108
		5.1.1	The Data Set	108
		5.1.2	Blinding Scheme	108
	5.2	The B	ackground Budget	110
		5.2.1	Surface Background	110
		5.2.2	Cosmogenic Neutron	113
		5.2.3	Radiogenic Neutron	113
		5.2.4	Electronic Recoil Background	115
	5.3	Cheren	nkov Background Cuts	117
		5.3.1	S1 Prompt Maximum Frac Cut	118
		5.3.2	Veto Prompt Cut	120
		5.3.3	Drift Time Cut	122
		5.3.4	Maximum F90 Cut	124
		5.3.5	Radial Fiducial Cut	124
		5.3.6	Minimum S2/S1 Cut	126
		5.3.7	Negative Log Likelihood Cut	127
	5.4	Model	Evaluation in Test Regions	128
		5.4.1	Prompt Veto Tag	128
		5.4.2	Additional Test Regions	128
	5.5	WIME	P Search Results	139

		5.5.1	Designing the WIMP box	 132
		5.5.2	Exposure and WIMP Acceptance	 133
		5.5.3	Final Unblinding	 134
		5.5.4	The Exclusion Limit	 136
6	Con	clusio	on and Outlook	138
	6.1	Summ	nary	 138
	6.2	Future	e Outlooks	 139
$\mathbf{A}$	Digi	itizer (	Correction	142
	A.1	V1720	0 and V1724	 142
	A.2	Recon	nstructing V1724 Data	 143
	A.3	ADC (	Correction Algorithm	 144
		A.3.1	The Correction Maps	 146
		A.3.2	Correcting F90	 148
	A.4	Valida	ation	 148
		A.4.1	The Alpha study	 149
В	The	"Che	erenkov Tail"	152
	B.1	The Fe	Features	 152
	B.2	The P	PMT Dark Noise	 153
$\mathbf{C}$	Tecl	hnical	G4DS Implementations	158
	C.1	Useful	l features	 158
	C.2	G4DS	S Speed-up Scheme	 159
	C.3	Slim S	Storage Scheme	 161
	C.4	The Ir	nstructions	 161
D	Dat	a Stab	oility in the 70-day Campaign	162
	D 1	TPC S	Stability	162

D.2 LSV Stability	 	•	 •		 •		•				•		•	•	•		17
Bibliography																	17

## List of Tables

2.1	Nuclear recoil quenching factors measured by SCENE	24
4.1	The Cherenkov production thresholds	52
4.2	Summary of counting results used for the normalization	63
4.3	Summary of PMT radioactivity used in the normalization	64
4.4	The parameters of recombination probability function	95
4.5	The ER backgrounds in the blinding box by the radioactive sources	107
5.1	Additional test regions	132
5.2	Summary of the background estimate surviving all cuts	135
A.1	Major differences between two digitized outputs	143
A.2	Summary of the fit parameters for all channels	151

# List of Figures

1.1	CMB power spectrum	2
1.2	A galaxy lacking dark matter	4
2.1	DarkSide-50 Time Projection Chamber	17
2.2	Liquid Argon Scintillation	18
2.3	S2/S1 and PSD discrimination	21
2.4	Argon-39 depletion factor	25
3.1	Reduction of beta activity in LAr and TMB	32
3.2	The stability of veto trigger time	33
3.3	S1-late spectrum from the null field data	38
3.4	Comparison of F90 profiles between AAr data and UAr data	40
3.5	70-day NR acceptance as a function of energy	43
3.6	WIMP search results from 70-day analysis	45
3.7	The comparison between $f_{90}$ spectra beyond Ar-39 endpoint	46
3.8	F90 characteristics of the 70-day data under various cuts	48
3.9	F90 profiles of the UAr data after various S1 maximum fraction cuts	49
4.1	Illustration of external gamma induced Cherenkov background in DarkSide-50	54
4.2	Fused silica Cherenkov background in the 70-day data	55
4.3	Single pulse events in the 70-day UAr data	57
4.4	Single pulse events in the 70-day data	59

4.5	Evidence of the PTFE Cherenkov by comparing the UAr and the Na22 data	61
4.6	MC: Cherenkov from electron uniformly generated in the PTFE	67
4.7	Sellmeier's equation and the parameters for our FS	69
4.8	The empirical extrapolation of the refractive index and the extinction coefficient	71
4.9	The Reflectance, transmittance, absorption from the Sernelius's model	71
4.10	The ITO's transmission and reflection measured at Princeton	72
4.11	PMT overall reflectivity measured at Princeton	73
4.12	The quantum efficiency used in G4DS simulation	74
4.13	<sup>22</sup> Na energy spectrum	77
4.14	Optics tuning on Na-22 pure Chernekov events	78
4.15	The simulated pure Chernekov events as compared to the UAr data	80
4.16	S1 maximum fraction for pure FS Chernekov events in the UAr data $\ \ldots \ \ldots$	81
4.17	F90-S1 cut to select pure Cherenkov events in AmBe data	83
4.18	Data-model comparison on AmBe pure Cherenkov events	84
4.19	The final version of the PMT geometry implmented in the G4DS	85
4.20	The study of systematic errors in PTFE Cherenkov light yield	89
4.21	A Flowchart of the MC-data hybrid model	92
4.22	Modeling S1 LY at 200V/cm as a function of energy	93
4.23	Data-driven S2 profiles used to mimic S2 in MC	99
4.24	Data-model comparison of S2/S1	101
4.25	The S1 pulse finder efficiency	103
4.26	Data-Model comparison of the veto prompt spectrum	104
4.27	The F90 Model of ER background	105
5.1	The blinding box	109
5.2	Alpha energy spectrum in WIMP search data	111
5.3	Neutrons in Veto Prompt Tag sample	114
5.4	The spectrum fit to the gamma peaks in the 540-day WIMP search data	117

5.5	The acceptance of the S1 prompt maximum fraction cuts	119
5.6	The improvement of S1 prompt maximum fraction cuts on F90 shoulder	121
5.7	Pure Cherenkov events from diving bell/cathode window	122
5.8	Defining the maximum F90 cuts on <sup>241</sup> Am-Be NRs	123
5.9	Comparison of the top F90 contours with the "Two-Tail" model	125
5.10	The radial fiducialization used in the 540-day analysis	126
5.11	The minimum S2/S1 cuts defined on $^{241}$ Am-Be NRs	127
5.12	F90 data-model comparison in the Veto Prompt Tag sample	129
5.13	Definitions of the additional test regions	130
5.14	Defining the final WIMP box for the 540-day data	134
5.15	540-day NR acceptance as a function of energy	135
5.16	Final WIMP search results of the 540-day analysis	137
A.1	An simplified DarkArt flowchart incorporating V1724 data stream	145
A.2	An example fit on channel 20 to S2-like pulses	147
A.3	Energy spectrum of the surface alpha's	150
B.1	Waveform demonstrates the Cherenkov tail feature	153
B.2	The Cherenkov tail size verus S1	154
В.3	The Cherenkov tail size to S1 ratio	154
B.4	S1 vs the maximum channel (Cherenkov tail)	155
B.5	The PMT dark noise	157
D.1	TPC aseline width (sigma)	163
D.2	TPC single PE response mean (PMT gain)	165
D.3	TPC single PE response sigma	166
D.4	TPC single PE response resolution (sigma/mean)	167
D.5	TPC LY stability from the Ar-37 peak	168
D.6	The maximum drift time stability trend	169

D.7	Electron drift lifetime in the UAr at $E_{drift}$ =50 V/cm	170
D.8	Veto electronic noise trend in pre-prompt ROI	172
D.9	Veto mean LY trend from the <sup>57</sup> Co peaks	173

## Chapter 1

### Introduction

Several decades of cosmological observations suggest that perhaps the majority of matter in our universe is non-luminious, or dark. According to WMAP's analysis on CMB, the mass-energy content of the universe is approximately 73% dark energy, 23% dark matter, and 4.6% baryonic matter [1].

In Sec. 1.1, I will describe some compelling astronomical evidence for the existence of dark matter hypothesis. In Sec. 1.2, I will describe one type of popular dark matter candidates – the Weakly Interacting Massive Particles, or WIMPs. Finally in Sec. 1.3, I will focus on the theoretical calculation of the WIMP scattering rate in direct detection experiments. Experimental limitations and a calculation of annual modulation will be discussed as well.

#### 1.1 Cosmological Evidence

#### 1.1.1 Galactic Rotation Curve

A rotation curve describes the orbital speeds of visible stars and interstellar gas as a function of their radial distance from their galaxy's center. It was first discovered by Fritz Zwicky that the visible baryonic matter cannot explain the apparent rotational velocity, assuming the

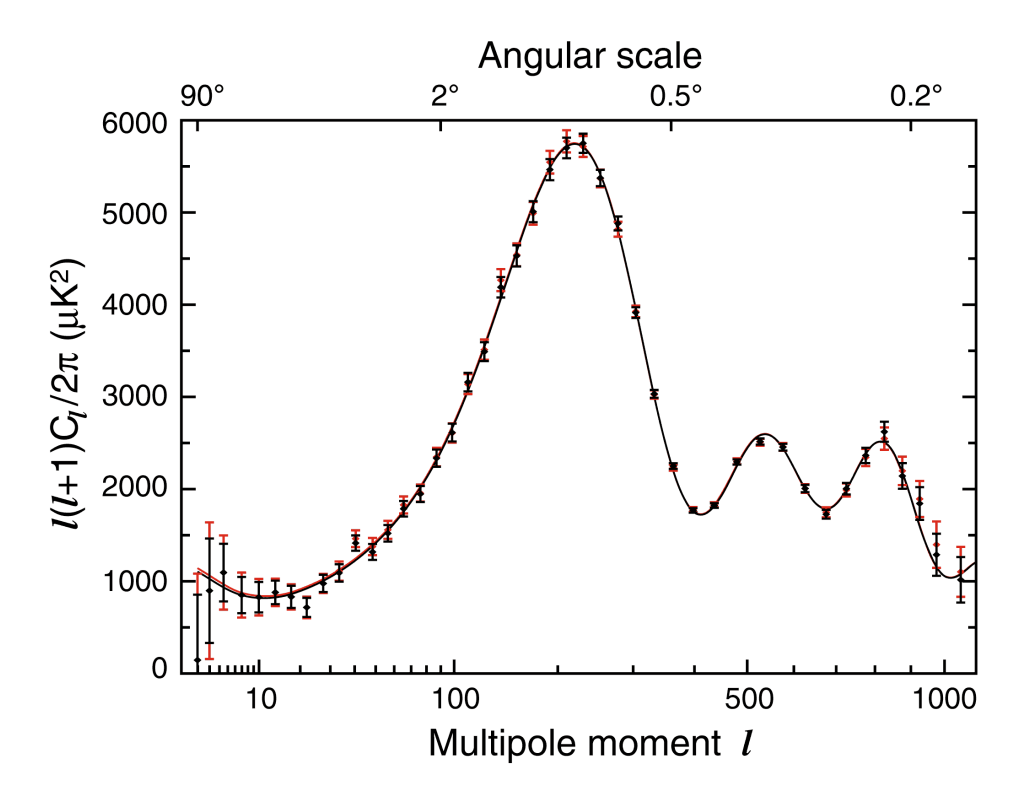


Figure 1.1: The CMB power spectrum measured by WMAP nine-year data. This plot shows two estimates of the CMB temperature fluctuations at different angular scales on the sky, along with the best-fit model spectra from each [1].

inverse square law of gravity holds at the cosmic scale [2]. The hypothesis of the existence of non-luminous dark matter was postulated to account for the discrepancy.

#### 1.1.2 CMB

The Cosmic Microwave Background (CMB) is the gravitationally red-shifted ( $z \sim 10^3$ ) radiation from the time when protons and electrons combined into neutral hydrogen in the early universe. It is an almost-uniform background of radio emission, and the measurements of the slight fluctuations in intensity across the sky provides us a map of the early universe. Since the shape of the power spectrum is determined by oscillations in the hot gas of the early universe, knowing the resonant frequency and amplitude of thes oscillation helps determine its composition at the time.

According to the  $\Lambda$ CDM (Lambda cold dark matter) model in the Standard Model of cosmology, the dark matter (DM) mass density parameter  $\Omega_D$  plays a big part in determining the structure of the CMB's angular power spectrum. As shown in Fig 1.1, the position of the first peak tells us about the curvature of the universe (total mass), while the ratio of heights between the first and second peaks tells us how much of the matter is baryonic.

#### 1.1.3 Bullet Cluster

The Bullet Cluster (1E 0657-558) is one famous example of two colliding clusters of galaxies that can be observed through the visible spectrum, the Chandra X-ray telescope, and by gravitational lensing techniques. The visible light and X-rays emission is a measure of the compressed and heated interstellar gas distribution while the gravitational lensing is a measure of the total mass distribution. When astronomers analyzed the visible and X-rays spectra of these two colliding galaxy clusters, they found that the hot gas seems to decelerate as the two clusters collided, which is expected from the electromagnetic interactions between baryonic matter. However, when analyzing the total mass distribution from gravitational lensing, the analysis suggests that most of the mass content passed through each other unperturbed. This suggests the majority of the mass in the clusters is non-baryonic.

#### 1.1.4 A Galaxy Lacking Dark Matter

Most galaxy surveys have shown that the total stellar mass is couple to the mass of the DM halo, and their mass profile functions vary smoothly together. For galaxies near  $5 \times 10^{10}$  solar mass, the average ratio  $(M_{\rm halo}/M_{\rm stars})$  has a minimum of about 30. However a recent study of NGC1052-DF2, an ultra-diffuse galaxy (stellar mass  $\sim 2 \times 10^8 \ M_{\odot}$ ), has shown that the ratio,  $M_{\rm halo}/M_{\rm stars}$ , is in fact on the order of unity. As shown in Fig 1.2, when comparing the enclosed mass to the expected mass from the stars alone (orange line) and to the models with different halo masses, it shows that NGC1052DF2 is extremely deficient in DM. This

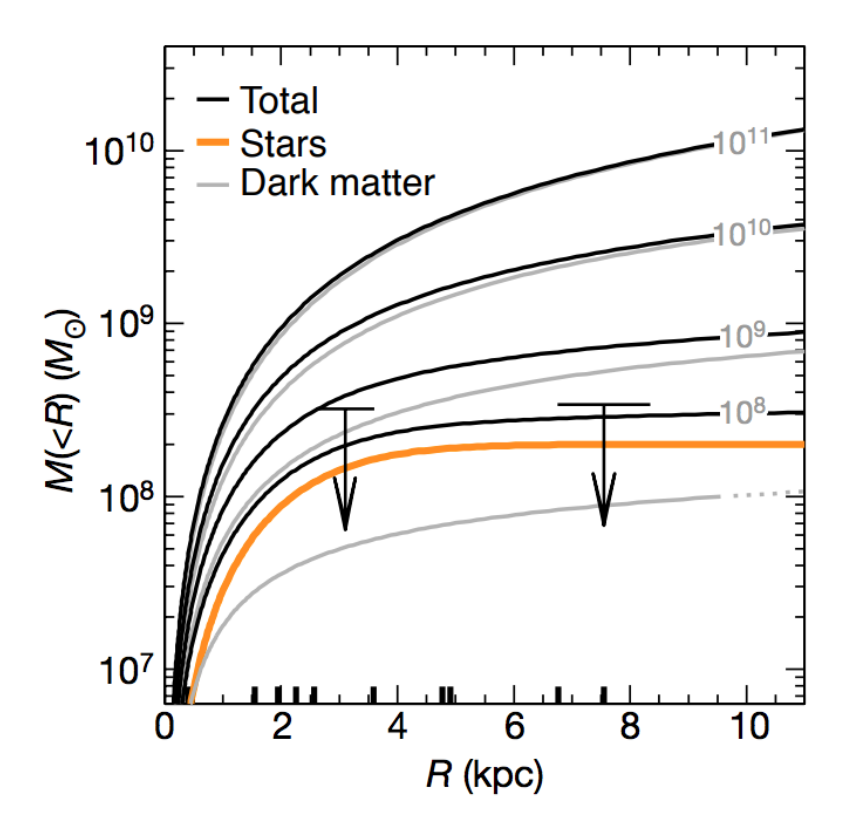


Figure 1.2: The enclosed mass profiles of DM halo  $(M_{\rm halo}(r))$  for NGC1052DF2 as a function of radius (grey) at various total halo masses  $(10^8~M_{\odot},~10^9~M_{\odot},~10^{10}~M_{\odot}$  and  $10^{11}~M_{\odot})$ . The enclosed mass profile  $(M_{\rm stars}(r))$  for the stellar component is shown in orange, and the enclosed total mass profiles  $(M_{\rm total}(r) = M_{\rm stars}(r) + M_{\rm halo}(r))$  is shown in black. The short vertical bars on the horizontal axis indicate the locations of individual clusters. The 90% upper limits on the total enclosed mass of NGC1052DF2 (the arrows) constrains the upper limit of the halo mass at  $1.5 \times 10^8~M_{\odot}$ . [3]

surprising result implies that DM, if it exist, is not always coupled with baryonic matter on a galactic scale.

NGC1052DF2 may paradoxically falsify the alternatives to DM. Modified Newtonian dynamics (MOND) is one alternative hypothesis to explain the "DM phenomena" without the existence of DM. The lack of DM presents a challenging case against MOND. Since MOND postulates that the gravitational force deviates from the inverse square law at a cosmic scale, it would imply that the effect of the MOND should be consistently observed in every Galaxy cluster.

#### 1.2 WIMP Dark Matter

#### 1.2.1 The "WIMP miracle"

WIMPs became a popular DM candidate because of the weak scale miracle argument. The early universe is a hot soup. The DM-DM annihilation reaction creates the Standard Model (SM) particles, and its rate is expected to be in thermal equilibrium with the reverse process. The rate of annihilation will only depend on the thermally averaged annihilation cross section  $\langle \sigma_A v \rangle$  and the DM number density n:

$$\Gamma_{-} = \int \sigma_{A} \frac{d\Theta}{dv} dv = n \langle \sigma_{A} v \rangle. \tag{1.1}$$

As the universe expands and the temperature drops, the DM number density reaches a constant ("freeze-out"). DM particles becomes so dilute that they cannot find each other to annihilate, while SM particles no longer have enough energy to produce heavier DM particles. The time evolution of DM number density (n(t)) is described by the Boltzmann equation,

$$\frac{dn}{dt} = -3Hn - \langle \sigma_A v \rangle (n^2 - n_{eq}^2) : \tag{1.2}$$

where H is the Hubble constant. On the right hand side, the -3Hn term comes from the expansion of space. The  $-\langle \sigma_A v \rangle n^2$  term arises from  $\chi \chi \to SMSM$  that destroys DM particles, and the  $-\langle \sigma_A v \rangle n_{eq}^2$  term arises from the reverse process.

Let's rewrite Eqn 1.2 in terms of Y = n/s, where s is the entropy density. Due to the conservation of the total entropy, the density s is diluted by the space expansion as

$$\frac{ds}{dt} = -3Hs. (1.3)$$

Combining Eqn 1.3 with Eqn 1.2, and using chain rule, we obtain:

$$\frac{dY}{dt} = -\langle \sigma_A v \rangle \, s(Y^2 - Y_{eq}^2),\tag{1.4}$$

where we approximate  $s = s_{eq}$ .

It's convenient to express this yield equation in terms of a dimensionless temperature variable  $x = m_{\chi}/T$ . First, we replace the Hubble's constant by:

$$H = \sqrt{\frac{8\pi G\rho}{3}},\tag{1.5}$$

where G is the gravitational constant, and  $\rho$  is the mass density of the early universe. In a radiation dominated domain, the early universe has  $\rho = \pi^2 g_{eff} T^4/30$  and  $s = 2\pi^2 h_{eff} T^3/45$ . Here  $g_{eff}$  is the effective degrees of freedom for the energy, and  $h_{eff}$  is the effective degrees of freedom that depends on temperature. With some effort, we obtain a new form of this yield equation:

$$\frac{dY}{dx} = -\sqrt{\frac{\pi g_s}{45G}} \left(\frac{m_\chi}{x^2}\right) \langle \sigma_A v \rangle \left(Y^2 - Y_{eq}^2\right),\tag{1.6}$$

where  $g_s = h_{eff}^2/g_{eff}$  parametrizes the relativistic degrees of freedom.

To solve Eqn. 1.6, Dodelson [4] develops an analytical solution by making the following approximation. First we define a dimensionless parameter,

$$\lambda = \sqrt{\frac{\pi g_s}{45G}} m_\chi \langle \sigma_A v \rangle. \tag{1.7}$$

In the limit of  $T \gg m_{\chi}$  ( $x \ll 1$ ), dY/dx is so large with respect to  $Y^2 - Y_{eq}^2$  term that the DM abundance is closely related to the equilibrium value. In the limit of  $T \ll m_{\chi}$  ( $x \gg 1$ ),  $dY/dt \to 0$ , which means Y becomes a constant. At large temperatures,  $Y_{eq}$  drops exponentially, so we can approximate 1.6 as:

$$\frac{dY}{dx} \sim \frac{\lambda Y^2}{x^2}. (1.8)$$

Let's designate  $x_f$  and  $Y_f$  as the temperature and density at the moment of freeze-out. Integrating Eqn 1.8 from  $x_f$  to present, we have:

$$\frac{1}{Y_0} - \frac{1}{Y_f} = \frac{\lambda}{x_f}. (1.9)$$

Assuming the present day abundance  $Y_0$  is much smaller than the freeze-out  $Y_f$ , we have  $Y_0 \approx x_f/\lambda$ . Numerical solutions show that the freeze-out temperature  $(x_f \sim 20 \ [5])$  varies only slightly with WIMP mass. Thus the fraction of critical density contributed by DM is

$$\Omega_{\chi} = \frac{m_{\chi} s_0 Y_0}{\rho_c} = \sqrt{\frac{45G}{\pi g_s}} \frac{s_0}{\langle \sigma_A v \rangle}$$
(1.10)

Plugging in numbers yields:

$$\Omega_{\chi} \approx \frac{10^{-36} \,\mathrm{cm}^3/\mathrm{s}}{\langle \sigma_A v \rangle}$$
(1.11)

This is known as the "WIMP miracle". When using the thermally averaged cross-section at  $\langle \sigma_{weak} v \rangle \approx 10^{-36} \, \mathrm{cm}^3/\mathrm{s}$ ,  $\Omega_X$  is close to unity. This is consistent with the DM relic abundance from cosmological observation.

An significant virtue of the "WIMP miracle" is that it connects the DM problem to the electroweak scale where we expect to find new physics related to the hierarchy problem of the Standard Model (SM). Furthermore, if the DM-SM cross-section is not too far way from the weak scale, it provides hopes for the possibility of experimental direct detection.

#### 1.2.2 Vanilla WIMPs

There are various extension to the SM that lead to WIMPs. In this section, we will simply discuss vanilla WIMPs – the simplest form that we could add to the SM with the fewest assumptions. From an experimental perspective, what matters the most is the theoretical prediction of the WIMP-nucleons cross-section.

When we talk about the WIMP-nucleon interaction, we inevitably need to specify the mediator. In the simplest tree level Feynman diagram, suppose the WIMP and nucleon interact via a Z-boson exchange. Most models predict that the SI cross section is  $\sigma_{\rm SI} \approx \alpha^2 m_N^2/M_Z^4 \approx 10^{-38} \, {\rm cm}^2$ , where  $\alpha$  is the weak coupling constant,  $m_N$  is the mass of target nucleus, and  $M_Z$  is the mass of Z boson. Suppose the mediator is the Higgs boson, most models predict  $\sigma_{\rm SI} \approx \alpha^2 m_N^4/M_\chi^2 M_Z^4$  where  $M_\chi$  is the mass of a WIMP particle. For a 100 GeV WIMP,  $\sigma_{\rm SI} \approx 10^{-43} \, {\rm cm}^2$ . As of 2018, the above two scenarios have been excluded by many noble liquid based experiments (XENON [6], LUX [7], PandaX [8], DarkSide-50 [9], and DEAP-3600 [10]) for WIMP mass between 10 GeV to 10 TeV.

Given Higgs mediated interactions are not observed by many experiments, it means either loop level coupling is involved, or some exotic mechanisms beyond the SM suppresses the interaction. One possible hypothesis suggests the existence of "dark Higgs" living in a dark sector and giving WIMPs masses. Then the WIMP-nucleon cross-section could be arbitrarily small.

#### 1.3 Direct Detection

#### 1.3.1 Event Rate

The differential event rate is expressed in terms of counts per kilogram per day per keV for a WIMP mass  $m_{\chi}$  and a nucleus mass  $m_{N}$ :

$$\frac{dR}{dE_R} = \frac{\rho_0}{m_N m_\chi} \int_{v_{\min}}^{\infty} v f(v) \frac{d\sigma_{\chi,N}}{dE_R} (v, E_R) dv, \qquad (1.12)$$

where  $\rho_0$  is the local WIMP density,  $E_R$  is the recoil energy,  $\frac{d\sigma_{\chi,N}}{dE_R}(v, E_R)$  is the differential cross-section for the WIMP-nucleus elastic scattering, and f(v) is the WIMP speed distribution in the detector frame normalized to unity [11].

The local density  $\rho_0$  is calculated at the solar radius (distance to the galactic center,  $R_0 = (8.0 \pm 0.5) \text{ kpc}$ ) [12] by applying observational constraints of galactic rotation curves to model the Milky Way. A recent study using the spherical halo models finds  $\rho_0 = (0.30 \pm 0.05) \text{ GeVcm}^{-3}$  [13].

The recoil energy  $E_R$  is easily calculated in terms of the scattering angle  $\theta$  in the center of mass frame:

$$E_R = \frac{\mu_N^2 v^2 (1 - \cos \theta)}{m_N},\tag{1.13}$$

where  $\mu_N = m_\chi m_N/(m_\chi + m_N)$  is the WIMP-nucleus reduced mass. Notice, a minimum velocity  $v_{\rm min}$  is reached at a given  $E_R$  when the WIMP back-scatters ( $\cos \theta = -1$ ) from the nucleus. Therefore,  $v_{\rm min} = \sqrt{(m_N E_R)/(2\mu_N^2)}$ .

As a convention, direct detection experiments use the standard halo model with an isotropic Gaussian (Maxwellian) velocity distribution for the rate calculation. The f(v) is:

$$f(v) = \frac{1}{\sqrt{2\pi}\sigma} \exp\left(-v^2/2\sigma^2\right),\tag{1.14}$$

where the derivation  $\sigma$  is connected to the local circular speed by  $\sigma = \sqrt{3/2} \ v_c$  and  $v_c = (220 \pm 20) \ \text{km/s}$  [14]. This simple model is not unreasonable as a first approximation. However, given recent observations and numerical simulations, it's likely that dark matter halo does not follow the same velocity distribution as the Milky Way. Thus, the systematic error associated with the local DM velocity could be big. For instance, when taking into account the earth's motion, there is a time dependence in the rate (see Sec. 1.3.4).

Putting explicitly together, the total event rate, in terms of counts per kilogram per day, is obtained by integrating equation 1.12 over  $E_R$ :

$$R = \int_{E_T}^{\infty} dE_R \frac{\rho_0}{m_N m_{\chi}} \int_{v_{min}}^{\infty} v f(v) \frac{d\sigma_{\chi N}}{dE_R} (v, E_R) dv, \qquad (1.15)$$

where  $E_T$  is the energy threshold that depends specifically on a detector's capability.

#### 1.3.2 Cross-section

The WIMP-nucleus differential cross-section is the main parameter that a direct detection experiment is trying to probe. Although the coupling strength depends fundamentally on the effective Lagrangian term describing a particular WIMP-quark and WIMP-gluon interaction, the measurement of cross-section is promoted as an expression of WIMP-nucleon cross-section, hiding the hadronic matrix elements. In general, the WIMP-nucleus cross-section can be separated into two parts:

$$\frac{d\sigma_{\chi N}}{dE_R} = \left(\frac{d\sigma_{\chi N}}{dE_R}\right)_{SI} + \left(\frac{d\sigma_{\chi N}}{dE_R}\right)_{SD},\tag{1.16}$$

where SI (SD) stands for spin-independent (spin-dependent), and  $F(E_R)$  is the nuclear form factor which accounts for the finite size of nucleus structure. The form factor leads to a suppression in the event rate.  $\sigma_0^{\rm SI}$  is the SI cross-section with zero momentum transfer. The SI part arises from WIMP scalar and vector couplings to quarks whereas the SD part arises from WIMP axial-vector couplings.

If we approximate the WIMP-neutron coupling strength to be about the same as WIMPproton,  $f_p \approx f_n$ , SI contributions (both scalar and vector couplings) can be expressed as

$$\left(\frac{d\sigma_{\chi N}}{dE_R}\right)_{SI} = \frac{2m_N A^2(f^p)^2}{\pi v^2} F^2(E_R), \tag{1.17}$$

where  $F^2(E_R)$  can be qualitatively understood as a Fourier transform of the nucleon density in terms of the momentum transfer q,

$$F^{2}(q) = \left(\frac{3j_{1}(qR_{1})}{qR_{1}}\right)^{2} \exp\left[-q^{2}s^{2}\right]. \tag{1.18}$$

Here  $j_1$  is a spherical Bessel function, and  $s \approx 1$  fm is a measure of the nuclear skin thickness.

The SD contribution of the WIMP-nucleus cross-section arises from the couplings of the WIMP-quark axial current. In the case of a fermionic WIMP, the differential cross-section

can be expressed as [11],

$$\left(\frac{d\sigma_{\chi N}}{dE_R}\right)_{SD} = \frac{16m_{\chi}}{\pi v^2} \Lambda^2 G_F^2 J(J+1) \frac{S(E_R)}{S(0)},$$
(1.19)

where J is the total angular momentum of the nucleus, and:

$$\Lambda = \frac{1}{J} [a_p \langle S_p \rangle + a_n \langle S_n \rangle]. \tag{1.20}$$

Although both SI and SD interactions contribute to the total cross-section, Eqn. 1.17 suggests that the SI part scales with the number of nucleons,  $A^2$ , whereas the SD part is proportional to the nuclear angular momentum, (J+1)/J. For most experiments that are based on heavy nuclei target (A > 20), such as Argon, Germanium, Iodine, and Xenon, the scalar component of the SI part dominates. Nevertheless, dedicated experiments exist that are also sensitive to the SD WIMP coupling through the choice of targets with a large nuclear angular momentum.

It is worth mentioning that, despite of the null results from other experiments, DAMA/LIBRA experiment has been reporting a positive annual modulation effect (Sec. 1.3.4) with 9  $\sigma$  statistical significance [15]. Using NaI(Tl) crystal as the DM target, the experiment has been operating at the LNGS facility for more than 15 years.

The DAMA/LIBRA abnormality may be explained by the inelastic scattering. In particular, a contribution from inelastic scattering will create either an excited nuclear state, an excited electronic state, or even an excited WIMP state. The last case, expressed as  $\chi N \to \chi^* N$ , is particularly interesting to explain the positive modulation signals observed by DAMA/LIBRA while not contradicting the null results from other experiments. If the WIMP mass difference,  $\delta = \chi^* - \chi$ , is the order of WIMP kinetic energy, the only kinematic change is the minimal WIMP velocity that can trigger a specific recoil energy, which is increased by  $\Delta v_{\min} = \delta/(2m_N E_R)$ . This will favor detection in heavy target such as Iodine (smaller  $\Delta v_{\min}$  and therefore high rate) [16].

#### 1.3.3 Detection of Electronic Recoils

Most experimental efforts are dedicated to detecting WIMPs scattering off an nuclei, but we cannot omit the possibility of light DM (LDM), whose mass may be in the range from keV to GeV. LDM is theoretically motivated if DM does not couple strongly to the visible sector. In particular, the mass of a particle in a hidden sector may be suppressed by small couplings between the hidden and visible sectors. Kinematically, LDM are likely to scatter off electrons over nuclei.

The process of DM scattering off electrons suffice to trigger inelastic atomic processes that leads to one of three visible signals:

- 1. Electron ionization (DM-electron scattering);
- 2. Electronic excitation (DM-electron scattering);
- 3. Molecular dissociation (DM-nuclear scattering).

In this section, I will simply focus on electron ionization in a noble liquid. DM-electron scattering may ionize a bound electron from energy level i to an unbounded state with positive energy. According to [17], the electronic recoils with energy  $E_R$  have the differential ionization rate,

$$\frac{dR}{d\ln(E_R/E_0)} = N_T \frac{\rho_\chi}{m_\chi} \sum_{nl} \frac{d \langle \sigma_{ion}^{nl} v \rangle}{d\ln(E_R/E_0)},\tag{1.21}$$

where  $\ln(E_R/E_0)$  is the natural log of ER energy normalized to dimensionless unit,  $N_T$  is the number of target atoms,  $\rho_{\chi}$  is the local DM density, and the velocity-averaged differential ionization cross-section for electrons in the (n, l) shell is given by

$$\frac{d \left\langle \sigma_{ion}^{nl} v \right\rangle}{d \ln(E_R/E_0)} = \frac{\bar{\sigma}_e}{8\mu_{\chi e}^2} \int q dq |f_{ion}^{nl}(k',q)|^2 |F_{\rm DM}(q)|^2 \eta(v_{\rm min}). \tag{1.22}$$

Here, we designate  $\bar{\sigma}_e$  as the DM-free electron scattering cross-section at fixed momentum transfer  $q = \alpha m_e$ ,  $F_{\rm DM}(q)$  is the DM form-factor encoding the q-dependence of the matrix

element,  $\eta(v_{\min}) = \left\langle \frac{1}{v}\theta(v-v_{\min}) \right\rangle$  is the inverse mean speed for a given velocity distribution as a function of the minimum velocity  $v_{\min}$ , and  $|f_{ion}^{nl}(k',q)|^2$  is the ionization form factor of an electron in the (n,l) shell. This (n,l) shield electron escapes with the final momentum  $k' = \sqrt{2m_eE_R}$  after receiving q momentum transfer. The ionization form factor can be explicitly written as:

$$|f_{ion}^{nl}(k',q)|^2 = \frac{4k'^3}{(2\pi)^3} \sum_{l'L} (2l+1)(2l'+1)(2L+1) \begin{bmatrix} l & l' & L \\ 0 & 0 & 0 \end{bmatrix}^2 \left| \int r^2 dr R_{k'l'}(r) j_L(qr) \right|^2, \quad (1.23)$$

where the matrix is the Wigner 3-j symbol,  $j_L$  are the spherical Bessel functions, and  $R_{k'l'}(r)$  are the radial wave-function of the outgoing unbound electrons solved in Schrodinger equation with a central potential  $V(r) = Z_{\text{eff}}(r)/r$  [18].

There is an uprising interest in pursing LDM searches in the field. Although experiments for high mass WIMP (10 GeV to 10 TeV) searches have achieved high exposure with low background, whether the same sensitivity can be replicated in LDM searches remains an open question. As of 2018, the most sensitive search for WIMPs is set by DarkSide-50 in the range of 1.8 GeV to 6 GeV [19], and for LDM is set by XENON-10 [20] and DarkSide-50 [18] in the range of ~10 MeV to ~1 GeV. Experiments targeting DM below ~10 MeV are still at the R&D phase. Since the best experiments are currently in the regime where the background statistics dominates, an increase in the exposure will not improve the sensitivity. Hence, the future LDM searches rest on the ability to further reduce the background rate.

#### 1.3.4 Annual Modulation

When the signal rate is large enough, a search for the annual modulation signature of DM is possible. A discovery of the modulation with the correct phase is necessary to convince the community that the observed excess is indeed DM not background.

The Earth's orbit about the Sun leads to an annual modulation in the differential event rate. With respect to the Galactic rest frame, the Earth's orbital speed is the largest in the beginning of June and lowest in the beginning of December. The Earth's orbit is inclined at  $\sim 60^{\circ}$  relative to the plane of the galactic disk. The energy at which the annual modulation changes phase is often referred to as the "crossing energy". Since the Earth's orbital speed is significantly smaller than the Sun's circular speed, the differential rate, assuming the standard spherical halo, can be approximated by to the first order Taylor series as:

$$\frac{dR}{dE_R} \approx \left(\frac{d\bar{R}}{dE_R}\right) \left[1 + \Delta E_R \cos(2\pi(t - t_0)/T)\right],\tag{1.24}$$

where T=1 yr, and  $t_0\sim 150$  days. Recall that  $v_{\rm min}\propto E_R^{1/2}$  with the constant of proportionality depending on the WIMP and target nuclei masses. The amplitude of the modulation is of order 1-10 %.

An annually modulation signal with the correct phase is a powerful DM signature, because most background signals, such as the radioactivity in detector components, are unlikely to exhibit this kind of time dependence.

## Chapter 2

## The DarkSide-50 Experiment

Located at the Laboratori Nazionali del Gran Sasso (LNGS), DarkSide-50 is the first physics detector of the DarkSide dark matter search program with liquid argon (LAr) as the target. At the center of the experiment, DarkSide-50 has a dual-phase Time Projection Chamber (TPC) with  $\sim 50$  kg active mass that looks for signals of nuclear recoils (NR) from WIMPs. The TPC is surrounded by a 4-meter diameter organic liquid scintillator vessel to actively reject neutron backgrounds. Surrounding the neutron veto is a 1000-tonne water-Cherenkov muon detector to actively reject cosmic ray induced backgrounds.

A direct DM experiment is a rare event search. The principle of any direct DM analysis is essentially a process of elimination – remove all types of WIMP-like events whose physical origins are well understood (background), and the leftover excess events, by definition, are dark matter candidates. In this chapter, I will briefly discuss the main technologies of the DarkSide-50 detectors, and how those technologies together help reduce the WIMP-like backgrounds.

#### 2.1 Operational Timeline

After a successful DarkSide-10 prototype, DarkSide-50 is the second stage of the DarkSide program. The construction was completed in late 2012, and the physics data collection

started in October 2013. The collaboration has published papers from three WIMP search campaigns as of 2018. Data for the first campaign were collected with a batch of atmospheric argon whose radioactive  $^{39}$ Ar content was relatively high (  $\sim 1$  Bq/kg ) [21]; data for the second (April 2015 to July 31 2015) and third campaigns (August 2 2015 to October 4 2018) were collected with a batch of low-radioactivity argon extracted from an underground source and purified by Fermilab. The content of  $^{39}$ Ar in the underground argon was measured to be  $(0.73\pm0.11)$  mBq/kg [22]. Data from the initial two campaigns were analyzed in an open mode while the third campaign was analyzed with a blind analysis.

#### 2.2 Dual-phase TPC

As shown in Fig 2.1, when a particle deposits energy into the LAr target, the TPC detects two types of photon signals. The light produced within the LAr target is observed by 38 Hamamatsu R11065 3" PMTs (19 on the top and 19 on the bottom). Interactions in the LAr target generates 128 nm primary LAr scintillation light (S1) and ionization electrons. Since the quantum efficiency of the PMTs at 128 nm is typically low, we coated a layer of Tetraphenyl butadiene (TPB) on the inner surface of the diving bell (anode), cathode window, and PTFE reflector (Fig. 2.1). The TPB will act as a wavelength shifter and convert the UV photons to visible photons ( $\bar{\lambda}_{emission} \sim 420 \text{ nm}$ ). The TPB delayed emission lifetime is on the order of a few nanoseconds, and therefore will not significantly alter the time profile of the LAr scintillation (Sec. 4.1.2). A fraction of the ionization electrons is drifted away from the recombination with the ions. Once these electrons reach the surface of the LAr, a stronger electric field (2.8 kV/cm) will extract them into a layer of gaseous argon (GAr). The drift system consists of the ITO coated cathode and anode, and as well as copper field cage rings that establish a graded potential outside the cylindrical PTFE wall. This design ensures a uniform drift field throughout the active volume. The drift field is 200 V/cm in the standard WIMP search configuration. The liquid gas interface is maintained at

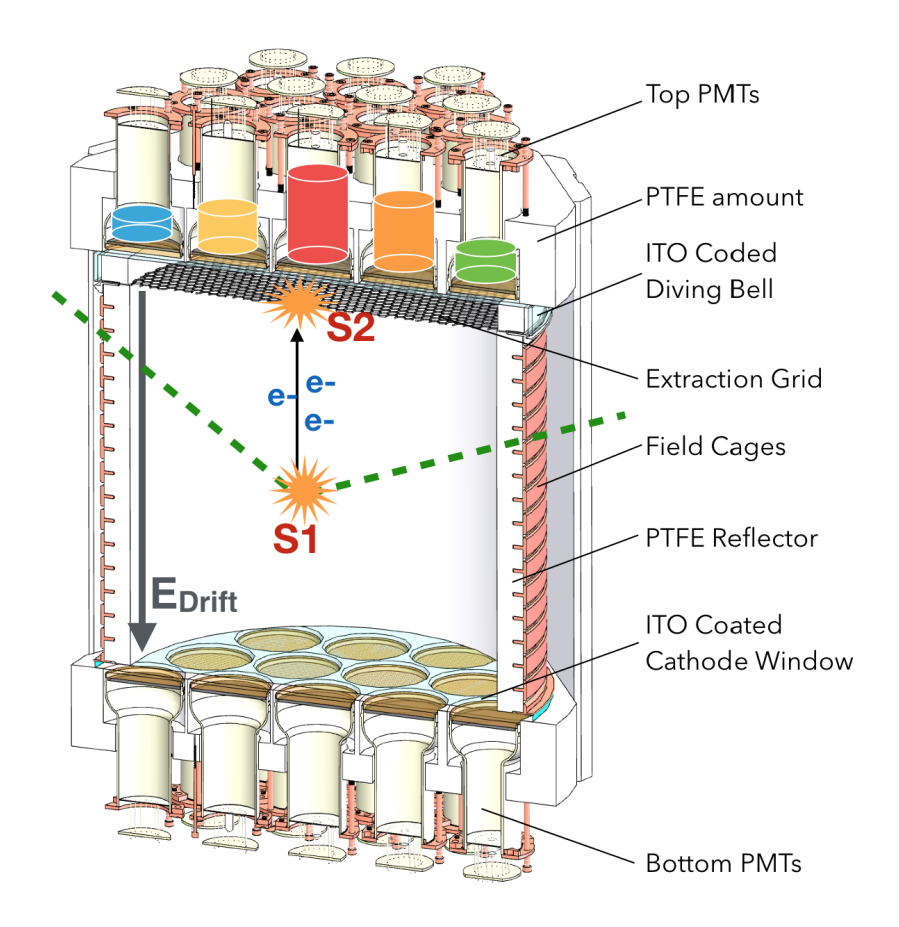


Figure 2.1: The DarkSide-50 dual-phase liquid argon Time Projection Chamber (TPC).

about 5 mm above the extraction grid. Once the electrons enter the gas pocket, they gain sufficient energy to induce electroluminescence light (S2) via proportional scintillation.

The delay time between S1 and S2 pulses gives the vertical (z) position of an event at millimeter precision. Meanwhile, the distribution of S2 light recorded by top PMTs are the inputs to a sophisticated positional reconstruction algorithm to obtain the transverse (xy) position [21].

#### 2.2.1 LAr Scintillation

DarkSide chose liquid argon because it not only offers excellent scintillation light yield  $(40 \sim 45 \text{ photon/keV} \text{ at null field})$  and ionization yield but also offers discrimination against

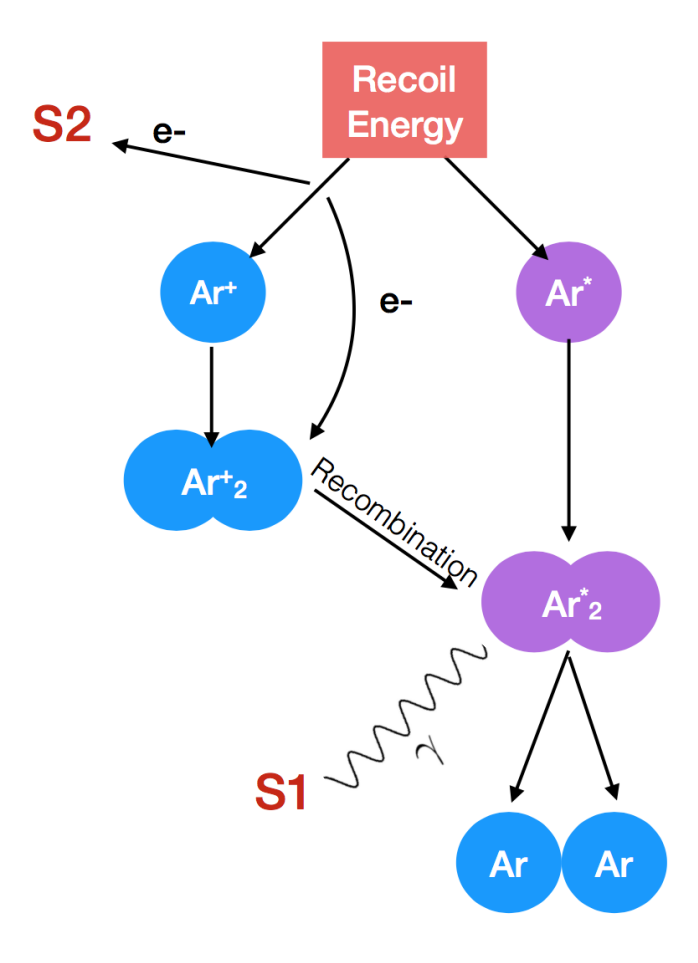


Figure 2.2: The mechanism of liquid argon scintillation to produce S1 and S2 signals. The excited states of argon atom and dimer are in purple.

electromagnetic backgrounds. When the TPC is filled with atmospheric argon (AAr), its light yield is  $7.9 \pm 0.4$  PE/keV at null drift field  $(7.0 \pm 0.3$  PE/keV at 200 V/cm) [21].

Fig 2.2 is an illustration of the scintillation mechanism. Energy deposition by ER first excites some Argon atoms and ionizes others at an ionization/excitation ratio of  $\sim 0.21$ . The excited atoms produce scintillation by forming a weakly bound dimer (Ar<sub>2</sub>\*).

Some of the electrons ionized by the initial interaction recombine with the positively charged ions dimmer (Ar<sub>2</sub>\*), while other electrons escape from recombination under the drift electric field. The drift field is maintained uniformly downward in the active volume, as shown in Fig 2.1, with a constant drift velocity of  $0.93 \pm 0.01$  mm/µs under the  $E_{\text{drift}} = 200$ 

V/cm configuration. Since a stronger drift field means lower recombination probability, the S2 yield is higher and the S1 yield is lower as  $E_{\text{drift}}$  increases.

Quenching is a mechanism that accounts for the observed light yield reduction in scintillators. At the keV or MeV scale, NR quenching is more significant than ER quenching in noble liquid. According to Mei et al [23], NR quenching is a result of two mechanisms – energy loss to heat due to nuclear collisions and scintillation quenching due to high ionization and excitation density induced by nuclear recoils. The heat loss for ER in noble liquids is negligible in the keV or MeV scale.

#### 2.2.2 Location Reconstruction

Having S2 signals allows us to reconstruct the position of the initial event site. The drift velocity was measured to be  $v_{\rm d}=0.93\pm0.01$  mm/µs at  $E_{\rm drift}=200{\rm V/cm}$ . The drift time  $(t_{\rm drift})$  between the start of the S1 pulse and the start of the S2 pulse determines the relative vertical (z) position with respect to the liquid-gas interface (z=0). For an event near the bottom cathode, we measure the maximum drift time  $t_{\rm max}=373\sim376$  µm. The vertical position resolution is mostly limited by the pulse reconstruction algorithm and the electron longitude diffusion (caused by Coulomb repulsion) as the electrons drift upward. The diffusion causes the reconstruction algorithm to identify the S2 start time earlier than for a pulse with zero diffusion [24].

For the reconstruction of the transverse (xy) position, we adopt J. Brosky's algorithm to make the best guess using the weighted least squares (WLS) method [25]. For a given event, the goodness of fit is defined as

$$\chi^2 = \sum_{i}^{PMTs} \frac{1}{\sigma_{M_i}^2} (M_i - L_i(x, y) M_{\text{tot}})^2, \tag{2.1}$$

where  $M_i$  is the measured S2 light in PMT i,  $M_{\text{tot}}$  is the total measured S2 in all PMTs,  $L_i(x, y)$  is the expected light collection (Light Response Function). The WLS method com-

putes all positions, and the objective is to find the best (x, y) values such that the WLS is minimized. Of course, this is an over-simplification of how the algorithm works. In reality, the challenge comes from the determination of the L(x, y) function and using a good  $\sigma_{M_i}^2$  definition [25].

The vertical location information is also encoded in the S1 signal. Depending on the vertical location, the light collection efficiency for scintillation varies between the top and the bottom of the TPC. In the absence of the S2 pulse, an S1 Top-bottom asymmetry (TBA) parameter, defined as

$$TBA = \frac{S1_{\text{top}} - S1_{\text{bottom}}}{S1_{\text{top}} + S1_{\text{bottom}}}$$
(2.2)

is normally used to roughly determine the z-position of an event. Due to the total internal reflection at the liquid-gas interface, the shape of the TBA spectrum drastically depends on whether or not the gas pocket is present. LAr scinitillation events near the bottom cathode window typically have TBA $\sim$ -0.3 while events near the top liquid-gas interface typically have TBA $\sim$ 0.5. It's worth mentioning that TBA is biased near the bottom cathode window, depending on whether the event occurs above a PMT or above the PTFE reflector in-between PMTs.

# 2.2.3 Background Discrimination

The ratio of ionization to scintillation (S2/S1) provides discrimination against electromagnetic backgrounds. The stopping power for a recoiling nucleus is much larger than for an electron, making the ionization to scintillation ratio higher for NRs ( $\sim 1$ ) than  $\beta/\gamma$ -induced ER ( $\sim 0.21$ ). This is the main background suppression technique used in xenon based experiments, such as LUX/LZ [7], XENON [6], and PandaX [8]. It is important to note that, since the recombination probability affects the S2/S1 ratio, most experiments need to adjust the applied drift field strength to achieve the best ER/NR separation power.

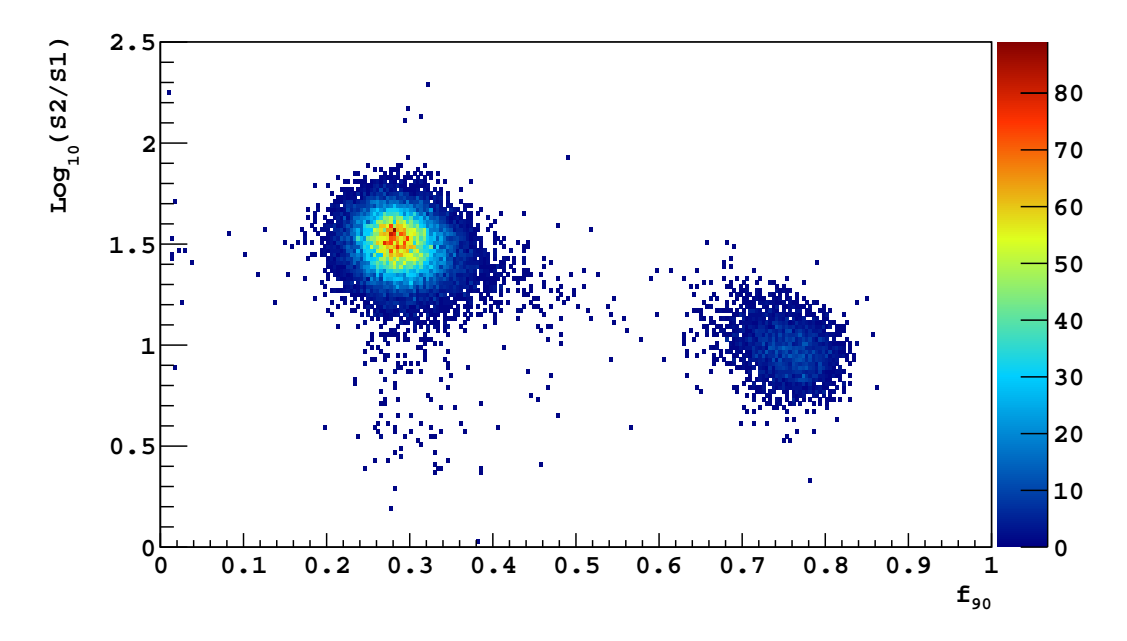


Figure 2.3: Comparison between S2/S1 and PSD discriminations. Events are from <sup>241</sup>Am-Be (a neutron source) calibration data where the S1 is in the range from 200 PE to 400 PE. The blob on the left (right) corresponds to ER (NR) events. The additional cuts are the quality cuts (Sec. 3.3.1) and the 70-day TPC cuts (Sec. 3.3.2).

The time profile (pulse shape) of the argon scintillation provides further discrimination power against electromagnetic backgrounds. This is because argon scintillation comes from the de-excitation of Ar dimers that forms either the singlet  $(I_1)$  or triplet state  $(I_3)$ , which have drastically different decay times of 6 ns and 1500 ns, respectively. The  $I_3$  has a substantially longer lifetime because the transition to the ground state is forbidden due to the conservation of angular momentum. While the lifetime of the individual states does not seem to depend on the ionization density (dE/dx), the number ratio of the singlet to the triplet state  $(I_1/S_3)$  does. According to [26] [27], the  $I_1/I_3$  is typically higher for NR (higher dE/dx) than ER (lower dE/dx). The conversion of  $I_1$  (the higher energy state) to  $I_3$  by free electrons has been proposed as the mechanism for the positive correlation between dE/dx and  $I_1/I_3$ —lower dE/dx have the recombination occurring on longer time scales and consequently have a greater chance of converting states.

This powerful Pulse Shape Discrimination (PSD) technique to suppress  $\beta/\gamma$  activity is the main motivator for the choice of liquid argon in the DarkSide experiment over liquid xenon, which does not have a strong PSD. In the DarkSide-50 experiment, we choose  $f_{90}$  as the PSD parameter.  $f_{90}$  is defined as the fraction of S1 light in the first 90 ns. Fig. 2.3 shows how impressive the  $f_{90}$  parameter is in terms of the separation power when compared to the S2/S1 parameter.

Although it's observed that the scintillation pulse shape also depends on the applied drift field strength [28], the scale of variation is not as drastic as the S2/S1 parameter.

#### 2.2.4 Signal Corrections

The S1 and S2 signal sizes depend on the xyz spatial location of the event. To correct the location dependence of the S1 and S2 signals, we conducted multiple internal calibrations with a  $^{83m}$ Kr source.

The  $^{83m}$ Kr was introduced into the active volume via the cryogenic and purification circulation system.  $^{83m}$ Kr is produced by  $^{83}$ Rb decays ( $\tau \sim 124.4$  day). While  $^{83}$ Rb, in the form of RbCl compound, is firmly adsorbed onto activated charcoal,  $^{83m}$ Kr escapes into the argon stream. The  $^{83}$ Rb source activity at the time of preparation was 8.5 kBq (September 2012) [21]. The  $^{83m}$ Kr will not remain in the argon thanks to its short  $\sim 2.6$  hours lifetime. A  $^{83m}$ Kr decay releases two sequential X-rays (32.1 keV and 9.4 keV) where the intermediate state has a mean lifetime of only  $\sim 222$  ns. Because of the slow component of LAr scintillation, the two X-rays jointly produce a single deposition of 41.5 keV.

To obtain a sample of events dominated by  $^{83m}$ Kr, we fit a Gaussian (in the case of the AAr data, Gaussian +  $^{39}$ Ar  $\beta$ -decay spectrum) function to the 41.5 keV peak ( $\mu_{S1} \sim 288.8$  PE and  $\sigma_{S1} \sim 20.0$  PE at 200 V/cm), and select events in the range from  $\mu - 3\sigma$  to  $\mu + 3\sigma$ . We assume the  $^{83m}$ Kr is uniformly distributed throughout the active volume. We define the correction maps by first plotting the signal (either S1 or S2) as a function of  $t_{drift}$  and (x,y), and then extracting a data-driven map to correct the signals to the TPC center (r = 0 and

 $t_{\text{drift}} = t_{\text{max}}/2$ ). For example, we calculated the ratio  $S2_{\text{center}}/S2(x, y)$  for every (x,y) bin and obtained a map of the radial correction factor for S2 signals.

Most corrections turn out to be small with two exceptions, the z-correction for S1 and the radial correction for S2. The z-dependence of S1 is mainly due to the TPC optics, such as the internal reflection at the liquid-gas interface and the light absorption on the extraction grid. The bottom events are observed to be, on average,  $\sim 10\%$  larger than top events. As for the radial dependence of S2, the S2 yield is about 4 times higher at the center than at the edge. One hypothesis suggests that the large radial dependence may be caused by the deflection of the extraction field grid due to the electric static attraction. Another similar hypothesis blames the dependence on the sagging of the anode window. Either the deflection of grid or the sagging of anode would create a higher electric field at the center of the gas pocket than the edge. The two hypotheses were investigated by C. Zhu [29]  $^{1}$ .

#### 2.2.5 Reconstructing the Recoil Energy

The combination of S1 and S2 allows us to reconstruct the recoil energy. First, the location dependence needs to be corrected as discussed in the previous session. Then, the energy is calculated by

$$E_{ee} = \frac{W}{1+f} \left( \frac{S1}{\epsilon_1} + \frac{S2}{\epsilon_2} \right), \tag{2.3}$$

where W = 23.6 eV/quantum is the energy required to make one ion-electron pair, f = 0.21 (f = 1 for NR) is the ratio of the excitation to ionization, and  $\epsilon_1 = 0.181$  PE/quantum ( $\epsilon_2 = 33.3$  PE/quantum) are detector dependent signal collection efficiency. Those parameters were studied in detail in  $^{83m}$ Kr calibration data [30].

In order to get the NR energy ( $E_{ee} = E_{nr} \times \mathcal{L}_{nr}^{\text{eff}}$ ), we adopt the measurement of NR quenching factors in LAr from the SCENE experiment, which is summarized in the Tab. 2.1.

<sup>&</sup>lt;sup>1</sup>The calculation shows that the gas pocket height needs to be  $3 \sim 4$  mm at center and 1 cm at the edge in order to get the observed S2 yield variation. Two hypotheses can both be true given the scales of the anode window ( $\sim 40$  cm diameter and 3 mm thick) and the grid.

Table 2.1: The expected NR quenching factor of DarkSide-50 at 200 V/cm based on the measurements by SCENE [28].

$E_{nr} [\mathrm{keV}]$	$\mathcal{L}_{nr}^{ ext{eff}}$		
16.9	$0.202 \pm 0.008$		
20.5	$0.227 \pm 0.010$		
25.4	$0.224 \pm 0.010$		
36.1	$0.265 \pm 0.010$		
57.2	$0.282 \pm 0.013$		

# 2.3 Underground Argon

One challenge of scaling up dual-phase liquid argon TPCs comes from  $^{39}$ Ar, a radioactive isotope naturally occurring in atmospheric argon (AAr).  $^{39}$ Ar undergoes  $\beta$ -decay with an endpoint at 565 keV and a half-life of 269 yr and is the dominant source of background ( $\sim 1$  Bq/kg) in AAr. Because  $^{39}$ Ar is mostly produced by cosmic ray activation, its content in argon will gradually decay away if stored deep underground. Although AAr works fine at the scale of DarkSide-50, a kHz level trigger rate will cause too many pile-up events for a ton-scale two-phase TPC (the  $t_{\rm max}$  is usually on the order of hundreds of µs). Hence, the Underground Argon (UAr) is absolutely necessary to perform a WIMP search at the ton-scale. We extracted a total of 155 kg of low radioactivity UAr in six years of effort. The batch of UAr was deployed in DarkSide-50 detector in April 2015.

The <sup>39</sup>Ar depletion factor was later determined to be  $(1.4 \pm 0.2) \times 10^3$  during the 70-day UAr campaign (section 3), as shown in figure 2.4. The presence of <sup>85</sup>Kr is confirmed by an independent analysis searching for  $\beta$ - $\gamma$  coincidences from <sup>85</sup>Kr decays into <sup>85m</sup>Rb (branching ratio  $\sim 0.43\%$ ). Its presence in the UAr ( $\sim 5 \text{mBq/kg}$ ) is a surprise but not a concern. After all, an argon experiment is not afraid of  $\beta$ -decays, and cryogenic distillation could easily remove its content in the UAr for future experiments.

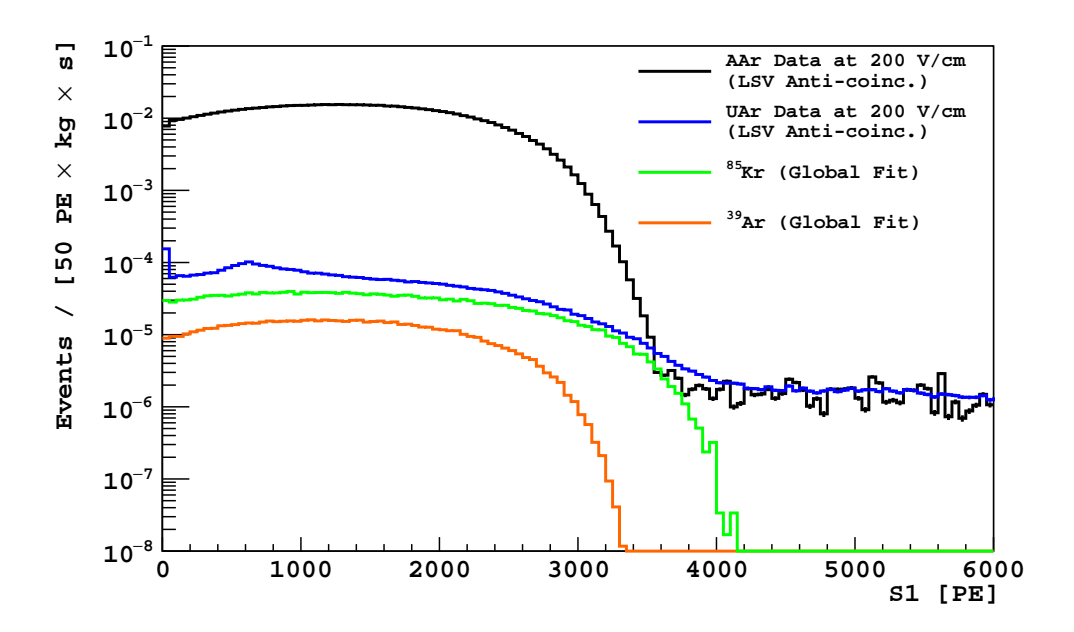


Figure 2.4: S1 spectra of the WIMP search data. The depletion factor is estimated by comparing the AAr data spectrum (black) to the MC fitted 39Ar spectrum (orange) of UAr data (blue). The <sup>39</sup>Ar spectrum in UAr data is obtained by performing a multi-dimensional fit which incorporates all  $\beta$  and  $\gamma$  activity in one simultaneous fit over both energy and drift time spectra. Plot from Ref. [22].

### 2.4 Neutron Veto

It is challenging for an experiment to rely only on passive shielding to reduce neutron-related backgrounds, especially for DarkSide-50 TPC which cannot afford heavy fiducialization. This makes the interpretation of a few WIMP-like signals problematic in a rare event search. The use of a neutron veto provides a better technique to actively suppress neutron-related backgrounds. In the case of the LNGS laboratory, since it has a comparably shallow depth of only 3800 meters water equivalent), the rate of cosmogenic neutrons will be higher than other sites, such as Jinping, SNO lab, and Sanford Underground research facility.

In addition to rejection, having an active veto allows us to reliably classify the origins of the neutrons. This not only minimizes assumptions in the final neutron background prediction, which traditionally relies on a Monte Carlo based estimator but also provides the number of specific  $(\alpha, n)$  neutrons for developing NeuCBOT, an  $(\alpha, n)$  reaction neutron calculator based on TALYS. Neutron classification will be discussed in Ch. 5.

#### 2.4.1 Liquid Scintillator Vessel

The Liquid Scintillator Vessel (LSV) is a 4.0 m diameter stainless steel sphere filled with 30 metric tonnes of boron-loaded organic liquid scintillator. The inner surface of the vessel was covered up with Lumirror, and the scintillator light is closely monitored by 110 Hamamatsu R5912 8-inch PMTs. The scintillator cocktail has three primary components: pseudocumene (PC, C<sub>6</sub>H<sub>3</sub>(CH<sub>3</sub>)<sub>3</sub>), trimethylborate (TMB, B(OCH<sub>3</sub>)<sub>3</sub>), and 2,5-diphenyloxazole (PPO, C<sub>15</sub>H<sub>11</sub>NO). The PC is the primary scintillator while the TMB introduces <sup>10</sup>B which increases the neutron capture cross-section. A few grams per liter of wavelength shifter (PPO) was added to increase the detection efficiency of the LSV. The LSV scintillator operates at room temperature.

### 2.4.2 Signal Formation

The outer detector DAQ systems (both the neutron veto and water tank) are jointly triggered by the TPC. Once the TPC is triggered, the veto opens a 70 µs DAQ window and records the coincident signals. When a neutron escapes the TPC to enter the LSV, it produces two signals — first a thermalization (prompt) signal as the neutron slows down, and second a delayed capture signal mainly from captured on <sup>10</sup>B, hydrogen, and carbon nuclei.

The prompt signal alone can reject over 99% of the neutrons in the LSV with less than 1% acceptance loss. The acceptance loss is minimal because the thermalization signals typically occur shortly after the TPC trigger. This feature, along with good veto timing, allows us to narrow the search window of the thermalization signal down to -50 ns to 250 ns with respect to the TPC trigger time. Since a WIMP would not give a coincident signal in the veto, the acceptance loss primarily comes from random coincident noise, such as in-situ  $^{14}$ C  $\beta$ -decay or random thermal noise from PMTs. In addition to neutrons,  $\gamma$ -rays can penetrate

the TPC cryostat and produce prompt signals as well about 25% to 50% of the time. The prompt signals from the  $\gamma$ -rays have a light yield of 0.52 PE/keV<sub>ee</sub>, while according to the neutron calibration studies, the scintillation from proton recoils is quenched to about 5 to 10% of that from electron recoils of the same kinetic energy, while carbon recoil scintillation is quenched to about 1 to 5%.

The veto timing is calibrated by matching  $^{60}$ Co peaks from WIMP search data.  $^{60}$ Co from the TPC cryostat and PMTs emits two  $\gamma$ -rays (1.17 MeV and 1.33 MeV) simultaneously. The energetic  $\gamma$ -peaks are easily spotted in both the TPC and LSV. We define the rising edge of the  $^{60}$ Co  $\gamma$ -ray signal in veto as the prompt time.

Once the neutron slows down in the scintillator, the second delayed capture signal typically occurs within  $\sim 20~\mu s$  of the prompt signal. The capture signal is independent of the initial kinetic energy of the neutron, but its size and delay time depends on specific isotopes with a time scale on the order of 1 to 100  $\mu s$ . We studied the capture signals in  $^{241}Am$ -Be and  $^{241}Am$ - $^{13}C$  calibration data and used them to identity and separate neutrons from  $\gamma$ -rays, which is an important tool used for the neutron counting in the blind analysis (section 5).

As an example, when a neutron is captured on <sup>10</sup>B, the decay product deposits energy through one of the two channels:

$$^{10}$$
B +  $n \to {}^{7}$ Li (1015 keV) +  $\alpha$  (1775 keV),  
 $\to {}^{7}$ Li\* +  $\alpha$  (1471 keV)  $\to {}^{7}$ Li (1015 keV) +  $\alpha$  (1775 keV).

Since the capture location is likely to be very close to the TPC cryostat, there is a non-negligible probability that the  $\gamma$ -ray can go right back toward the TPC cryostat and lose all energy in the steel <sup>2</sup>. The  $\alpha$ 's, on the other hand, will always deposit its full energy in LSV scintillator thanks to its extremely short track length. One downside of the  $\alpha$ -signals is its relatively high ionization quenching factor, which reduces the scintillation light output down

<sup>&</sup>lt;sup>2</sup>This is an argument that boron-loaded scintillator is comparably better than gadolinium which only whose decay products only involves  $\gamma$ -rays.

to an equivalent of 50 to 60 keV<sub>ee</sub> energy deposit. Therefore, having a low background and high light collection efficiency is crucial to detect those  $\alpha$ 's from captures. The delay signal cut will have the heaviest acceptance loss.

#### 2.5 Water Cherenkov Veto

The water tank, also known as the Water Cherenkov Veto (WCV), was borrowed from the Borexino counting test facility. It provides a powerful shield against the external background ( $\gamma$ -rays and neutrons from the rock). It vetoes cosmic rays (muons) via Cherenkov radiation. The interior surface of the WCV and the exterior of the LSV sphere are covered with a layer of Tyvek reflector. The WCV is monitored by 80 8-inch PMTs with 56 of them mounted on the cylindrical tank wall and 24 on the floor. Only 80 PMTs are needed because the cosmic-ray-induced Cherenkov signals are typically hard to miss.

The muon flux at Hall C of LNGS, was measured in veto self-trigger data by requiring a large WCV signal (> 100 PE). The study returns 1.1 muon/m<sup>2</sup>/h, which is consistent with the Borexino measurements [31].

# 2.6 Data Processing Software

In the first stage of data processing, the raw waveform from the TPC are processed by an event reconstruction software called DarkArt, which is built within the Fermilabs art framework [32]. A brief description of DarkArt algorithm goes as the follow.

- 1. Baseline finding. For each TPC channel, DarkArt first determines a baseline using a 80 ns moving average and subtracts the baseline from the raw waveform. In the region of single PE or cluster of PEs (a pulse), the baseline is linearly interpolated between the start and the end of the region;
- 2. **PE normalization**. For each TPC channel, DarkArt scales the baseline-subtracted waveform to the unit of PE using the single PE response mean obtained from the laser calibrations (App. D.1);

- 3. Channel summation. For each TPC channel, the baseline-subtracted waveform is zero-suppressed with an amplitude threshold of 0.1 PE/sample, and then accumulated to the summed-channel waveform. The step of zero-suppression is necessary to avoid any coherent noise from constructively adding up during the channel summation.
- 4. **Pulse identification**. On the summed-channel, the pulse finding algorithm scans over the entire waveform and identifies pulses (e.g. pulse start time, pulse end time). The pulse finder efficiency is unity for S1-like pulses above 15 PE and for S2-like pulses above 40 PE [33]. For each pulse, DarktArt also computes integrals over a fixed 7  $\mu$ s and 30  $\mu$ s window from the pulse start time.

We use DarkArtOD, a different software also built in the art framework, to process the raw waveform from the vetoes. The PE normalization and the channels summation steps for the LSV and the WT are similar to the TPC. A brief description of the key algorithms goes as the follow.

- Baseline finding. The veto DAQ records 20 samples (16 ns) before and after each pulse, and DarkArtOD uses the average of first 15 samples to define a pulse baseline due to the DAQ-level zero-suppression (no continuous baseline in raw data). The zero-suppression is necessary for the sake of saving data storage space;
- Cluster identification. DarkArtOD performs a clustering algorithm on the summed-channel waveform using a "top-down" iterative process to search for clusters. The algorithm first finds the peak above 2 PE amplitude threshold and then iteratively search for the cluster start time (end time) to the left (right) until it reaches a 20 ns wide empty waveform. The clusters are used to determine the LY and in-situ background (e.g. <sup>14</sup>C, <sup>60</sup>Co) in the LSV;
- LSV Slider. The slider is a 500 ns wide window scanning over the delayed coincident region (DCR). As it slides, it computes the charge (integral) within the running window and returns the maximum charge in the DCR. The DCR is defined from the end of the prompt window to the end of the veto acquisition. Most veto runs have a 200  $\mu$ s long data acquisition. The slider is used to reconstruct the neutron capture signals.

In the second stage, a higher level of event reconstruction software called SLAD (Slim Analysis Data) takes the DarkArt outputs and computes the TPC related physical variables, such as S1, S2,  $f_{90}$ , S1MF, and  $t_{drift}$ . By default, SLAD identifies the first pulse as the S1 signal, the second as the S2, and the time difference between the start time of the first two pulses as  $t_{drift}$ . For an event with three pulses, if the time difference between the second and third pulse approximately equals to the  $t_{max}$ , the third pulse is identified as a S2-echo. Then,

the xy algorithms take place to estimate the best (x,y) positions per S2 pulse. Finally, a veto matching algorithm finds the veto events for every TPC event base on the time stamps and flag the event if the matching is unsuccessful.

# Chapter 3

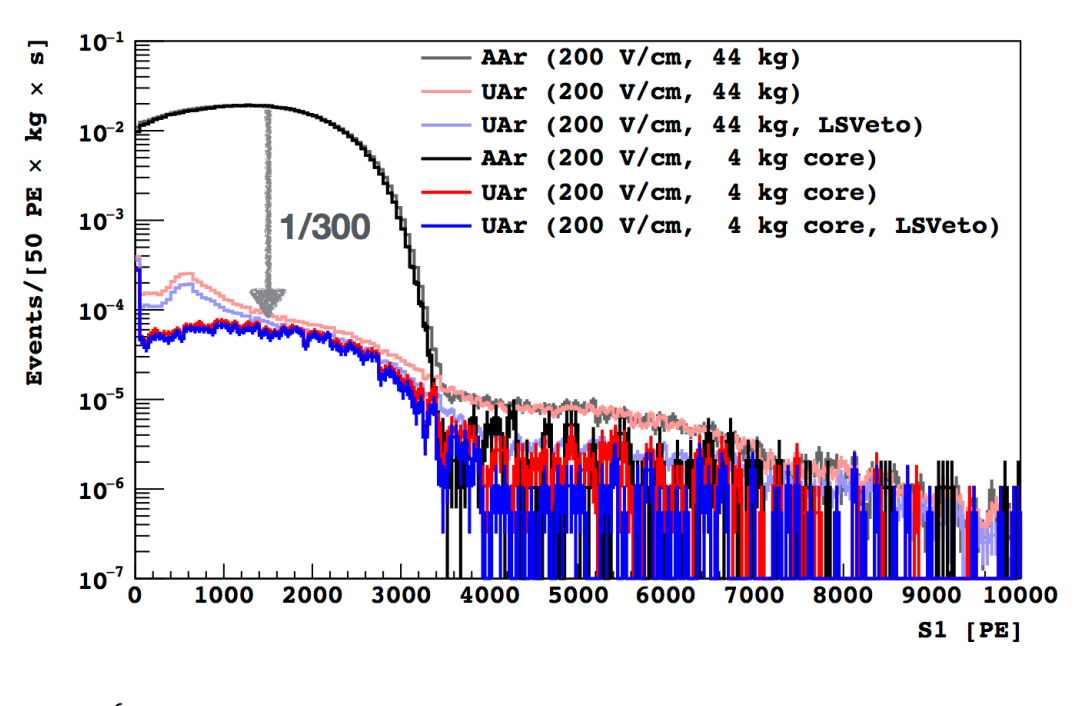
# The First Analysis with the UAr

In this chapter, we report results from the first WIMP search performed using low radioactivity argon extracted from an underground source (UAr), followed by a detailed investigation of the electronic recoil (ER) backgrounds. The procedure for setting ER leakage curve is described. While making the ER prediction, we discover a  $\gamma$  related background that cannot be described by an analytic  $f_{90}$  model.

# 3.1 The 70-day Campaign

The TPC was filled with AAr during the first DM search campaign. In March 2015 we replaced the AAr with a batch of UAr and had a second DM search campaign with a total exposure of 70.9 live-days (April 8 2015 to July 31 2015). The WIMP search data with the UAr target was divided into runs of 6-hour duration, with TPC laser calibration (lasting 10 minutes) runs taken every two WIMP search runs. As expected, the UAr data had a much lower trigger rate ( $\sim 1.6$  Hz) than that of the AAr data ( $\sim 50$  Hz) thank to the UAr. The overall  $\beta$ -decay rates are reduced by approximately a factor of 300, as shown in Fig. 3.1. The composition of the ER backgrounds will be discussed in Sec. 3.4.1.

The 70-day UAr campaign is also the first DM search with a fully functional neutron veto, which uses boron-loaded liquid scintillator produced by adding tri-methyl borate (TMB)



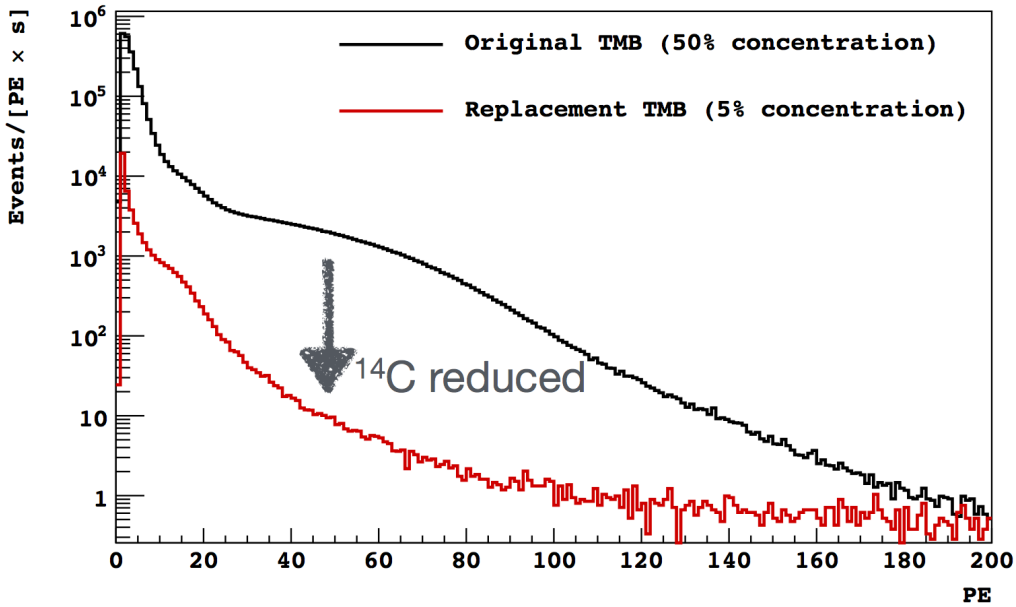


Figure 3.1: Top: Comparing the S1 spectra of AAr data to the heavily fiducialized UAr core data. The shapes of the 4 kg core at the center of TPC (blue and red) resembles the  $\beta$ -spectrum shape of <sup>39</sup>Ar (black). The comparison shows that the overall  $\beta$  activity is reduced by a factor of 300 since the previous AAr campagin. Plot from M. Wada. Bottom: The energy spectra in the neutron veto before and after TMB replacement shows the overall reduction of <sup>14</sup>C activity. Plot from Ref. [34]

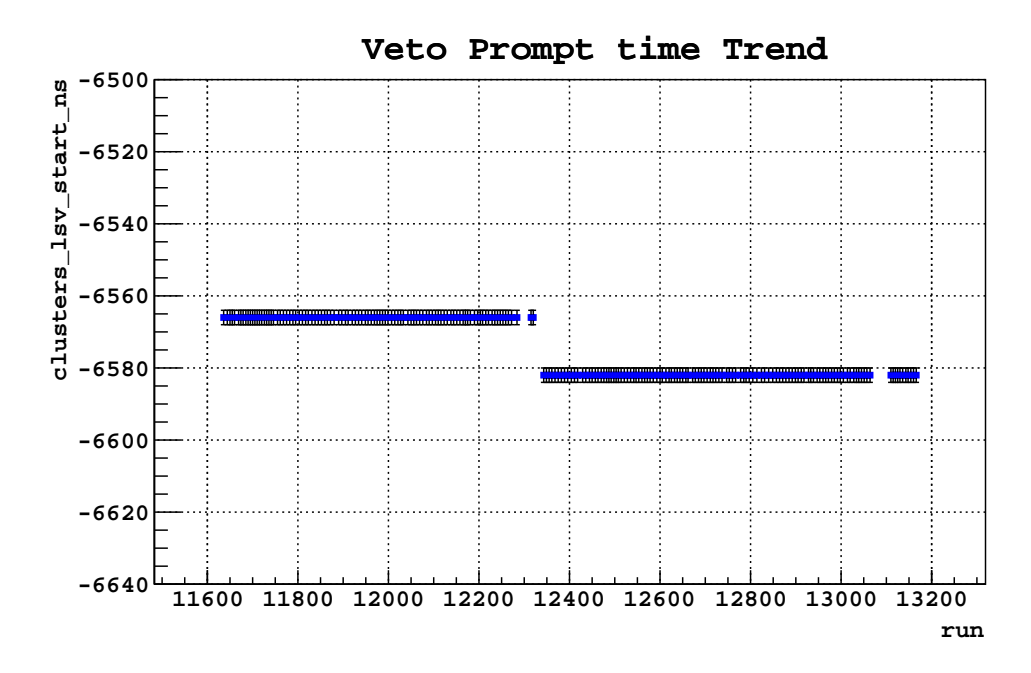


Figure 3.2: The veto prompt time as a function of run number. The prompt time is defined as the start time of the first signal in veto.

to a standard scintillator cocktail. Due to the high rate of accidental coincidences from the unexpectedly high  $^{14}$ C content in the TMB ( $\sim 6.7$  Bq/kg), the liquid scintillator veto performance was limited in the preceding AAr campaign. Following that we replaced the TMB with a low-activity TMB ( $\sim 8.3$  mBq/kg) (Fig. 3.1), the veto achieved a neutron veto efficiency greater than 99.5% with a WIMP acceptance loss less than 16% [34].

### 3.2 Data Selection and Validation

DarkSide-50 had been taking data under various configurations, and selecting a good set of UAr data for WIMP search in an unbiased way was by no means a trivial task. First, we selected a set of runs with the desired type, duration, and the number of events. This step was automatically completed by scanning through the DAQ database. The run type forced the selection of runs taken with a 440 µs acquisition window, 200 V/cm drift field, 2.8 kV/cm extraction field, and a non-collapsing gas pocket, etc. A non-crashing run in the WIMP mode is 6 hours long, but once in a while, the DAQ system would crash right after a

new run started. The minimal run duration (15 minutes) and the minimal number of events (1000) criteria avoided the questionable short runs with negligible loss of livetime. Next, the non-WIMP search runs, such as <sup>85</sup>Kr and <sup>241</sup>Am-<sup>13</sup>C calibration runs, were manually excluded. This step was completed by human scanning over the electronic logbook because many of those non-WIMP search runs have the identical DAQ configurations.

The validation step involves checking the stability of the detectors over time. This was accomplished by selecting a list of key parameters that represented the performance of the detectors and plotting them as a function of time over the entire UAr campaign. The checklist included TPC trigger rate, TPC and veto electronic noise (baseline mean and variance), TPC PMT performance (e.g., gain, occupancy), TPC and veto light yields, TPC maximum drift time, and neutron veto prompt time. A rapid change in parameter values indicates either inaccurate data reconstruction or unstable detector performance. The problematic runs are either removed or re-processed with corrections. For example, when checking the stability of veto prompt time (the physical time corresponds to TPC trigger times), we discovered a 16 ns constant shift in the middle of the UAr campaign as shown in Fig 3.2. After checking the electronic logbook, we determine the shift was due to a veto DAQ system upgrade and therefore not physical. We then manually adjusted the offset in the reconstruction code and reprocessed the data since the upgrade, so that we have a consistent veto timing.

Please see App. D for the stability check of other features on the list.

# 3.3 The Analysis Cuts

### 3.3.1 Quality Cuts

The quality cuts are a set of rudimentary requirements applied to almost any DarkSide-50 analysis. The purpose is to make sure that the detector recording is in stability conditions when an event is recorded. We defined the following quality cuts to pass an event.

- 1. **NChannel Cut**. We require all 38 TPC channels are alive. The acceptance of this cut is close to unity;
- 2. **Baseline found cut**. We require the baseline is successfully found in all 38 channels <sup>1</sup>. The acceptance of this cut is close to unity;
- 3. Veto present cut. We require the veto data to be present. We expect the one-to-one correspondence between a TPC event and a veto (LSV/WT) event. Because the event IDs are not necessarily aligned (veto may skip n events for example), the matching algorithm search veto events whose GPS time-stamps are in proximity for each TPC event. Although occasionally the time-stamps may not be aligned, the acceptance of this cut is close to unity as a result of using the time matching algorithm;
- 4. Livetime cut. The start time of the acquisition is at least 1.35 ms after the acquisition of the previous event ends. There is an 810  $\mu$ s long inhibit-time window ( $t_{\rm max} \sim 376 \,\mu$ s) immediately following the acquisition window where no data will be recorded. The inhibit-time window prevents the DAQ from triggering on S2 echo or S2 long tail. A S2 echo comes from single electrons emitted from TPC cathode which is struck by bright S2 scintillation light. But if an event (S1 and S2 pulses) falls in the inhibit-time window, we may end up triggering on the S2 echo or S2 tailing. The livetime cut eliminates this scenario. The acceptance of this cut is close to unity.

#### 3.3.2 TPC Analysis Cuts

Since we expect a WIMP to give a single scatter NR uniformly distributed in the active LAr volume, we designed the following standard TPC analysis cuts to pass an event.

- 5. **2-pulses cut**. We require two pulses OR three pulses in the event with the third pulse being a S2 echo. S2 echo is defined as a S2-like ( $f_{90} < 0.2$ ) pulse that occurs exactly 373 µs (the maximum drift time,  $t_{\text{max}}$ ) after the real S2 pulse. The purpose of this cut is to select events with two physical pulses. The acceptance of this cut is close to unity;
- 6. Trigger time cut. We require the start time of the first pulse (presumably S1) to be in coincidence with the expected trigger time ( $-6.1\,\mu\text{s} < t < -6.0\,\mu\text{s}$ ). The time 0 is not the TPC trigger time. Occasionally when the TPC is triggered by a S2-like pulse (slow rise as compared to a S1 pulse), the start time identified by the pulse finding algorithm is likely to fall outside of the 100 ns narrow window. The acceptance of this cut is close to unity;
- 7. **S1 saturation cut**. The first pulse (presumably S1) does not saturate any channels of the V1720 digitizer. The acceptance of this cut is unity because S1 does not start

<sup>&</sup>lt;sup>1</sup>The term "sum baseline cut" is often used. The sum does not mean the sum channel, because the baseline finding algorithm is implemented to check at a channel by channel basis.

saturating the ADC until  $\sim 900$  PE while the WIMP search focuses on low energy (< 450 PE);

- 8. 95% S1MF cut. We require the S1 maximum fraction (S1MF) to be below the predefined S1MF thresholds. S1MF is defined as the fraction of the total S1 light in the dominant channel. Since the variable S1MF depends on the S1 size and vertical event location, to enforce a uniform acceptance loss, we defined the thresholds as a function of S1 and  $t_{\text{drift}}$ . An event is compared to the threshold at the corresponding S1 bin and  $t_{\text{drift}}$  bin. The purpose of this cut is to remove the fused-silica Cherenkov background. The acceptance of this cut is 95% by design. Later in the 540-day analysis, we improved this cut by changing it to S1pMF cut (Sec. 5.3.1);
- 9. **S2**  $f_{90}$  cut. We require the second pulse to be S2-like ( $f_{90} < 0.2$ ). This cut removes events whose S2 is unreasonably large since a normal S2 pulse is expected to have  $f_{90} < 0.01$  due to the slow rise time. The acceptance of this cut is close to unity;
- 10. **Minimum S2 cut**. We require the second pulse (presumably S2) to be greater than 100 PE after the xy (radial) correction. This is a loose cut intended to remove events whose second pulse is inconsistent with being an S2 from either a NR or ER. The acceptance of this cut is close to unity. Later in the 540-day analysis, we change it to cut on the uncorrected S2 variable to decouple it from the xy algorithm;
- 11. **40** µs  $t_{\text{drift}}$  **cut**. We require the drift time of an event to be greater than 40 µs and smaller than 334.6 µs. The maximum drift time during the UAr campaign is 375.9 µs. Since the drift velocity is  $0.93 \pm 0.03$  mm/µs, this is equivalent to cutting off ~43.0 mm from the top and ~44.4 mm from the bottom of the TPC. The remaining mass after the  $t_{\text{drift}}$  cut is  $(36.9 \pm 0.6)$  kg [22].

The combination of cut 5, 9, and 10 is also called **single-scatter cut**, which in principle select events with an S1 as the first pulse and an S2 as the second pulse. Unless specified otherwise, cut 11 is the standard fiducial cut in z and the combination from cut 5 to 11 is the **70-day TPC cuts**. We do not apply any radial cut until the 540-day analysis.

#### 3.3.3 Veto Cuts

We do not expect the WIMP to leave any signal in the LSV/WT. Hence to remove events with any coincident veto signals, we reject an event with the following cuts.

12. **Veto prompt cut**. We reject an event if the signal in the prompt window is greater than 1.0 PE. The prompt window is defined from -50 ns to 250 ns with respect to the TPC trigger time. The main purpose of this cut is to remove events with neutron thermalization signal in LSV. This cut also removes  $\gamma$ 's about 25-50% of the time if

- the  $\gamma$ 's manage to escape the TPC cryostat. The acceptance of this cut is 0.995 while the efficiency on rejecting neutron by this cut alone is 0.9927  $\pm$  0.0005 [9];
- 13. Veto delay cut. We reject an event if the maximum charge identified by the slider in the delayed coincident region (DCR) is greater than 3 (before run 12638) or 6 (after run 12638). The slider is described in Sec. 2.6. The purpose of this cut is to detect neutron capture signal in the form of  $\gamma$ -ray or  $\alpha$  (Sec. 2.4.2). The acceptance of this cut is close to 0.835 while the efficiency of rejecting neutron by this cut alone is 0.9958  $\pm$  0.0004 [9];
- 14. **Veto pre-prompt cut**. We reject an event if the maximum charge identified by the 500 ns slider in the pre-prompt region is greater than 3 PE. The pre-prompt region is defined from the start of veto acquisition to the prompt time. It is conceivable that an external neutron can be created by a process in the LSV, such as the photonuclear interaction. The created neutron can then enter the TPC after the LSV signal. This cut removes events from this scenario. The acceptance of this cut is close to unity;
- 15. **Muon cut**. We reject an event if the total charge within the neutron veto acquisition window is greater than 2000 PE OR the total charge of the water tank (WT) is greater than 400 PE. The purpose of this cut is to remove muons. The acceptance of this cut is close to unity. Later in the 540-day analysis, we changed it to just cutting on the 400 PE since a muon entering the LSV has to leave signal while penetrating the WT;
- 16. Cosmogenic cut. We reject an event if the time elapsed since the last muon (identified by the muon cut) is less than 2 s. This cut removes cosmogenic neutrons. As the muon passed by, it can produce heavy nuclei which then release high energy neutrons. The decay lifetime of the cosmogenic nuclei is on the order of a few hundred milliseconds, which is much longer than the veto DAQ window. The acceptance of this cut is close to unity.

### 3.4 Main Results

# 3.4.1 ER Backgrounds

Fig. 3.3 is an energy spectrum using S1-late at null field. S1-late is defined as the integral from 90 ns to 7 µs with respect to a pulse start time. We use it instead of S1 (the first 7 µs integral) to avoid digitizer saturation which typically occurs in the prompt signal (first 90 ns). The  $\gamma$ -ray lines which originate from identified levels of <sup>238</sup>U, <sup>232</sup>Th, <sup>40</sup>K, and <sup>60</sup>Co in the detector construction materials are consistent with expectations based on our materials screening [22]. The resolution of the peaks in both the AAr and UAr data indicates a stable

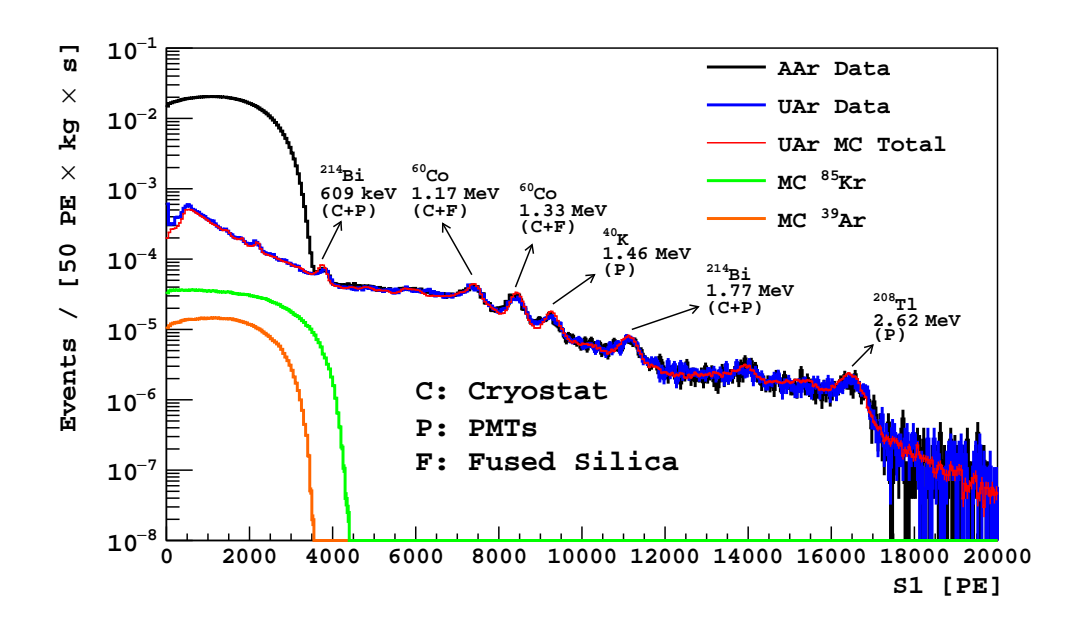


Figure 3.3: Live-time-normalized S1-late spectra obtained at zero drift field. S1-late is defined as S1 minus S1 prompt (integral over the first 90 ns). S1-late is used to avoid ADC saturation. Plot from Ref. [22].

light yield (LY) throughout the AAr and UAr campaign. The MC fit of the spectrum gives an estimate of  $\beta$  background from  $^{39}$ Ar and  $^{85}$ Kr in the argon, with activities of  $(0.73\pm0.11)$  mBq/kg and  $(2.05\pm0.13)$  mBq/kg respectively. The discovery of  $^{85}$ Kr in the UAr was unexpected but it can be easily removed via cryogenic distillation. The presence of  $^{85}$ Kr in UAr could be explained from atmospheric leaks, or by deep underground natural fission processes. Fission-produced  $^{85}$ Kr has been observed in deep underground water reservoirs at the same order of magnitude as those of  $^{39}$ Ar. It is speculated that underground nuclear explosion tests are possible as well.

# 3.4.2 Observing a F90 Shoulder

In this analysis, we observe a persistent shoulder on the right-hand side of the  $f_{90}$  distribution that would not go away after all WIMP search cuts, as shown in Figure 3.4-Bottom. A detailed investigation was conducted by comparing the  $f_{90}$  profiles to the 50-day AAr data

set and by studying the behavior of the excess under various analysis cuts (Sec. 3.5.2). The excess on the  $f_{90}$  shoulder will have a direct impact on setting the ER leakage curve.

#### 3.4.3 Designing the WIMP Box

The WIMP search box as shown in Fig. 3.6-top is bounded by  $f_{90} = 1$  from the top, a 90% NR acceptance curve from the bottom, an ER leakage curve from the left, and a S1=450 PE from the right. The 90% NR acceptance curve was obtained from the SCENE experiment.

#### An Analytic F90 Model

Hinkley's model is one of several analytic models to describe the  $f_{90}$  distribution. The analytic form is essentially a ratio of two Gaussians. We adopted it from [35], and modified the form in [36]. The probability distribution is,

$$P(x) = \frac{\mu x f_p \sigma_l^2 + \mu (1 - x)(1 - f_p) \sigma_p^2}{\sqrt{2\pi (x^2 \sigma_l^2 + \sigma_p^2 (1 - x)^2)^3}} \exp\left[-\frac{(\mu x (1 - f_p) - \mu (1 - x) f_p)^2}{2(x^2 \sigma_l^2 + (1 - x)^2) \sigma_p^2}\right],$$
 (3.1)

where x is the variable  $f_{90}$ ,  $\mu$  is the number of PE (S1),  $f_p$  is the median value of  $f_{90}$  at a given S1,  $\sigma_p^2$  is the variance of the number of PE in S1 prompt region (the first 90 ns), and  $\sigma_l^2$  is the variance of the number of PE in S1 late region. Thus, combining the two we have the variance of  $f_{90}$  as

$$\sigma_{\text{f90}}^2 = \frac{f_p^2 \sigma_p^2 + (1 - f_p)^2 \sigma_l^2}{\mu^2}.$$
 (3.2)

Several factors are contributing to the  $\sigma_p^2$  and  $\sigma_l^2$  terms. We further broke them down as,

$$\sigma_p = \sqrt{\mu f_p (F + \sigma_{\text{SPE}}^2 + \sigma_{\text{TPB}}^2) + \sigma_{n,p}^2},$$
(3.3)

$$\sigma_l = \sqrt{\mu(1 - f_p)(F + \sigma_{\text{SPE}}^2 + \sigma_{\text{TPB}}^2) + \sigma_{n,l}^2}.$$
(3.4)

(3.5)

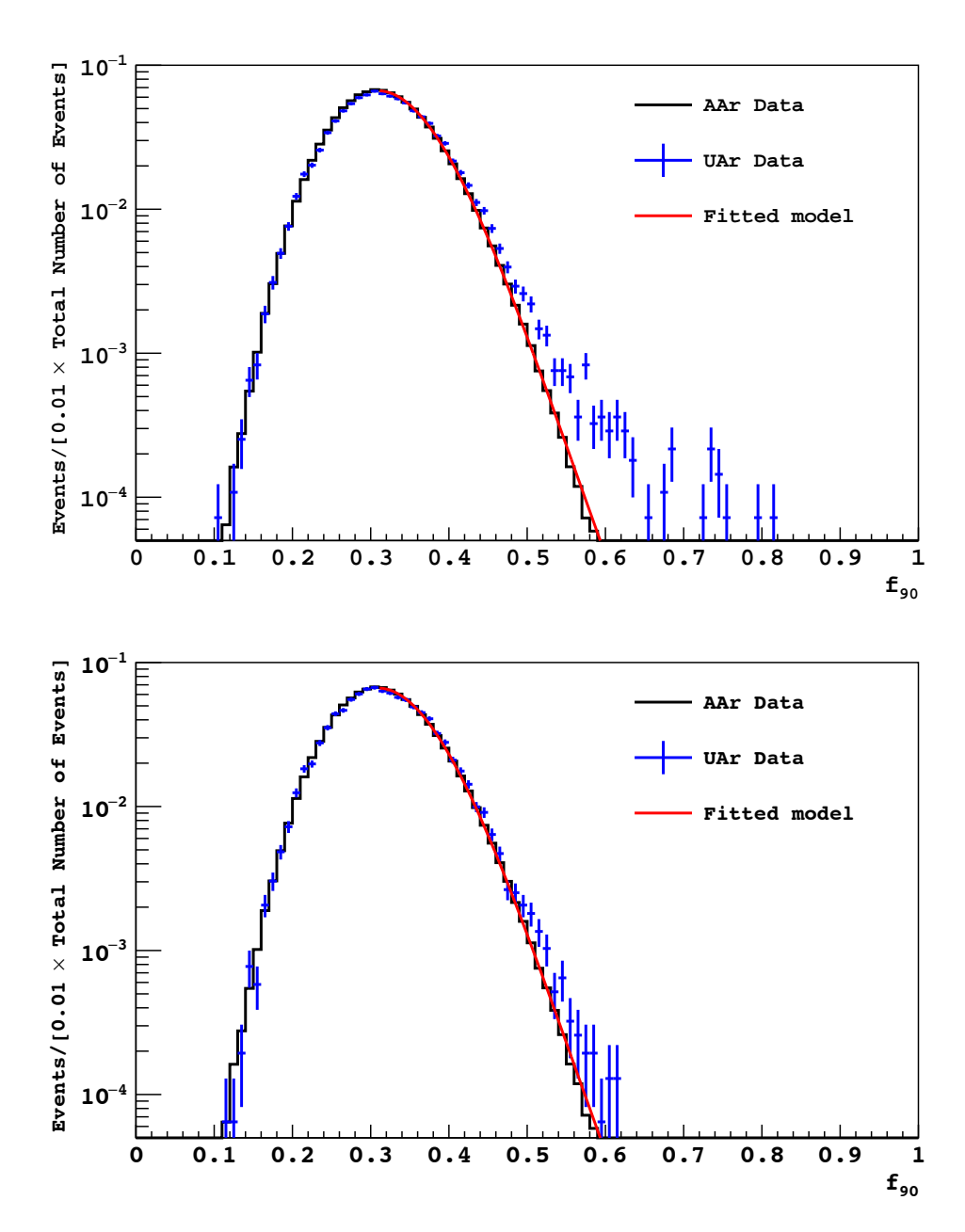


Figure 3.4: Comparing  $f_{90}$  distribution for a S1 bin of 60 PE to 120 PE between AAr data (black), UAr data (blue), and Hinkley's single-sited  $f_{90}$  model curve. The two spectra are normalized by the integral (the number of events in this S1 bin) for the comparison of  $f_{90}$  shape. The Hinkley's model is fitted to the high statistics AAr data. Top: the 95% S1MF cuts are removed, but other the standard TPC cuts and a veto prompt cut are applied. Bottom: the standard TPC cuts and veto prompt cut. The excess of the  $f_{90}$  shoulder in UAr data hints unknown  $\gamma$  induced ER background, which appears to have more leakage than the prediction of the analytic  $f_{90}$  model.

Here F is an effective Fano factor which is fixed to 1. The presence of F is merely for test purposes.  $\sigma_{\rm SPE}$  is the variance in the observed PEs due to the finite PMT SPE resolution. Since all the PMTs have roughly the same  $\sim 40\%$  resolution, we set  $\sigma_{\rm SPE} = 0.4$ .  $\sigma_{\rm TPB}$  is the variance of the observed PEs due to the TPB wavelength shifting process where the mean UV to visible conversion factor is bigger than 1 as a results of energy conservation. We treated the amplification as a binomial process for every UV photon:  $X_1 = 1 + B(1,p)$ , where p is the probability of emitting 2 visible photons. Hence with some statistics and algebraic manipulations, one can show that  $\sigma_{\rm TPB}^2 = (1+3p)/(1+p) - 1 = 2p/(1+p)$  [33]. Empirically we find that  $\sigma_{\rm TPB} = 0.49$  gives the best fit. This corresponds to a 1.14 mean conversion factor which is fairly close to the 1.2 measured in [37].

The  $\sigma_{n,p}^2$  and  $\sigma_{n,l}^2$  are the variance associated with the baseline fluctuation in the S1 prompt and late region whose values are to be determined in fit. Given the very narrow prompt region, we expect  $\sigma_{n,p}^2$  to be much smaller than  $\sigma_{n,l}^2$ .

#### Leakage Curve by Fitting the ER Data

Making an accurate prediction of the ER background is one of the most challenging aspects of the WIMP analysis. In the previous publication with the AAr target, a 0.05 event per 5 pe ER leakage curve was obtained by fitting the Hinkley's model to the data [21]. In this analysis, the same approach was no longer valid due to the complicated ER background composition. G. Koh built a model to improve the  $f_{90}$  modeling by incorporating the  $f_{90}$  from unresolved multi-sited events. While the improved model stands closer to making a prediction, it was still insufficient to model the excess in the  $f_{90}$  tail [38]. Furthermore, the multi-scatter model was still under validation at the time of publishing the UAr results. We eventually adopted a procedure in this non-blinded analysis by treating all ER events as single scatters.

We perform the following actions to the ER data after all of the standard TPC and veto cuts.

- 1. Projected the  $f_{90}$ -S1 distribution to obtain the  $f_{90}$  profiles per every 5 PE S1 bin <sup>2</sup>. This step is done for both previously published AAr data set and the 70-day UAr data set.
- 2. For each S1 bin, fitted the analytic model to the  $f_{90}$  profiles in the high statistics AAr data set and obtained the  $f_{90}$  quantile corresponding to 0.01 leakage events. The only free parameters in the analytic models were  $f_p$ ,  $\sigma_{n,l}$ , and the overall normalization.  $\sigma_{n,p}$  was fixed at 0.2 PE during the fit. Although we expected both noise parameters to be independent of the energy, we did observe a slight increasing trend for the  $\sigma_{n,l}$  as the energy increase. The dependence was caused by the linear interpolations of the pulse finding algorithm. The fit turned out to work well for all  $f_{90}$  profiles in the AAr data set as expected.
- 3. For each S1 bin, scaled down the normalization parameter to the number of  $f_{90}$  profile events in the UAr data.
- 4. Repeat step 2 and 3 for all S1 bin until we have a 0.01 events/(5-PE bin) leakage curve as a function of S1.

Fitting the analytic model to the high statistics AAr data not only makes sense but also helps reduce the uncertainty in determining  $f_p$ . Although this procedure underestimates the total ER leakage, it's an accurate and honest prediction of single-scatter events at the time. The curve allowed a total of 0.1 single-scatter ER background in the box.

#### NR Acceptance Curve

We follow the similar procedure as the ER leakage to obtain the acceptance contours for NR distributions. We applied the same analytic model to  $^{241}$ Am-Be data, except this time the only free parameters are  $f_p$  and the normalization. All the noise parameters ( $\sigma_{\text{SPE}}$ ,  $\sigma_{\text{TPB}}$ ,  $\sigma_{n,p}$ , and  $\sigma_{n,l}$ ) are copied over from the ER study. It is worth mentioning that the NR samples from the  $^{241}$ Am-Be data are contaminated by unresolved  $\gamma$  coincidence. The contamination occurs when the NR and ER have approximately the same vertical z. Fortunately the median parameter  $f_p$  is an intrinsic property of LAr which is not affected significantly by a few outliers from the contamination. We cross-check the fitted  $f_p$  values with the SCENE results under the same drift field and confirm the consistency.

<sup>&</sup>lt;sup>2</sup>The previous AAr analysis made projection every 10 PE bin in S1, but there is a 5 PE overlap between two consecutive bins. We decided not to follow the old procedure to avoid correlated  $f_{90}$  profiles from bin to bin.

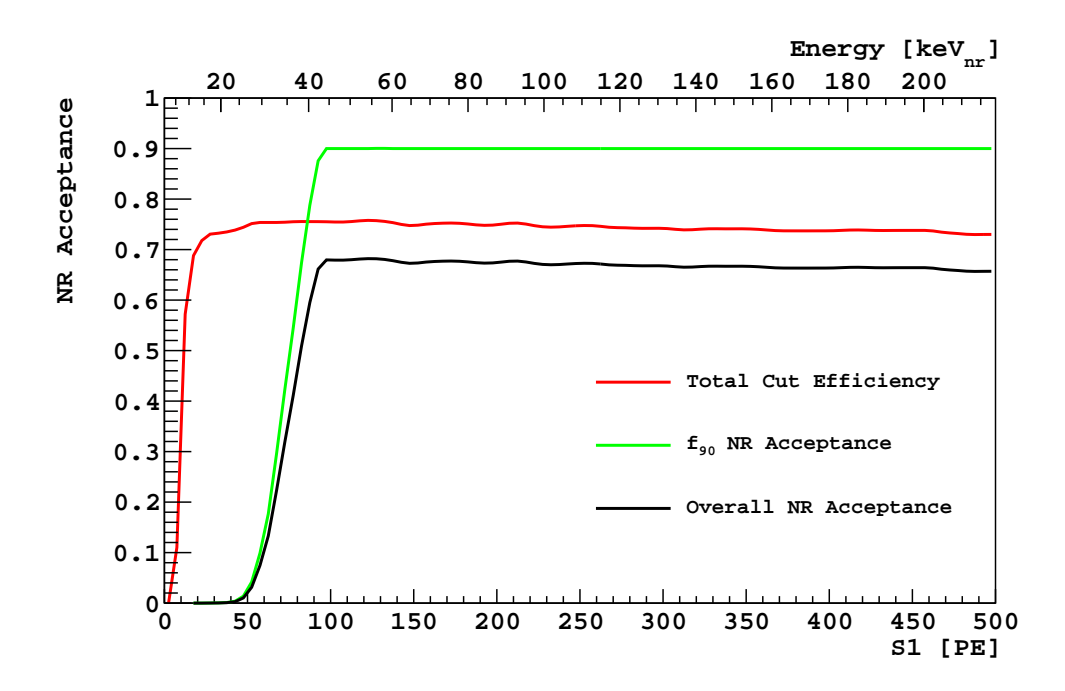


Figure 3.5: The NR acceptance a function of energy for the total cut and the  $f_{90}$  cut. The combined acceptance (black) is used for the calculation of the WIMP limit. Plot from Ref. [22].

#### 3.4.4 Exposure and WIMP Acceptance

Before calculating the exclusion limit, we need to estimate the total exposure and the WIMP acceptance for every cut defined in Sec 3.3. Given the counted total livetime is 70.9 d and the estimated fiducial mass is  $(36.9 \pm 0.6)$  kg, we conclude the total exposure is  $(2616 \pm 43)$  kg d. The livetime is defined as the time from the end of the previous event's inhibit window to the beginning of current acquisition window events trigger time. Hence livetime is a measure of the amount of time DarkSide-50 could have detected WIMPs. Since occasionally the DAQ system malfunctioning may cause ill-defined livetime variable, the accumulated livetime counter must be implemented after the basic quality cut. Additionally, for every event passing the livetime cut (Sec. 3.3) we minus 540 µs (1.35 ms - 810 µs) from the total counting. The uncertainty of fiducial mass is dominated by the TPC radius at the cryogenic LAr temperature since exact shrinkage of the PTFE wall is unknown.

We evaluated the WIMP acceptance as a function of S1 as shown in Fig. 3.5. Individual cut acceptance was studied by several authors. Ref. [33] has a good summary. The  $f_{90}$ 

acceptance was evaluated by generating a sample of simulated WIMP events in the 2D  $f_{90}$ -S1 plot and measured the fraction of the events falling into the WIMP box defined in Sec. 3.4.3. The simulation used the NR energy scale obtained from SCENE (LY adjusted for DarkSide-50) to reconstruct S1 and the fitted analytic model to reconstruct  $f_{90}$ .

#### 3.4.5 Exclusion Limit

The null result from the UAr campaign is shown in Fig. 3.6-top, where the dark matter search region is highlighted in shadow blue. Given the null result with the present exposure, we derive a 90% C.L. exclusion curve corresponding to the observation of 2.3 events assuming a spin-independent interaction. We use the standard isothermal galactic WIMP halo parameters:  $v_{\text{escape}} = 544 \text{ km/s}$ ,  $v_0 = 220 \text{ km/s}$ ,  $v_{\text{Earth}} = 232 \text{ km/s}$ ,  $\rho_{\text{dm}} = 0.3 \text{ GeV/(c}^2\text{cm}^3)$  [22].

When combined with our previous AAr exposure, we obtain an upper limit on the WIMP-nucleon spin-independent cross section of  $2.0 \times 10^{-44}$  cm<sup>2</sup> ( $8.6 \times 10^{-44}$  cm<sup>2</sup>,  $8.0 \times 10^{-43}$  cm<sup>2</sup>) for a WIMP mass of 100 GeV/c<sup>2</sup> (1 TeV/c<sup>2</sup>, 10 TeV/c<sup>2</sup>). Fig. 3.6-bottom compares our excursion results with other experiments.

### 3.5 A Hint of PTFE Cherenkov

### 3.5.1 Beyond the Ar-39 Endpoint

It is interesting to compare the UAr spectra beyond the  $^{39}$ Ar and  $^{85}$ Kr endpoints. In particular, we used the  $f_{90}$  spectrum as an indication of background compositions. In the absence of  $\beta$ 's, we expected a close match of the  $f_{90}$  shape between the UAr and the AAr data since the underlying background composition is expected to be the same. As shown in Fig. 3.7, the  $f_{90}$  distributions turned out to be very similar, as indicated by the small discrepancies in the mean ( $\sim 0.14\%$ ), the standard derivation ( $\sim 1.\%$ ), and the shape between the two.

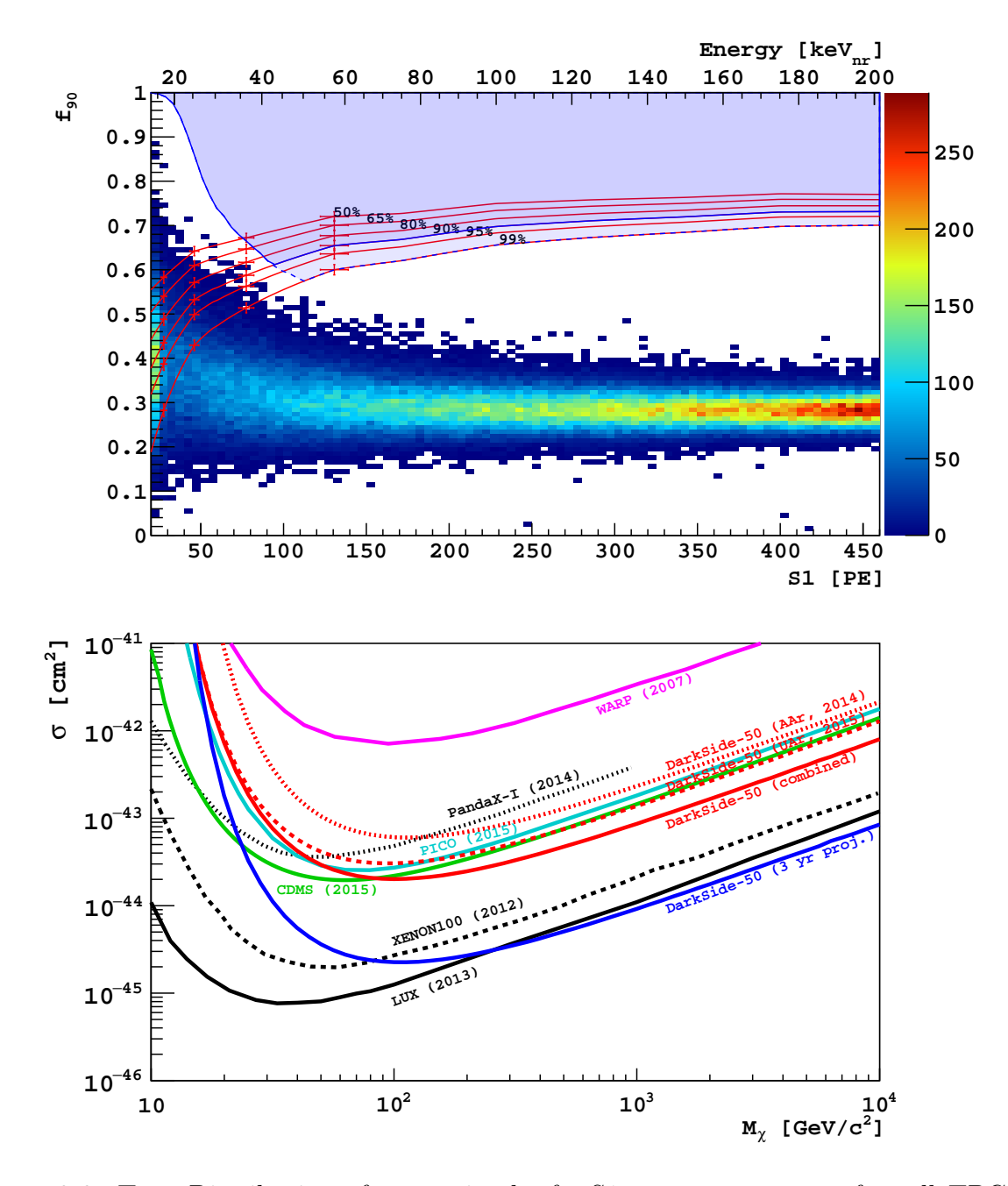


Figure 3.6: Top: Distribution of events in the  $f_{90}$ -S1 parameter space after all TPC and veto cuts. The shaded blue with solid blue outline is the WIMP search region. The NR acceptance contours (99%, 95%, 90% etc) was extrapolated from the SCENE measurements. Lighter shaded blue with dashed blue line show that extending the WIMP search region to 99%. Bottom: the 90% confidence exclusion curve (red) extrapolated from the null results, and a projected DarkSide-50 exclusion curve (blue) from a total of 3-year exposure. Plots from Ref. [22]

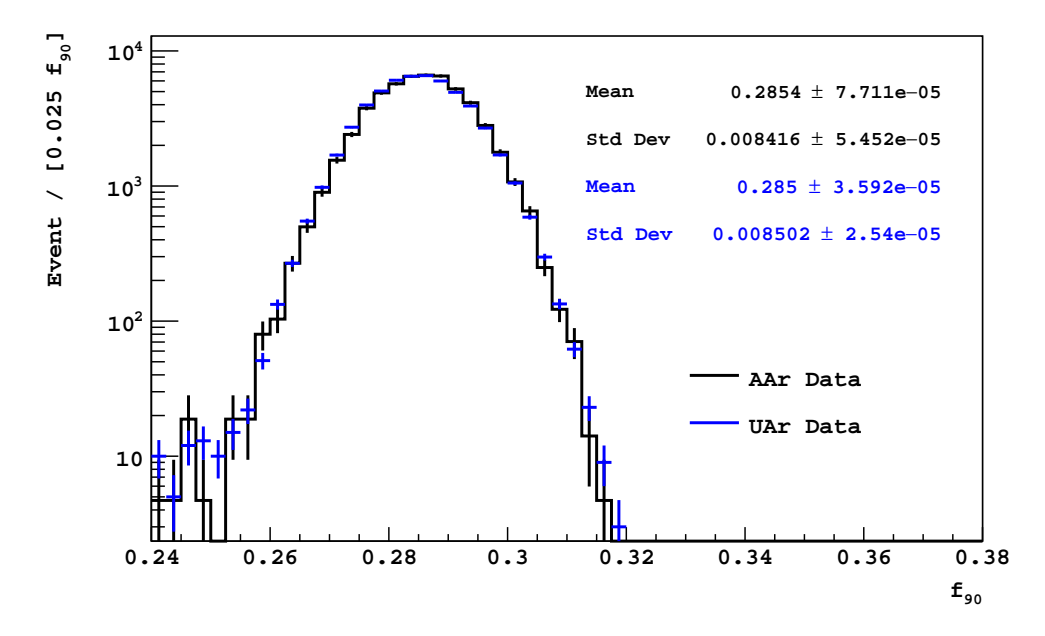


Figure 3.7: The comparison of the  $f_{90}$  spectrum beyond the <sup>39</sup>Ar and <sup>85</sup>Kr endpoints between the AAr data (black) and the 70-day UAr data (blue). The AAr spectrum is normalized to the number of events in the UAr spectrum. Both data are selected in the range of 4500 PE <S1< 8000 PE. Additional cuts: the quality cuts (Sec. 3.3.1), the single-scatter cut, the trigger time cut, and the 40  $\mu$ s  $t_{drift}$  cut (Sec. 3.3.2).

Although the agreement shows no changes in the composition of physical backgrounds from the AAr to the UAr campaign, we do not have sufficient evidence to exclude any instrumental changes, such as electronic noise. For instance, the instrumental changes may have impact on the low energy WIMP search but is too small to be observed at the scale of S1> 4500 PE.

### 3.5.2 Further Analysis on the Excess

When a  $\gamma$ -ray escapes into the neutron veto after Compton scattering in the TPC, it creates prompt coincident signals. Since  $\beta$ 's always stay in the TPC and neutrons are rare, events selected by requiring a veto prompt coincidence are mostly  $\gamma$  related (only  $\sim 1\%$  accidental coincidence). As shown in Fig. 3.8,  $\gamma$  related events, isolated by requiring veto prompt coincident signal (red), not only show a higher  $f_{90}$  mean and variance than the AAr data, but also show an enhanced  $f_{90}$  tail excess on the right-hand side. In fact, the UAr events

with veto prompt coincidence (red) have a higher  $f_{90}$  mean than the UAr events (blue) in general, as shown in Fig. 3.8-bottom.

On the other hand, when we attempted to reduce the  $\gamma$  related events by a combination of applying the veto prompt cut and a mild radial cut ( $r < 14.4 \,\mathrm{cm}$ ), we observed a spectrum (green) that closely resemble that of the AAr in terms of the  $f_{90}$  variance, mean, and the diminished excess on the  $f_{90}$  tail. If unknown instrumental changes are the reasons for the  $f_{90}$  discrepancy, the changes will affect all events in the same way. This evidence rejects the possibility of instrumental changes, and support the claim of having a stable detector across both campaigns. Moreover, given the radial cut only removes 3.4 cm from the wall, we knew the excess events is  $\gamma$ -ray related backgrounds coming from the TPC side wall.

We applied a more aggressive S1 maximum fraction cut to look for a possible correlation between the excess in the  $f_{90}$  tail and S1 light distributions across the PMTs. As shown in Fig. 3.9, the excess in  $f_{90}$  tail behaves just like regular ER events under the cut, even after an aggressive the S1 maximum fraction that removes roughly 50% of the events. The plot shows that we do not need a deeper S1 maximum fraction cut. Furthermore, the evidence again supports that the excess events are  $\gamma$  related backgrounds from the wall.

While looking at the  $f_{90}$  profiles at various S1, we notice two things — first the excess is not visible above 150 PE; second the excess is restricted to a S1 range between 50 PE and 150 PE with its activity peaked around 60 PE to 80 PE. While the second observation could be a statistical fluctuation, the first observation fits the scenario of scintillation plus PTFE Cherenkov coincidence (Sec. 3.5.3 and Sec. 4.1). Given the Cherenkov LY in PTFE is not high, an energy cut off for the background production is expected.

# 3.5.3 The Necessity for a PTFE Cherenkov Model

The presence of this excess was an issue because the analytic model that we relied on for ER background prediction clearly underestimated the number of events leaking into the WIMP region. We concluded that this excess is physical,  $\gamma$ -related backgrounds, and can

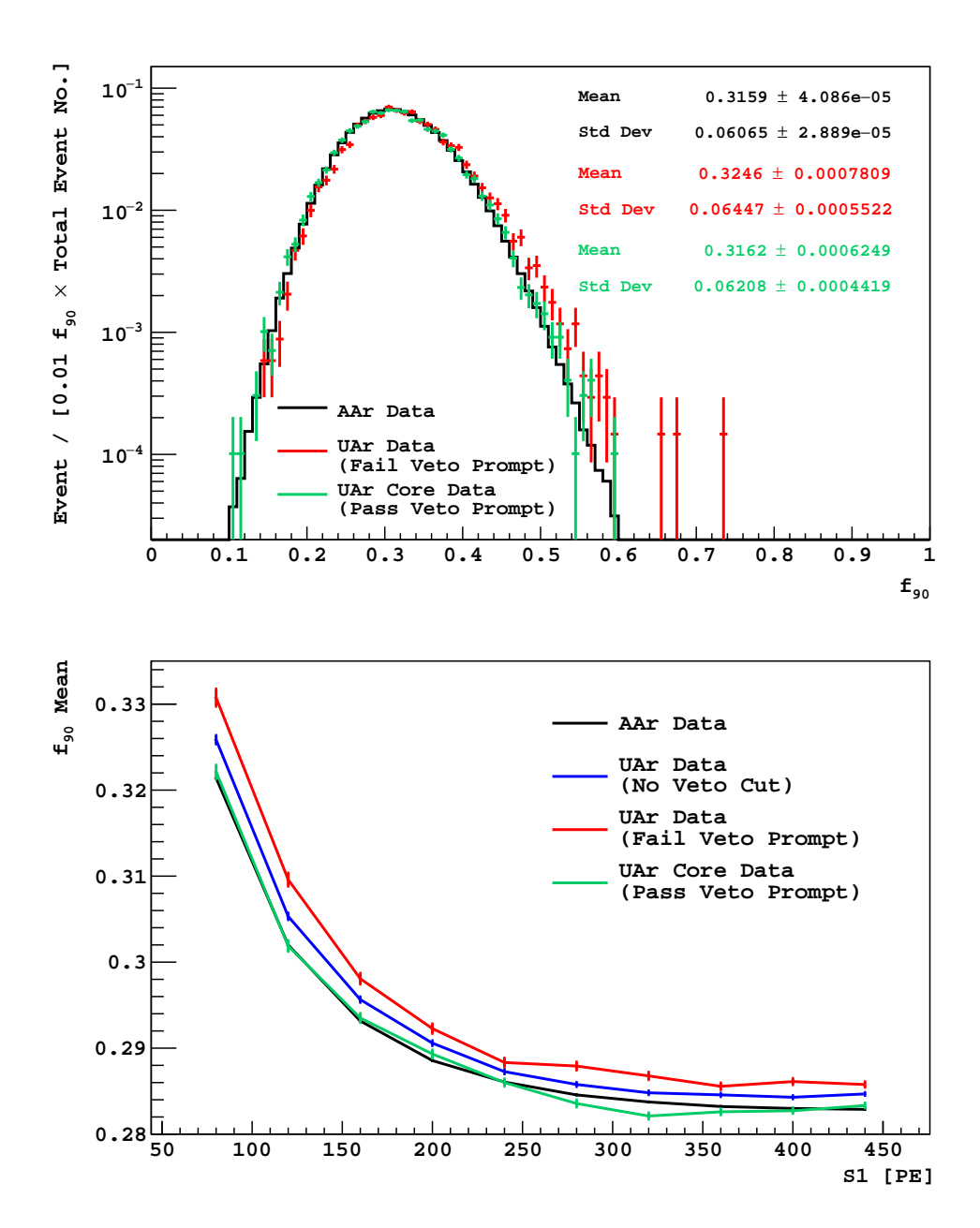


Figure 3.8: The characteristics of the UAr  $f_{90}$  spectra. All spectra and curves have the quality cuts (Sec. 3.3.1) and the 70-day TPC cuts (Sec. 3.3.2) applied. Top: The  $f_{90}$  spectra in the range from 60 PE to 120 PE for the AAr data (black) and the 70-day UAr data. All spectra have the total number of events normalized to unity. The UAr events failing the veto prompt cut (red) has shown an enhanced  $f_{90}$  tail on the right-hand side. The UAr events surviving the radial cut of r < 14.4 cm and the veto prompt cut (green) has a spectrum closely resemble to the AAr. Bottom: The trends of  $f_{90}$  mean as a function of S1. The color code is the same as the top plot except for the addition of the UAr data without any veto cuts (blue).

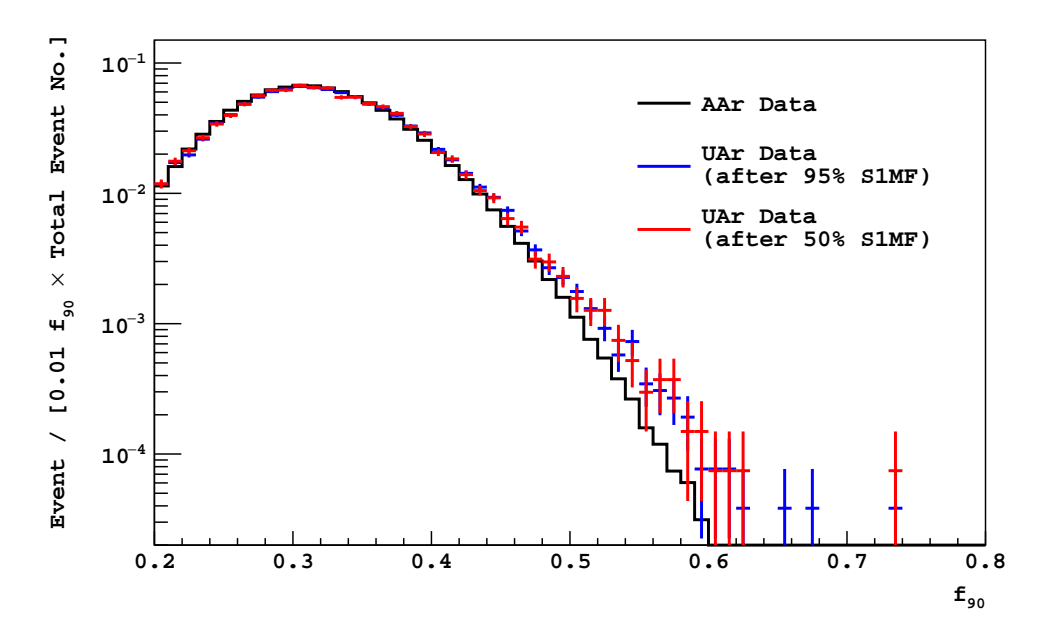


Figure 3.9: The  $f_{90}$  profiles in the range of 60 PE to 120 PE for the 70-day UAr data after various S1 maximum fraction (S1MF) cuts. All spectra have the total number of events normalized to unity. The additional cuts applied to all spectra are the quality cuts (Sec. 3.3.1), the 70-day TPC cuts (Sec. 3.3.2). The AAr  $f_{90}$  spectrum again serves as a reference for the single-sited ERs. An aggressive 50% S1MF cut (red) does not show an improved suppression of the  $f_{90}$  excess in the tail as compared to the standard 95% S1MF cut (blue).

be suppressed by a heavy radial fiducial cut and a veto prompt cut, but it appears that this excess would not be suppressed by an aggressive S1MF cut (Sec. 3.5.2). Furthermore, G. Koh showed that the excess is not explained by  $\gamma$ -ray multi-scattering in the LAr [38]. With all the evidence <sup>3</sup>, we hypothesize that the excess is caused by Cherenkov radiation in Polytetrafluoroethylene (PTFE,  $(C_2F_4)_n$ ) reflector in coincidence with LAr scintillation <sup>4</sup>.

Although it's possible to enhance PTFE Cherenkov background in calibration with a high energy  $\gamma$ -ray source, it's difficult to characterize the background and develop cuts in data due to the lack of features. A GEANT4-based Monte Carlo model incorporating the detector geometry and optics is absolutely necessary for the experiment to predict the backgrounds down to a fraction of an event.

<sup>&</sup>lt;sup>3</sup>A stronger argument regarding the existence of PTFE Cherenkov is made in Sec. 4.2.2

<sup>&</sup>lt;sup>4</sup>The hypothesis of the PTFE Cherenkov background existed long before DarkSide-50 was operating. Earlier toy-MC work to predict the rate of PTFE Cherenkov was done by A. Wright in August 2012 [39] and by T. Seiss in June 2015 [39].

# Chapter 4

# The Cherenkov Simulation

#### 4.1 Introduction

Cherenkov light is not an obvious threat in dual-phase noble liquid dark matter experiment, since this relativistic process releases a continuous spectrum of photons in a wide range over in a very short time window ( $\ll 1 \, \mathrm{ns}$ ). Therefore a pure Cherenkov event will have  $f_{90}$  approximately equal to 1 and no S2, and will not survive the WIMP search analysis cuts. However, when Cherenkov radiation happens in coincidence with a normal scintillation in the active LAr volume, it could potentially enhance the prompt signal of an ER event, making the event more NR-like in  $f_{90}$ . On top of that, since the Cherenkov process does not produce ionization electrons, the coincidence will lower S2/S1 as well. In this document, we refer to Cherenkov radiation as the light produced in the construction material of our TPC, such as the fused silica Diving Bell/Cathode Windows (DB/CW) and the PMT face-plates, the Polytetrafluoroethylene (PTFE,  $(C_2F_4)_n$ ) reflector side wall, and the PTFE support between PMTs. While the Cherenkov process in LAr can certainly radiate photons along with scintillation, any charged particle with sufficient kinetic energy to produce Cherenkov

radiation will be heavily dominated by scintillation photons, and will fall outside the high energy boundary of the WIMP search ROI <sup>1</sup>.

#### 4.1.1 The Mechanism

One mechanism to have the Cherenkov plus scintillation coincidence is by a  $\gamma$  multiple scattering in the TPC. Quantitatively sorting out of all possibly dangerous scenarios requring a detailed simulation of the detector geometry, but this should not stop us from pursuing a qualitative understanding.

There is an implicit kinematic constraint due to the relation between the Compton scattering angle and the  $\gamma$ 's energy. The Compton's formulas are:

$$\cos \theta = 1 - \left(\frac{m_e c^2}{E_\gamma}\right) \frac{\delta E/E_\gamma}{1 - \delta E/E_\gamma},\tag{4.1}$$

and

$$\delta E = \frac{(1 - \cos \theta) E_{\gamma}}{(1 - \cos \theta) + m_e c^2 / E_{\gamma}},\tag{4.2}$$

where  $\theta$  is the  $\gamma$ 's scattering angle,  $\delta E$  is the energy deposited (ex.  $\delta E = E'_{\gamma} - E_{\gamma}$ ), and  $E_{\gamma}$  is the initial  $\gamma$ -ray energy. There is also a constraint from the maximum deposited energy allowed by back-scattering. Let's define short-hand notations  $\alpha = \delta E/E_{\gamma}$  and  $\beta = m_e c^2/E_{\gamma}$ , and the back-scattering constraint can be simplified as  $\alpha \leq 1/(1+0.5\beta)$  (you can derive this simply by setting  $\cos \theta = -1$  in Eqn. 4.1). Notice,  $\alpha$  is a tiny number for an energetic  $\gamma$ -ray when we restrict  $\delta E$  to the WIMP Search ROI ( $\delta E < 65$  keV).

The dangerous mixed events are those with a high enough fraction of Cherenkov photoelectrons to give a mixed  $f_{90}$  falling in or near the WIMP box. There are many possible topologies to make a dangerous  $\gamma$ -ray induced Cherenkov coincidence. Fig. 4.1-left shows a

<sup>&</sup>lt;sup>1</sup>This is not necessarily true near the boundary. Since Cherenkov photons are mostly produced at the beginning of the track and LAr scintillation photons are produced near the end of the track, if a  $\beta$  starts in the LAr but ends in the PTFE wall, the Cherenkov process may dominate the photon production.

Table 4.1: The first column is index of refraction. The second column is the minimum kinetic energy threshold of an electron required to activate the Cherenkov process. The third, fourth, fifth and sixth columns are the initial energy of the  $\gamma$  if the scattering angle is  $180^{\circ}$ ,  $135^{\circ}$ ,  $90^{\circ}$  and  $45^{\circ}$  respectively. The  $180^{\circ}$  column sets the minimum energy for a  $\gamma$  to create any Cherenkov photons at all via Compton scattering. The n=1.35 (constant) and  $n(\lambda = 155 \text{ nm})=1.671$  rows are the actual refractive indices for Teflon and fused silica in G4DS.

n	$E_{\rm th} \ [{\rm keV}]$	$E_{\gamma}^{180^{\circ}} [\text{keV}]$	$E_{\gamma}^{135^{\circ}} [\text{keV}]$	$E_{\gamma}^{90^{\circ}} [\text{keV}]$	$E_{\gamma}^{45^{\circ}} [\text{keV}]$
1.1	715	915	943	1060	1530
1.2	413	592	615	711	1080
1.3	289	452	472	555	869
1.35	250	407	425	503	797
1.4	219	370	388	462	738
1.5	175	316	332	398	646
1.6	144	276	291	352	577
1.671	127	254	268	326	538
1.7	121	246	260	316	524

subset of topologies where a  $\gamma$ -ray first Compton scatters in the radiator before scattering again in LAr.

In general, the higher the  $\gamma$ -ray energy, the less angular constraint we can set on dangerous coincidences. Consider a 1 MeV  $\gamma$  traveling vertically down from a top PMT, and hitting a fused silica window ( $n \sim 4.7$ ,  $E_{\rm th} \sim 200$  keV). To reach the active LAr, the  $\gamma$  must be scattering forward ( $\theta < 90^{\circ}$ ) and producing an electron with sufficient kinetic energy (see Fig. 4.1) to radiate a significant number of photons. Suppose the electron needs to be >500 keV, this constrains  $\theta$  to be in the range from 60° to 90° according to Eqn. 4.1. However, when we consider a 2 MeV  $\gamma$ , the angular constraint is between  $\sim 24^{\circ}$  and 90°.

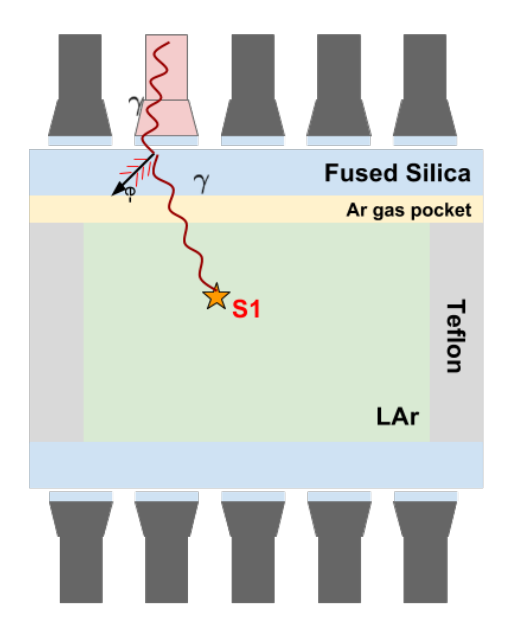
When we consider the case of a scattering in PTFE, backward scattering  $\gamma$ 's are the more problematic scenario as shown in Fig. 4.1-right. According to Eqn. 4.2, when a 2 MeV  $\gamma$  back-scatters ( $\theta > 90^{\circ}$ ), the  $\gamma$  will lose most of its energy to PTFE ( $\delta E > 1590$  keV), leaving a much less energetic  $\gamma$  to penetrate the LAr. This is a good thing for radial fiducial cuts. Although an energetic  $\gamma$  is likely to give a dangerous coincidence by back-scattering in PTFE, we need to keep in mind that the  $\gamma$  has a much higher probability to scatter forward than backward during a Compton scattering.

Reversing the order of the two scatters to have the first scatter in the LAr is also possible. Consider the FS Cherenkov case where a 2 MeV  $\gamma$ -ray from a top PMT first scatters in the LAr. When we constrain  $\delta E < 65 \text{ keV}_{ee}$  (the upper bound for WIMP search), the  $\gamma$  will have a very small scattering angle  $\theta < 7.5^{\circ}$ , according to Eqn. 4.1. This means the same  $\gamma$  is unlikely to give a coincident Cherenkov radiation in FS unless it travels all the way across the LAr volume and hits the bottom fused silica. However, when reversing the order of scatters for PTFE Cherenkov, we see the possibility of having an even more problematic scenario. If  $\theta$  is small, the  $\gamma$ -ray will remain energetic enough to travel a relatively long distance in LAr before making Cherenkov light in PTFE, which means it would be difficult to reject such an event via a radial fiducial cut without losing significant signal acceptance.

A  $\gamma$  coming from the cryostat steel can also give a coincidence, but this is less frequent than from the PMTs because our cryostat is farther away from the LAr and less radioactive than the PMTs. One can qualitatively sort the dangerous cases by similarly exploring their kinematic constraint.

There is another interesting special case that only has the  $\gamma$ -ray scattered once. When the scattering of the  $\gamma$ -ray occurs in the LAr but very close the PTFE reflector surface, the high energy recoil electron may travel into the PTFE radiator from the LAr, thus giving both scintillation and Cherenkov light. A back-of-the-envelope calculation based on ESTAR data suggests that a 2.6 MeV electron traveling toward the PTFE needs to be within  $\sim 330 \,\mu m$  of the surface so that the energy deposit in the LAr will be small enough to be a threat (WIMP search ROI:  $< 65 \, \text{keV}_{ee}$ ). This scenario is similar to the topology of surface background in the sense that the charged particle scintillates extremely close to the reflector surface and penetrates through the TPB coating. The radial fiducial cut will be effective, and the TPB long tail cut developed by C. Stanford may have some rejection on this type of Cherenkov background as well [40].

A  $\beta$ - $\gamma$  coincidence where a radioactive decay occurs internally in the detector material is another possible mechanism for the Cherenkov background. Such a mechanism can be



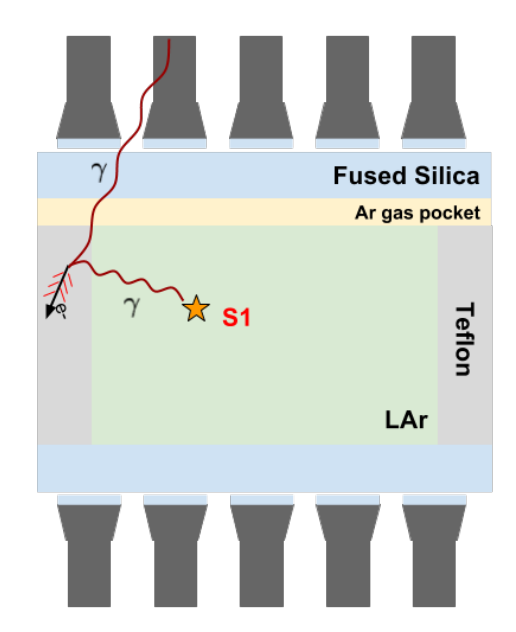


Figure 4.1: Illustration of two scenarios of external  $\gamma$ -ray induced Cherenkov background in DarkSide-50 TPC. Left: Cherenkov light is produced in fused silica (blue). The red PMT directly above the radiation receives an abnormally large amount of light compared to neighbor tubes. Right: Cherenkov light is produced in PTFE reflector (grey). In both cases, the  $\gamma$ -rays are originated from radioactive decays in PMTs. The PTFE mount between PMTs is not drawn here.

caused by a  $\beta$ -decay in fused silica or PTFE immediately followed by a  $\gamma$ -ray emission. Or, in addition to Cherenkov radiation, the same  $\beta$ -decay electron can create bremsstrahlung X-rays which then travel into the LAr and deposit energy. Since our FS/PTFE is extremely clean, this process is believed to be sub-dominant. The upper detection limit (no signal observed) for the  $^{238}$ U upper chain ( $^{234}$ Pa is a high energy  $\beta$  emitter with  $\sim$ 2270 keV endpoint) in the PTFE powder used for DarkSide-50 main reflector is  $\sim$ 70 µBq/kg ( $\sim$ 60 ppt) according to our NAA counting. Introducing radioactivity in the Cherenkov radiators in the simulation has another problem – we cannot normalize it to the data accurately. Its radioactivity level is so low that we cannot get an accurate assessment of the absolute rate. This study will focus on the  $\gamma$  induced coincidence and the simulation of  $\beta$ - $\gamma$  coincidence will not be discussed in this document.

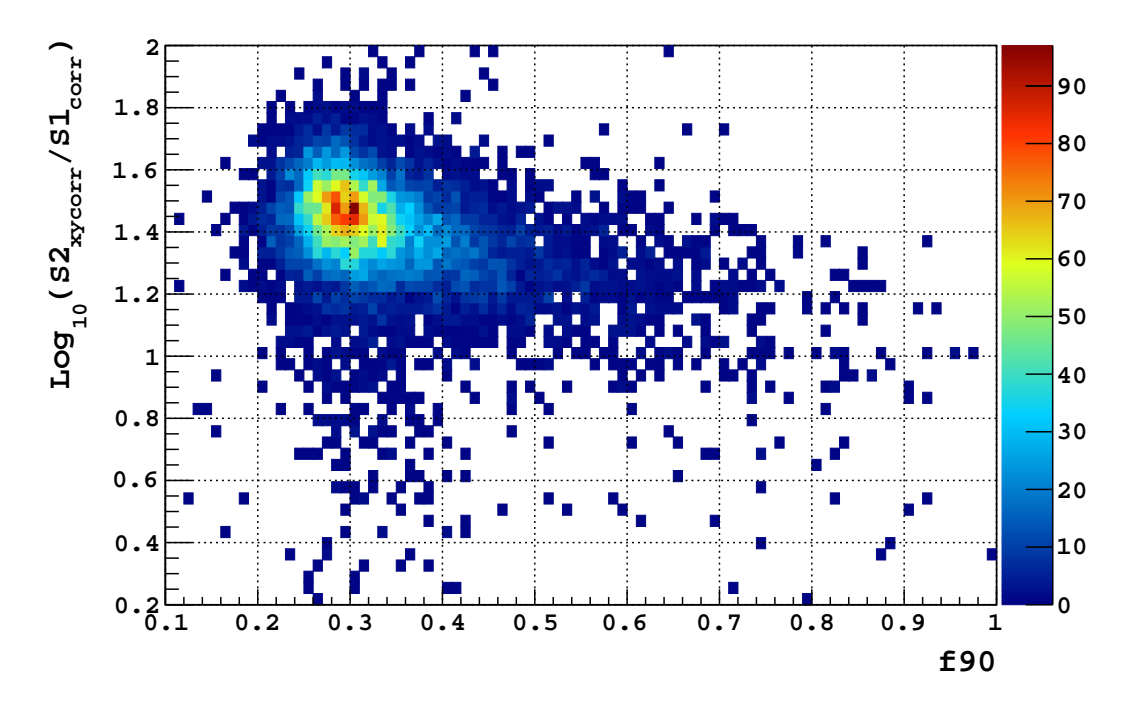


Figure 4.2: Evidence of the FS Cherenkov background events selected from the 70-day UAr data set. The brightest blob around  $f_{90} \sim 0.3$  is normal ER failing S1MF due to fluctuations. Cuts are the quality cuts (Sec. 3.3.1), the trigger cut, the single-scatter cut, failing the 99% S1MF cut, failing the 99% S1pMF cut (Sec. 3.3.2), and 50 PE < S1 < 150 PE.

#### 4.1.2 Influence on the Discrimination

The existence of FS Cherenkov in DarkSide-50 was established during the AAr campaign when we observed outliers in the NR region [21] before applying a 99% S1 maximum fraction (S1MF) cut. The S1MF cut (Sec. 3.3.2 and 5.3.1) rejects an event with an abnormally large amount of light concentrated in a single PMT. Although the cut was originally designed to clean up events after pulsing, it turns out to be quite effective in removing those outliers. We had suspected those outliers are FS Cherenkov background, but it was not until later, when we got the first complete Cherenkov simulation results, that the reason why the S1MF cut works so well was unveiled — the outliers are mostly the mixed events whose Cherenkov light originated in a PMT window. Thus, we can use inverted S1MF and S1pMF cuts (Sec. 4.4.5) to isolate FS Cherenkov events for studies.

We expect Cherenkov light in coincidence with scintillation to simultaneously boost  $f_{90}$  and lower S2/S1, resulting in an anti-correlation between S2/S1 and  $f_{90}$ . Using the inverted S1MF and S1pMF cuts, we can show the anti-correlation trend between the two discrimination parameters for the FS Cherenkov background, as illustrated in Fig. 4.2.

The evidence for PTFE Cherenkov background in the data is indirect; it comes from comparing pure Cherenkov spectra between the UAr and <sup>22</sup>Na calibration data, which will be discussed in Sec. 4.2.

## 4.2 Pure Cherenkov Events

#### 4.2.1 Event Selection

Pure Cherenkov events do not have a LAr scintillation component by definition and are populated in 1-pulse events in data (no S2). Since Cherenkov is prompt, we expect its signal to be fully contained within the first 90 ns pulse integral, hence having  $f_{90} \sim 1$ . The selection procedure does not turn out to be straight-forward because the 1-pulse events have a complicated structure, as illustrated in figure 4.3.

The  $f_{90} \sim 1$  population (region A) in Fig. 4.3 shows where the pure Cherenkov events are located in the  $f_{90}$ -S1 plane. Oddly, there is a band of events right below the pure Cherenkov population (region B), which sort of resembles a pure Cherenkov pulse followed by an "after-pulse" in the S1 late region (90 ns to 7 µs with respect to pulse start time). But a quick calculation reveals that the size of the "after-pulse" needs to be exactly 1 PE in order to quantitatively make sense, so it cannot be after-pulses which typically have sizes of > 10 PE. Other early theories suggest that perhaps the single "after-pulse" come from LAr scintillation or PMT dark noise. Typically S2/S1  $\sim$  100 for ER as its energy approaches 0, which means the LAr scintillation theory will need an explanation for the absence of a S2 pulse. We have also performed a quick study to show that DarkSide-50 PMTs operating at LAr cryogenics temperature have an average dark rate of 2  $\sim$  4 Hz/PMT (App. B.2), which

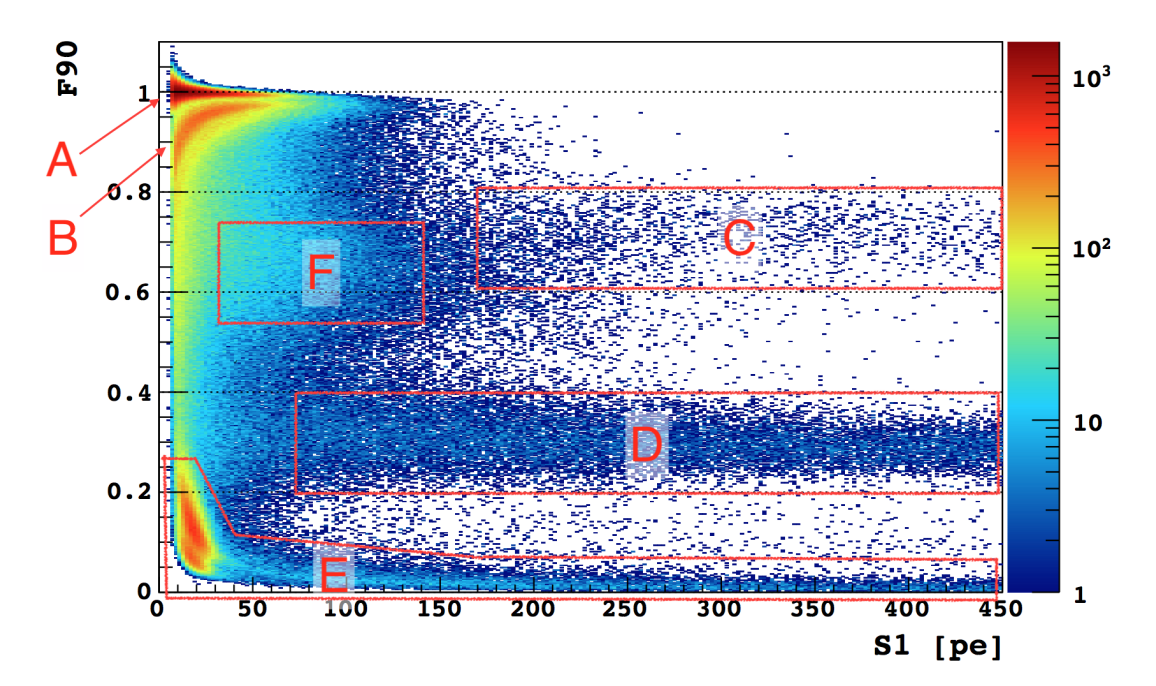


Figure 4.3: Single pulse events in 70-day UAr data. Region A ( $f_{90} \sim 1$ ) is where pure Cherenkov events are expected to be; region B appears to be a pure Cherenkov pulse followed by a single PE "after-pulse" in the S1 late window; region C contains surface  $\alpha$  events whose S2's mysteriously disappear; region D contains normal ER events; region E contains single S2 events and events whose S1 overlaps with S2; region F is not well understood, but possibly contains  $\alpha$ -related events on the surfaces of diving bell and cathode windows (they disappear drastically with the S1MF< 0.3 requirement as shown in figure 4.4).

is too low to explain the population ratio between region A and B (4 Hz/PMT  $\times$  38 PMTs  $\times$  7 µs  $\approx$  0.1%). When we took a closer inspection on the waveform of events in region A and B, we discovered that the primary all-prompt S1 signal is usually followed not by one PE but a stream of single PE that lasts for a few milliseconds. This strange "Cherenkov tail" feature resembles the TPB long tail to a certain extent. A rough estimate says a large fraction ( $\sim$  80%) of the region A events are also accompanied by this long tail. If a long tail happens to give one PE in the S1 late window, this event will fall into region B. Further study of this strange "Cherenkov tail" will be discussed in appendix B.1.

The complication of the pure Cherenkov events should not stop us from selecting them for further study. The strange single PE "after-pulse" made up about 22% of the total population of pure Cherenkov events in the UAr data. We adopt a graphic cut on the  $f_{90}$ -S1

plot, as illustrated in Fig. 4.4 by the red dashed curve, to include both region A and region B as our pure Cherenkov sample. This graphic cut may be a source of systematic error as it cuts off region B at low S1 and may bias selection at high S1.

We impose S1MF< 0.3 to separate PTFE Cherenkov from FS Cherenkov. Since pure PTFE Cherenkov events have lower S1MF and lower LY than FS Cherenkov events, we expected a decrease of S1 range of after the cut, as confirmed in Fig. 4.4. The S1MF< 0.3 cut makes the separation between region A and B easier to define. Another interesting thing is that region A's f<sub>90</sub> mean appears to decrease as S1 increases, but it appears to stop going down after S1MF< 0.3 cut. This phenomenon is observed for the UAr, Na22, and AmBe data. Inspecting waveforms suggests that this is a reconstruction effect, but we don't have a conclusive answer yet.

### 4.2.2 Comparing to Na-22 Data

The <sup>22</sup>Na calibration was originally proposed to study the PSD of ERs with a high statistics sample. The source decays at a rate of 11.2 kHz, which is too hot to run with our regular 440 µs gate. Instead, <sup>22</sup>Na data was taken with a 15 µs gate and without a gas pocket (no S2). In the absence of S2, there was too much background to proceed with the originally proposed PSD study, but since the source was blasting 1.27 MeV and 511 keV  $\gamma$ -rays through the PTFE, we should expect to see an enhanced population of pure PTFE Cherenkov events.

Fig. 4.5 plots Top Bottom Asymmetry (TBA) against S1MF for pure Cherenkov events from the 70-day UAr data and the  $^{22}$ Na data. TBA gives a rough measure of the z position of an event (defined at 2.2.2). The events from both data sets are selected by the same criteria described in previous section  $^2$ . The blank triangle is a forbidden region due to a mathematical constraint between TBA and S1MF. For example, in an extreme case when S1MF=1, all PE are detected by one PMT. Consequently the TBA has to be  $\pm 1$ . In the UAr data,  $\gamma$ -rays mostly come from the top and bottom PMTs where we expect them to

 $<sup>^2</sup>$ In the  $^{22}$ Na data, region B makes up about 16.6% of the Cherenkov events selected by the graphic cut without the S1MF cut; with the S1MF cut, it makes up about 12.8%.

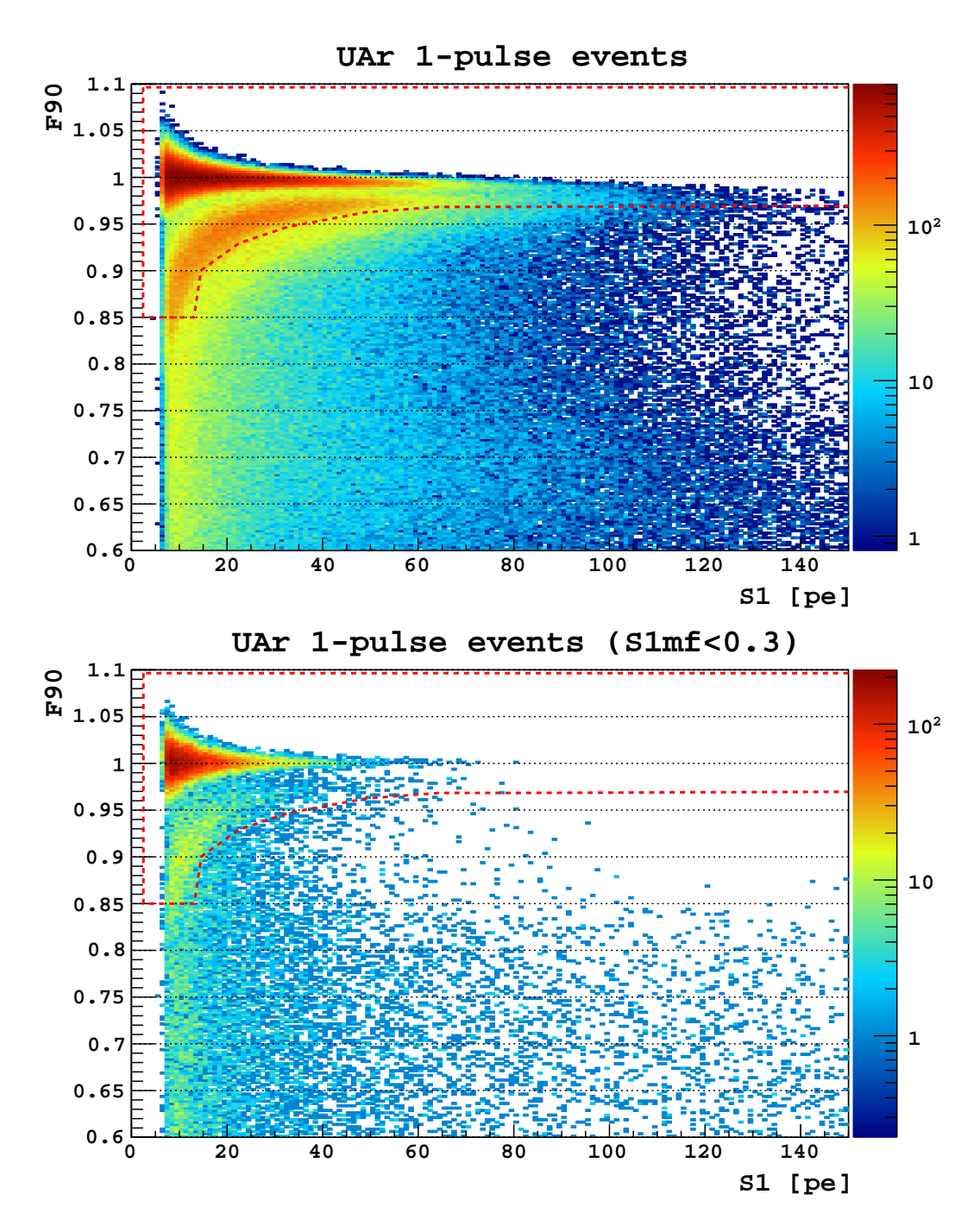


Figure 4.4: UAr 1-pulse events in the 70-day data. The horizontal band at  $f_{90} \sim 1$  corresponds to pure Cherenkov events. The red dash line illustrate the selection cut of the pure Cherenkov events. The bottom plot has an additional S1MF< 0.3 requirement.

produce more FS Cherenkov events. PTFE Cherenkov events, on the other hand, populates the blob at left-center. The enhancement from the UAr to the <sup>22</sup>Na is what we expected. This is a stronger argument for the existence of PTFE Cherenkov than the ones presented in Sec. 3.5.

# 4.3 Modeling the Cherenkov Radiation in G4DS

### 4.3.1 The Physics

When the velocity of a charged particle in a transparent medium meets the following conditions

$$\frac{1}{\beta} < n(\lambda), \tag{4.3}$$

the particle produces Cherenkov radiation. GEANT4 uses the classic Frank-Tamm equation to calculate the number of Cherenkov photons per unit traveled distance dx

$$\frac{d^2N}{dxd\epsilon} = \frac{\alpha Z^2}{\hbar c} \left( 1 - \frac{1}{\beta^2 n^2(\epsilon)} \right),\tag{4.4}$$

where  $\alpha$  is the fine structure constant, Z is the charge of the particle, and  $\epsilon$  is the emitted photon energy. Integrating Eqn. 4.4 yields

$$\frac{dN}{dx} = \frac{\alpha Z^2}{\hbar c} \left[ \epsilon_{\text{max}} - \epsilon_{\text{min}} - \frac{1}{\beta^2} \int_{\epsilon_{\text{min}}}^{\epsilon_{\text{max}}} \frac{d\epsilon}{n^2(\epsilon)} \right], \tag{4.5}$$

where  $\epsilon_{\text{max}}$  and  $\epsilon_{\text{min}}$  correspond to a UV cut off and a IR cut off, respectively. We define the effective index of refractive as

$$\frac{1}{n_{\text{eff}}^2} = \frac{1}{\epsilon_{\text{max}} - \epsilon_{\text{min}}} \int_{\epsilon_{\text{min}}}^{\epsilon_{\text{max}}} \frac{d\epsilon}{n^2(\epsilon)}.$$
 (4.6)

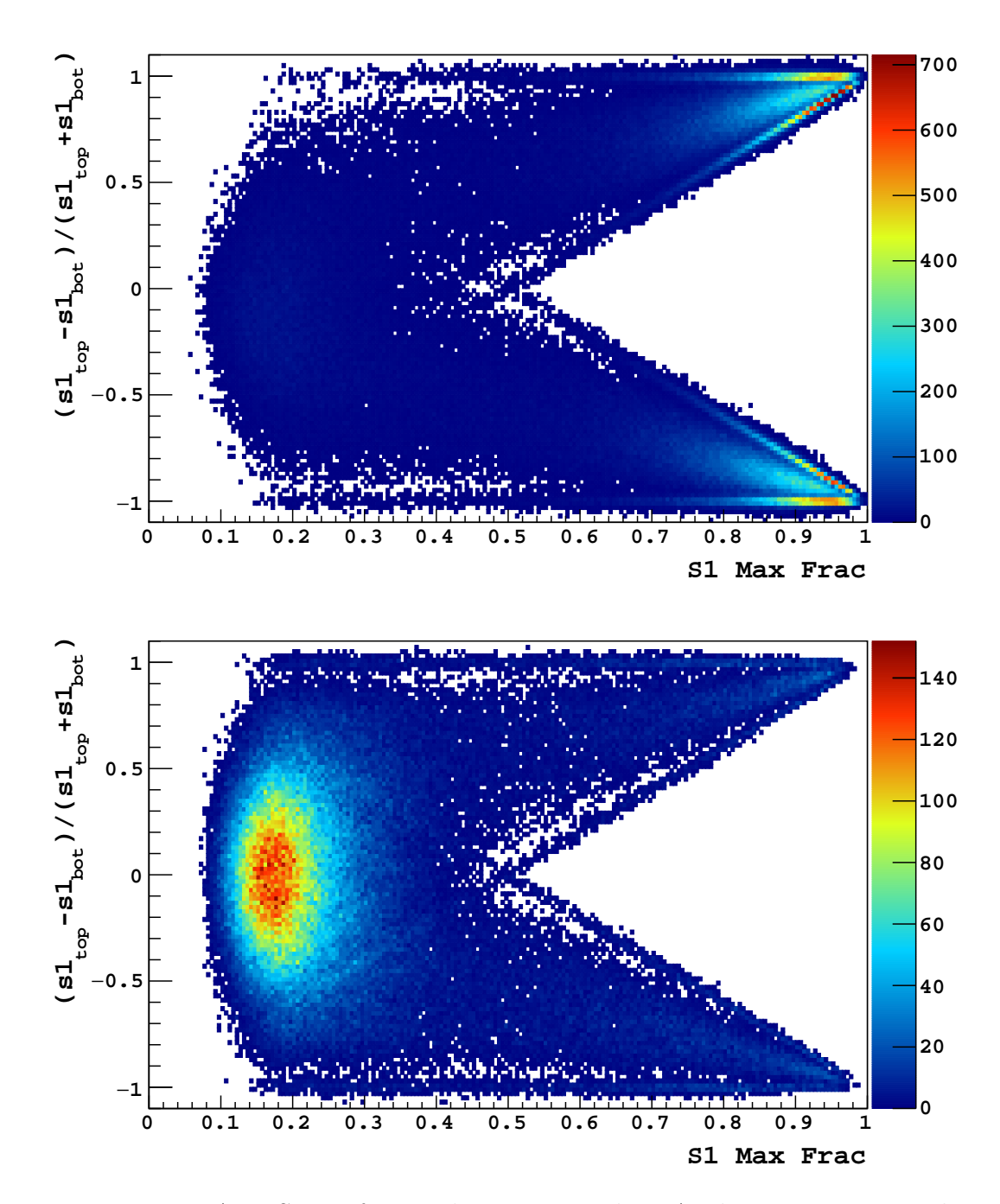


Figure 4.5: Top: TBA vs S1MF for 1-pulse events in the UAr data. Events are selected by the graphic cut in Fig. 4.4. Bottom: the same plot with the same selection criteria but for  $^{22}$ Na data.

Then the total number of Cherenkov photons can be expressed as

$$N = \frac{\alpha Z^2}{\hbar c} (\epsilon_{\text{max}} - \epsilon_{\text{min}}) \int_{E_{\text{th}}}^{E_0} \left(\frac{dE}{dx}\right)^{-1} \left[1 - \frac{1}{\beta^2 n_{\text{eff}}^2}\right] dE, \tag{4.7}$$

where  $E_0$  is the initial kinetic energy and  $E_{\rm th}$  is the minimum kinetic energy. Normally  $n(\lambda)$  is a monotonic decreasing function as  $\lambda$  increases, so the  $E_{\rm th}$  is typically defined at UV cut off of a material to satisfy the condition in Equation 4.3.

Since the integral depends on the total stopping power dE/dx which is a sum over all physical processes, it is important to make sure the Cherenkov process takes place last in any simulations that internally calculates dE/dx. By default, the Cherenkov process is the last one in GEANT4. GEANT4 assumes the energy loss due to Cherenkov is negligible compared to the sum of other processes, which is a very good approximation.

As a particle slows down, a cone of Cherenkov photons measured with respect to the particle momentum is formed. The maximum light cone angle  $\theta_{\text{max}}$  is determined by the highest index of refraction by

$$\cos \theta_{\text{max}} = \frac{1}{\beta n_{\text{max}}},\tag{4.8}$$

which decreases as the particle loses energy.

Qualitatively speaking, as the particle slows down, the average energy of photons produced increases because the IR bound of the spectrum need to satisfy Eqn. 4.3. Meanwhile the number of photons produced decreases according to Eqn. 4.5.

Therefore, in terms of light production the relevant parameters are  $n(\lambda)$ , the UV cut off  $\epsilon_{\text{max}}$ , and the IR cut off  $\epsilon_{\text{min}}$ .

# 4.3.2 Sources of Radioactivity

The major contributors of radioactivity in the UAr data are the PMT, the TPC Cryostat (inner and outer vessel, 5 mm stainless steel), the cryostat multilayer-insulation, the outer flange (25 mm stainless steel), the o-ring, and the inner flange (25 mm stainless steel).

Table 4.2: Summary of counting results used for the normalization of simulated radioactivity. 1- $\sigma$  uncertainty is used for the upper and lower bound. When only an upper bound is available, the upper bound rate is used. The  $^{60}$ Co rate in the table is corrected to the start of the 70-day UAr data-taking,  $\sim 3$  years after the counting was done (the  $^{60}$ Co half-life is 5.2 years). Additional correction to  $^{60}$ Co will be applied for the 500-day analysis (Ch. 5). Outer flange column includes the activity from the o-ring. The upper and lower  $^{238}$ U chains are measured separately due to the broken secular equilibrium where we assume  $^{222}$ Ra is the first element of lower chain.

Isotope	Cryostat	Inner flange	Outer flange	
	[Bq]	[Bq]	[Bq]	
<sup>60</sup> Co	1.3±0.1	$0.12 \pm 0.01$	$0.12 \pm 0.01$	
$^{40}\mathrm{K}$	< 0.004	< 0.027	$0.13^{+0.02}_{-0.05}$	
$^{232}\mathrm{Th}$	$0.05 \pm 0.01$	$0.05 \pm 0.01$	$0.09^{+0.01}_{-0.02}$	
$^{235}\mathrm{U}$	$0.015 \pm 0.003$	$0.013^{+0.002}_{-0.007}$	$0.018^{+0.002}_{-0.012}$	
$^{238}\mathrm{U}_{\mathrm{low}}$	$0.13^{+0.03}_{-0.10}$	$0.021^{+0.001}_{-0.020}$	$0.23^{+0.01}_{-0.03}$	
$^{238}\mathrm{U_{up}}$	$0.35 \pm 0.07$	$0.35^{+0.05}_{-0.15}$	$0.57^{+0.05}_{-0.37}$	

The locations of radioactivity within the PMT are further divided into the kovar shell, the ceramic insulators, and the borosilicate glass (PMT stem) according to the ratios specified in reference [41]. The PMT activities (the sum of ceramic, stem, and kovar) are obtained from a systematic approach of multi-dimensional fitting while activities from other components are fixed to the measured counting results. The actual rates used to normalize residual  $\gamma$ 's are summarized in Tab. 4.3. As a step to simplify the simulation, the o-ring is grouped into the outer flange activity, and the multi-layer insulation is grouped into the cryostat vessels.

In G4DS, each event is a decay of a radioactive element in a decay chain but in data each event is a DAQ trigger. Thus we need a way to re-scale the MC samples so that not only the spectral shapes but also the absolute spectral amplitudes can be meaningful when the MC is compared to the data. This is especially important for the final Cherenkov background prediction. We normalize the MC as the follows:

1. Generate high statistics MC samples for each decay chain ( $^{238}$ U-chain,  $^{232}$ Th-chain, K40, Co60, Ar39, Kr85) for each material. Record the number of appearances of the first element in the chain ( $N_{\rm MC}$ ).

Table 4.3: PMT and bulk LAr activity rates [42] used for the normalization of simulation for the 500-day analysis. The "best rates" numbers are from the spectrum fits along with the upper limit (UL) and lower limit (LL) [38]. There is no need to correct the <sup>60</sup>Co rate since they are fitted number directly from the data set. As a comparison to the fitted values, the last column shows the assay results from counting three PMTs. These three PMTs were not actually deployed in the TPC.

Source	Isotope	Best Rate	UL Rate	LL Rate	Meas. Results
		[Bq]	[Bq]	[Bq]	[Bq]
PMT	$^{232}\mathrm{Th}$	0.291	0.297	0.286	$0.23 \pm 0.04$
	$^{40}\mathrm{K}$	2.83	2.90	2.82	$3.00 \pm 0.42$
	$^{60}\mathrm{Co}$	0.17	0.19	0.15	$0.31 \pm 0.02$
	$^{238}\mathrm{U}^{\mathrm{low}}$	0.85	0.88	0.84	$0.69 \pm 0.02$
	$^{238}\mathrm{U}^{\mathrm{up}}$	3.42	3.75	3.11	$5.72 \pm 0.42$
	$^{235}{ m U}$	0.16	0.17	0.14	$0.27 \pm 0.02$
UAr	<sup>85</sup> Kr [/kg]	0.0030	0.0032	0.0028	$0.0021 \pm 0.0001$
	$^{39}$ Ar [/kg]	0.00062	0.00078	0.00042	$0.0007 \pm 0.0001$

- 2. Use the rates in Tab. 4.2 and 4.3 to normalize each MC sample to its respective number of decays expected in data for a given live-time. For example, suppose the data has a 540 day livetime, the scaling factor for  $^{232}$ Th<sub>PMT</sub> is: 0.291 Bq × 540 day/ $N_{\rm MC}$ .
- 3. Sum all MC samples to give a comprehensive representation of the  $\gamma$  activities in the UAr data.

In the first step, a full decay chain has its radioactive generator in G4DS randomly select a coordinate within the corresponding material volume for the first element (ex. <sup>238</sup>U). The subsequent decaying elements are attributed to a different MC event (if the mean decay lifetime is greater than 100 ns) and are at the same position as the first element until the end of the chain is reached. In the second step, we assume that secular equilibrium of the <sup>238</sup>U-chain is broken at <sup>226</sup>Ra (<sup>226</sup>Ra is the first element of the lower chain), so a <sup>238</sup>U MC sample is actually used twice in normalization, once for the upper chain (skip lower chain events in the analysis) and once for the lower chain (skip the upper chain).

## 4.3.3 Optics of PTFE

#### **Photon Creation**

The diffusive nature of PTFE makes it hard to precisely measure its optical properties. Billmeyers measured the refractive index of PTFE by shining yellow sodium light (589.0 and 589.6 nm) on a thin PTFE film and obtained a refractive index n = 1.376. The density of the sample was measured to be 2.12 g/cm<sup>3</sup> [43]. The refractive index of PTFE varies with its density according to,

$$\frac{n^2 - 1}{n^2 + 2} \frac{1}{\rho} = K, (4.9)$$

where  $\rho$  is the density of PTFE and K is a constant [44]. DarkSide-50 TPC reflector uses DuPont NXT 85 PTFE, whose average density is  $\sim 2.19 \text{ g/cm}^3$  at room temperature [45]. Given a 2% shrinkage in volume at LAr temperature [46] ( $\rho \sim 2.23 \text{ g/cm}^3$ ), the resulting refractive index could be as large as 1.399 g/cm<sup>3</sup>. In another attempt to measure the reflectance of the PTFE in liquid xenon,  $n(\lambda)$  is measured to be 1.51  $\pm$  0.07 (175 nm), 1.31  $\pm$  0.03 (250nm), 1.31  $\pm$  0.02 (310 nm), and 1.36  $\pm$  0.02 (550 nm) [47]. These numbers help give a sense of the physical range, but the exact  $n(\lambda)$  has to be tuned against our calibration data, as different conditions and assumptions drastically influence the results.

We adopt an effective parameter approach which assumes a constant n at all wavelengths. According to Eqn. 4.7, there exist a  $n=n_{\rm eff}$  so that the total number of Cherenkov photons N can be modelled perfectly by this effective parameter approach. We fix  $\epsilon_{\rm min}=1.6314\,{\rm eV}$  because our PMTs cannot detect photons above 760 nm (Fig. 4.12). Now n and  $\epsilon_{\rm max}$  are the only two numbers to play with and they are degenerate with each other. Notice  $N \propto \epsilon_{\rm max} - \epsilon_{\rm min}$  according to Eqn. 4.7. So increasing  $\epsilon_{\rm max}$  and n will give the same effect as increasing N. Also notice that the  $\epsilon_{\rm max} - \epsilon_{\rm min}$  term is proportional to N for all energies of the charged particle.

According to Eqn. 4.4, the Cherenkov photon wavelength spectrum goes like  $\sim 1 - 1/\beta^2 n(\lambda)^2$ . The effective approach (using a constant n instead of  $n(\lambda)$ ) means that the

wavelength spectrum is flat per unit distance dx at a given particle energy. One concern is that in reality, there is an energy dependence on the collection efficiency of the Cherenkov photons. For example, if an UV photon has a lower probability than a visible photon to enter the active LAr volume, the effective approach will likely to overestimate the collection efficiency assuming  $n(\lambda)$  is a monotonically decreasing function.

In our case, the PTFE optics are tuned on low energy calibration data ( $^{22}$ Na, 1.27 MeV  $\gamma$ -ray) while the UAr data contains  $\gamma$  rays with various energies, such as  $^{208}$ Ti from  $^{232}$ Th chain (2.61 MeV). The effective approach may bias energies beyond the 1.27 MeV  $\gamma$ -ray. However, the final value n from the optics tuning does not have to be equal to the  $n_{\text{eff}}$  in reality. The influence on wavelength spectrum may be compensated by tuning on the detected PE, which makes it a higher order effect. An estimate of the total Cherenkov systematic related to G4DS will be discussed in Sec. 4.3.8.

The number of Cherenkov photons produced for a given initial electron energy is shown in Fig. 4.6-left. According to this plot, the kinetic energy threshold in the PTFE is about 300 keV, and the photon production seems to rises faster as the kinetic energy increases. Keep in mind that any toy MC needs to incorporate this energy dependence. In reality, we also need to consider boundary conditions as part of the simulation. Higher energy implies a higher chance for an electron to escape the PTFE reflector and hit the surrounding material (e.g. field cage rings, TPB, LAr). To obtain a clean version of this plot, we apply energy cuts to remove events with any LAr depositions and excessive energy depositions in the field cage rings.

#### Photon Propagation

PTFE diffusion can be modeled by letting each photon random walk. Although the true scattering of an optical photon in PTFE is not isotropic (therefore not a random walk) on a microscope scale, the model intends to reproduce the diffuse properties at a macroscopic scale thanks to the central limit approximation. We assume the scattering angle in PTFE

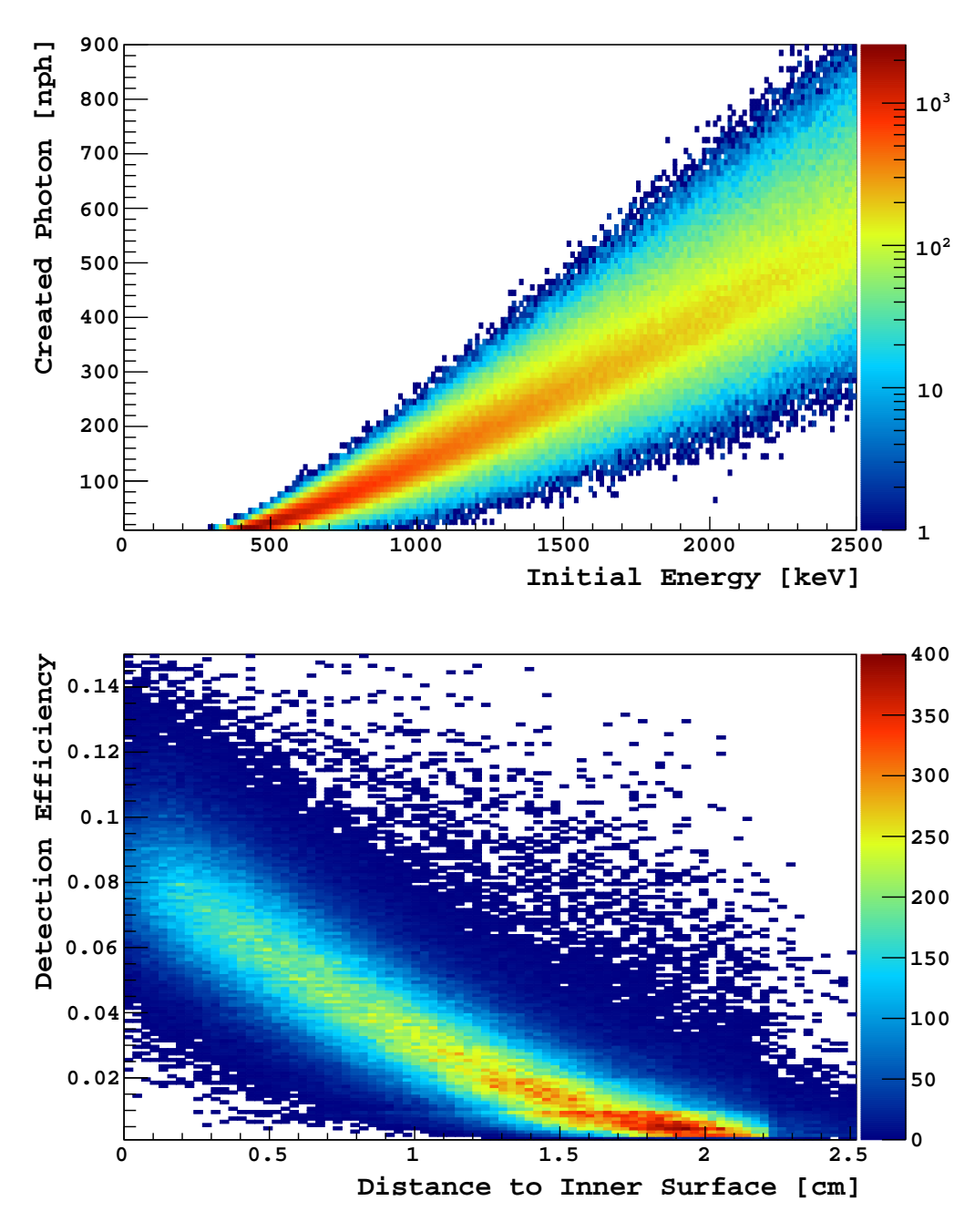
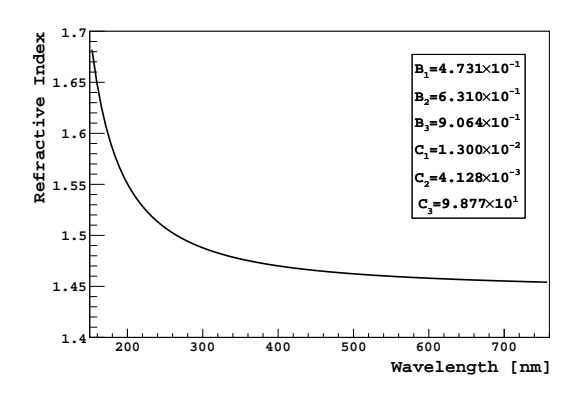


Figure 4.6: Electrons from 0 to 2.5 MeV are uniformly generated in the PTFE reflector. Top: the number of photons produced  $(N_{\rm ph})$  as a function of initial kinetic energy. We require no energy deposited in the LAr and 99% energy deposited in the PTFE (sometimes the electron hits the copper cage rings inserted in the back of the reflector). Bottom: the detection efficiency  $(N_{\rm pe}/N_{\rm ph})$  as a function of electron's initial distance to the inner surface. Here  $N_{\rm pe}$  is the number of photons detected by PMTs. We require  $N_{\rm ph}>100$  to remove events with high statistical fluctuation for a better visibility. The glitch at  $\sim 2.25$  cm are due to the realistic T-shape copper cage rings. Events with 0 efficiency are not drawn for clarity.

is not biased in either the forward or backward direction. Rayleigh scattering with a short fixed mean free path is selected as the scattering process for optical photons because it satisfies this assumption. The two relevant parameters are the mean free path of the photon  $(\lambda)$  and the absorption length  $(l_{\rm abs})$ , and they are degenerate with each other. To visualize the degeneracy, consider a naive picture of the relation  $R \sim \sqrt{N} \sim \sqrt{l/\lambda}$ , where R is the average distance traveled from the center, N is the number of steps, and  $\lambda$  is the step length. Absorption probability depends on the physical distance travelled l as  $P \sim e^{l/l_{\rm abs}} \sim e^{R^2/l_{\rm abs}\lambda}$ . Of course, since  $\lambda$  is the mean free path and we need to consider the PTFE boundary, the exact relation above shouldn't be used as a constraint. As will be discussed in Sec. 4.3.6, we set  $\lambda = 0.2$  mm [48] and tuned on  $l_{\rm abs}$ .

While defining the optical boundary surfaces, we set the transmission to 100% for the PTFE—TPB direction, but 0% for the TPB—PTFE direction. There is no reflection on the PTFE—TPB direction. This means that once a photon exits the PTFE and enters the TPB volume, it cannot re-enter the PTFE volume again. The reflectance for a photon going from the TPB—PTFE direction is 97.5%. This number is globally tuned by C. Zhu (Sec. 4.3.6 for a brief description). With this boundary implementation, once a Cherenkov photon hits TPB, regardless of its wavelength, it enters the active LAr volume. The optics regarding the bulk LAr scintillation was tuned by C. Zhu and the Paris group. Therefore, if we are correctly simulating the total number of photons exiting the reflector, the rest is handled by the bulk LAr optics, and the effective approach should be fine to first order.

The resulting detection efficiency  $(N_{\rm pe}/N_{\rm ph})$ , in Fig. 4.6-right, shows a much higher probability closer to the PTFE surface for a Cherenkov photon to be eventually detected. As one may notice, the T-shape field cage rings do have a sizeable impact for Cherenkov light near the outer PTFE surface.



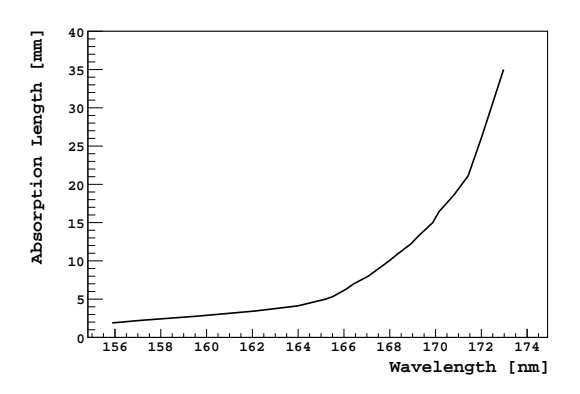


Figure 4.7: Left: Sellmeier's equation and the parameters for our FS. Right: The absorption length at a UV range near the cut off, obtained from extrapolating the transmission measurement data by Heraeus. Below 155 nm,  $l_{\rm abs}$  is arbitrarily short while above 190 nm,  $l_{\rm abs}$  is arbitrarily long.

### 4.3.4 Optics of Fused Silica

The refractive index of fused silica (FS) is well described by Sellmeiers equation as

$$n^{2} - 1 = \frac{B_{1}\lambda^{2}}{(\lambda^{2} - C_{1})} + \frac{B_{2}\lambda^{2}}{(\lambda^{2} - C_{2})} + \frac{B_{3}\lambda^{2}}{(\lambda^{2} - C_{3})},$$
(4.10)

where  $B_i$  and  $C_i$  are specific parameters to be determined sample by sample experimentally. The DarkSide-50 diving bell and cathode window use Heraeus Surprasil 312, which has measured data available from 190 nm to 1240 nm [49]. The fitting of Sellmeier's model is done by the manufacturer in this range, with the parameters summarized in Fig. 4.7. This numeric function allows us to smoothly extend the refractive index from the IR cut off (760 nm) all the way to the UV cut off (155 nm) for the diving bell and cathode window FS in G4DS.<sup>3</sup> The PMT face-plate is made of FS as well but from a different manufacturer. We used exactly the same function to model the PMT face-plate, whose predicted  $n(\lambda)$  values has been crossed checked with Hamamastu's data in the available wavelength range [50].

The absorption length is unknown but can be extrapolated from the manufacturer's transmission measurements. The manufacturer shined laser light of various wavelengths

<sup>&</sup>lt;sup>3</sup>Although the plot x-axis is in the unit of nanometer, the equation with these 6 parameters require wavelength inputs in the unit of micron.

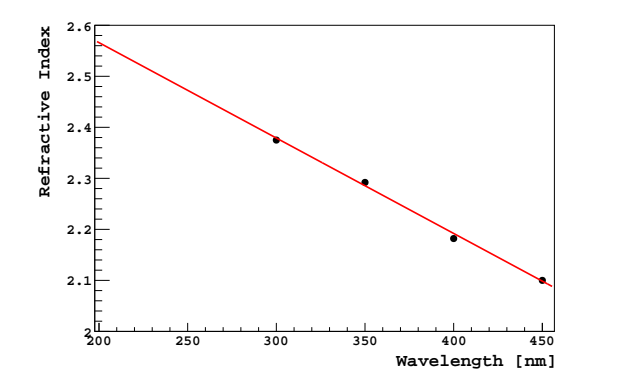
perpendicular to a 1 cm thick FS sample and measure the total transmission (T) and reflection (R) [49]. The assumption is that the fraction of light absorbed by going through a sample of thickness d goes like  $A = e^{-d/l_{abs}}$ . To the first order, T is related to A and surface Fresnel reflection r by  $T \approx (1-A)(1-r)^2$ , where the term  $(1-r)^2$  is due to Fresnel reflection loss. The calculated  $l_{abs}$ , shown in Fig. 4.7, is implemented in G4DS as a material property. The absorption length for the PMT face-plate is obtained by the same procedure but used Hamamastu's transmission data [50].

### 4.3.5 Other Relevant Optics

### The ITO Modeling

The diving bell (anode) and cathode windows are coated on both faces by 15 nm thick conductive indium tin oxide (ITO) films, whose optical response to light strongly depends on the incident angle and wavelength. In G4DS, the ITO films are treated as boundary surfaces between two dielectric mediums, e.g. between FS and LAr for the top side of the diving bell. A custom model, based on Sernelius's treatment for a metallic medium sandwiched by two parallel dielectric plates [51], was first coded up by an undergraduate student at Princeton. The model requires both real and imaginary (extinction coefficient) parts of ITO's refractive index at various wavelengths as the input parameters, which we obtained as theoretical values from Evaporated Coatings, Inc. However, the input data is not available below 300 nm and FS Cherenkov produces a continuous spectrum from the IR cut off (760 nm) to the UV cut off (155 nm). The missing input parameters down to 155 nm are extrapolated by fitting empirical functions to the available data, as shown in Fig. 4.8. 100% absorption is assumed below 155 nm. We have to admit that this is a weak point of the FS Cherenkov modeling, as UV radiation is abundant.

Fig. 4.9 shows the prediction of the ITO model's reflectance, transmittance and absorption of photons going from FS to LAr. When a photon crosses the ITO interface, the model reads the refractive indices for both mediums. There is another weak point when one medium



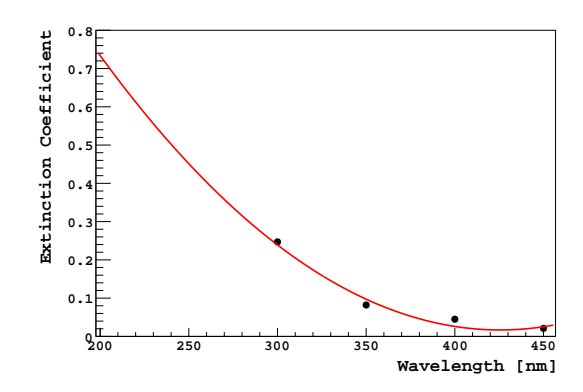
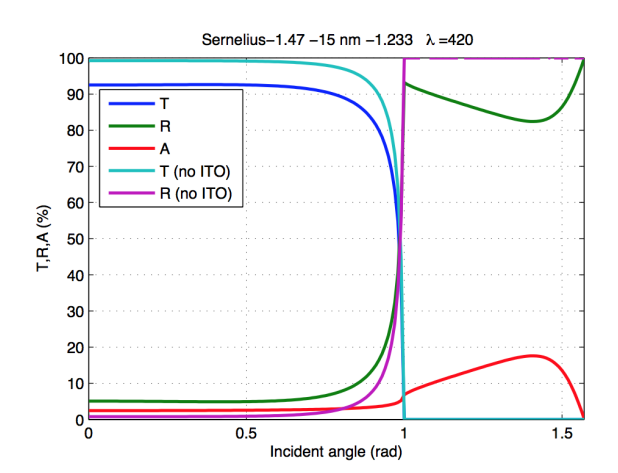


Figure 4.8: The empirical extrapolation of the refractive index (linear) and the extinction coefficient (second order polynomial) based on 4 available data points near UV. The extrapolation is extended down to 155 nm.



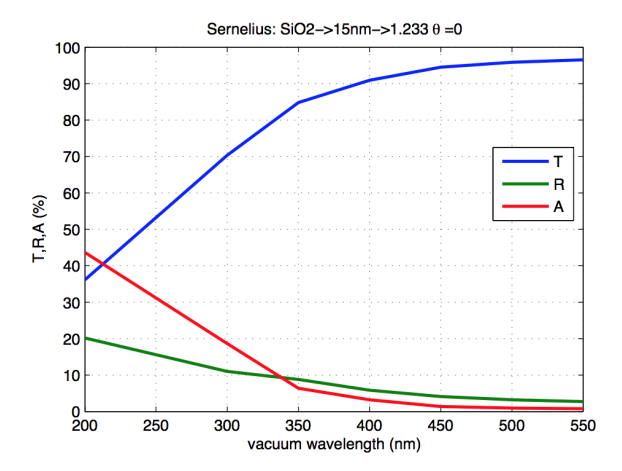


Figure 4.9: Left: Sernelius's model for 420 nm photon from FS (n=1.47) to LAr (n=1.233). Reflectance (R), transmittance (T) and absorption (A) as a function of incident angle. Right: Reflectance (R), transmittance (T) and absorption (A) as a function of incident photon wavelength from FS (refractive index depends on wavelength) to LAr (n=1.233).

is TPB — the TPB index of refraction is set to 1.5 while we don't have an assessment of its accuracy.

The ITO model is validated against data measured at Princeton. A Perkin-Elmer Lambda 650 spectrophotometer measures the reflection and transmission of an ITO coated FS sample from 800 nm to 200 nm, shown in Fig. 4.10. It was a piece of ITO coated fused silica window sample done by the same Company, with ITO coating on one side of the sample. We borrowed a Thorlab UV mirror from a AMO lab at Princeton in order to provide a

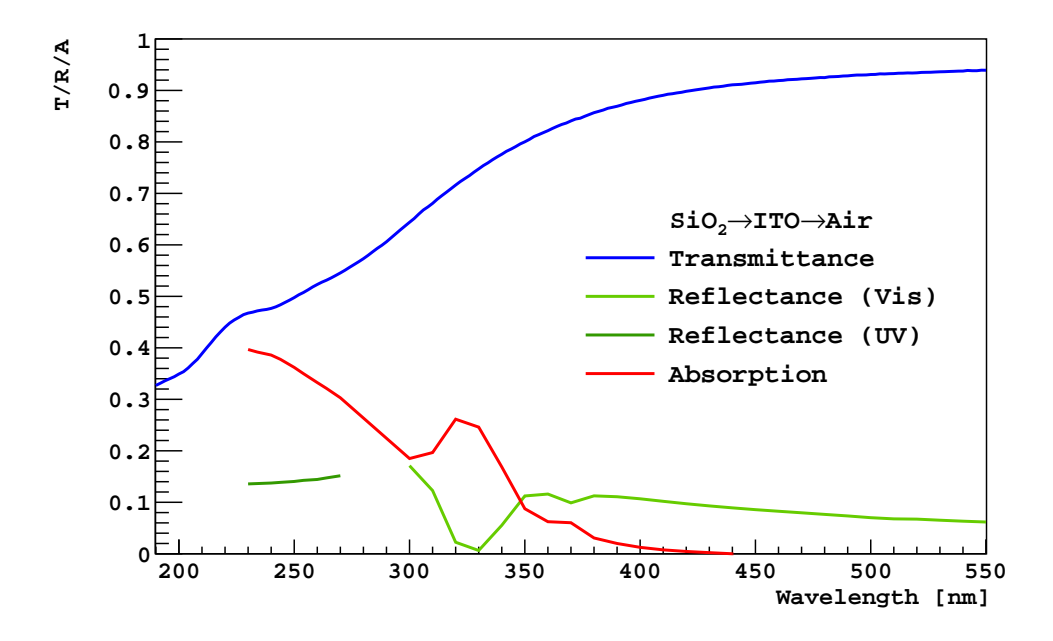


Figure 4.10: The ITO's transmission (T), reflection (R), measured at Princeton's spectrophotometer. The T measurement uses air as the 100% transmission reference (no sample is placed). The R measurement is done by two parts, one using a visible mirror as a reference, one using a borrowed UV mirror as the reference. The dip of the R curve between 300 nm to 350 nm is a result of inaccurate visible mirror reference values. Both T and R are done with ITO coated side faces away from the laser (measuring  $SiO_2 \rightarrow ITO \rightarrow Air$ ). All reflecting samples have a 7-degree incident angle with the laser beam. The spectrophotometer can not measure below 200 nm. The absorption (A) is calculated via A = 1 - T - R.

reference for specular reflection below 400 nm. After we collected the data, the same ITO sample was sent to Evaporated Coatings Inc as a cross-check measurement.

#### PMT's Reflection and Quantum Efficiency

At the end of photon tracking, if an optical photon is absorbed by a PMT's photocathode, it is converted into a photoelectron with a probability defined by  $QE(\lambda)$  (Fig. 4.12). The  $QE(\lambda)$  data sheet from Hamamatsu does not decouple the actual QE (conversion from photon to PE) from the PMT's collection efficiency and photocathode reflection. Although having the collection efficiency folded in the Hamamatsu's curve is practically not a concern, the photocathode reflection does have an impact on the S1 and S2 light distribution per channel, especially for FS Cherenkov events. For example, without the reflection, many FS Cherenkov

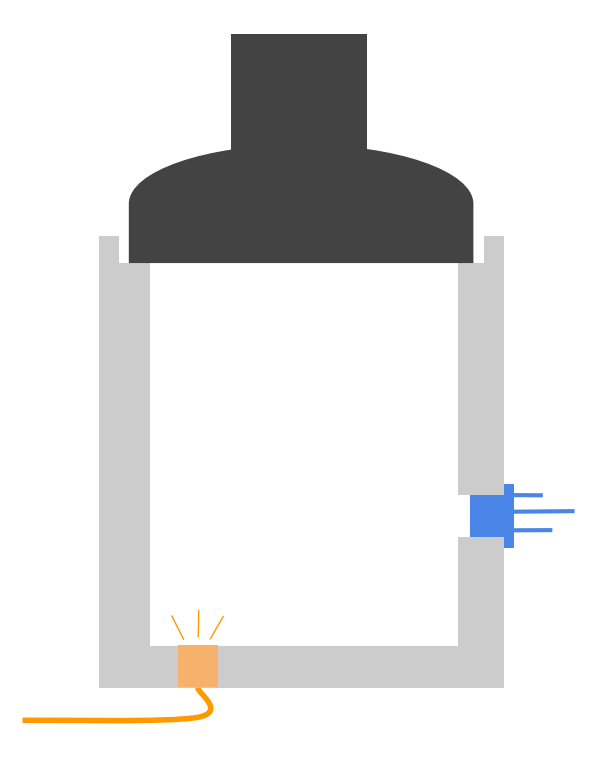


Figure 4.11: The illustration of the simple measurement of the PMT overall reflectivity done in Princeton. The PTFE cup is in grey, the PMT is in black, the optical fiber is in orange, photo-diode is in blue, and the PTFE cup is filled with air. The entire set up is in a black box. A 420 nm LED produces 420 nm light, which is then delivered into the PTFE by an optical fiber. The signal recorded by the photo-diode is read off from oscilloscope measurement.

events will not even satisfy the majority trigger condition which requires that two or more PMTs see signals. It's important to point out that the PMT geometry as illustrated in Sec. 4.3.7 is not able to produce the complicated light reflections inside a real PMT for many reasons<sup>4</sup>. Thus the so-called "PMT reflectivity" in G4DS is a constant parameter that effectively represents the overall reflections in a PMT.

A rough attempt to measure this PMT reflectivity was done at Princeton by shining a 420 nm LED light onto a R11065 PMT in a PTFE cup. The set up is illustrated in Fig. 4.11. First, we measured the photo-diode voltage when the PMT is placed on top of the cup, and

<sup>&</sup>lt;sup>4</sup>In reality, the bialkali is coated on both the inner surface (between FS and vacuum) of FS face-place and the curve metallic surface in PMT head. Photons will be converted into PE on both surfaces. In G4DS, the PMT geometry has bialkali coated on the inner surface of FS face-plate only. Since the bialkali in G4DS has arbitrary short absorption length for optical photons, photons will be absorbed immediately after they enter the bialkali volume.

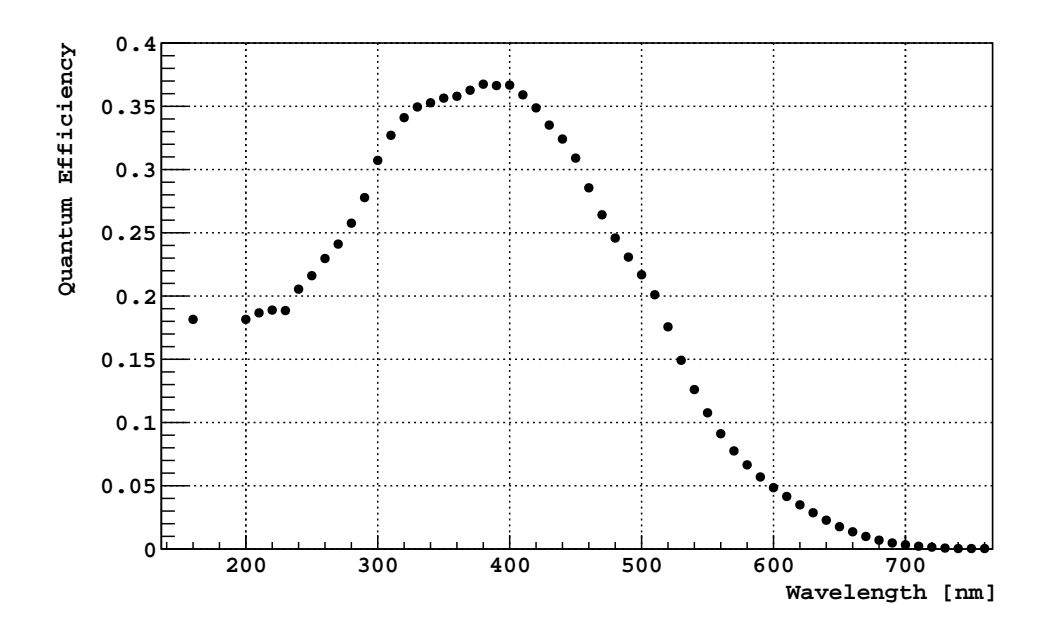


Figure 4.12: The quantum efficiency used for TPC PMTS before making the constant correction due to PMT reflection. The QE is 0 below 160 nm and above 760 nm.

then we took off the PMT (reflection  $\sim 0\%$ ) and measured the voltage again. The assumption here is that the voltage difference is proportional to the reflectivity. For the reference sample, we want it to be as close to the actual PMT reflectivity as possible (to minimize any non-linear effects). So we calibrated many reference samples in the spectrophotometer until we found the ones that have voltage readings close to the PMT's. This method returned a value of 19% without an evaluated systematic error.

In the final optics simulation, we actually set the PMT reflectivity to 10% ( $\lambda > 200$  nm) and 12% ( $\lambda < 200$  nm). The former 10% was tuned by C. Zhu in the second round of global tuning (4.3.6) where he compared the S2 Top Bottom Asymmetry (TBA) distribution between the MC and the AAr data. As it turns out, the 10% PMT reflection seems to make the overall optics agreement better. The 12% value was fine-tuned by comparing S1MF distributions of pure FS Cherenkov events between MC data and the UAr data (Sec. 4.3.6). If Hamamatsu's QE measurement does not correct QE due to reflection, applying this set of reflection values means we need to scale up the QE( $\lambda$ ) curve by  $\sim 1.11$ . The corrected QE( $\lambda$ ) curve is used in G4DS.

Another minor optical parameter is the reflectance between the inner PMT kovar walls and the LAr ring around the FS (Fig. 4.19, the LAr ring is in purple). kovar has specular reflection with its reflectance equals to a constant of 95% in the range from 155 nm to 1.25 µm, and 10% below the range. Optical tuning suggests the impact of this parameter is minimal.

#### An Artificial LY Scale Factor

The artificial scaling factor was introduced during the most recent <sup>22</sup>Na tuning, where the PMT window part of the pure Cherenkov spectrum clearly seems to have a deficiency of LY. Instead of going back to tune the FS related optics, we simply multiply the QE by a factor if a Cherenkov photon hitting the photocathode is from the PMT window. In the other words, it specifically scales up the LY for PMT-window-originated Cherenkov light. The final value is tuned to 1.2. Introducing this factor avoids complicated last-minute tuning, which could have impaired the effort of global tuning.

## 4.3.6 Cherenkov Related Optics Tuning

### An Overview

The brief history of optics tuning goes as the following. We had two rounds of global turning done by C. Zhu, aiming at matching the optical response of G4DS to the high statistics AAr data. The first round fixed the discrepancy of S1 top bottom asymmetry (TBA) and the drift time dependence of S1 light yield. The solution to the TBA discrepancy introduced a layer of non-scintillating LAr in front of the TPB on the diving bell. The solution to the latter discrepancy required an increase of attenuation length of 128 nm light in LAr. Since the first round of the global tuning, we had implemented all necessary optics to perform Cherenkov simulation and had tuned the model on pure Cherenkov to give a good agreement to  $^{22}$ Na data. Then we checked the impact on 70-day UAr data using the PMT geometry and the  $\gamma$  rate available at the time. The insights from the UAr comparison help us update

the understanding of optics and the radioactive sources. It's important to point out that although we check the pure Cherenkov spectrum in UAr from time to time, the UAr data simply serves as a guideline. The actual tuning is iteratively done on <sup>22</sup>Na until we have a satisfied MC-data spectrum agreement. We then had a second global tuning because the new Cherenkov-related optics, for example, the addition of PMT reflection, had some distortions on TPC bulk light distributions. The second global tuning attempted to re-adjust the bulk optics back to match the LAr scintillation in the AAr data. In particular, having the PMT reflectivity allowed us to abate the long-standing discrepancy of S2 channel light distribution. Finally, we tuned the Cherenkov related optics again but only adjusted parameters that did not distort the global parameters. Optics tuning has been completely frozen since opening a sample of the blinded data for testing.

### Tuning with the <sup>22</sup>Na Data

The Cherenkov related optics is tuned mainly on  $^{22}$ Na data because we know exactly the  $\gamma$ -ray energies (1.27 MeV and two 511 keV), the source decay rate (11.2 kHz). Furthermore, since the  $\gamma$ -rays are coming from the side (the holder position was located at exactly the same coordinates as the AmC simulation),  $^{22}$ Na not only enhances the amount of Cherenkov in the PTFE reflector for our interest, but also decouples the optics of FS Cherenkov from PMT geometry (as opposed to UAr whose  $\gamma$ 's are mostly originated from specific components within PMTs, and the detailed geometry implementation does have a sizable impact). Furthermore, since the  $^{22}$ Na rate absolutely dominates over the in-situ  $\gamma$  activities, we don't need to perform any background subtraction.

To predict the absolute Cherenkov rate, we perform a live-time normalization to both MC and data using the source decay rate (11.2 kHz) and the total live-time of the usable data set (5.1482 hours). The normalization factor to MC is the product of the rate (11.2 kHz) and the total number of  $^{22}$ Na decay in MC ( $N_{\rm MC}$ ). We checked the live-time normalization by comparing the entire energy spectrum of ER events in the range of  $0.2 < f_{90} < 0.4$ 

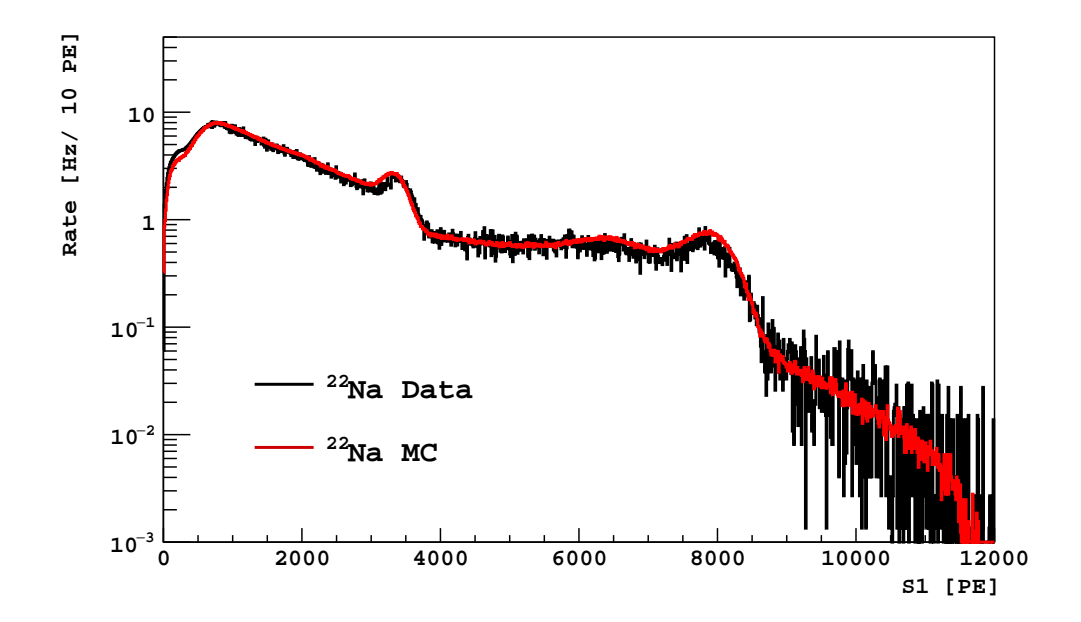


Figure 4.13: The live-time normalized  $^{22}$ Na spectrum from MC plotted against the data. The pre-scale correction is applied to the data (see text). A manual LY correction factor of 1.045 is applied to all MC events (see text). Cuts: basic quality cut, trigger cut,  $N_{\text{pulse}} = 1$  cut, and  $0.2 < f_{90} < 0.4$ .

(Fig. 4.13). The detailed scheme for modeling S1 and  $f_{90}$  will be discussed in Sec. 4.4. The decent agreement of the amplitudes in the entire  $^{22}$ Na energy range implies an accurate normalization factor.

The trigger system of <sup>22</sup>Na runs has pre-scaled factors designed to avoid an overwhelmingly large amount of data flow. The system defines two thresholds based on the multiplicity of hits in an adjustable time window. The three pre-scale factors are independently defined between the two thresholds, with each factor defining the fraction of events being randomly recorded by the DAQ system. Thus we have to perform an inverse pre-scale correction to recover the spectrum in the <sup>22</sup>Na data.

The TPC light collection efficiency is slightly higher in the absence of the gas pocket because there is no internal reflection at the liquid-gas interface. We took <sup>22</sup>Na data without any gas pockets to allow the system to handle high trigger rate. Since the S1 modeling scheme (Sec. 4.4.3) does not propagate scintillation photons, we have to apply a constant

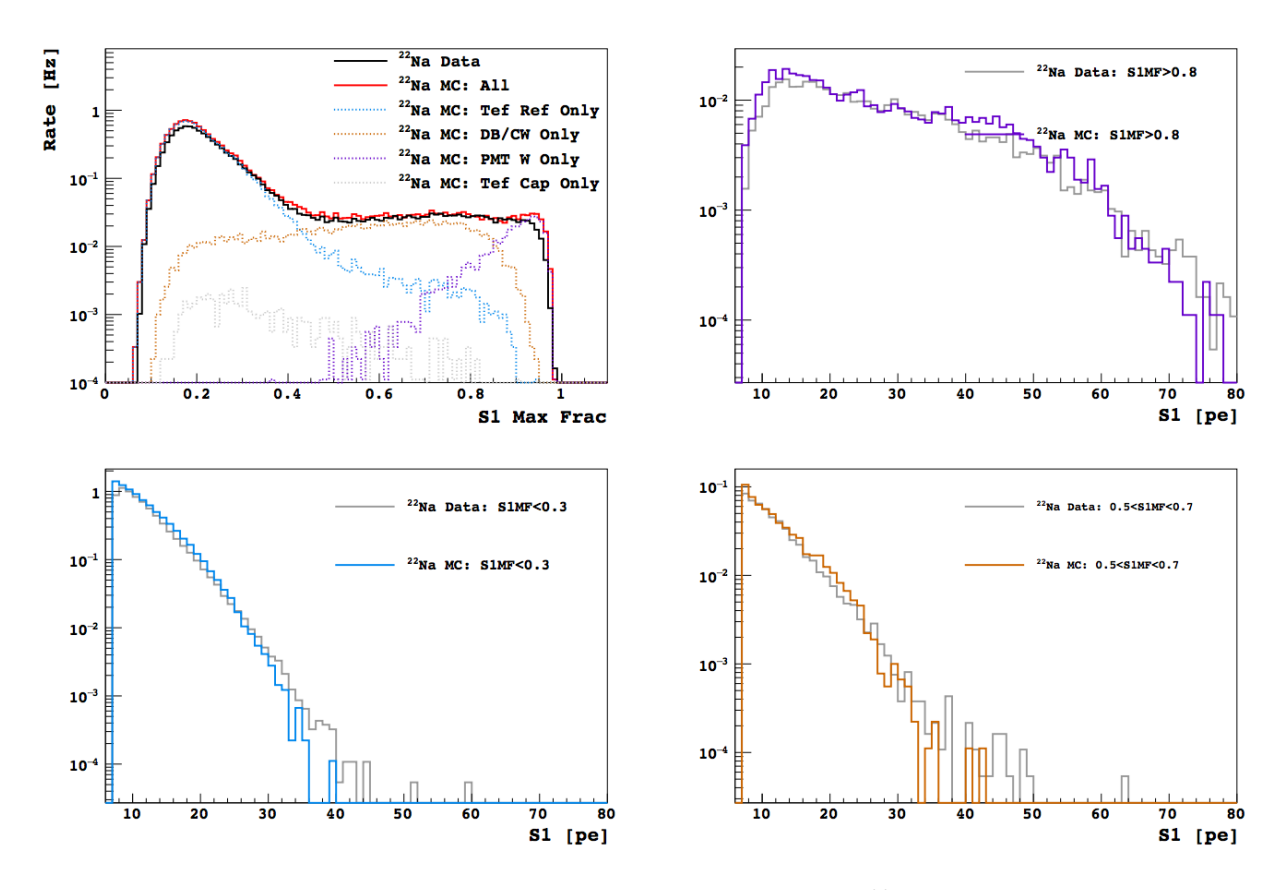


Figure 4.14: Finalized optics tuned by comparing model to <sup>22</sup>Na data. The data selection criteria are the same as Sec. 4.2.2. All plots are live-time normalized. The dashed lines in top left plot show S1MF can be used to distinguish different Cherenkov radiators.

S1 LY correction factor of 1.045 to all MC events. Although we did not estimate the actual LY correction factor in data, it is sufficient to show that the normalization was correctly implemented.

The final results are shown in Fig. 4.14. The S1 maximum fraction distribution provides a guideline to break down one S1 spectrum into three. As shown in Fig. 4.14 top left, pure PTFE Cherenkov (blue) dominates low S1MF end (S1MF< 0.3), PMT window Cherenkov (purple) dominates the high S1MF end (S1MF> 0.8), and the diving bell cathode window Cherenkov (orange) dominates the middle range (0.5 <S1MF< 0.7). With the S1MF cuts, we can enhance the Cherenkov population from a particular radiator to make sure that we

actually model each of the three radiators correctly. <sup>5</sup> The tuning process is done iteratively until a decent agreement is achieved for all three Cherenkov radiators. A decent agreement in both shape and the overall amplitude of the spectra implies a good representation of the underlying mechanism and prediction of the overall Cherenkov rate.

#### Checking with the UAr Data

The simulated pure Cherenkov spectrum in Fig. 4.15-Top shows a deficit of population at high S1MF. By decomposing the MC into separate radiators, we see that this deficiency comes from Cherenkov in the PMT windows. One hypothesis to explain this deficiency suggests the existence of contamination in close proximity to the PMT windows. For example, there are reports of  $^{238}$ U-chain activity in the aluminum sealing of similar Hamamatsu's PMT by the XMASS experiment. Since the aluminum sealing is in direct contact with the PMT window, adding a small amount of radioactivity in aluminum could give a large amount of PMT window Cherenkov while still having a negligible impact on the overall  $\gamma$  spectrum in LAr. We have postponed any detailed studies of this hypothesis because FS Cherenkov background will become negligible after the 95% S1MF cuts and z-fiducial cut. On the low S1MF end of the spectrum, the pure PTFE Cherenkov is in good agreements with data. We select these by a S1MF < 0.25 cut for detailed S1 comparison (top-right). There is a slight overestimation at S1>50 PE and underestimate below at S1< 15 PE. The PTFE agreement is good overall.

We heavily rely on S1MF to reject the majority of FS Cherenkov background. To get a reliable estimate of the rejection power, it's important to make sure that S1MF is correctly simulated in G4DS for both top and bottom PMTs. Since Cherenkov in PMT window has the highest LY than the other Cherenkov radiators, we can impose a minimum S1 cut on pure Cherenkov events to study the relevant distribution of S1MF, as shown in Fig. 4.16

<sup>&</sup>lt;sup>5</sup>Please do not get confused about the colors. In 4.14 top left plot, the color curves are pure Cherenkov from respective Cherenkov radiators. In the three S1 spectrum plots, the color curves are the total pure Cherenkov in MC; a color simply indicates the dominance of a specific radiator.

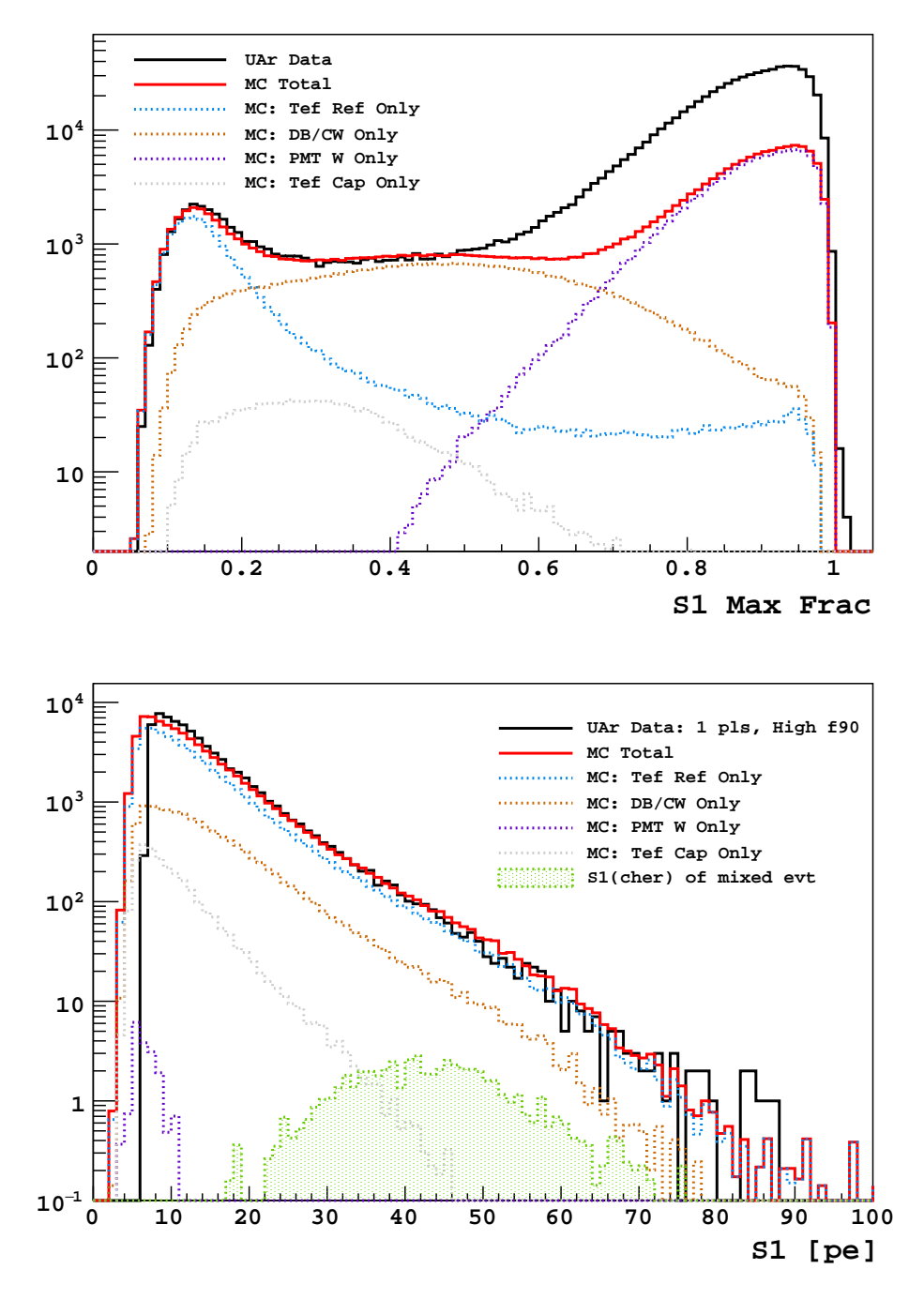


Figure 4.15: The simulated pure Chernekov events as compared to the UAr data. The data events selection is the same as Sec. 4.2. Top: the S1MF distribution. An additional S1> 15 PE cut is applied to remove low PE statistics events. Bottom: the S1 distribution. An additional S1MF< 0.25 cut is applied to select pure PTFE Cherenkov events. The cliff in the data at low S1 is a result of the pulse finder efficiency (Sec. 4.4.9). The simulation of the efficiency is turned off in MC. The interpretation of the green shadow will be discussed in Sec. 4.3.8.

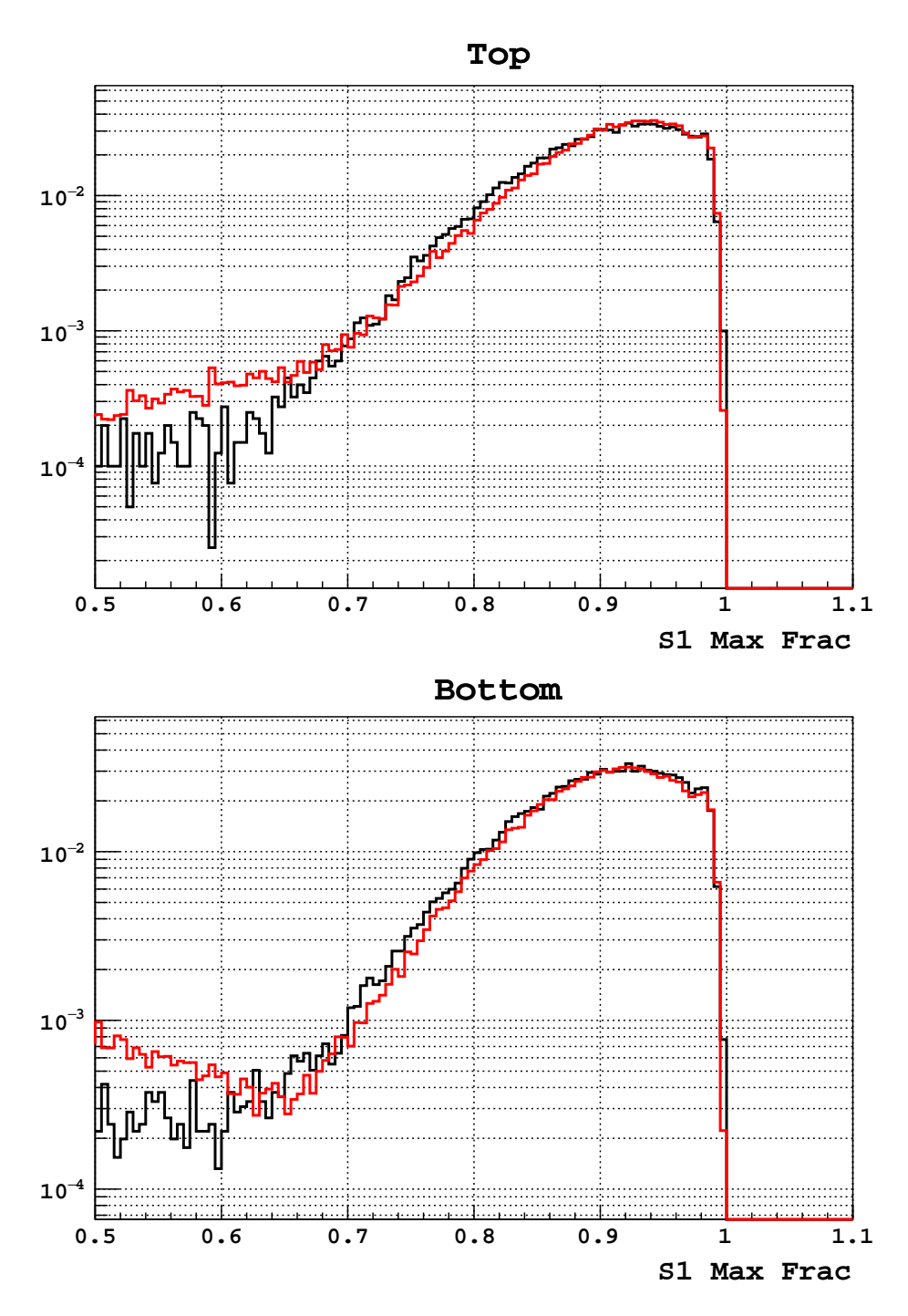


Figure 4.16: The comparison of S1MF distribution shapes for pure FS Chernekov events in the UAr data. Both plots have an additional S1> 30 PE cut imposed to emphasize on Cherenkov radiated in the PMT windows. The MC is scaled such that the peak height matches the data. Top: Cherenkov occurs in the top windows. Bottom: the Cherenkov occurs in the bottom windows. The excess of MC at low S1MF is expected because we know the MC is underestimating the population of PMT window Cherenkov.

bottom. The agreement means we can trust the S1MF rejection for PMT window Cherenkov background.

#### A check with AmBe

In June 2016, we had a neutron calibration campaign, which used a 160 n/s  $^{241}$ Am-Be source borrowed from the XENON collaboration. This campaign resulted in  $\sim 5.7$  live-days of usable data. According to the G4DS, this AmBe source, 36% of the time produces one neutron only, 61% of the time produces one neutron plus one 4.4 MeV  $\gamma$ -ray, and 3% of the time produces one neutron plus two  $\gamma$ -rays (4.4 MeV and 3.2 MeV). Although  $^{241}$ Am-Be calibration data is traditionally used for the NR calibration, it also comes with high energy  $\gamma$ -rays to be used as a check of our Cherenkov model. This is also an interesting check because it explores possible systematic error introduced by applying the effective PTFE Cherenkov model at an energy range that is higher than what it was tuned on.

Getting the source position right is important for the overall rate. We position the <sup>241</sup>Am-Be source holder at the same coordinates (center right outside of the cryostat) as the AmC simulation tuned by H.Qian.

Knowing the neutron rate, branching ratios, and the livetime of the  $^{241}$ Am-Be campaign, we can again perform a livetime normalization. The  $^{241}$ Am-Be simulation in G4DS has one neutron emission regardless of which one of the three channels it is simulating. Thus, we can treat the  $^{160}$  n/s  $^{241}$ Am-Be source as a  $^{160}$  Bq radioactive decay, and the rest is similar to what we've done before for normalizing  $^{22}$ Na. In summary, the normalization factor N is:

$$N = 160 \,\mathrm{Bq} \times \tau / N_{\mathrm{MC}},\tag{4.11}$$

where  $\tau$  is the livetime in seconds of the <sup>241</sup>Am-Be data set, and  $N_{\rm MC}$  is the total number of events produced by G4DS.

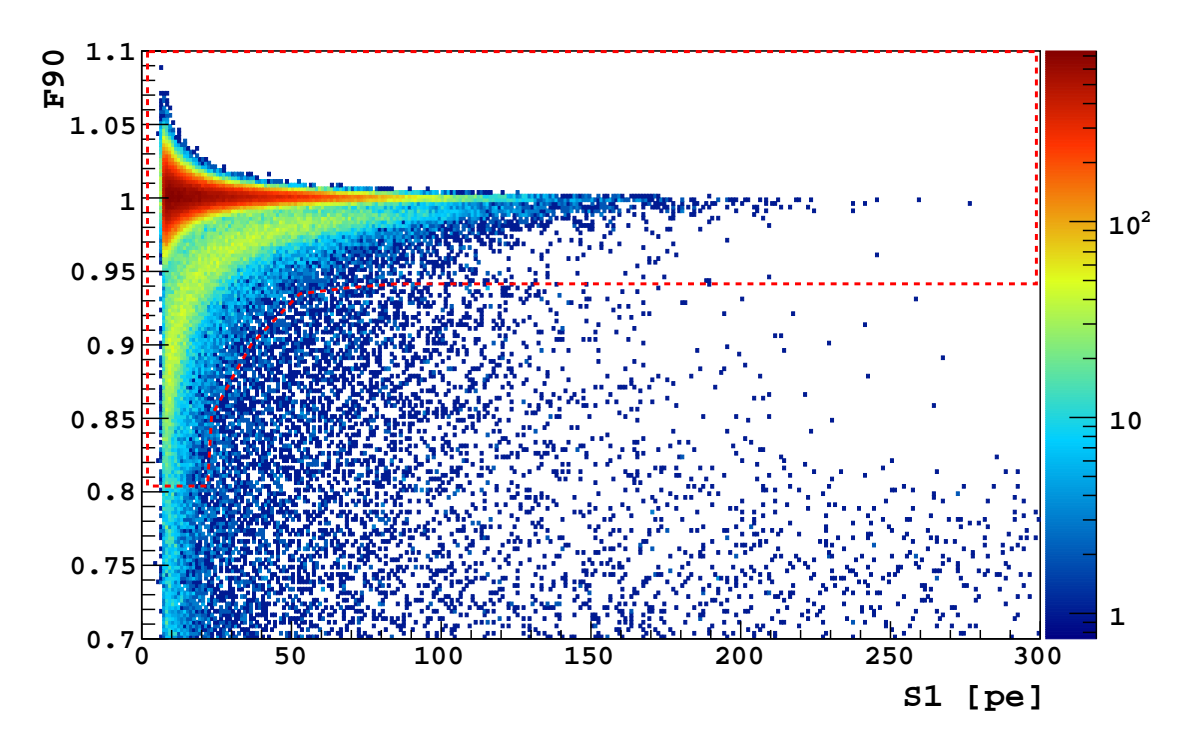
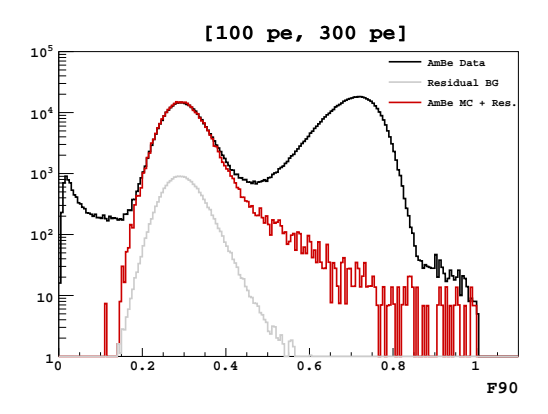


Figure 4.17: The graphic contour used as a  $f_{90}$ -S1 cut on one pulse events from  $^{241}$ Am-Be data. Cuts: the quality cuts (Sec. 3.3.1), S1 trigger time cut (Sec. 3.3.2), 1-pulse cut, and S1pMF< 0.25.

As a validation check for the normalization, we plot the normalized  $^{241}$ Am-Be  $f_{90}$  spectrum produced by MC against data, as shown in Fig. 4.18 left. The good agreement with the ER part of data shows the normalization is working. We intentionally skip reconstructing any NR events because the current Data/MC hybrid model doesn't reconstruct  $f_{90}$  for NR (it's not okay to simply turn off neutron generation because neutrons can produce  $\gamma$ -rays in the LSV, which can then enter TPC and give Cherenkov radiation). The skipping is done in the clustering algorithm where the algorithm identifies and excludes the energy deposited by argon nucleus. This is perfectly fine since the goal here is to fix the rate of  $\gamma$ -rays so that we have a trustworthy normalization method for pure Cherenkov.

Having checked the normalization, we compare pure Cherenkov spectrum from <sup>241</sup>Am-Be MC to data, as shown in Fig. 4.18 right. The selection of pure Cherenkov events in <sup>241</sup>Am-Be data is similar to what we have done previously in <sup>22</sup>Na, namely applying basic quality cuts,



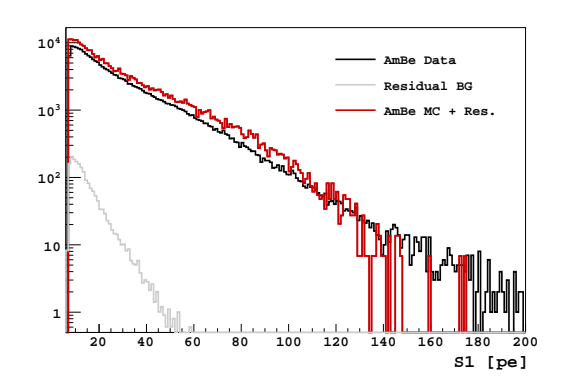


Figure 4.18: Left: Live-time normalization of MC  $^{241}$ Am-Be spectrum to data. Cuts: quality cuts, trigger time cut,  $N_{\text{pulse}} \geq 2$ , and drift time> 10 µs. The residual background (grey) comes from UAr data under the same cuts scaled down to the live-time of  $^{241}$ Am-Be data set. As it turns out, the MC spectrum needs an additional 0.87 scale factor to fine match the data. This implies a 13% adjustment to MC counting. Right: Comparing the pure Cherenkov spectrum in  $^{241}$ Am-Be. Cut: the quality cuts (Sec. 3.3.1), the trigger time cut (Sec. 3.3.2), 1-pulse cut, S1pMF< 0.25, and a graphic cut described in Fig. 4.17. The residual BG means the pure Cherenkov events in UAr data scaled down to  $^{241}$ Am-Be data live-time. The same 0.87 scale factor is also applied to MC.

s1 trigger time cut, one pulse cut, and a graphic cut using the contour showed in Fig. 4.17. We made one adjustment to the contour to select those  $f_{90} \sim 1$  events by extending the range to a higher S1 value due to the presence of much higher energy  $\gamma$ -rays. In addition, we include a S1pMF< 0.25 cut to focus on pure PTFE Cherenkov. Omitting the FS Cherenkov is mainly due to the difficulty of selecting a clean sample of events in <sup>241</sup>Am-Be data as they spread out to well below  $f_{90} \sim 1$  region. Since getting the PTFE part of modeling correct is the absolute priority, we have to delay the comparison for possible later study<sup>6</sup>. The MC spectrum turns out to be in a reasonably good agreement with data, despite the fact that model is tuned on <sup>22</sup>Na whose  $\gamma$ -rays energies are a factor of 4 lower.

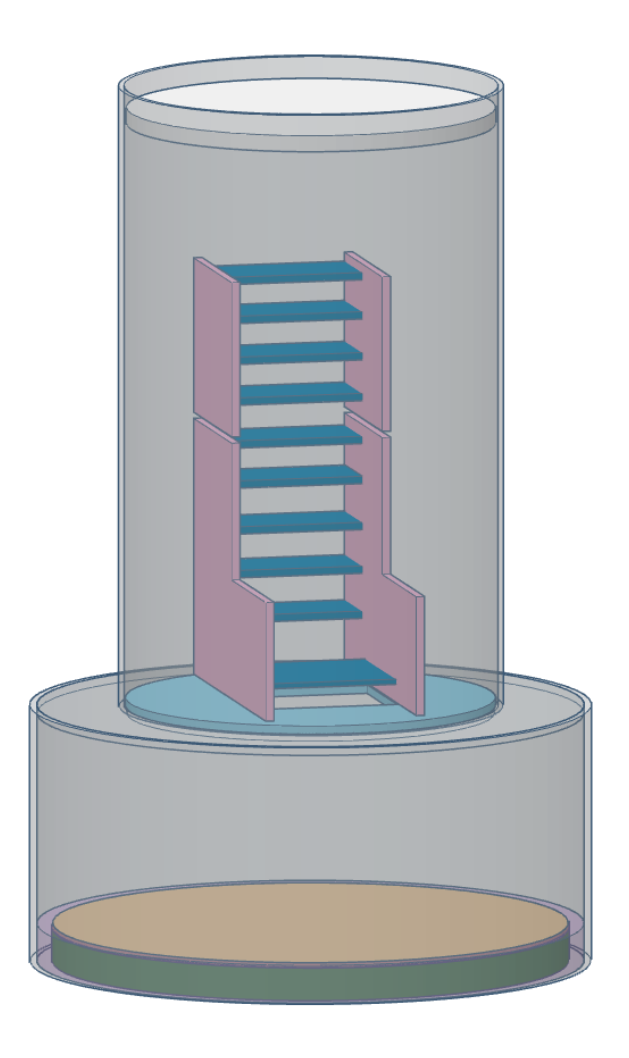


Figure 4.19: A 3D illustration of the PMT geometry in G4DS. From top to bottom, the components are: a cylindrical PMT stem made of boronsilicate glass (white), two parallel L-shape ceramic insulator plates (pink), nine cuboid steel dynodes (blue), the first cuboid steel dynode (blue), a cylindrical steel front plate with a rectangular hole at the center (cyan), a thin layer of photocathode (orange), a cylindrical PMT face-plate made of FS (green), and a ring of non-scintillating LAr (purple). All of them are surrounded by a metal shell made of kovar. Due to a technical challenge, we have to leave a gap (~1 mm) of vacuum which breaks one ceramic piece into two parts. The exact dimension coded in G4DS may be slightly different from this drawing.

## 4.3.7 Modeling the PMT Geometry

The original version of the PMT geometry implemented in G4DS before the Cherenkov study was quite simple: it contained a thin stem (0.55 mm) at the far back of the PMT and a cylindrical face-plate at the front (where the FS faceplate, photocathode, and LAr ring locates now). The face-place was made of this hybrid material called "fakephotocathode", which had the same physical properties of fused silica (same density and molecular composition), but the optical properties of Bialkali (absorbing photons). The region between the stem and the face-place was the vacuum. It was soon realized that this geometry is insufficient to explain the large amount of high S1MF (S1MF> 0.6) 1-pulse events observed in data. After separating the FS from the photocathode, we were able to use MC to identify those events as pure Cherenkov radiation in the fused silica window. Later studies introduced the ceramic insulators, dynodes, and an internal front plate into the tube, after we realized that most pure Cherenkov events produced by MC were actually induced by  $\beta$ -decays in the stem hitting the FS window rather than  $\gamma$ -rays. Previous studies put all the radioactivity in the stem, as this is considered to be the worst case for radiogenic neutron background. But for Cherenkov background, since the tube was mostly empty (except for a ~83 µm thin photocathode), it creates a direct path of vacuum for  $\beta$ -decay electrons to hit the FS face-plate from the stem, producing an excess of  $\beta$ -induced Cherenkov events.

The goal is to build the best representation of the geometry for the model without wasting too much time to implement the insignificant details. For this purpose, we open up a dead Hamamatsu R11065 PMT to get an accurate idea of the inside structure and to measure the masses and dimensions of parts. Photos of the opened tube are available at Ref. [52]. Having gone through many versions of geometry updates, we finally settled on the one shown in Fig. 4.19. Surprisingly, the actual color of the ceramic turns out to be pink, and it is determined

 $<sup>^6</sup>$ In  $^{241}$ Am-Be data, a class of events with extremely concentrated S1MF populates the region between  $f_{90}$  from 0.8 and 1. They resemble pure PMT window Cherenkov events with a strange feature of the "Cherenkov-tails". The nature of "Cherenkov tails" is still unknown, but it seems to be positively correlated with  $\gamma$ -ray energy and can drastically lower the  $f_{90}$ .

to be the largest source for  $^{238}$ U upper chain by GDMS measurement. Knowing this, we simulated the two ceramic plates according to their exact measured mass (5.135 g each) and dimension ( $\sim 1$  mm thick). The front steel plate below ceramic insulators, which prevents  $\beta$ -decay electrons from directly hitting FS, has an effective thickness of 0.7 mm constrained by its measured mass. In an effort to mimic the real tube, we raise the first dynode up by 1 mm from the front plate, allowing some  $\beta$ -decay electrons to travel to the face-plate from the bottom of the ceramic insulators. The first dynode has a measured thickness of  $\sim 0.4$  mm, and the same length and width as the square hole<sup>7</sup>. As a result of omitting other steel parts (ex. dynode supporting rod, and vertical plates that cover the dynodes), the other 9 dynodes are thicker than they actually are, so that the total steel mass still sum up to the measured 25.17 g. Finally we updated the stem thickness to 2.7 mm and moved it downward by  $\sim 6.5$  mm.

### 4.3.8 Systematics of the Cherenkov Response in G4DS

The systemic uncertainty associated with the Cherenkov modeling mainly come from three parts — the uncertainty in the radioactivity activity, the uncertainty related to the G4DS simulation, and the uncertainty in reconstructing a mixed event. In this section, we will mainly discuss the uncertainty related to G4DS.

We could have studied the G4DS uncertainty by varying every optical parameter in G4DS, but this is not practical because it is extremely time-consuming and the optics have complex degenerate nature. We adopt an alternative approach by modeling the optics uncertainties as the variation of Cherenkov LY. The procedure is as follows.

- 1. Define an arbitrary LY scale factor:  $SF_{tef}$ , and specifically apply it to the PTFE Cherenkov photonelectrons:  $npe_{tef} = npe_{tef} \times SF_{tef}$ ;
- 2. Compare the MC pure Cherenkov spectrum against the data, and adjust the parameter  $npe_{tef}$  such that we have the best agreement;

<sup>&</sup>lt;sup>7</sup>The real dynodes are curved plates, and the square hole is a representation of a mesh in real PMT

- 3. Apply the same  $SF_{tef}$  to the PTFE Cherenkov part of mixed events to calculate the mixed total S1 and  $f_{90}$ ;
- 4. Check the variation of the predicted BG in a WIMP search box.

In order to have a quantitative way to gauge the overall goodness of the match in step 2, I calculate the Pearson's reduced  $\chi^2$  in a range of S1 from 20 PE to 70 PE. This range is chosen by plotting the Cherenkov part of the mixed background events on top of the pure Cherenkov spectrum (green shadow in Fig. 4.20). One remark is that the very end of the S1 spectrum is not responsible for making background events in a final WIMP box, and the statistics is high enough in the relevant range to give a meaningful comparison.

- When  $SF_{tef} = 1$  (no scaling factor),  $\chi^2_{reduced} = 1.6$  in [20 PE, 70 PE] and  $\chi^2_{reduced} = 1.5$  in [35 PE, 70 PE]. The expected  $N_{BG}$  in 70-day WIMP box is 8.4 events/year after the cuts;
- When  $SF_{tef} = 0.95$ ,  $\chi^2_{reduced} = 4.2$  in [20 PE, 70 PE] and  $\chi^2_{reduced} = 1.1$  in [35 PE, 70 PE]. The expected  $N_{BG}$  in 70-day WIMP box is 7.7 event/year after the cuts.

According to this procedure, we show a 5% LY change propagates to a 9% change in background, while a wild 20% LY change propagates to a factor of two change in background. Given a 20% change seems unlikely judging the bottom spectra in Fig. 4.20, the upper limit of the sysmatics in G4DS is below a factor of two<sup>8</sup>.

Since the radioactivity determined by fitting the  $\gamma$ -ray spectrum is used to normalize the MC Cherenkov spectra to the UAr data, the uncertainty in  $\gamma$ -ray rates is the corresponding uncertainty of background estimate. According to [42], systematic uncertainty related to the radioactive rate is about  $\pm 10\%$ , obtained using propagating the upper and lower bounds of the  $\gamma$  rates (Tab. 4.3).

We have the uncertainty in reconstructing a mixed event because we adopt a data-driven  $s1 f_{90}$  model approach as oppose to getting a complete event with optics fully turned on from

<sup>&</sup>lt;sup>8</sup>One theory suggests that the data-model agreement is a result of having the optics tuned on the pure Cherenkov in UAr. As a remark, the optics were not tuned on UAr 1-pulse events, but on Na22 1-pulse events. While its true that we looked at UAr 1-pulse events from time to time (make sure were not wildly off the track), the tuning itself was trying to best match Na22 1-pulse S1. It just turned out that the 1-pulse events in the UAr roughly agree.

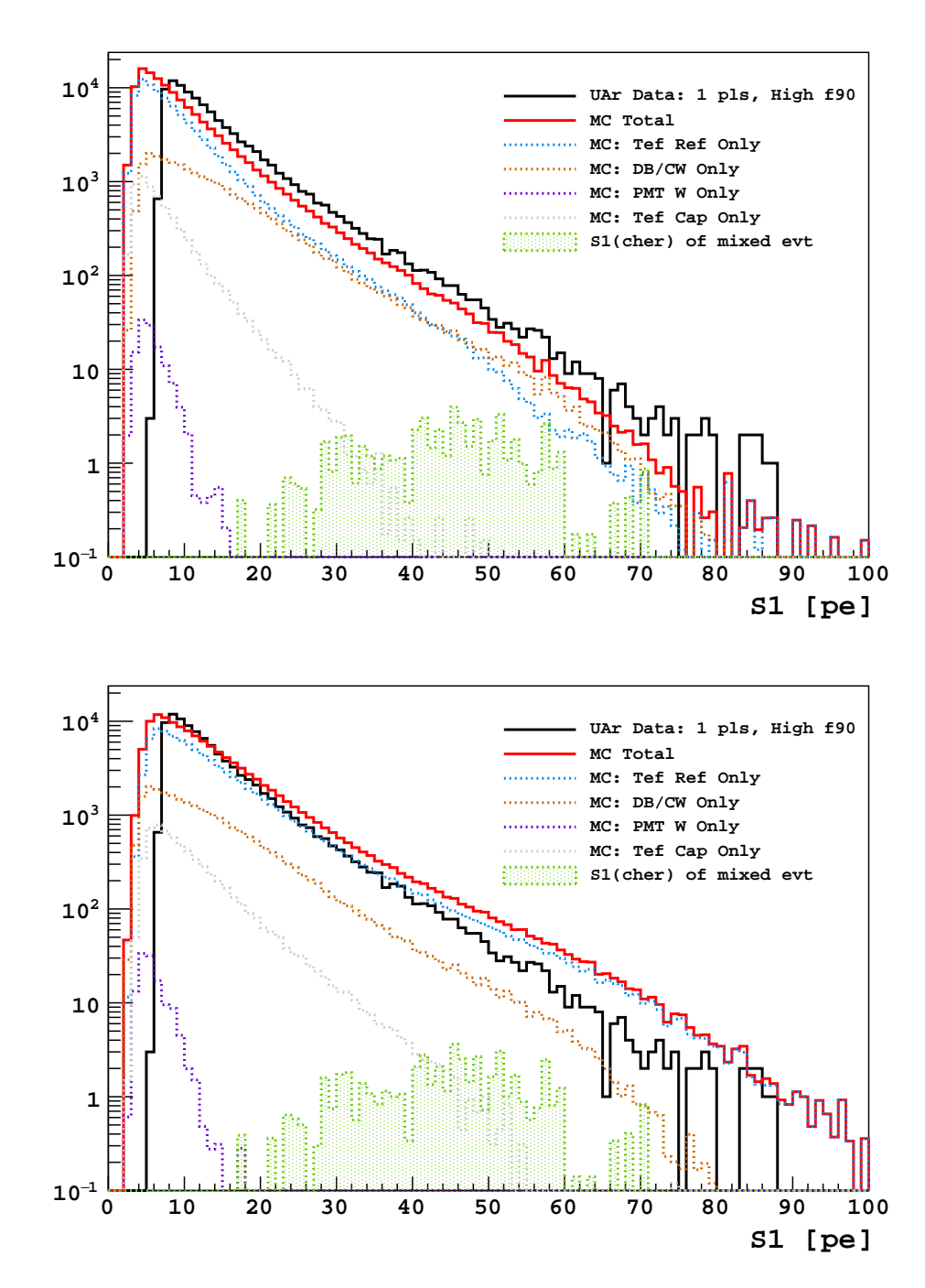


Figure 4.20: The pure Cherenkov spectrum under wild adjustmentments in  $SF_{tef}$ . Top:  $SF_{tef} = 0.8$ . The expected  $N_{BG}$  is 4.4 events/year. Bottom:  $SF_{tef} = 1.2$ . The expected  $N_{BG}$  is 15.5 events/year. For both plots, the  $N_{BG}$  are estimated in the 70-day WIMP box after the quality cut (Sec. 3.3.1), the 70-day TPC cuts (Sec. 3.3.2), and a veto prompt cut (Sec. 3.3.3).

G4DS in the current framework. We are adopting this approach because of the constraint on the computation power, and the need for a more accurate  $f_{90}$  model to account for multiple sited events. Variations in reconstructing a full compound event, such as the proximity-based clustering algorithm conditions, mimicking unresolved multiple scatters, computing the LAr scintillation S1, applying a data-driven  $f_{90}$  model, and applying cuts, are computed in a separate stage after the G4DS process. The response to reasonable variations of parameters are summarized in [42] Tab. 2. According to [42], the systematics ranges from +4% to 13% in the model.

Assume the three systematic errors are independent, we have a lower bound of the total uncertainty:  $\sim -19\%$  and an upper bound of  $\sim +14\%$ . The statistical fluctuations in the expected background numbers are the limiting factors.

# 4.4 Building a Compound Model for ER Backgrounds

#### 4.4.1 Overview

We adopted a MC-data hybrid model to simulate the compound ER event in data. The steps leading to the S1, S2,  $f_{90}$ , S1pMF, TDrift, and (x, y) are illustrated in a flowchart (Fig. 4.21). Although the G4DS with optics is capable of producing the parameters such as S1 and  $f_{90}$  without reference to the data, this seemingly complicated scheme is absolutely necessary for three reasons. First, it saves storage and computation time by skipping the photon tracking of pure scintillation events (App. C.2). We are only interested in propagating photons to preserve the PMT information for the Cherenkov background events. Second, it decouples the simulation of Cherenkov S1 from the scintillation S1. Fine tuning the optics for an accurate Cherenkov LY inevitably alters the bulk scintillation LY in G4DS (by a few percent). The hybrid scheme allows a more accurate computation for the combined S1. Third, the data-driven approach is simply more accurate for the  $f_{90}$ — a very crucial

parameter in the model. The scheme allows us to skip a careful tuning of individual PE timing in G4DS.

The procedure to compute S1, f<sub>90</sub>, and S1pMF will be briefly discussed in Sec. 4.4.3, 4.4.4, 4.4.5, and 4.4.6. The technical topics regarding the tuning of the clustering algorithm, validation of S1 LY, S2-resolution, and systematic errors associated with the hybrid model are described in [38].

### 4.4.2 Clustering Deposits into Scatters

Geant4 records the step-by-step energy depositions by a particle while it is slowing down in a medium. However, the relevant variables are those associated with each individual scatter, such as the scatter's energy and location. Thus, we need to a clustering algorithm to group those step-by-step depositions into clusters (scatters) and compute the relevant variables.

There are currently two ways to cluster deposition in G4DS. One is a track based algorithm grouping deposits with the same track ID. The other is a proximity-based algorithm which groups deposits by their relative distance to one another. We use the former algorithm to compute scatters in Cherenkov radiators such as PTFE and FS. The advantage is that the grouping is independent of the energy and track length of an electron. This track based algorithm was used in early stage of the model developing to locate Cherenkov in the radiators. The latter algorithm is used to compute scatters in LAr, and its clustering condition depends on the energy of the scatter. In both algorithms, a cluster position is an average of its component deposits positions weighted by their respective deposit energies, while the cluster time is the first deposit time  $^9$ . This algorithm was first developed by our Paris collaborators to mimic realistic detector response. G. Koh tuned the clustering condition in WIMP search energy regime ( $< 80 \text{ keV}_{ee}$ ) by matching of the number of pulses to UAr data. His conditions are 2 ns and 0.04 cm.  $^{10}$ . The track based algorithm may have difficult to

<sup>&</sup>lt;sup>9</sup>Given the ADC time resolution is 4 ns, it does not matter which deposits' time to pick within each cluster.

<sup>&</sup>lt;sup>10</sup>In AmBe study, I used a 4 ns and 0.4 cm clustering condition in LAr to avoid a large amount of clusters.

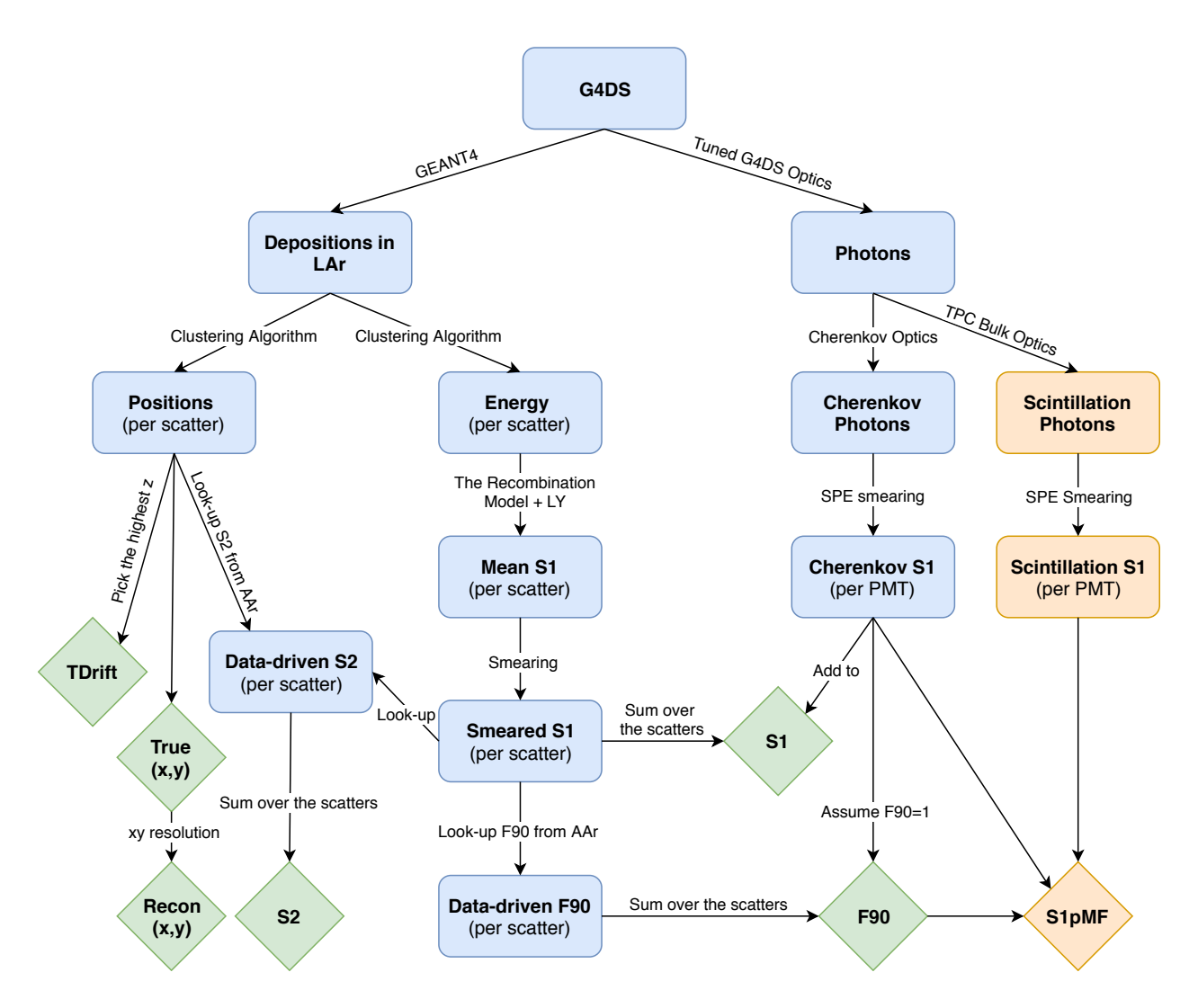


Figure 4.21: A flowchart of the MC-data hybrid model that illustrates the steps leading to the simulated observable parameters (diamond) in TPC. The steps and parameter in orange are only available when the photon tracking conditions are met (App. C.2). The true (x, y) parameters are the averages of individual clusters (x, y) weighted by their respective cluster energies for the case of an unresolved multi-sited event. The reconstructed (x, y) parameters are trying to mimic J. Brodsky xy algorithm [25]. The SPE smearing comes from the work of the TPC electronic simulation by A. Fan [33].

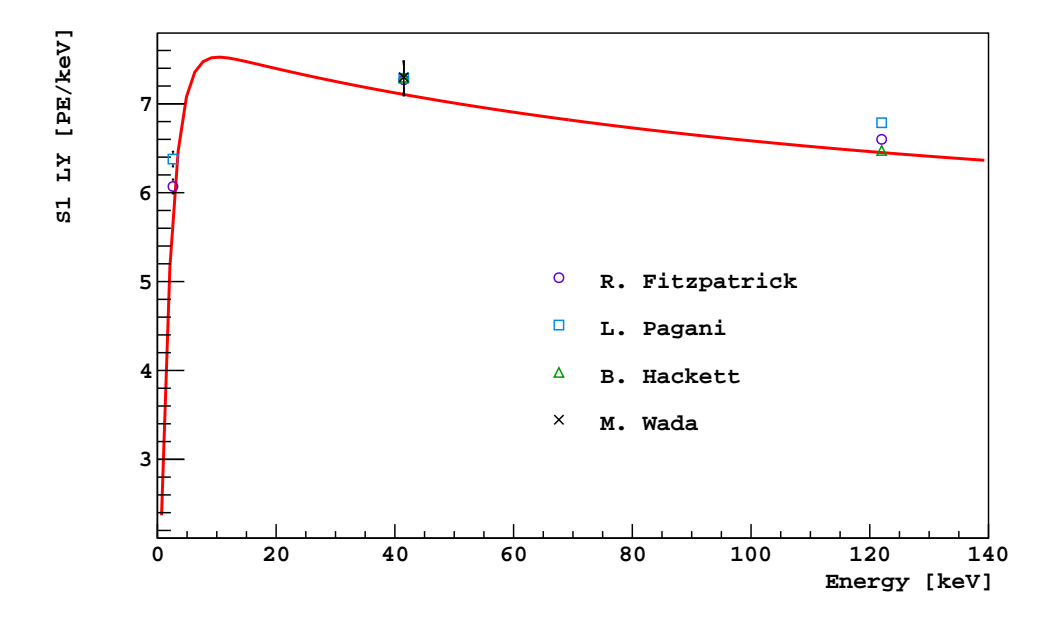


Figure 4.22: The S1 LY model at 200V/cm with the gas pocket on. The model was compared to the measurements of <sup>37</sup>Ar (2.62 keV), <sup>83m</sup>Kr (41.5 keV), and <sup>57</sup>Co (122 keV) peaks in the calibration data by several authors [53] [30] [54]. The systematic errors for the <sup>83m</sup>Kr peak and the <sup>37</sup>Ar peak come from [22] and [55] respectively. The statistical errors are too small to be significant while the systematic error for the <sup>57</sup>Co peak was not found.

deal in the presence of a large number of delta rays. The G4DS threshold to produce delta rays is low in the LAr but high in the PTFE.

## 4.4.3 Calculating S1 from the Energy

The scheme to calculate the S1 variable was first implemented by the Pair's collaborators in G4DS where the microscopic LAr scintillation mechanism was described in Sec. 2.2.1. We adopted it in the hybrid model to calculate one S1 variable per event. The steps are the following,

- 1. Obtain the amount of the deposited energy per cluster  $(E_{\text{dep}}^{\text{cl}})$  converted into the scintillation energy per cluster  $(E_{\text{scin}}^{\text{cl}})$ .
- 2. Obtain the mean S1 ( $\mu_{S1}^{cl}$ ) per cluster from the scintillation energy per cluster ( $E_{scin}^{cl}$ ).
- 3. Obtain the S1 per cluster (S1<sup>cl</sup>) by smearing the mean S1.

4. Obtain the total S1 by summing over individual cluster S1 (S1<sup>cl</sup>). Add Cherenkov S1 S1<sub>cher</sub> to the total S1 if any.

In the first step, we neglect ER quenching due to the heat loss in LAr. This is a fairly good approximation in the energy scale of our interest. Then we compute the recombination probability (r) based on the empirical function developed by [56],

$$r = p_0 \times (1 - p_1 e^{p_2 x}) \times e^{p_3 x^{p_4}} + p_5, \tag{4.12}$$

where  $x = E_{\text{dep}}^{\text{cl}}$  in the unit of keV, and the parameters  $p_i$  are summarized in Tab 4.4. The recombination function was obtained with  $^{37}\text{Ar}$  and  $^{83m}\text{Kr}$  constraint at 200 V/cm drift field strength. Next we compute the  $E_{\text{scin}}^{\text{cl}}$  for ER by

$$E_{\text{scin}}^{\text{cl}} = E_{\text{dep}}^{\text{cl}} \frac{\alpha + r}{1 + \alpha},\tag{4.13}$$

where  $\alpha = 0.21$  is the ionization to scintillation ration for ER [28].

In the second and third step, we apply a constant LY factor of 8.057 PE/keV to  $E_{\rm scin}^{\rm cl}$  to obtain the  $\mu_{\rm S1}^{\rm cl}$ . This LY factor was calibrated against the <sup>37</sup>Ar (2.6 keV), <sup>83m</sup>Kr (41.5 keV), and <sup>57</sup>Co (122 keV or 136.5 keV) peaks. To account for the statistical fluctuations, we randomly draw a S1<sup>cl</sup> from the Poisson distribution (P(x;  $\mu = \mu_{\rm S1}^{\rm cl}$ ) if  $\mu_{\rm S1}^{\rm cl} < 20$  PE. If  $\mu_{\rm S1}^{\rm cl} > 20$  PE, S1<sup>cl</sup> is randomly drawn from a Gaussian distribution with mean  $\mu_{\rm S1}^{\rm cl}$  and the variance twice of the mean ( $\sigma_{\rm S1}^{\rm cl} = 2 \times \mu_{\rm S1}^{\rm cl}$ ). The factor of 2 in variance comes from tuning against <sup>57</sup>Co spectrum.

In the fourth step, we sum over  $\mathrm{S1}^{\mathrm{cl}}$  and add  $\mathrm{S1}_{\mathrm{cher}}$  to obtain the total S1 per event as

$$S1 = S1_{scin} + S1_{cher} = \sum_{cl} S1^{cl} + S1_{cher},$$
 (4.14)

where  $S1_{cher}$  comes from G4DS optics described in previous section.

Table 4.4: The parameters of recombination probability function. All parameters are dimensionless.

$\overline{p_0}$	$p_1$	$p_2$	$p_3$	$p_4$	$p_5$
0.296766	3.95496	0.517812	0.0138485	0.912436	0.661046

The simulated S1 LY for single-sited events at the center of TPC in the standard WIMP search mode is shown in Fig 4.22. Since the  $^{83m}$ Kr peak is essentially two X-rays (32.1 keV and 9.4 keV) and the  $^{57}$ Co peak comes from multi-scattering  $\gamma$ -rays, we expect the measured LY to be slightly higher than the curve.

#### 4.4.4 Data-driven F90 Modeling

I will briefly describe the algorithmic steps toward modeling the  $f_{90}$  in this section, while the technical details, such as selecting the AAr data sample for the use of reference, investigation of the spectral dependence of  $f_{90}$ , and the validation of the  $f_{90}$  modeling on the multiscattering ER events, are well documented in [38].

The data-driven  $f_{90}$  model, built from the <sup>39</sup>Ar dominated AAr data set, was designed to simulate the  $f_{90}$  response of all ER events. One underlying assumption is that the S1 time profile of an  $\beta$ -decay is the same as a single-scatter from a  $\gamma$ -ray. This is a fair assumption. Another assumption implies no significant instrumental change from the AAr data to the UAr data. For example, an increase in the baseline fluctuation will likely to increase the  $f_{90}$  variance. After inspecting the stability of the electronic noise, we did not expect this assumption to be invalidated.

The steps to obtain one  $f_{90}$  variable per event are the following,

- 1. Pick a  $f_{90}$  per scatter (cluster). If 10 PE < S1<sup>cl</sup> < 700 PE, the F90<sup>cl</sup> was drawn from the  $f_{90}$  profile corresponding to the S1 bin (1 PE/bin). If S1<sup>cl</sup> < 10 PE, the F90<sup>cl</sup> was drawn from a uniform distribution between 0 and 1. If S1<sup>cl</sup> > 700 PE, F90<sup>cl</sup>=0.28;
- 2. Compute the  $f_{90}$  by scintillation (F90 $_{\rm scin}$ ) by summing over F90 $^{\rm cl}$ :

$$F90_{\text{scin}} = \frac{1}{S1_{\text{scin}}} \sum_{\text{cl}} F90^{\text{cl}} \times S1^{\text{cl}};$$
 (4.15)

3. Compute the final  $f_{90}$  variable by adding the Cherenkov S1:

$$F90 = \frac{S1_{\text{scin}} \times F90_{\text{scin}} + S1_{\text{cher}}}{S1_{\text{scin}} + S1_{\text{cher}}}.$$

$$(4.16)$$

In the first step, we used a uniform distribution below 10 PE because the data reference is not available. The 10 PE cut off is limited by the S1 pulse finder efficiency. Above 700 PE the G2 prescaling kicks in and limits the statistics. Although the data-driven  $f_{90}$  model is not reliable in the region beyond 700 PE, it will not affect our background prediction within the WIMP search ROI (< 450 PE).

#### 4.4.5 Modeling S1 Prompt Maximum Fraction

The S1pMF variable in MC is expected to match the AAr data well because of the global optical tuning done C. Zhu. However, since G4DS does not simulate the additional time smearing added to PE after the photon absorption on the photocathode, there is an ambiguity on how to define the S1 prompt region in MC. For instance, the MC has a different PE time profile than the actual pulse shape in data due to the absence of detailed electronics simulation. In data, the first 90 ns window is used to contain most of the S1 prompt light (fast Ar-dimer singlet state), while in MC a shorter window (ex. 40 ns) is sufficient to contain most of prompt light. One may argue that because S1pMF presents itself as a fraction, the exact signal size should not matter. In practice, we do observe a slight change as a result of varying the prompt definition while we are computing the acceptance of S1pMF in MC.

We instead use the data-driven  $f_{90}$  model to compute S1pMF. By definition, S1pMF is expressed as  $S1_{\text{prompt}}^{\text{max}}/S1_{\text{prompt}}$  where  $S1^{\text{max}}$  stands for the PMT with the maximum prompt light. The algorithm to simulate S1pMF goes as the following:

- 1. Take the data-driven  $f_{90}$  value and compute  $S1_{prompt}^{LAr} = S1_{prompt}^{LAr} \times f_{90}$ , where  $S1_{prompt}^{LAr}$  is the S1 prompt from LAr scintillation.
- 2. Assume Cherenkov light is contained within the first 90 ns of S1 and compute  $S1_{\text{prompt}} = S1_{\text{prompt}}^{\text{LAr}} + S1_{\text{cher}}^{\text{Cher}}$ , where  $S1_{\text{prompt}}$  is the total S1 prompt.

- 3. For each PE from LAr scintillation, use the  $f_{90}$  value to randomly assign the PE to be either S1 prompt or S1 late and then add the PE to its corresponding PMT. For example, if the data-driven  $f_{90}$  value is 0.3 and this PE is detected by PMT 8, this PE will have 30% chance being assigned to S1 prompt in PMT 8, and the charge of this PE will be accumulated to PMT 8. After looping over all PEs from LAr scintillation, we now have  $S1_{\text{prompt, pmt}}^{\text{LAr}}$  for all 38 PMTs.
- 4. Loop over all PMTs, and compute  $S1_{\text{prompt, pmt}} = S1_{\text{prompt, pmt}}^{\text{LAr}} + S1_{\text{prompt, pmt}}^{\text{Cher}}$  per each PMT. Then we find the  $S1_{\text{prompt}}^{\text{max}}$  out of the 38 PMTs.
- 5. Finally compute S1pMF =  $S1_{\text{prompt}}^{\text{max}}/S1_{\text{prompt}}$ .

This approach has the advantage of incorporating correlation with the data-driven  $f_{90}$  but has the disadvantage of not incorporating any geometrical correlation (eg, photons in the maximum channel may arrive earlier simply because their origin is closer to the maximum channel). We eventually adopt this approach to make background predictions because the geometrical correlation seems weak, and it's more important to get the correlation with data-driven  $f_{90}$  correct.

#### 4.4.6 Data-driven S2 Modeling

The motivation for this S2 modeling comes from the Cherenkov background study. Since ER has a higher ionization to scintillation ratio than NR, S2/S1 is used to discriminate against pure ER backgrounds in LAr. The S2/S1 bands for NR and ER are merging at the low energy below  $\sim 100$  PE of S1. However, in mixed events, the Cherenkov contribution lower S2/S1, making an even smaller S2/S1 value for the mixed events than NR. This gives rejection power against Cherenkov background at lower energy. Given the time and resource constraint, it's not possible to produce large amount MC statistics with S2 optics turned on. For this reason, we built a Data/MC hybrid model for S2 in the MC. The basic idea is similar to the  $f_{90}$  model we look up S2 from single-sited reference data.

With uniformly distributed  $\beta$ -decays from <sup>39</sup>Ar, AAr is an excellent data set for this purpose. Since the mean of  $S2_{xycorr}$  changes rapidly with energy while the variance of  $S2_{xycorr}$  changes with radius, we have to build reference PDFs at every S1 and  $R^2$ . As shown in Fig.

4.23, the AAr data are sliced every 2 PE in S1 and every  $40\,\mathrm{cm^2}$  in  $R^2$ . To remove the outliers on the left-hand side of S2, we fit an empirical student-t function to data and obtain a -3.3  $\sigma$  cut-off threshold from the function. The choice of the t-function is not motivated by any underlying physical mechanisms but rather motivated by the fact that its shape resembles the bell shape of a Gaussian with a wider and exponential-like tail. The reason for introducing an empirical fitting comes from the increased presence of the outliers on the left-hand side — the outliers bias the cut-off threshold directly derived on the data. As for the right-hand side, we directly define a 99.9% quantile (correspond to 3.3  $\sigma$  in Gaussian) threshold on data.

When we compared the S2 distributions from 70-day UAr data to 50-day AAr data, we found an offset between the two spectrum peaks, which possibly due to the change of S2 LY. A similar offset ( $\sim 7-8\%$ ) in S2 means is also observed in Kr calibration data taken before and after the deployment of UAr. To model S2 in UAr, we need to apply a constant shift to correct the reference PDFs for every  $R^2$  bin and every S1 bin. The offset is computed by fitting a Gaussian to both AAr and UAr S2<sub>xycorr</sub> distributions, and taking the difference in Gaussian means.

Once we have look-up tables for  $S2_{xycorr}$ , the algorithm to make a mixed event as the following:

- 1. For every LAr scatter (cluster), calculate its S1(scint) and true xy location.
- 2. Based on the S1(scint) and R values, choose a corresponding PDF from the reference file and randomly generate a  $S2_{xycorr}$  value from that PDF for this LAr scatter.
- 3. For each LAr scatter, apply xy-uncorrection to get raw S2 per LAr scatter. The xy-uncorrection algorithm first uses the true xy position of the scatter (cluster position) to look up the corresponding xy-correction factor from the xy correction map, and then multiply the inverse of the xy-correction factor to  $S2_{xycorr}$  to get raw S2.
- 4. Sum up raw S2 from all LAr scatters to get the total S2, S2<sup>tot</sup>, for this event.
- 5. Apply xy-correction to  $S2^{tot}$  to get  $S2^{tot}_{xycorr}$  using the average xy position. The average xy position is weighted by raw S2 sizes for unresolved multi-scatters.

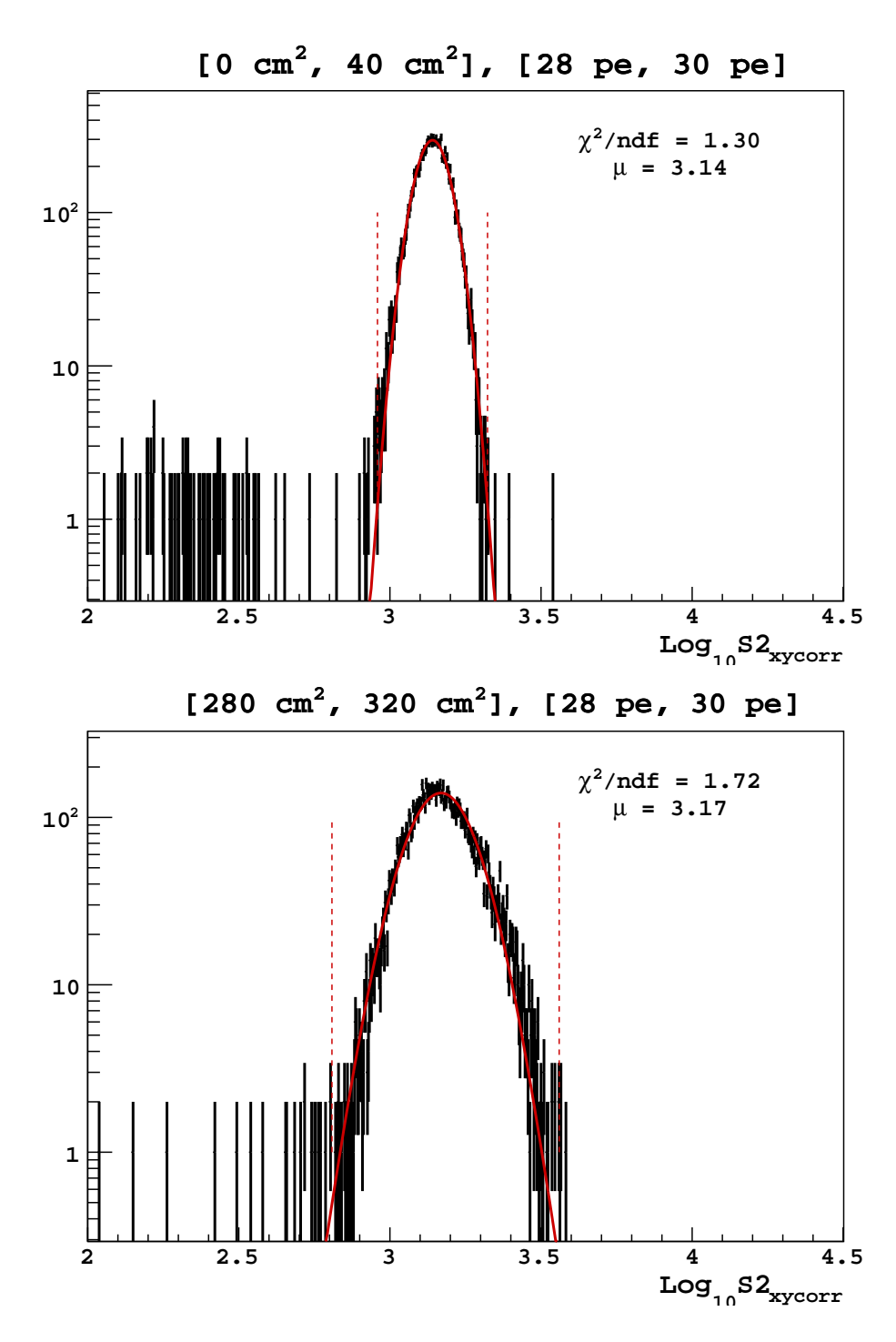


Figure 4.23: Example of selecting S2 PDFs from AAr data for 28 to 30 PE S1 bin. Top: Events at the center with  $R^2 < 40 \text{ cm}^2$ . Bottom: Events near the TPC edge with 280  $< R^2 < 320 \text{ cm}^2$ . For both plots, the cuts are: the quality cut (Sec. 3.3.1, single scatter cut (Sec. 3.3.2), a 95% S1pMF (Sec. 5.3.1), and 10 µs drift time fiducial cut top and bottom.

We draw S2 per LAr scatters because the presence of the unresolved multiple scatters in UAr data. Although the results of this model look fine, the logic is not as clean as the data-driven  $f_{90}$  model because S2 has significant radial dependence and is inevitably coupled to the complicated xy-algorithm. One assumption requires that the xy algorithm returns reasonable values for the unresolved multiple scatter, which is unverified. Although a cleaner algorithm which uses the average xy position to compute  $S2_{xycorr}^{tot}$  without computing at scatter level is preferable, given the multiple scattering events are unlikely to contribute to the final background we will not have a second trail on developing the S2 modeling.

Fig. 4.24 shows modeled S2/S1 spectrum plotted against the UAr data. Overall the agreement with the UAr data is very good with an exception of the left tail. One hypothesis for the origin of the left tail comes from the so-called "the wall effect", where the ionization electrons get lost in close proximity to the reflector surface while being drifted upward. The other hypotheses suggest that the origin comes from the bias in the xy reconstruction, where the xy algorithm artificially pushes an event toward TPC center, causing a lower S2 xy-correction factor than its actual value. Since "the beard events" makes S2/S1 even lower, not having it as a part of look-up reference is conservative for the Cherenkov background in terms of the background rejection power of an S2/S1 cut.

## 4.4.7 Modeling the Number of Pulses

When the clusters (scatters) are spatially well-separated, the number of pulses  $(N_{\text{pulse}})$  is essentially one more than the number of clusters  $(N_{\text{pulse}} = N_{\text{clus}} + 1)$ . However, sometimes the number of pulses  $(N_{\text{pulse}})$  does not represent the actual number of scatters. This is because the pulse-finding algorithm of the DarkArt is not capable of distinguishing two S2 pulses when the time separations  $\Delta t$  between the two pulses is too small. The threshold below which two S2 pulses are classified into one is called S2 resolution. According to the study from the DarkSide-50 electronics simulation, the S2 resolution depends on the size of S2 pulses and is typically in the range of 3-6 µs (2.79-5.58 mm). G. Koh had shown that,

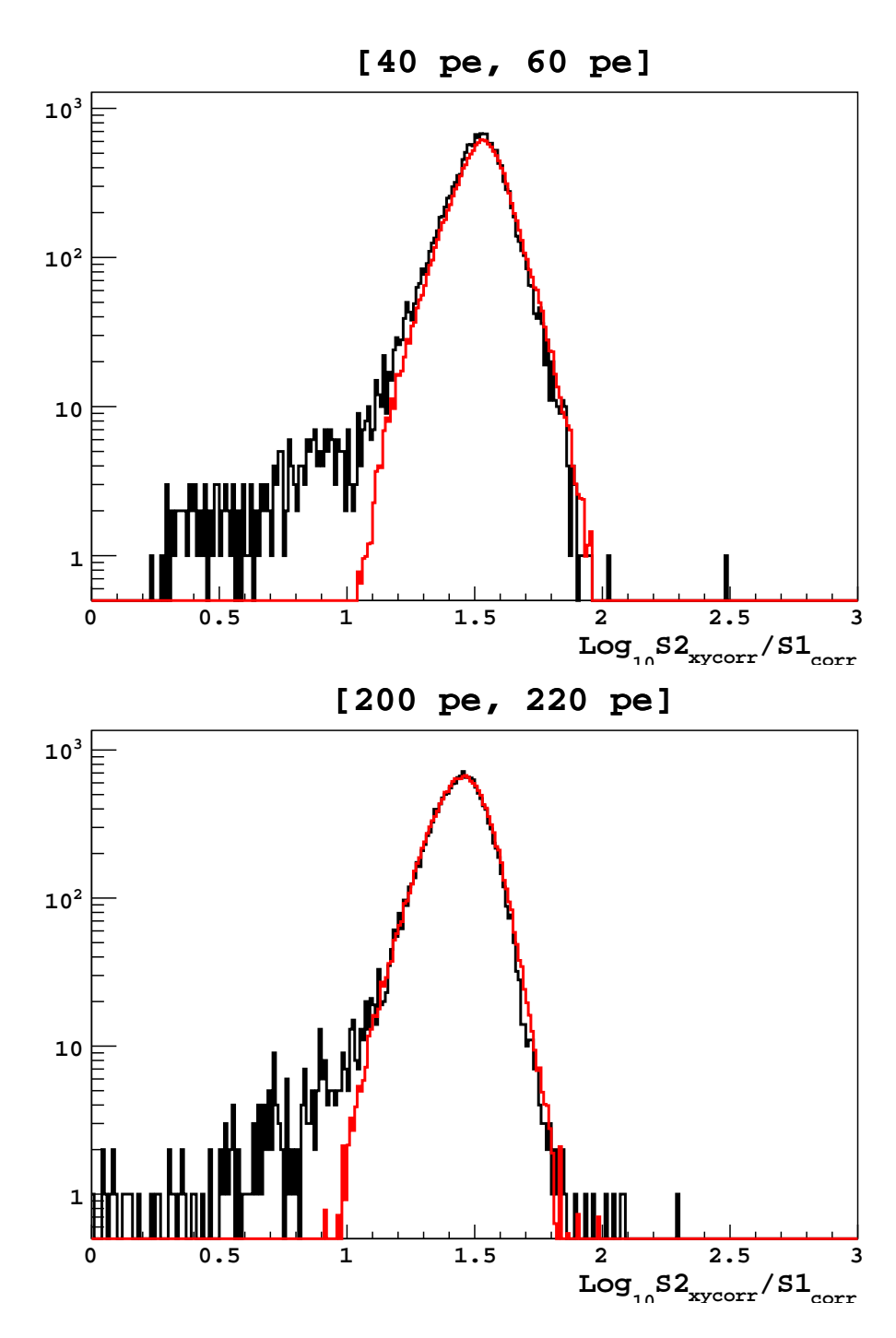


Figure 4.24: The examples of the modeled S2/S1 spectrum (red) as compared to the UAr data (black)

when the S2 resolution is set to 5 µs (4.65 mm), we have the best  $N_{\text{pulse}}$  spectrum matching between the MC and the <sup>57</sup>Co data [38].

#### 4.4.8 Modeling the Drift Time

The drift time ( $t_{\text{drift}}$ ) computation depends on the number of pulses similar to how it is computed in the data reconstruction algorithm. We assume the drift velocity is a constant throughout the active region.

$$t_{\text{drift}} = \frac{(z_{\text{max}} - z) \times t_{\text{max}}}{(z_{\text{max}} - z_{\text{min}})}$$
(4.17)

where  $z_{\text{max}} = 14.132$  cm is the vertical position of the grid in G4DS,  $z_{\text{min}} = -21.439$  cm is the vertical position of cathode window in G4DS,  $t_{\text{max}} = 375.9$  µs is the maximum drift time ( $t_{\text{max}} = 373$  µs for the AAr data) for an event located near the cathode window, and z is the location of the cluster. In the case of multi-scattering ( $N_{\text{pulse}} > 2$ ), the cluster closer to the grid is used to computed  $t_{\text{drift}}$ . In the case of  $N_{\text{pulse}} = 0$ , the  $t_{\text{drift}}$  is set to -999, an nonphysical number easily to be spotted.

## 4.4.9 Modeling S1 Pulse Finder Efficiency

The pulse-finding algorithm in the DarkArt data reconstruction code identifies clusters of PE close in time. We implemented the S1 pulse finder efficiency in the simulation as a way to mimic ER events ( $f_{90} \sim 0.3$ ) at very low energy. The curve shown in Fig. 4.25 was adopted from the electronic simulation [33] where the efficiency was validated against the fraction of  $^{37}$ Ar events picked-up by the algorithm (the  $^{37}$ Ar analysis uses ROI integral at the trigger time to define the total number of events at each S1 bin).

It is important to point out that the efficiency depends on  $f_{90}$ . curvature search algorithm is sensitive to the S1 prompt light. For example, the efficiency is lower for S2 pulses while is  $\sim 30\%$  higher for pure Cherenkov events ( $f_{90} = 1$ ).

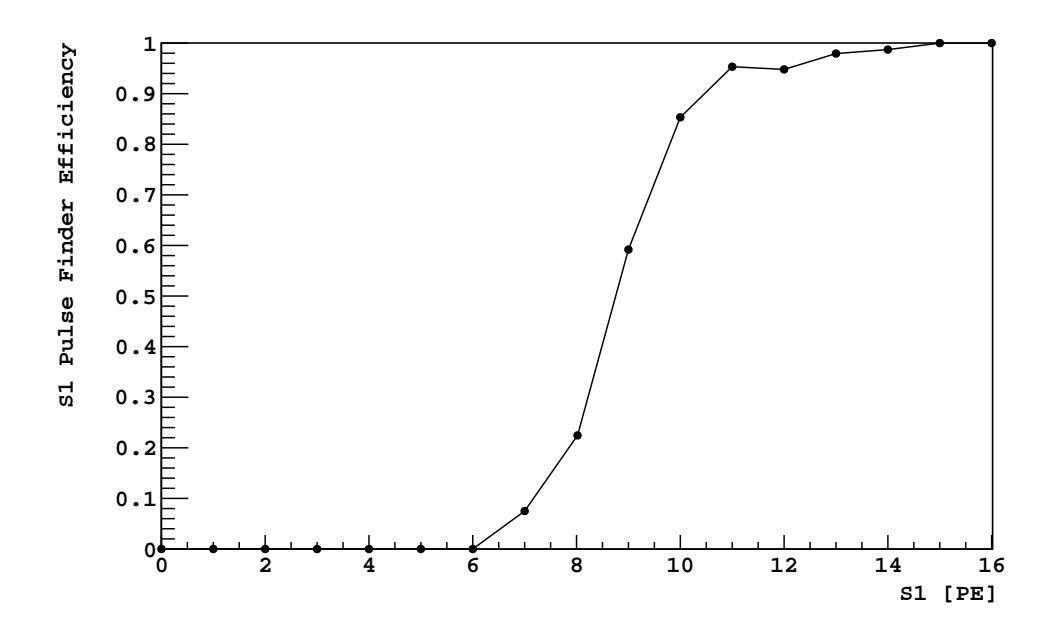


Figure 4.25: The S1 pulse finder efficiency as a function of S1. The efficiency is 1 beyond 15 PE and 0 below 6 PE.

#### 4.4.10 Modeling the Veto Prompt Charge

The veto prompt charge variable is designed to capture the coincident signals of the neutron thermalization and  $\gamma$ -rays escaping the TPC. In data, the veto prompt charge is an integral over the neutron veto waveform in the prompt ROI window. The prompt ROI is a 300 ns wide ROI window defined around the TPC trigger time. In the model, the veto prompt charge is calculated as the following to mimic the data:

- 1. Define the first PE arrival time as the TPC trigger time  $(T_0)$ . In the absence of optical photons, we define the first LAr cluster (scatter) time as the trigger time;
- 2. Obtain the unquenched energy  $(E^{\rm lsv})$  in prompt ROI by summing over the depositions in the LSV scintillator whose time  $(t_{\rm dep})$  is within [-50, 250) ns with respect to  $T_0$   $(-50 \, {\rm ns} \le t_{\rm dep} T_0 < 250 \, {\rm ns});$
- 3. Obtain the mean number of PE ( $\mu_{\rm npe}^{\rm lsv}$ ) by applying a constant LY of 0.5255 PE/keV (from H. Qian) to  $E^{\rm lsv}$ ;
- 4. If  $\mu_{\rm npe}^{\rm lsv} < 20$  PE, randomly draw a charge from the Poisson distribution. Otherwise, draw a charge from a Gaussian distribution where  $\sigma^2 = 2 \times \mu_{\rm npe}^{\rm lsv}$ .

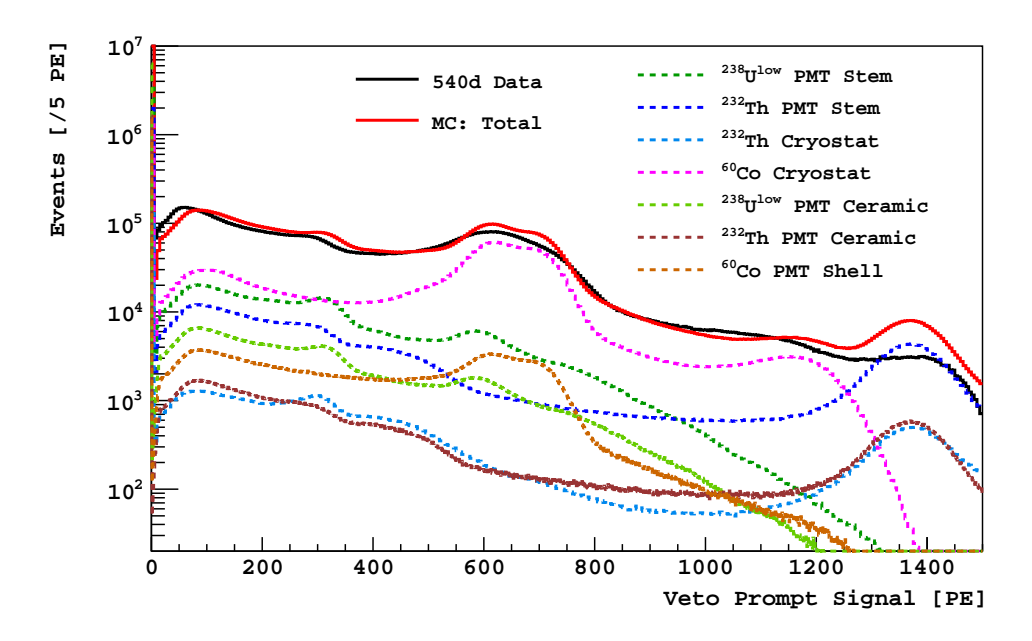


Figure 4.26: The reconstructed veto prompt spectrum in MC (red) as compared to the veto spectrum in the 540-day UAr data (black). The normalization uses the rates in Tab. 4.3 and 4.2. In data, only the basic quality cuts are required. In MC, we require the energy deposited in active LAr is greater than 0 OR the number of PEs is greater than 2 (pure Cherenkov does not deposit energy in LAr but can trigger the TPC). The fractions of events surviving veto prompt cut (Sec. 3.3.3) are 0.2997 (data) and 0.3033 (MC). A selected list of radioactive sources are shown in dash lines.

As shown in Fig. 4.26, this is a crude modeling for the LSV prompt charge. First of all, the lack of the quenching model is not an issue for the simulation of ER backgrounds, since the quenching of  $\gamma$  deposits in LSV liquid scintillator is close to 1. Second, the acceptance loss due to the random coincidence of the noise and is not modeled. Thanks to the narrow 300 ns time window, the actual coincidence loss is small ( $\sim 1\%$ ). Thirdly, the smearing method is simple with the Gaussian width empirically tuned to 1.41 by comparing the spectrum to the data. Given the remarkably low veto prompt cut threshold of 1 PE, the detailed modeling of the veto spectrum shape is not very crucial for simulating the cut<sup>11</sup>. Rather an accurate prediction for the fraction of event seeing any veto prompt signal at all is important in this analysis.

<sup>&</sup>lt;sup>11</sup>A better scheme to model the veto prompt charge is used by H. Qian [57].

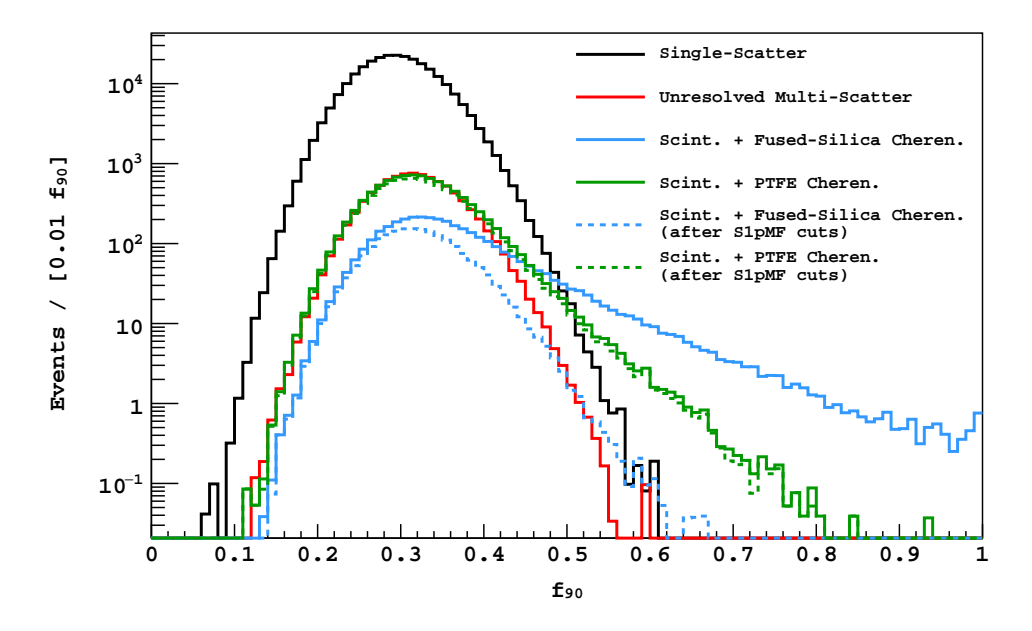


Figure 4.27: The simulation results from the data-driven  $f_{90}$  model showing the spectrum shape of different types of ER backgrounds in the UAr data. The S1 range is from 100 PE to 180 PE. The normalization uses the  $\gamma$  activity obtained from the spectrum fit (Tab. 4.3) and the counting results (Tab. 4.2). Plot from [9].

### 4.5 The Model Results

## 4.5.1 The Characteristics of ER Backgrounds

Using the compound model in the previous section, we simulate the  $f_{90}$  response in the UAr data by generating in-situ radioactivities in various TPC components. As shown in Fig. 4.27, although the unresolved multi-scattering  $\gamma$ -rays result in a different spectrum shape, it does not contribute any more than the single-scatters in terms of the background counts in the WIMP search ROI. The fused-silica Cherenkov background, although contaminating the ROI the most, becomes less of a threat than PTFE Cherenkov after applying the S1pMF cut (Sec. 5.3.1). The choice of S1 range in the plot came from designing the WIMP box (Sec. 5.5.1) where 100-180 PE is roughly the range of the  $f_{90}$  cut. Thus we expect the PTFE Cherenkov to drive the ER background leakage curve.

#### 4.5.2 Decomposing the Radioactive Sources

It is interesting to know which radioactive sources contribute to the Cherenkov background the most. Tab. 4.5) are the estimated ER events in the blinding box predicted by the model. Despite of the high activity of  $^{238}\mathrm{U^{up}}$ , the  $f_{90}$  requirement makes  $^{238}\mathrm{U^{up}}$  less relevant in terms of background production. The two dominant decay chains are the  $^{238}\mathrm{U^{low}}$  and  $^{232}\mathrm{Th}$  chains, with  $^{232}\mathrm{Th_{PMT}}$  having the highest yield of Cherenkov background. Thus, only the uncertainties associated with  $^{238}\mathrm{U_{PMT}^{low}}$  and  $^{232}\mathrm{Th_{PMT}}$   $\gamma$  rates matter significantly when it comes to error propagation. According to the upper and lower bound in Tab. 4.3, the total error associated with the Cherenkov background propagated from the two components (weighted by the yield) is about -1.6% to 2.5%.

Table 4.5: The 1-year equivalent ER backgrounds in the blinding box broken down by the radioactive sources. From left to right, it shows the number of single-scatter events, unresolved multi-sited events, fused silica Cherenkov plus scintillation events, Teflon (PTFE) Cherenkov plus scintillation events, any Cherenkov (fused-silica or Teflon) plus scintillation events, and the Cherenkov background yields. The counting uses the  $\gamma$ -rates from Tab. 4.3 and 4.2. The PMT includes the activities from the stem, the ceramic insulators, and the Kovar shell. The cryostat numbers include inner/outer cryostat, multilayer-insulation, inner/outer flange, and the o-ring. The blinding box is defined in Sec. 5.1.2. The zero rows of  $^{39}$ Ar and  $^{235}$ U<sub>cryo</sub> mean the counts are so low that the MC statistics (13.2 and 6.4 years respectively) is not enough to make prediction. The cuts are: the basic quality cut, trigger time cut, single-scatter cut, the 95% S1pMF cuts, 40 µs <  $t_{\rm drift}$  <  $t_{\rm max}$  µs.

each single search each time con sipilities and to perform the max per-							
Source	Isotope	Single	Mult.	FS Ch.	Tef. Ch.	All Ch.	Yield
							$[\mathrm{MBq}^{-1}]$
PMT	$^{238}\mathrm{U^{up}}$	0.197	0.0173	0.0599	0.574	0.633	0.0303
	$^{238}\mathrm{U}^{\mathrm{low}}$	2.06	0.473	3.86	24	27.5	5.28
	$^{232}\mathrm{Th}$	0.641	0.247	1.79	20.9	22.6	12.7
	$^{235}U$	0	0	0.0254	0.0509	0.0763	0.0779
	$^{60}\mathrm{Co}$	0.775	0.108	1.81	2.56	4.31	4.14
	$^{40}\mathrm{K}$	0.339	0.106	1.05	4.09	5.01	0.289
Cryostat	$^{238}\mathrm{U}^{\mathrm{up}}$	0	0	0	0.0781	0.0781	0.01
	$^{238}\mathrm{U}^{\mathrm{low}}$	0.106	0.0338	0.0588	2.21	2.27	0.973
	$^{232}\mathrm{Th}$	0.0745	0.0105	0.0464	3.03	3.07	2.64
	$^{235}{ m U}$	0	0	0	0	0	0
	$^{60}\mathrm{Co}$	1.32	0.52	0.682	7.98	8.71	1.09
	$^{40}\mathrm{K}$	0.00211	0	0	0.0483	0.0483	0.0491
UAr	$^{39}\mathrm{Ar}$	0	0	0	0	0	0
	$^{85}{ m Kr}$	0.0264	0	0	0.0793	0.0793	0.0931
	Total	5.54	1.52	9.38	65.6	74.3	27.4

## Chapter 5

# The Blind Analysis

#### 5.1 Overview

#### 5.1.1 The Data Set

Since August 2, 2015, the collaboration accumulated more than 600 live-days of blinded data with the UAr target as of October 2017. We occasionally performed calibration campaigns, such as <sup>83m</sup>Kr, <sup>241</sup>Am-Be, <sup>241</sup>Am<sup>13</sup>C which only lasts for a few days to a few weeks. The calibration data are all open. Next, we conducted a detailed data validation study similar to the procedure described in Sec. 3.2. A list of bad runs was identified and excluded. Two main issues for the live-time loss are the hardware failures and large baseline noise in neutron veto detector (32.6 days [57]). The final data set to be published has a total exposure of 532.4 live-days before any cuts.

## 5.1.2 Blinding Scheme

There are two steps of data processing to produce the standard WIMP search data. The first reconstruction software (DarkArt), developed in the Fermi National Accelerator Laboratory's art framework, converts the raw data to an event-by-event structure. The output of DarkArt requires library dependence and cannot be analyzed easily, so we make further simplification

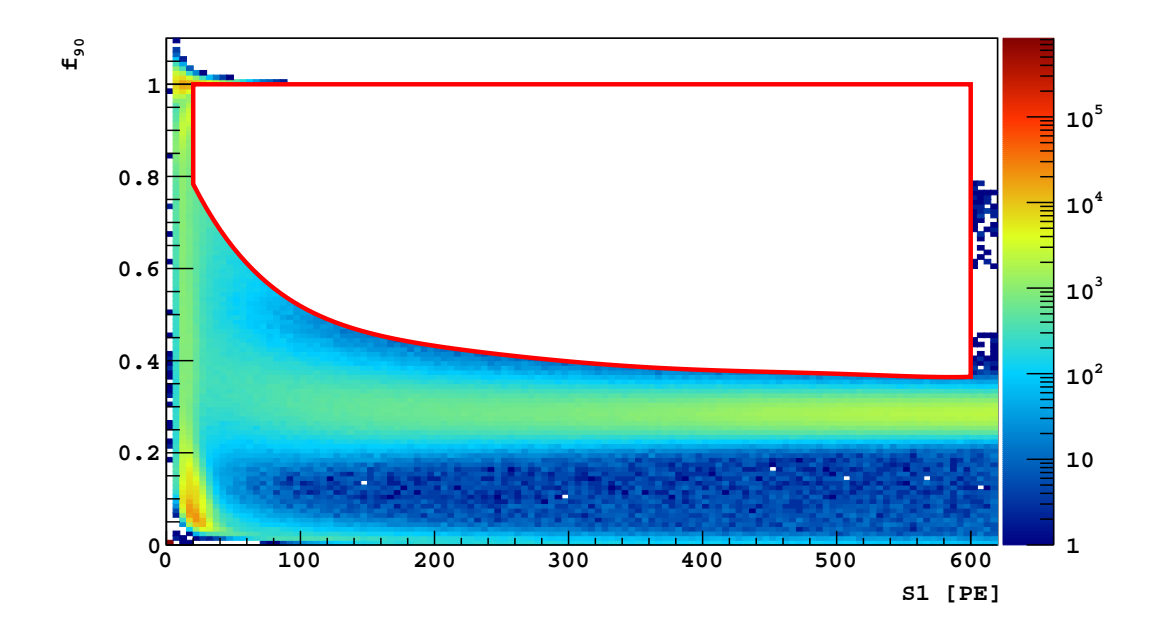


Figure 5.1: The Blinding box. The box hides all events whose  $(S1, f_{90})$  falls underneath it. in the second round of data processing to produce SLAD root files. SLAD stands for SLim Analysis Data.

The DarkArt stage of data processing is time-consuming. For this reasons, we implement a "blinding module" in the SLAD software to hide all events under the blinding box as shown in the Figure 5.1, plus a tiny random fraction (roughly 1 in 50000). Adding a random fraction ensure analyzers can play with the blinded data without knowledge of the number or the properties of the blinded events. The outputs of DarkArt and SLAD were initially not blinded, but they're securely located in a directory where its access permission is limited to two experts. We then run the "blinding module" of SLAD separately to produce the blinded SLAD files. Finally, we run veto matching code to produce the merged data set ready for analyzers. In this scheme, once we decided to open a fraction of events, we can quickly generate the new SLAD files without reprocessing the entire data set.

We took a special care of imposing the blinding scheme on event display. When an analyzer accidentally uses the event display to visualize a blinded event, the imposed module will return junk along with an error a message.

The blinding box is bigger than any prospective WIMP boxes by design (Fig. 5.1). The lower and upper boundary of S1 is at 20 PE (3.19 keV<sub>ee</sub>) and 600 PE (90.2 keV<sub>ee</sub>). The top  $f_{90}$  boundary is 1 while the bottom  $f_{90}$  boundary is designed to hide sufficient ER backgrounds for later testing. Once the background studies are ready, we will design and open a fraction of blinded events to verify background predictions and cuts. The test regions will also be used to gauge model systematics and measure the efficiency of cuts. Finally, we choose cuts and final search box to give less than 0.1 total events of predicted background after all cuts.

When it comes to designing the test regions to evaluate background predictions, the rules of thumb are:

- 1. Regions must contain enough statistics for the studied backgrounds;
- 2. Regions must minimize WIMP candidates.

In addition, we decided to freeze background models before opening any test regions, although other experiments have used test regions to tune model.

## 5.2 The Background Budget

The list of significant backgrounds in this analysis includes the surface background, cosmogenic neutron, radiogenic neutron, and electronic background. The electronic background is further divided into single sited ER, multi-sited ER, and ER Cherenkov coincidence.

## 5.2.1 Surface Background

Radon daughters in the Uranium and Thorium chains are the primary producers for  $\alpha$ 's. Radon is a gas, and it can easily stick to the surfaces by diffusing out from the detector components, or simply by exposing the surfaces to air during the detector constructions.

Alpha decays (5  $\sim$  8 MeV) in the bulk of LAr are not a concern because they are outside of the WIMP search energy region. When the radon daughters are embedded in the detector

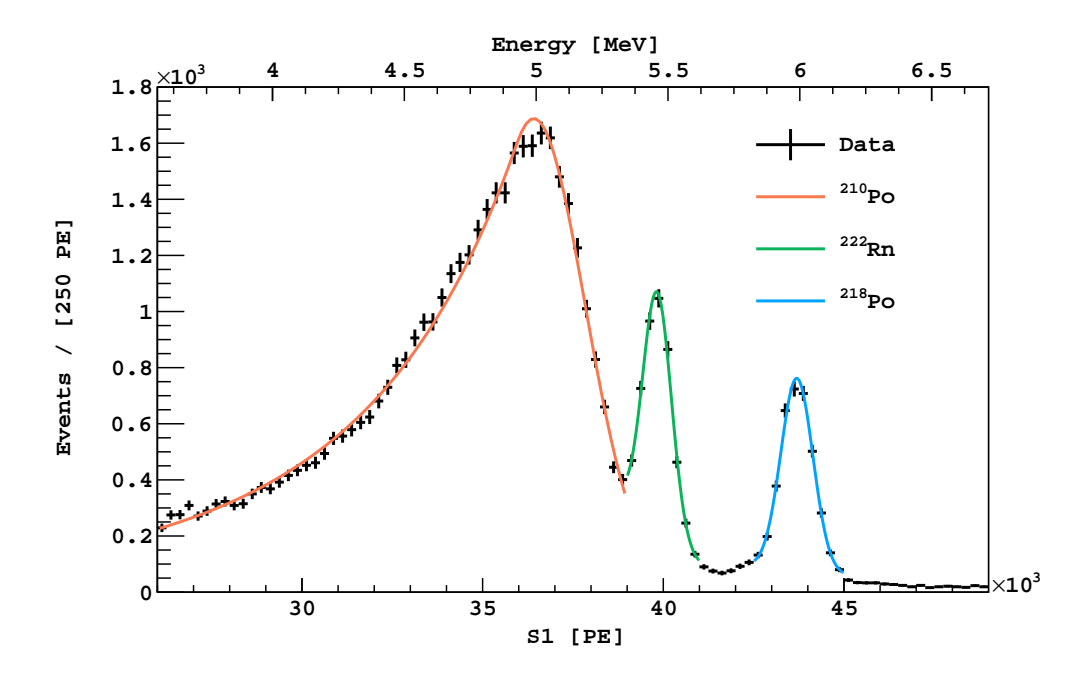


Figure 5.2:  $\alpha$  energy spectrum. The events were selected by requiring the first pulse to be alpha-like (0.5<f<sub>90</sub> <0.9). Two corrections have been applied to S1. The first corrects for ADC saturation and the second corrects for the z-dependence of the light yield. The <sup>222</sup>Rn and <sup>218</sup>Po peaks were fitted with Gaussian functions, and the energy scale at the top of the plot is set by the <sup>218</sup>Po peak. The <sup>210</sup>Po is fitted with a crystal ball function, whose shape suggests that the <sup>210</sup>Po is on the surface beneath the TPB. Plot from Ref. [9].

surfaces, the  $\alpha$ 's can exhibit a degraded energy spectrum by losing energy in the material. This scenario is dangerous because the  $\alpha$ 's can fall within the WIMP search energy range. In Fig. 5.2, the shape of <sup>210</sup>Po indicates that the  $\alpha$ 's are beneath the TPB layer. The other dangerous scenario occurs when radon daughters are decaying on the surfaces. If the  $\alpha$  particle goes into the wall, the recoiling low energy nucleus ( $\sim 100 \text{ keV}_{nr}$ ) will head into LAr, making a WIMP-like signal.

In the open data sets, we do not observe any surface backgrounds because of the "wall effect". The wall effect hypothesize that when an event is extremely ( $< 500 \mu m$ ) close to the surface of the PTFE reflector, its ionization electrons will get lost while being drifted upward. This hypothesis was backed-up by the data that, we indeed observed regular ER events ( $f_{90} \sim 0.3$ ) with abnormally small S2 near the surface. One possible mechanism suggests that the transverse diffusion will cause electrons to hit the surfaces and be absorbed. Being extremely

close to the wall, most surface  $\alpha$ 's (range  $\sim$ 94 µm for an 8 MeV  $\alpha$ -particle in 1.4 g/cm<sup>3</sup> LAr) will likely not survive the wall effect and populated in the "S1-only" events. Thus, the surface background is further classified into two types – Type I for  $\alpha$  with a survived S2, and type II for "S1-only"  $\alpha$  randomly piled up with a "S2-only" event.

To minimize the surface background, we design the following four cuts:

- 1. **TPB scintillation cut**. We remove events with excess PE between the end of S1 pulse and the beginning of S2 pulse [40]. To enforce a uniform acceptance, this cut is designed to be as a function of S1 and  $t_{\text{drift}}$ . The acceptance of this cut is 0.987;
- 2. Maximum and minimum S2/S1 cuts. We remove events whose S2/S1 is either too large or too small when compared to the expected NRs. The maximum and minimum S2/S1 thresholds are defined as a function of S1 using the NRs from the <sup>241</sup>Am-Be data. The combined acceptance is 0.986;
- 3. Maximum and minimum TBA cuts. We remove events whose S1 Top-bottom asymmetry (TBA) value is either abnormally too large or too small when compared to the expected TBA values. Since normal scintillation events have correlated TBA and  $t_{\rm drift}$ , the maximum and minimum TBA thresholds are defined as a function of  $t_{\rm drift}$  using the 70-day UAr data. The combined acceptance is 0.998;
- 4. Radial cut. We select events whose reconstructed radial position is in the fiducial volume. The detail of radial cut is described in Sec. 5.3.5.

The first cut aims at both type I and type II surface backgrounds. Regardless of the direction of an  $\alpha$  decay, the dangerous scenarios involve a  $\alpha$  particle penetrating through the TPB layer. It was discovered by an independent R&D experiment that when an  $\alpha$  or  $\beta$  goes through a TPB layer, it produces a long tail of single PEs that last on a millisecond timescale. The long tail feature allows a cut rejection power on the order of  $\sim 10^3$  according to [40]. The acceptance loss is low because of the low PMT dark noise at LAr temperature B.2. The second and third cuts aim at minimizing type II surface background. Since a random S2 pulse does not exhibit a correlation with the S1 pulse, imposing minimum and maximum requirements on S2/S1 and TBA reduce the chance of random S2 piled up. Lastly, although the radial fiducial cut is designed around the Cherenkov background, it is effective against surface background as well.

The final estimated uppers limit for the exposure of this analysis are  $0.0006 \pm 0.0001$  (type I), and  $0.00092 \pm 0.00004$  (type II) [9]. This is an upper bound because we did not include the additional rejection expected from the radial cut and the minimum uncorrected S2 cut (Sec. 3.3.2) in the final estimate.

#### 5.2.2 Cosmogenic Neutron

Cosmogenic neutrons are produced by cosmic-ray muons penetrating the rock above the laboratory and activating the detector material and surrounding material in the lab, which may result in high energy neutrons. This background prediction was entirely done by 48.7-year equivalent FLUKA simulation. The simulation study predicts a conservative upper limit of  $< 3.5 \times 10^{-4}$  events passing all cuts for the exposure of the data set [9].

Muons are easily identified in the water tank and neutron veto due to their abnormally large light. When we remove the water tank muon cut, the rate of simulated single-scatter cosmogenic neutron events in WIMP search energy range is  $\sim 2$  per year, which is in agreement with the observation of 3 cosmogenic neutrons in the VPT sample (Sec. 5.4.1).

## 5.2.3 Radiogenic Neutron

The WCV and LSV are very good shielding against radiogenic neutrons originating outside of the detectors. The primary neutron sources are the TPC constructional material, including the PMTs, the PTFE, and the cryostat. Radiogenic neutrons are produced by  $(\alpha, n)$  reactions and spontaneous fission (mostly from <sup>238</sup>U chain). Fission process normally produces more than one neutron simultaneously. Considering the DarkSide-50 veto efficiency is very high, fission neutrons are a higher order concern. Thus the radiogenic neutron background is dominated by the  $(\alpha, n)$  reactions.

We do not need to rely on simulation to make the predictions thanks to the efficient neutron veto. Instead, we made the background estimate in three steps.

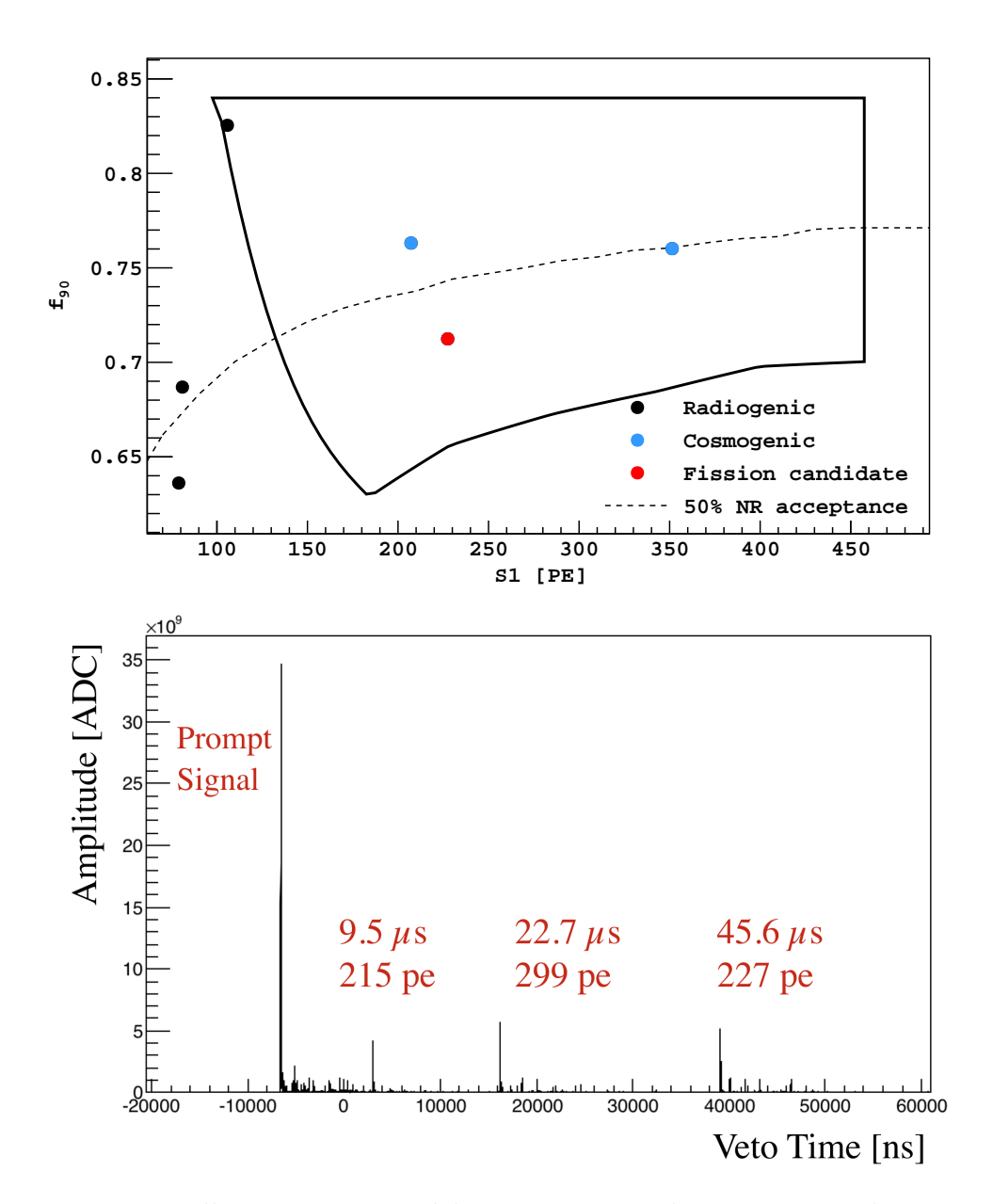


Figure 5.3: Top: all neutrons tagged by capture signal in VPT sample in WIMP energy range. Plot from Ref. [9]. Bottom: a fission neutron waveform showing multiple neutron capture signals. The small pulses between the neutron signals are likely the after-pulses.

- 1. We measured the neutron veto efficiency using  $^{241}\text{Am-}^{13}\text{C}$  calibration data. The total efficiency combining the LSV prompt and delay cuts is  $99.64 \pm 0.04\%$  ( $\epsilon_{\text{AmC}}$ ).
- 2. We opened the VPT sample (Sec. 5.4.1) and counted the number of radiogenic neutrons from the  $(\alpha, n)$  reaction in the WIMP box  $(N_{(\alpha,n)}^{\text{VPT}})$  after all TPC cuts. We used the delayed capture signals in LSV to identify generic neutrons, the WT coincidence singal (Sec. 3.3.3) to identify the cosmogenic neutrons, and the number of LSV capture signals to identify the fission neutron (two or more). The fission neutron can be easily spotted by inspecting the waveform as shown in 5.3-Bottom. The efficiency ( $\epsilon_{\text{tag}} = 79\%$ ) to identify a neutron candidate by the capture signal is calculated from the  $^{241}$ Am- $^{13}$ C study, with most of the inefficiency coming from the loss of  $^{10}$ B  $\alpha$ -only capture.
- 3. We calculated the expected number of neutron background surviving all cuts as

$$N_{\rm n}^{\rm exp} = N_{(\alpha,n)}^{\rm VPT} / \epsilon_{\rm tag} \times (1 - \epsilon_{\rm tot}). \tag{5.1}$$

The identified neutron from VPT sample are shown in Fig. 5.3-Top. With only one  $(\alpha, n)$  neutron in the prospective WIMP box, we predict a total of  $N_{\rm n}^{\rm exp} = 1/0.79 \times (1-0.9964) < 0.005$  radiogenic neutron background after all cuts for the exposure of this analysis.

The  $^{241}$ Am- $^{13}$ C data is ideal for the neutron efficiency study. The  $^{241}$ Am- $^{13}$ C source has a thin layer of gold leaf (on the order of  $\mu$ m) between  $^{241}$ Am and  $^{13}$ C to degrade the  $\alpha$  kinetic energy to below the 5.05 MeV excitation of  $^{16}$ O. With a 2 mm lead shielding absorbing the 60 keV X-rays from  $^{241}$ Am, the  $^{241}$ Am-Be source was producing a clean sample of neutrons without any contamination of ER coincidence. Since the  $(\alpha, n)$  reaction in the WIMP search data produced higher energy neutrons than the  $^{241}$ Am- $^{13}$ C source, we expected an efficiency that is higher than  $\epsilon_{\rm AmC}$  in reality. Hence the above estimate of neutron background is only an upper bound. Ideally we should make MC-based corrections to account for the origin and spectrum, but the upper bound is already small enough comparing to the Cherenkov background.

## 5.2.4 Electronic Recoil Background

The origins of electromagnetic backgrounds are the radioactive decays in the detector components. Since the WCV and LSV completely block  $\beta$ 's and  $\gamma$ s originating outside the TPC

cryostat, only radioactivity in the TPC components, such as LAr, PMTs, and Cryostat creates a significant amount of ER backgrounds. In the PMT and the cryostat, the  $\gamma$ -rays are the major causes for ERs since  $\beta$ 's do not travel far enough to reach the active volume. In the active LAr,  $\beta$ -decay is the primary source. The  $\beta$  emitters in the active volume are <sup>39</sup>Ar  $(0.73 \pm 0.11)$  mBq/kg and <sup>85</sup>Kr  $(2.05 \pm 0.13)$  mBq/kg (also see Sec. 3.4.1).

There are three types of ER backgrounds – single-scatters, unresolved multi-scatters, and the Cherenkov background. Multiple scatters in LAr are mostly removed by requiring exactly one S1 pulse and one S2 pulse. If the vertical separation of any two scatters is larger than 4.3 mm, the pulse finder algorithm is able to separate the S2 pulses. The main mechanism of Cherenkov coincidence comes from the multi-scattering  $\gamma$ -rays where at least one of the scatters happens in Cherenkov radiators.

The ratio of single- to multi-sited events depends on the  $\gamma$  energy. Since the photoelectric absorption is the dominant process below 100 keV, we expect the lower energy  $\gamma$ -rays to be the main producer of single scatters along with the  $\beta$  emitter in the UAr data. In the range from 100 keV to 10 MeV, the Compton scattering of  $\gamma$ -rays takes over as the dominant process which favors the production of and multi-sited ERs. The main producer for the dangerous Cherenkov events are the high energy  $\gamma$ -emitter, such as  $^{214}$ Bi ( $E_{\gamma}=1.8$  MeV,  $\Gamma=1.5\%$ ;  $E_{\gamma}=2.2$  MeV,  $\Gamma=4.9\%$ ;  $E_{\gamma}=2.5$  MeV,  $\Gamma=1.5\%$ ) from  $^{238}$ U chain and  $^{208}$ Ti ( $E_{\gamma}=2.6$  MeV,  $\Gamma=99.8\%$  BR) from  $^{232}$ Th chain. The quantitative numbers of ER background by different decay chain are also shown in Tab. 4.5.

Knowing the absolute radioactivity rate of every detector components is necessary for the normalization of the Cherenkov background model. PMTs have the biggest uncertainty of radioactivity because none of the only three Assayed tubes were actually installed in the TPC. The energy spectrum of ER in Fig. 5.4 shows good energy resolutions of individual  $\gamma$  full absorption peaks. We adopt an iterative fitting procedure over the energy spectrum to obtain the best estimate of the PMT radioactivity while fixing the cryostat radioactivity

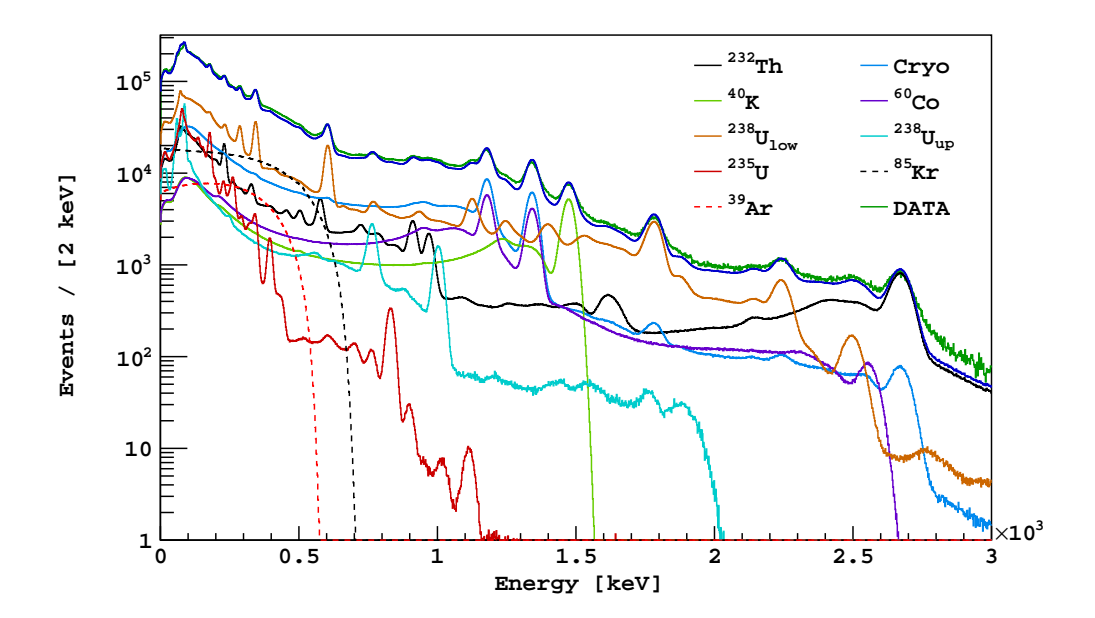


Figure 5.4: The  $\gamma$ -ray energy spectrum (green). The energy variable combines S1 and S2 signals. The decay chains from cryostat are fixed to their measured assayed numbers and are grouped together as a single curve (light blue). The <sup>39</sup>Ar and <sup>85</sup>Kr activities are fixed to the previous published number [22]. The rest are decays chains from PMTs whose activities are free parameters to be determined by the fit. Plot from Ref. [9].

to the measured assayed numbers. The results turn out to be roughly consistent with the assay numbers (Tab. 4.3 [38]).

## 5.3 Cherenkov Background Cuts

Since many of the analysis cuts are similar to the 70-day analysis (Sec. 3.3), I shall not repeat their definition. Ref. [38] is also a good source of information for the 540-day cut summary. In this section, we will discuss all the cuts that have any rejections against the Cherenkov background.

Before diving into the cuts, we need to address the selection of a clean NR sample which is a necessary first step to evaluate many of the cut acceptances. The data come from a 160 n/s <sup>241</sup>Am-Be source. Without further mentioning, we will use the term "clean NR cuts" as an abbreviation for the following cuts,

- 1. The basic quality cuts (Sec. 3.3.1);
- 2. S1 trigger time cut (Sec. 3.3.2);
- 3. Single scatter cuts (Sec. 3.3.2);
- 4. Vertical fiducialization cuts (10  $\mu$ s <  $t_{drift}$  <  $t_{max}$ -10  $\mu$ s). This is a looser version than the standard 40  $\mu$ s  $t_{drift}$  cut (Sec. 3.3.2);
- 5.  $\gamma$ -tagging cut. We select events with the full  $\gamma$  energy (4.4 MeV) deposited in LSV. By requiring a large LSV signal in the veto prompt ROI (2000 PE < lsv\_prompt\_signal < 3800 PE), we minimize the chance for the source  $\gamma$ -rays to enter the TPC. This cut greatly reduces the contamination of ER coincidence in the NR sample. The exact cut were copied from E. Edkins, who had tuned the cut values to maximize the NR/ER ratio by trail and error [58];
- 6. 99% NR f<sub>90</sub> cut. We select events in above the 99% NR acceptance curve. The construction of the curve was described in 3.4.4;

#### 5.3.1 S1 Prompt Maximum Frac Cut

Historically, S1 Maximum Fraction (S1MF) cuts were first introduced to remove after-pulses but were discovered to have good rejection against fused silica Cherenkov background. The proximity of the FS windows to the PMTs implies that Cherenkov light will have a high probability of being concentrated in a single PMT. Thus, it's natural to remove events with the highest channel concentrations of S1 light. S1 Prompt Maximum Fraction (S1pMF) cuts are considered an improvement on S1MF to reject Cherenkov background. By S1 prompt, we mean the integral of the first 90 ns of S1. Instead of computing the fraction of S1 light in the maximum channel, we purposely neglect light in the S1 late region (90 ns to 7  $\mu$ s) and restrict the computation of maximum channel fraction to the S1 prompt region. The motivation of this change comes from the realization that Cherenkov will only occur in the S1 prompt region, making an even more extreme channel pattern than S1MF. Of course, the change also means we no longer have the rejection against after-pulses, but given after-pulses tend to occur in S1 late region and lower  $f_{90}$ , they're not considered a background threat.

Similar to S1MF, this cut is defined on AAr data as a fixed 95% quantile per 5 µs  $t_{\text{drift}}$  bin and per 5 PE S1 prompt bin to ensure uniform acceptance. We check the uniformity of

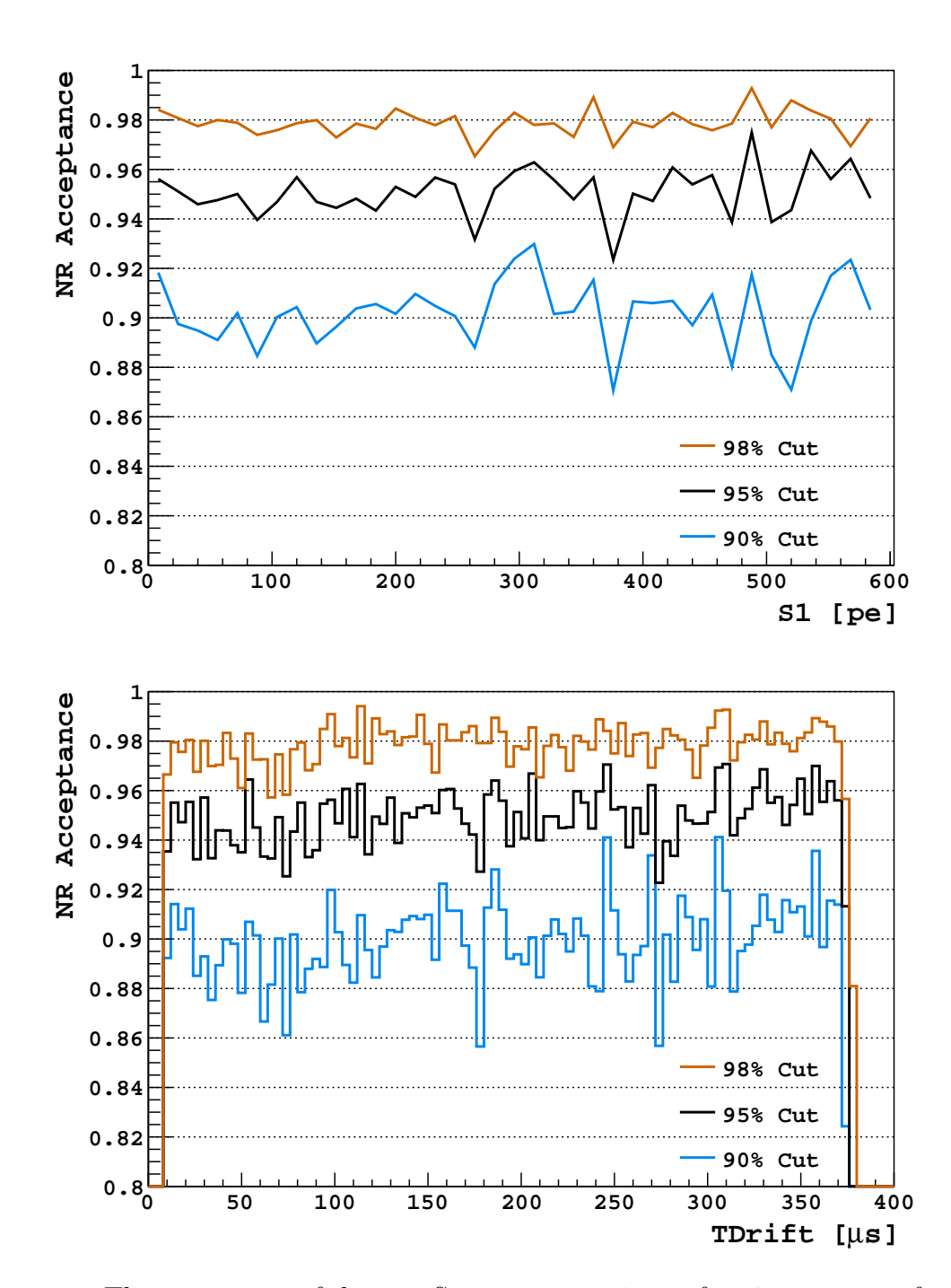


Figure 5.5: The acceptance of the new S1 prompt maximum fraction cuts as a function of S1 and drift time. Both plots have the acceptance defined as the fraction of NR events surviving the cuts. The NR events are selected from the 160 n/s  $^{241}$ Am-Be data set. Preceding cuts are the "clean NR cuts".

the acceptance across both S1 and drift time on NR events from <sup>241</sup>Am-Be data, as shown in figure 5.5. The improvement on the rejection side is checked on the UAr 70-day sample by comparing the f<sub>90</sub> distributions surviving old and new cuts. With the same acceptance loss, the new S1pMF cuts are a clear winner in terms of reducing the leakage of ER background into NR band in figure 5.6. We will use a 95% S1pMF cut for the 500-day analysis.

When a Cherenkov radiation happens in the diving bell and cathode windows (DB/CW) but not directly underneath the PMTs, we expect a lower S1MF as a result of the light distribution being shared by the neighbor PMTs. This implies a lower rejection power from S1MF cuts for those mixed events whose Cherenkov radiation occurring between the PMTs in DB/CW. To study this effect in MC, we first need to define a special xy cut to separate the regions between PMTs versus directly underneath PMTs. For a given xy location (the average location of energy deposition computed by the clustering algorithm), we calculate the distance to the nearest PMTs center. The distance is then compared to the radius of PMT window (3.755 cm). Greater than 3.755 cm means the location is between PMTs; smaller or equal to 3.755 cm means the location is under PMTs. Having a well-defined cut, the big contrast in S1MF are shown in Figure 5.7-left, where pure Cherenkov between PMTs shows a much lower S1MF. Drift time fiducialization should clean up those events.

As a note, when applying the 95% S1pMF cuts to MC sample with the condition photon tracking (CPT) turned on (see Appendix C.2), we need to use a random generator to randomly select the 5% of pure ER events to lose. This is because the CPT method does not generate photons for pure ER events.

## 5.3.2 Veto Prompt Cut

The veto prompt cut is a 1.51% acceptance loss cut [59] and remain the same since the 70-day analysis (Sec. 3.3.3). The loss is mainly due to the random coincidence from either noise or <sup>14</sup>C activity in the veto prompt ROI. The veto prompt cut rejects roughly the 50% of PTFE Cherenkov background, while the same cut rejects roughly 25% of FS Cherenkov

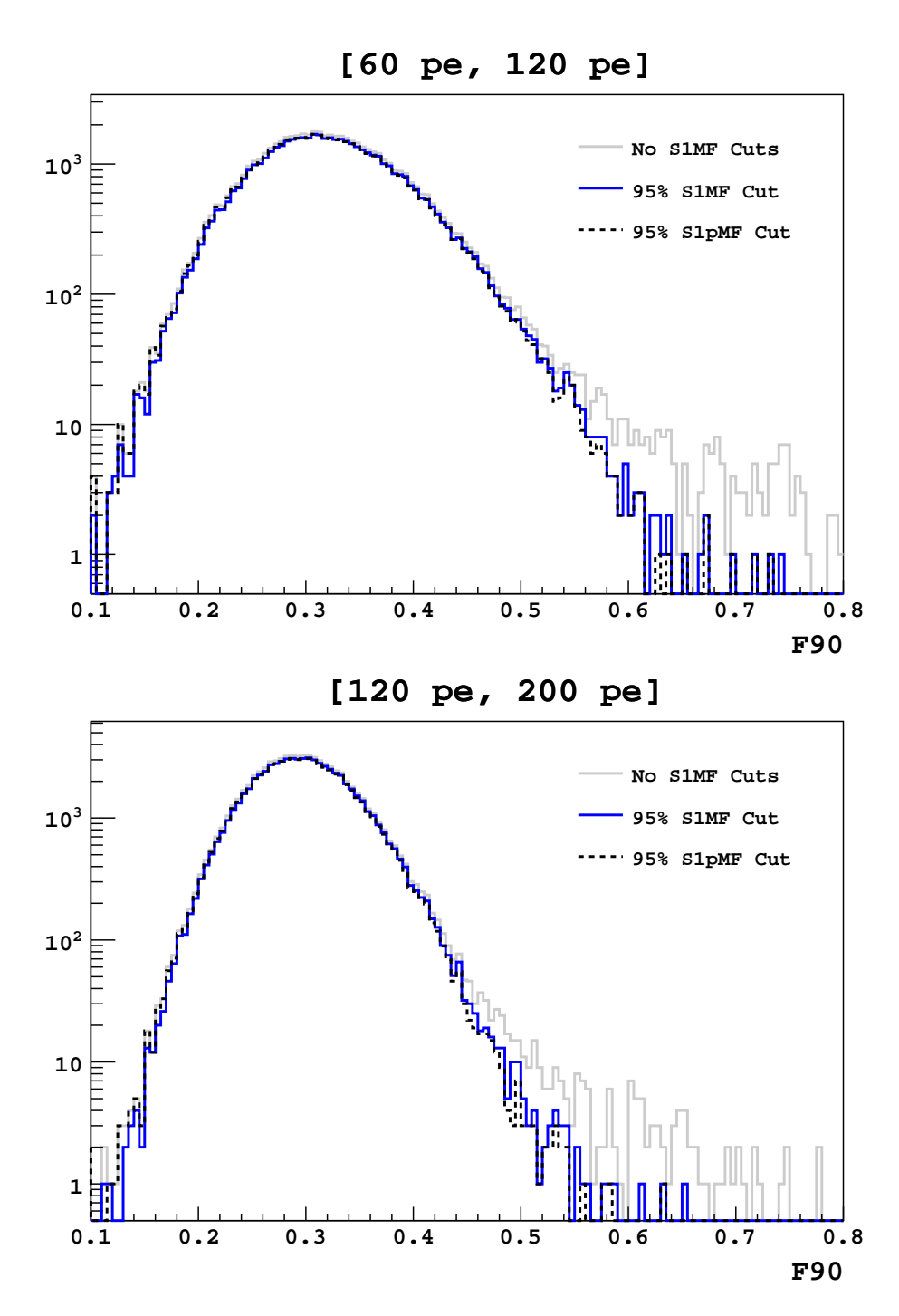


Figure 5.6:  $f_{90}$  profiles of the 70-day UAr data under the same percentile 95% S1MF cuts. The improvement on rejection by moving from S1MF to S1pMF is visible on the plots. The higher S1 range (right plot) has more improvement. Preceding cuts: quality cuts, trigger cut, single scatter cut, 10 µs drift time cut from top and bottom.

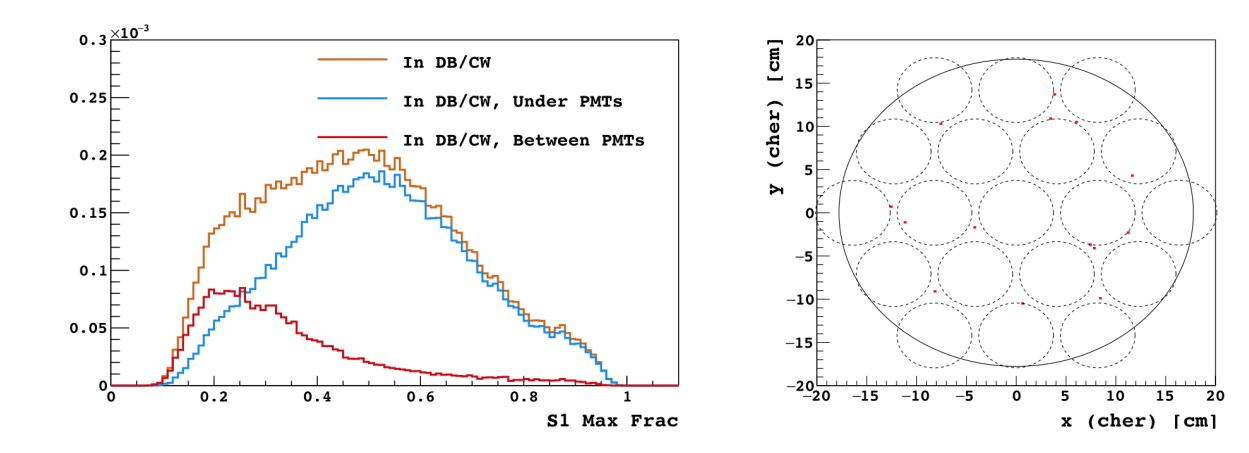


Figure 5.7: Pure Cherenkov events from diving bell/cathode window. Both MC plots are normalized to 70-day equivalence of the UAr data. Left: S1MF distributions for the pure Cherenkov events in diving bell and cathode windows. Events between the PMTs versus under the PMTs are selected by a specialized xy cuts (see main text). Right: the mixed background events surviving a 95% S1MF cuts. The plot shows the xy location of Cherenkov radiation in diving bell and cathode windows.

background (after 95% S1pMF cuts). The rejection comes from  $\gamma$ -rays escape into neutron veto. The cut intends to remove events if the signal is larger than 1 PE in the veto prompt window (-50 ns to 250 ns with respect to TPC trigger time).

#### 5.3.3 Drift Time Cut

This 40 µs ( $\sim$  43 mm) fiducial cut is the same as the previous 70-day analysis. Its main rejection is on FS Cherenkov background, with some rejection on PTFE Cherenkov background. We expect the S1pMF to clean up most FS Cherenkov background, and we expect this cut to clean up events whose Cherenkov radiation occurs in-between PMTs in DB/CW. The rejection on the PTFE Cherenkov is mainly a consequence of the fact that most  $\gamma$ -rays are coming from PMTs causing higher fraction PTFE Cherenkov with the scintillation located near the top and bottom of the TPC.

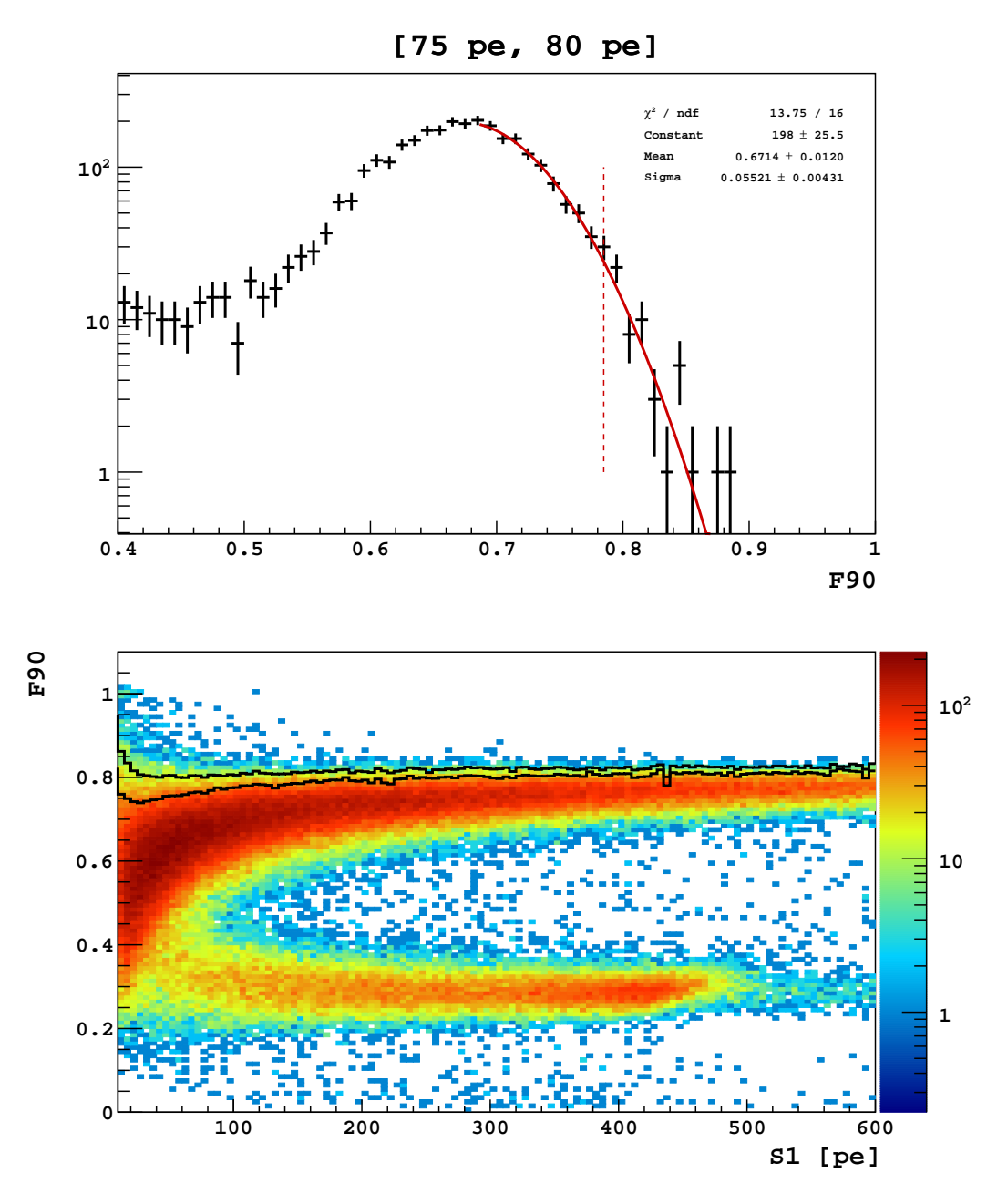


Figure 5.8: Top: a  $f_{90}$  distribution from the  $^{241}$ Am-Be NR sample with a Gaussian fit. The dash lines are the extrapolated 95% quantiles. Bottom: the extrapolated 99% and 95% quantiles from the  $^{241}$ Am-Be data is plotted.

#### 5.3.4 Maximum F90 Cut

Since the Cherenkov component can push the  $f_{90}$  of a mixed event beyond a typical NR  $f_{90}$ , having a tighter  $f_{90}$  box from above with minimal acceptance loss is just safer. The actual maximum  $f_{90}$  cuts are defined as fixed quantiles from the <sup>241</sup>Am-Be NR sample to ensure a uniform NR acceptance across S1 and  $t_{drift}$ , as shown in figure 5.8.

- 1. We project the 2D  $f_{90}$ -S1 histogram to obtain a  $f_{90}$  profile per every 5 PE S1 bin
- 2. For each  $f_{90}$  profile, we fit a Gaussian function to the spectrum twice. The first fit finds the peak location of NR (Gaussian mean), and the second fit is carried out in the ranges from the peak location to 1.
- 3. We extract the quantiles (1%, 5%) etc) from the second fit function.

This simple approach turns out to be stable, returning reasonable reduced  $\chi^2$  values for all S1 bins. Another set of contours is extracted from the "Two-Tail" model which was developed by Paris group to describe NR and ER  $f_{90}$  distributions. E. Edkins adopted it in a detailed study of NR contours in <sup>241</sup>Am-Be data [58]. The comparison between the Gaussian quantiles and quantiles from the Two-Tail model (in figure 5.9) shows a decent agreement, except at the very low S1. Given the mean  $(\mu)$  of NR band decreases and the width  $(\sigma)$  increases as S1 decreases, the feature where the Gaussian curves first down and then go up as  $S1 \to 0$  intuitively makes sense to me (ex. F90<sub>1%</sub> =  $\mu$  + 2.33 $\sigma$  in a Gaussian approximation).

We eventually adopted a  $f_{90} = 0.84$  straight line as the maximum  $f_{90}$  cut instead of the energy-dependent curve derived above for the aesthetic and historical reasons. The acceptance loss for the  $f_{90} = 0.84$  line was estimated to be roughly 0.5%.

#### 5.3.5 Radial Fiducial Cut

A major motivation for introducing a radial cut came from the observed excess of high $f_{90}$  events in the test region when we partially open the data, as discussed in Sec. 5.4.2. Other than  $f_{90}$ , the radial cut provides the second most rejection power against the PTFE

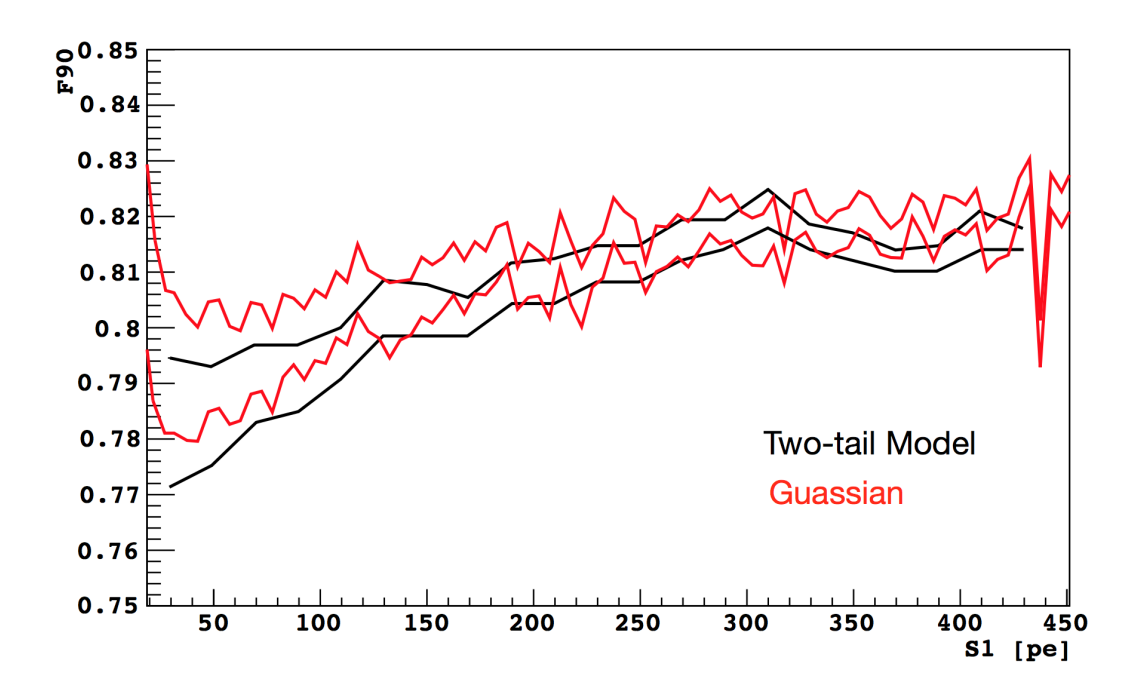


Figure 5.9: Comparison the top 1% and 2%  $f_{90}$  contour with the "two-tail" model in the range from 20 PE to 450 PE. The two-tail model contours are not available beyond 430 PE. No smoothing is done for the Gaussian curves.

Cherenkov background. This statement is true for both the true MC positions and the empirically smeared xy-position. The smeared xy-positions in data. The reconstructed radial position in data is algorithm dependent, making it difficult to mimic accurately in MC. In particular, we attempted to mimic the smearing for J. Brodsky's xy algorithm [25].

The acceptance estimate is non-trivial. Despite the fact that <sup>39</sup>Ar is uniformly distributed, being an ER means its S2 size is significantly larger than WIMP's S2 at the same S1. Similarly, although <sup>241</sup>Am-Be NRs have the correct S2 representation for the WIMP-nucleus scattering, the spatial distribution is not uniform. The solution is to combine the two data sets.

1. We generated a toy MC simulating WIMP uniformly in the LAr. The toy MC uses the energy scale from the SCENE experiment with the LY adjusted to DarkSide-50 TPC to produce the S1;

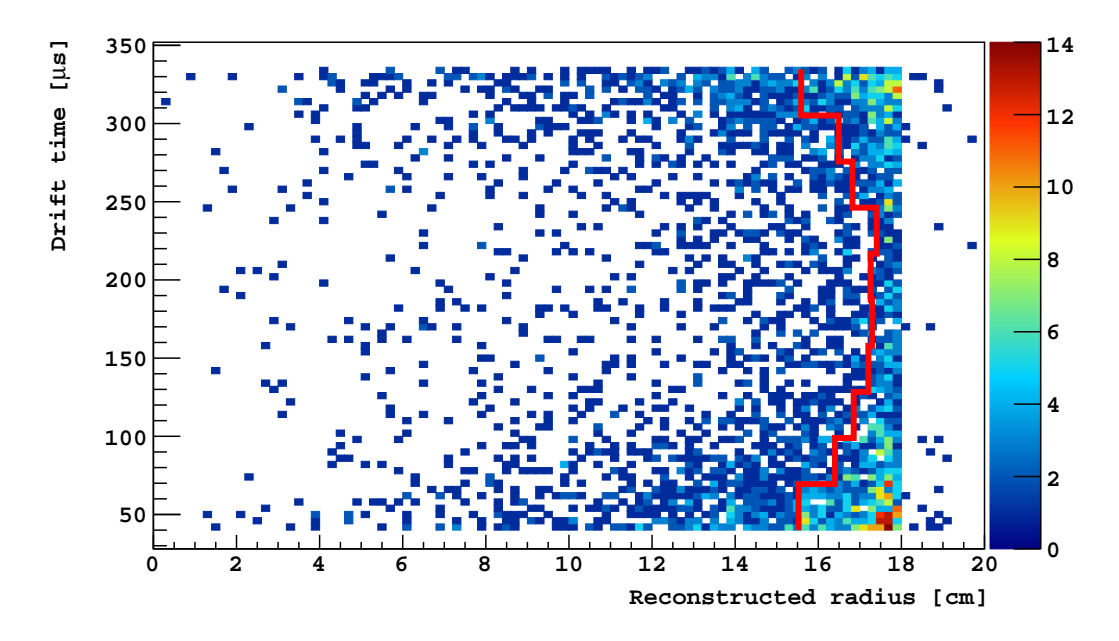


Figure 5.10: The radial fiducialization (red curve) defined as a function of  $t_{\text{drift}}$ , is designed to have 50% rejection efficiency according to the PTFE Cherenkov model. The cut removes  $\sim$ 4 mm from the wall at the center of the TPC, and  $\sim$ 23 mm at the top and bottom. After applying this cut on the test region data (Sec. 5.4.2), we determine that the cut efficiency is 56.7%. The acceptance is evaluated on <sup>241</sup>Am-Be and AAr data. Plot from Ref. [9]

- 2. For each S1 bin, we found the corresponding mean value of the xy-corrected S2 (S2 $_{xycorr}$ ) from the  $^{241}$ Am-Be NR data. The mean of S2 $_{xycorr}$  supposes to be independent from the radial position by design;
- 3. We obtained a sample of uniformly distributed <sup>39</sup>Ar events from the AAr data by selecting the events around the S2 value in step 2;
- 4. We applied the radial cut and computed the fraction of the <sup>39</sup>Ar events survived the cut. Repeat the above steps for different S1 bins until we have a cut acceptance as a function of S1.

## 5.3.6 Minimum S2/S1 Cut

As discussed in Sec. 4.4.6, we attempted to reject the Cherenkov background by imposing a minimum S2/S1 cut. The acceptance of the S2/S1 cut is defined as fixed quantiles directly extracted from the NR data. For example, the 5% quantile is shown in Figure 5.11. Since we expected the S2/S1 for the Cherenkov background to be negatively correlated with the  $f_{90}$ , there must be some correlation with the maximum  $f_{90}$  cut. Indeed, although a 5% S2/S1

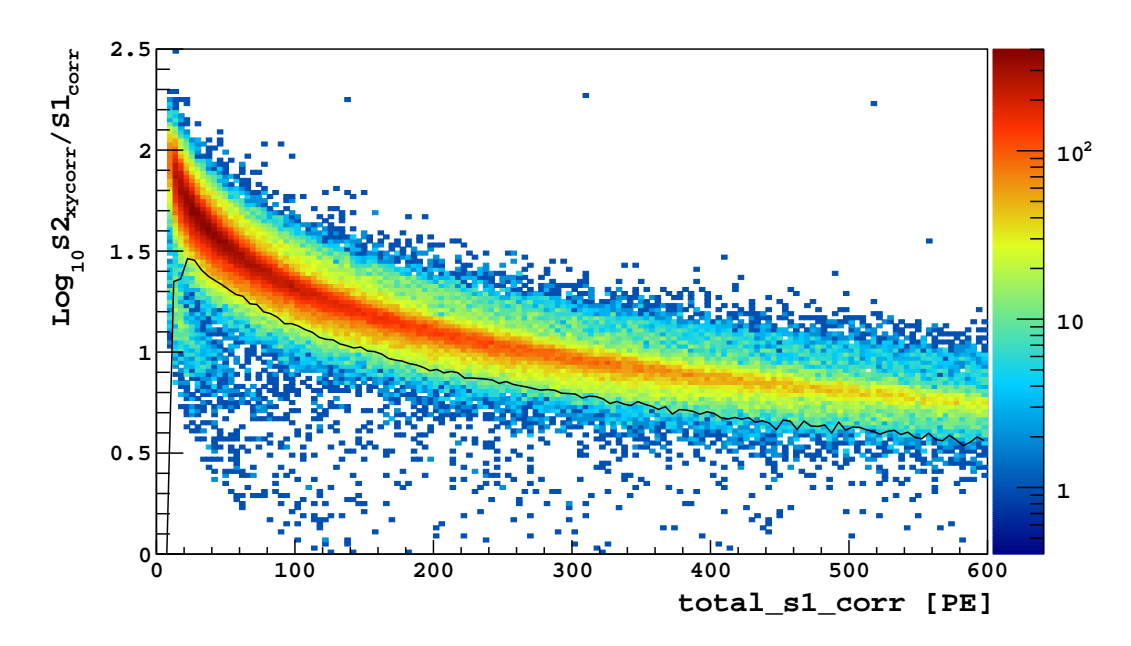


Figure 5.11: The 5% quantile directly extracted from NR data. The NR events are selected from the 160 n/s  $^{241}\text{Am-Be}$  data set with the "clean NR cuts". The rapid drop below 20 PE is due to limitation of statistics.

cut gives  $\sim 1.45$  rejection after the 95% S1pMF cut, the veto prompt cut, and the 40 µs  $t_{\rm drift}$  cut, we observed a significantly reduced rejection (< 1.07) predicted by the MC after applying the maximum  $f_{90}$  cut (Sec. 5.3.4) and a radial cut that remove 2 cm (using the true xy-position) from the wall. However, since the variance of  $S2_{xycorr}$  profile increases with the radial position (r), the variance of  $S2_{xycorr}/S1_{corr}$  also increases with r. The actual acceptance loss would certainly be lower than the defined cut values after applying any radial fiducial cuts.

The original motivation for the cut came from the observation that the S2/S1 trends for ER and NR are merging at  $\sim 100$  PE. Hence adding Cherenkov S1 to ER scintillation will make an even lower S2/S1 than NR. However, since the  $f_{90}$  cut is essentially setting an energy threshold at  $\sim 100$  PE (Sec. 5.5.1), we did not expect any rejections from the S2/S1 cut.

#### 5.3.7 Negative Log Likelihood Cut

The Negative Log Likelihood (NLL) cut is developed by T. Johnson from UC Davis [42]. Basically, the cut compares the pattern of the signal on the PMTs to a pure ER template and calculates a NLL per event. The thresholds were defined as fixed quantiles on the AAr data. Since the NLL is essentially an advanced version of the S1pMF cut, we expect a strong correlation between the two. It's known that the S1pMF cut does not do well when the Cherenkov occurs in the anode and cathode window between PMTs (Fig. 5.7). After T. Johnson integrated the NLL cut into the 540-day analysis framework, we decided to have a 1% acceptance loss NLL cut to add additional insurance to the background events. The technical construction of this cut is rather complicated and will not be described here.

## 5.4 Model Evaluation in Test Regions

#### 5.4.1 Prompt Veto Tag

The two motivations for opening Veto Prompt Tag (VPT) sample are neutron counting and evaluating the Cherenkov model. The results of neutron counting in the VPT sample was described in Sec.5.2. By definition, we open all events that fail the veto prompt cut (veto\_roi\_lsv\_charge\_vec[0]  $\geq$  1 PE). The acceptance to WIMP is less than 2%. Events in VPT sample include neutrons,  $\gamma$ -rays, cosmic rays, and in-situ radioactivity in LSV scintillator. Cosmic rays related events are identified by large WT signals. Neutron is separated from  $\gamma$ -rays by checking the delay neutron capture signal. The rest are mostly  $\gamma$ -rays escaping the TPC. The in-situ radioactivity (e.g. <sup>14</sup>C) appears in the prompt ROI purely by random coincidence ( $\sim$  4%). The VPT sample also eliminates in-situ  $\beta$ 's in LAr, so we expected an enhancement of the f<sub>90</sub> shoulder. Fig. 5.12 shows a decent agreement in f<sub>90</sub> between the VPT data and the ER model.

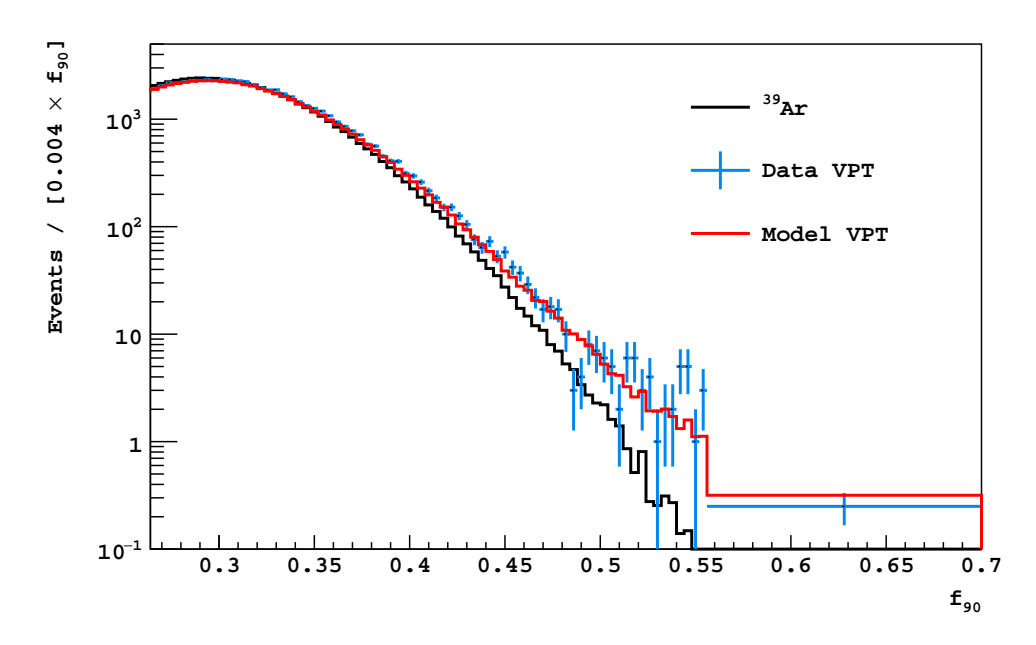


Figure 5.12:  $f_{90}$  comparison in VPT sample. The S1 selection is in the range from 100 PE to 180 PE. Events above  $f_{90} = 0.556$  are averaged into one bin for comparison. The  $f_{90}$  spectrum as predicted by the ER model (red) agrees well with the data (blue). The black  $^{39}$ Ar distribution is normalized to the integral of the VPT data. The  $^{39}$ Ar serves as a reference for the shape of single scatter  $f_{90}$  distribution.

### 5.4.2 Additional Test Regions

With the confidence in the ER model from the VPT sample, we proceed with additional test regions. The purpose of having the secondary test region is to validate PTFE Cherenkov prediction and as well as the radial cut rejection on PTFE Cherenkov background.

The region A and region B in Fig. 5.13 are motivated by the Cherenkov model because the model suggests these two regions will be almost all dominated by PTFE Cherenkov. By defining the regions below 99% (region A) and 90% (region B) NR band, we reduce the chance of accidentally see a WIMP by at least a factor of 10. The data model comparison is summarized in Tab 5.1. We chose to combine the statistics in regions A and B, and interpreted the observed discrepancy between data and model, a factor of 1.5, as a measure of the model's systematic error. The choice to scale up the model prediction is a conservative approach because we assume the observed excess in the two test regions is attributed to the Cherenkov background.

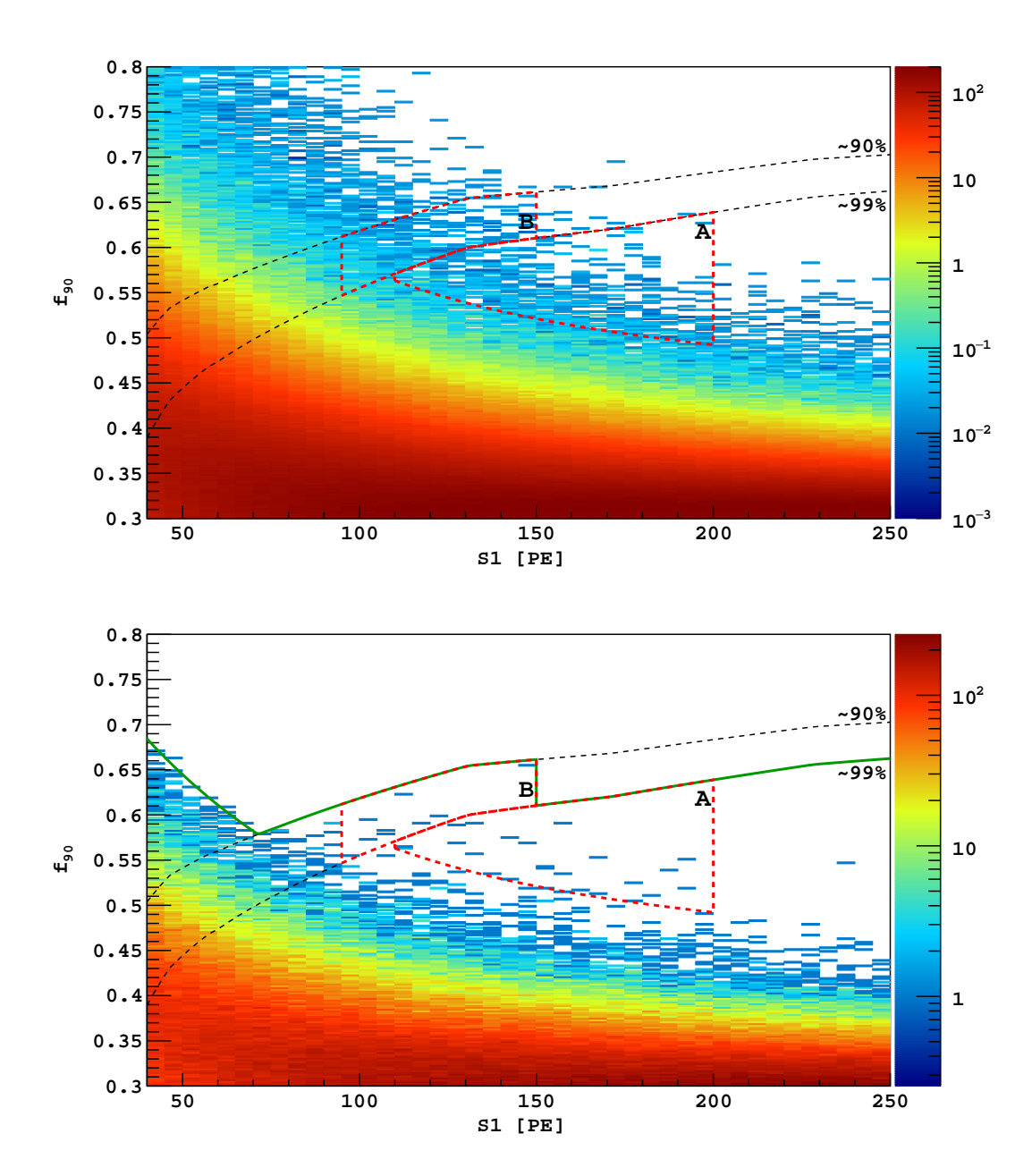


Figure 5.13: Additional test regions. Top: model. Bottom: data. Overlaid on the plot are the two final test regions (dashed red). Data above the green curve is still blinded. The choice of the two regions are motivated by the model. The upper boundaries of the test regions were guided by approximately the NR 90% and 99% acceptance contours. Note, one dot in data corresponds to one event, but one dot in the model plot corresponds to a fraction of events. This is because we scale the 90 years equivalent model statistic down to match the data exposure. Plot modified from Ref. [9].

We estimated the rejection efficiency of radial fiducialization on the events observed in regions A and B. After applying all the finalized cuts except for the LSV delay signal cut, we observed 30 events in region A and B before the radial cut, and 13 survived after the cut. The measured 56.7% rejection is statistically consistent with the designed 50% rejection by the model. We decided to use the measured number as the final rejection efficiency.

Roughly 1/3 of the data events in region A possess abnormally low S2. Inspecting the transverse locations indicate that they tend to locate near the wall. This resembles the characteristic of the "wall effect" (Sec. 5.2.1). One hypothesis from by J. Martoff suggests that those events could be a signature of surface Cherenkov –  $\beta$ -decays toward PTFE while producing a simultaneous X-ray in coincidence. This is a very interesting hypothesis because it not only explains the extremely low S2 feature but also connects Cherenkov to surface background study. We see evidence of <sup>210</sup>Po embedded underneath of TPB layer (Fig. 5.2). The <sup>210</sup>Bi from the same <sup>210</sup>Po chain could release  $\beta$  (1.16 MeV endpoint) along with a 10.3 keV X-ray (5.6% branch ratio) which could then produce PTFE Cherenkov coincidence. The range of a 10.3 keV X-ray in LAr is only about  $\sim$  110 µs. According to [40], the rate of <sup>210</sup>Po (with and without S2) is 2.306 mBq/m² from the wall. When combining with the surface area of the PTFE reflector ( $A \sim 0.39 \,\mathrm{m}^2$ ), this yields  $4.2 \times 10^4$  decays in 540 days, which is not a negligible number.

We perform a back-of-the-envelope calculation. A factor of 1/4 is applied for the X-ray heading into LAr and the  $\beta$  heading into PTFE. The probability of having a  $\beta$ -decay electron greater than 1.1 MeV is  $4.5 \times 10^{-4}$ . Thus,  $N = 4.2 \times 10^4 \times (1/4) \times (5.6\%) \times (4.5 \times 10^{-4}) = 0.26$  events which have  $\sim 20$  PE from Cherenkov process. Given the region A is in the range from 110 PE to 200 PE, Cherenkov process is less than 18% of the combined S1. A quick arithmetic shows that 18% Cherenkov is not enough to boost a normal ER event into the box. Hence the surface Cherenkov hypothesis did not work out quantitatively.

Although the physical mechanism is not well understood, it's clear that the low S2 events in region A are originated from the surface. We designed a minimum S2 cut and a radial cut

Table 5.1: Model data comparison in the additional test regions. The cuts are event quality, single scatter cuts,  $t_{\text{drift}}$  time, the S1pmf cut, the uncorrected S2, and the LSV prompt signal cut.

Region	Model	Data
A	13.3	24
В	8.7	9
A+B	22	33

aiming at reducing the Cherenkov background, but these two cuts also protect the experiment from an unknown source of surface-related background.

### 5.5 WIMP Search Results

#### 5.5.1 Designing the WIMP box

The final WIMP box (Fig. 5.14) is bounded by  $f_{90} = 0.84$  line from the top, a 99% NR acceptance curve from the bottom, a S1 < 450 PE energy cut off from the right, and a  $f_{90}$  cut from the left. Both the  $f_{90} = 0.84$  line and the 99% curve are coming from SCENE data where each cut off 1 % of NRs. However, after checking with the  $^{241}$ Am-Be data, we found small derivations in terms of the acceptance – the acceptance loss for the  $f_{90} = 0.84$  line is actually less than 1% and the acceptance loss for the bottom curve is actually higher than 1%. Since we simulated the WIMP distributions using a model fitted to the  $^{241}$ Am-Be data, the derivation will not affect the final WIMP acceptance estimate.

The  $f_{90}$  cut from the left is also known as the ER leakage curve because it defines the number of ER background accepted. In the previous open analysis, we fitted an analytical model of single scatter to the  $f_{90}$  distributions. When repeated this procedure at every S1 bin, we were able to build the leakage curve admitting equal ER background from the fitted function. In this analysis, we will use the ER model to drive the ER leakage. Given the estimation of other background numbers, we chose to limit ER events to 0.08 events. We generated a MC set that is equivalent to 90 years exposure. The model statistics is still

insufficient to derive a smooth leakage curve. To save time, we took the following steps to generate a smooth leakage curve.

- 1. We used the model to derive a smooth 0.07 events per 5 PE bin. The model statistics was sufficient because the curve accepted more ER backgrounds.
- 2. We fixed the shape while shifting the leakage curve vertically up until a total of 0.08 ER background events in data is reached.

The total number of predicted background in data  $(N_{BG}^{\text{data}})$  is related to the number of model events  $N_{BG}^{\text{data}}$  by

$$N_{BG}^{\text{data}} = N_{BG}^{\text{data}} \times \epsilon_r \times \frac{N_{A+B}^{\text{data}}}{N_{A+B}^{\text{data}}}, \tag{5.2}$$

where the  $\epsilon_r = 0.43$  is the radial cut background acceptance estimated from test region A+B data (14 survived events out of 33. See Sec. 5.3.5), and  $\frac{N_{A+B}^{\text{data}}}{N_{A+B}^{\text{data}}}$  comes from the 1.5 scaling factor applied to the model (Sec. 5.4.2). The  $\epsilon_r$  term is needed because we did not apply the radial cut to the model, which will certainly hurt the statistics (the vertical location of the leakage curve is constrained by 7 MC events<sup>1</sup> without the radial cut).

Since a background-free operation requires less than 0.1 total background events, we choose the final  $f_{90}$  cut to give  $N_{BG}^{\rm data} = 0.08 \pm 0.04$  ER events in the 530-days exposure, given the sum of neutron and surface background prediction is < 0.01 events. The 50% uncertainty is driven by Feldman-Cousins' statistics in the model.

### 5.5.2 Exposure and WIMP Acceptance

The total exposure was calculated to be  $(16660 \pm 270)$  kg d in the same way as Sec. 3.4.4, except for two minor changes. First we subtract 400 µs instead of 540 µs from the total for every event passing the livetime cut, as a result of adjusting the livetime cut from the 70-day. The accumulated livetime was 532.4 d. Second the fiducial mass need to take into account of both the  $t_{\text{drift}}$  cut and the radial cut. Unlike the  $t_{\text{drift}}$  cut, the remaining mass

<sup>&</sup>lt;sup>1</sup>One model event (0.012 in data) ends up at the middle of WIMP box (Fig. 5.14). The event is a result of high energy ( $\sim 7$  MeV)  $\gamma$ -ray produced from ( $\alpha, \gamma$ ) reaction. This  $\gamma$ -ray later create PTFE Cherenkov background.

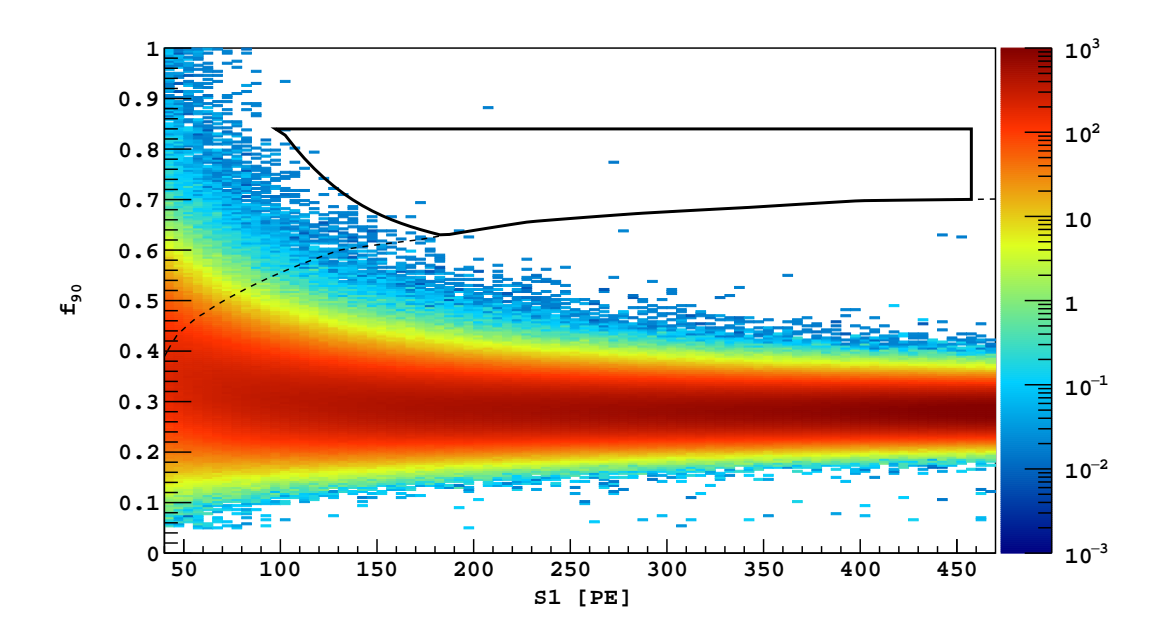


Figure 5.14: The final WIMP box. The events are all from the ER model. The definition of the box is described in text.

after the radial cut is evaluated as a function of S1 since the xy resolution get better as the energy increases. The final estimated mass is  $31.3(5) \,\mathrm{kg}$  [9].

The total WIMP acceptance as a function of energy is shown in Fig. 5.15. The  $f_{90}$  acceptance is estimated from WIMP recoils in a toy MC similar to Sec. 3.4.4, except that the NR  $f_{90}$  distribution was obtained by fitting an analytic "two-tail" model to the <sup>241</sup>Am-Be data. The "two-tail" model was developed by D. Franco to incorporate both ER and NR events. The actual fitting was done by E. Edkin [58]. The rapid drop-off of the  $f_{90}$  NR acceptance at  $\sim 60 \text{ keV}_{nr}$  essentially sets the WIMP search energy threshold. Other than the  $f_{90}$  cut, the S1pMF cut (Sec. 5.3.1) has the most individual acceptance loss (5%) out of the cuts designed for rejecting Cherenkov backgrounds, followed by the 1% NLL cut (Sec. 5.3.7). The LSV delay signal cuts is a significant source of acceptance of loss, but it is not designed for rejecting Cherenkov background.

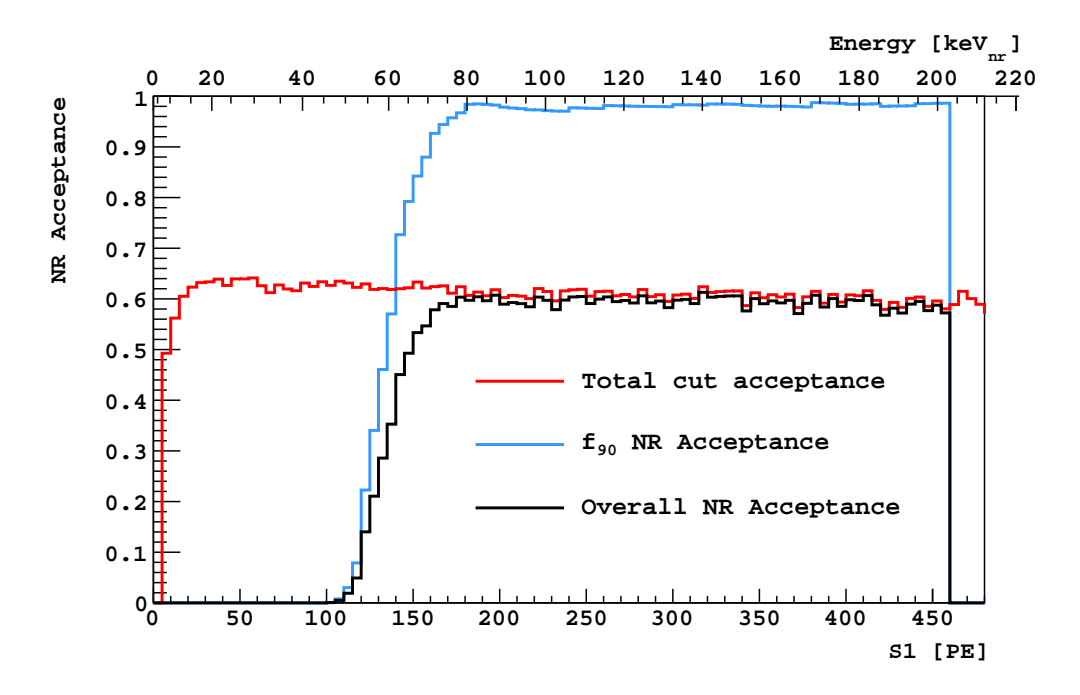


Figure 5.15: The WIMP acceptance as a function of S1. Plot from Ref. [9].

#### 5.5.3 Final Unblinding

While we were getting ready to unblind the rest of data set, we performed a peer review of the analysis notes which documented the technical detail of every aspect of the analysis. Before the unblinding, we also had a final round of bug hunting by assigning multiple analyzers to proof-read different sections of the code. After we reviewed the cuts in the analysis meeting, we set up a protocol specifying the actions once the box is open. Of course, if the observation in the WIMP box is 0, no further action is required. If it was non-zero, that would mean more work. First we would perform a manual inspection to exclude pathological events (events with clear signatures of background or noise). Then we would cross check out background models. Finally, we would calculate the significance of the remaining events, but left the decision to the entire collaboration.

With the finalized background summarized in Tab. 5.2, we open the rest of the data set on Febuary 10, 2018.

Table 5.2: Summary of the background estimate surviving all cuts. The 0.08 ER events are driven by Teflon Cherenkov, with the uncertainty of 0.04 driven by the 7 model statistics. The 50% error are determined by [60]

Background	After all cuts		
Surface Type I	$0.0006 \pm 0.0001$		
Surface Type II	$0.00092 \pm 0.00004$		
Radiogenic Neutron	< 0.005		
Cosmogenic Neutron	< 0.0035		
Electronic Recoil (Cherenkov)	$0.08 \pm 0.04$		
Total	$0.09 \pm 0.04$		

#### 5.5.4 The Exclusion Limit

After applying all cuts, we report the null result in the designed WIMP search ROI as shown in Fig. 5.16-Top. The collaboration has demonstrated a successful background-free operation in a blind analysis. Although we observed 0 WIMP events in the ROI, we set a 90% confidence exclusion for 2.3 spin-independent WIMP events. The 2.3 expected WIMP events comes from the Poisson statistics where  $P(x=0,\mu=2.3)=10\%$ . We use the standard isothermal galactic WIMP halo parameters ( $v_{escape}=544$  km/s,  $v_0=220$  km/s,  $v_{Earth}=232$  km/s,  $\rho_{DM}=0.3$  GeV/( $c^2$  cm<sup>3</sup>)) [9] to calculate the expected recoil rate. The current DarkSide-50 limit, as of May 2018, is a little bit better than DEAP-3600 experiment (Fig. 5.16-Bottom), but still order of magnitude behind Xenon based experiment. We set an  $1.14 \times 10^{44}$  cm<sup>2</sup>,  $(3.79 \times 10^{44}$  cm<sup>2</sup>,  $1.10 \times 10^{44}$  cm<sup>2</sup>) limit for 100 GeV/ $c^2$  (1 TeV/ $c^2$ , 126 GeV/ $c^2$ ) DM particles.

The increase of energy threshold by raising the  $f_{90}$  cut is inevitable as a result of the Cherenkov background. Higher threshold has a bigger impact on WIMP sensitivity especially at the low mass range. As shown in Fig. 5.16-Bottom, the sensitivity of previously open 70-day analysis is better than the current limit under 50 GeV. This result shows the importance of minimizing the Cherenkov background at the R&D stage for the next generation experiment.

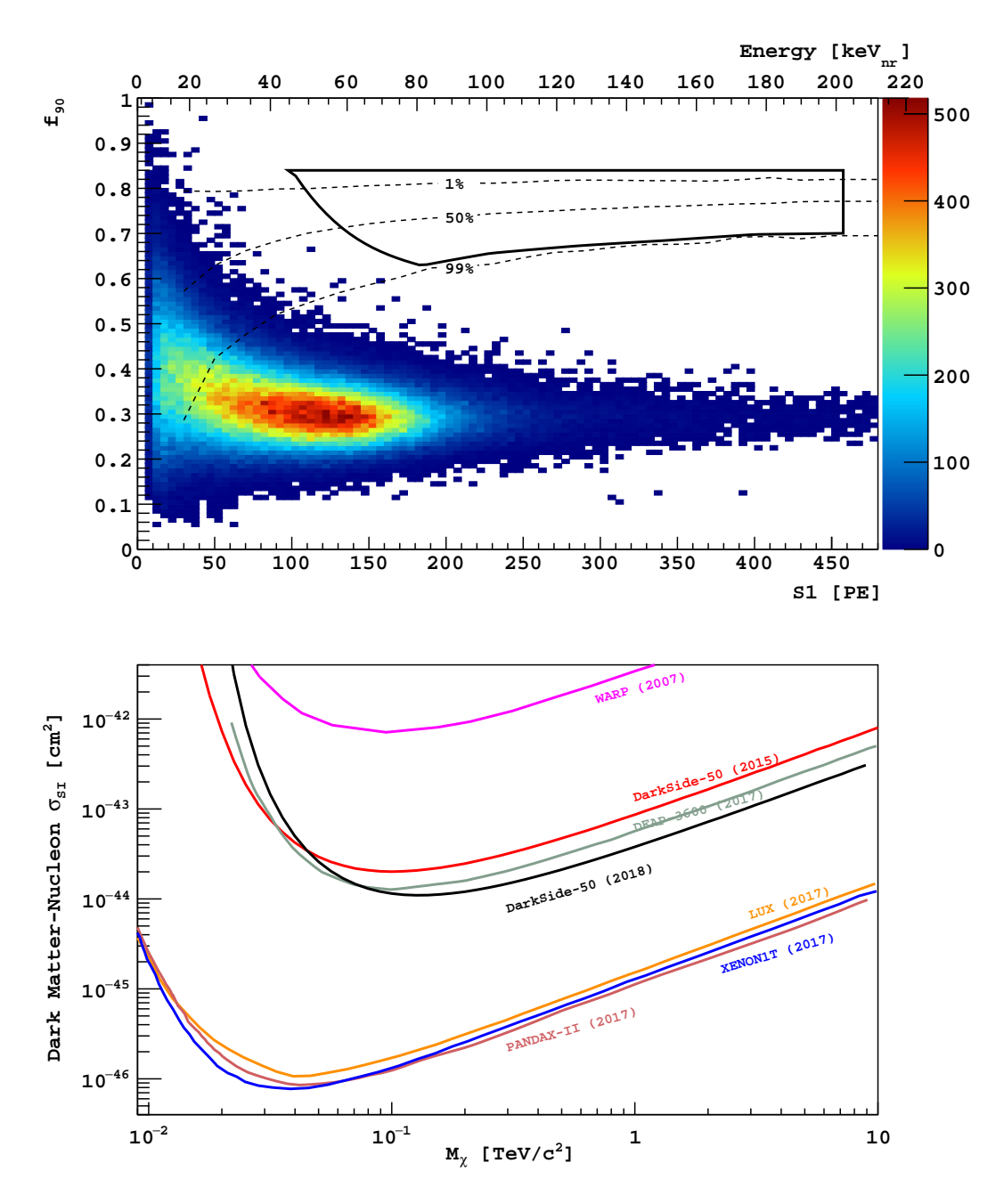


Figure 5.16: Final WIMP search results. Top:  $f_{90}$  vs S1 plot with no events in the search box. Bottom: the published exclusion curves as of March 2018. Plots from Ref. [9].

# Chapter 6

# Conclusion and Outlook

## 6.1 Summary

WIMPs are still an appealing DM candidate for direct DM detection experiment. The DarkSide-50 three detectors have been very stable over the past 4 years. The working principles of the key experimental technologies, from the Argon based dual-phase TPC, to the low radioactive UAr, to the active neutron veto system were first described in Chapter 2.

With those technologies in place, we first performed the WIMP searches with a batch of AAr. After the AAr analysis campaign, the DarkSide-50 detectors have been operating in a low-background condition with the UAr target. The first WIMP search data with  $\sim$ 70-day exposure of the UAr target was analyzed in a non-blinded fashion. Several keys studies of the WIMP analysis were described such as the data selection and quality validation, the analysis cuts, designing the  $f_{90}$  leakage curve, and the final exclusion limit. Although the 70-day analysis returned a null result, a closer look at the  $f_{90}$  spectra reveals traces of  $\gamma$ -induced Cherenkov plus scintillation backgrounds in TPC.

We identify three types of ER backgrounds – single scatter, unresolved multiple scatter, and Cherenkov plus scintillation. Since the end of the 70-day campaign, we have built

a hybrid ER model incorporating both the G4DS simulation of the Cherenkov response and the AAr data set to mimic the Cherenkov plus scintillation backgrounds in TPC. The optics for both the fused silica and PTFE originated Cherenkov response was first tuned individually against pure Cherenkov events in the <sup>22</sup>Na calibration data, and then checked in the UAr WIMP search data and the <sup>241</sup>Am-Be calibration data. Next, we described the steps to build a complete hybrid model to simulate all three types of ER events. Finally, we established with the model that PTFE originated Cherenkov plus scintillation events are the most stubborn ER background after all cuts.

We analyzed the second ~540-day exposure UAr data set in a blinded fashion where we identified the surface events, cosmogenic neutrons, radiogenic neutrons, and the ER backgrounds as the main threats. Out of all the cuts we had explored with an intention to suppress the Cherenkov backgrounds, we did not find a magic cut — PSD and fiducialization remain the two most effective weapon against PTFE originated Cherenkov background. Next, we tested the model predictions by opening a fraction of the blinded events. The model survived the test within statistical uncertainty. Using the model we designed the final WIMP box for the 540-day analysis and reported a null result after the complete opening.

### 6.2 Future Outlooks

Although the presence of the Cherenkov backgrounds in DarkSide-50 is a pain in the neck, it does not prevent the LAr technology from achieving the background-free in the future. Rather it is a design flaw, which can be avoided if we take preventive actions at the designing stage of the next generation experiment. The future outlook is summarized below based on the experience we gained in DarkSide-50, since a detailed simulation is beyond the scope of this work.

DarkSide-20 plans to replace the PTFE side reflector with a specular reflector hoping to eliminate Cherenkov background from the side. The current design uses an acrylic - 3M

foil - acrylic sandwich geometry as the specular reflector. Although we do not yet have the exact optical measurements (reflectivity/absorption/transmission) done in LAr, using the measurements in water, T. Johnson has shown that the side reflector is negligible in terms of the Cherenkov production [61]. Of course, this study should be repeated with updated information.

Higher UV absorption means less Cherenkov light yield. The fused silica of diving bell and cathode window have less Cherenkov light survived because of the ITO surface coating which attenuates UV heavily. Furthermore, DarkSide-20k plans to use UVA acrylic which supposes to suppress the background even more [62]. However, DEAP-3600 collaboration has observed a higher Cherenkov light yield in their UVA acrylic than the expected (conversation with S. Westerdale). One hypothesis suggests that the acrylic may act as a wavelength shifter. Regardless whether this is true, the detailed optical information needs to be collected if DarkSide-20k plans to use the same UVA acrylic. Meanwhile, the ITO model needs to be improved near UV as mentioned in Sec. 4.3.5.

In DarkSide-50 we had tried to use the early super-prompt feature of Cherenkov radiation to develop cuts (e.g.  $f_{30}/f_{90}$ ), although all of them turn out to be ineffective. The next generation DarkSide-20k will use SiPM instead of PMT as the photon sensors. The excellent timing of SiPM may allow resolving Cherenkov light from scintillation light. It is important for the DAQ to record the early pulse shape information if DarkSide-20k does not intend to save the entire waveform for the concern of storage.

Radial fiducialization is an effective cut but an accurate xy reconstruction is a prerequirement. DarkSide-50 struggled for an accurate xy-algorithm mainly because the PMT arrays were so close to the gas pocket that the S2 light tends to concentrate on a single tube rather than separating out. DarkSide-20k can afford more fiducial volume loss and the design team is already planning to move the SiPMs away from the gas pocket. Since the dynamic range of a SiPM module is only  $\sim$ 50 PE, there may be some concerns on the performance of the xy-algorithm from the S2 saturation. The spatial channel pattern based cuts (e.g. S1pMF) work very well in DarkSide-50 because the PMTs are close to the fused silica window. Once the SiPM modules are moved away, it may impact the performance of any pattern cuts. On the other hand, due to the square shape of SiPM, DarkSide-20k supposes to have better coverage than DarkSide-50, which favors the spatial channel pattern based cuts.

In summary, since the side reflector originated Cherenkov will be eliminated by the new reflector design and the cathode/anode window originated Cherenkov can ultimately be suppressed by deep a  $t_{\rm drift}$  cut, I am optimistic that Cherenkov background will not stop DarkSide-20k from achieving the background-free operation.

# Appendix A

# **Digitizer Correction**

### A.1 V1720 and V1724

A large dynamic range brings more options to calibrate our detectors, improves detector performance such as improving xy-correction at higher energy, and allows various background studies such as reconstructing surface  $\alpha$  and  $\gamma$ -rays energy spectrum.

The DAQ system of TPC has two CAEN digitizers processing waveform data in parallel for the purpose of achieving higher ADC dynamic range. The hardware work of integrating the two digitizers into the DAQ system was done by Yann Guardincerri. The amplifier provides four analog outputs with different signal conditions. One shaped amplifier output with a ×10 V/V gain are sent to V1720, a 250 MHz 12-bit digitizer. Another output was attenuated with a ×0.5 V/V gain and reduced to bandwidth of 40 MHz; the low gain signals was sent to V1724, a 100 MHz 14-bit digitizer. Both digitizer types are one unit 6U VME64X VME modules, servicing eight channels, with circular memory buffers of 10 Ms/ch, and are locally FPGA compliant. All ADCs are synchronized with a common 50 MHz clock and external trigger. They run in parallel and require three common control signals: a Trigger, a Run-enable, and a Clock. Together they cover a larger dynamic range with linear response

from 1 to 10,000 PE [63]. The major differences between the two digitized waveforms are highlighted in table A.1

Table A.1: Major differences between two digitized outputs

	V1720	V1724
Sample Rate	250 MHz	100 MHz
Gain	20x	1x
Resolution	12 bits	14 bits
Input Range	$2 V_{pp}$	$2.25 \ V_{pp}$
Bandwidth	$125 \text{ MHz } V_{pp}$	$40 \text{ MHz } V_{pp}$

## A.2 Reconstructing V1724 Data

Despite of having a large dynamic range, since WIMP NR typically happens at a low energy scale of a few keV, the priority of DarkArt event reconstruction goes to the high gain V1720 digitized data. The V1724 was introduced after the 50-day AAr campaign. The development of DarkArt algorithm, including reading raw data, finding baseline, finding pulses, and calculating variables (ex. S1, S2, F90) was completed and validated before this ADC correction work. The raw data from V1724 was never reconstructed by DarkArt until this study.

The first step is to make DarkArt process V1724 data. Building on the success of DarkArt on V1720 data, we can re-use many modules with a change of module tags in the FHiCL file<sup>1</sup>. First we run the V1720 modules as usual regardless of existence of V1724. Then we run the V1724 chain. But since the V1724 chain depends on the V1720 reconstruction, we need to include the V1720 in this chain. Fortunately, art is smart enough to run the duplicated modules only once and will not run them a second time over V1720 data.

After DarkArt read raw data, the first thing it needs to do is finding a baseline to subtract. The subtracted channel waveforms are added up to get a summed waveform, which will subsequently have a zero-suppression applied to summed waveform. The zero-suppression algorithm keeps the original waveform unchanged where it's above a pre-defined

 $<sup>^1</sup>$ FHiCL file is the run-time configuration adopted by <code>DarkArt</code>

threshold, but setting the amplitude to 0 once it goes below the threshold. While applying zero-suppression helps increase processing efficiency and reduce output file size, it kills V1724 waveform when PE are spread out in time. For instance, a S1 pulse from V1724 will likely to only have prompt signal survived the suppression. Therefore, the threshold must be re-tuned to a lower value to keep necessary pulse information when processing V1724 waveform.

One challenge to reconstruct V1724 data is the pulse finding. In DarkArt, a pulse is defined by start time and end time. The algorithm scans through a down-sampled waveform and compares its second derivative to a pre-defined fixed curvature threshold. The start time was set once it passes the threshold. The algorithm requires a minimum pulse width after the start time, and then looks for the end time by again comparing the second derivative to a lower pre-defined curvature threshold. However, this algorithm, when applied to V1724 waveform, often returns different number of pulses, pulse start time and pulse end time than V1720 waveform. It's not only impossible to make saturation correction without causing bias, but also a pain in the neck for analyzer to use the corrected variables (ex. pulse id is not always one-to-one matched). For this reason, we decide on an alternative simple approach. After we run pulse finder over V1720 waveform, instead of running it again over V1724 waveform, we built a new module that copies over the start time and end time from V1720 data and use them to define pulses on V1724 waveform.

Originally the corrected variables were added to V1720 tree while the V1724 reconstructed data was saved to a different tree, but for the official release, we decide not to keep the V1724 tree so that DarkArt outputs remain slim. The general structure and data flow of the updated DarkArt is summarized in the figure A.1.

## A.3 ADC Correction Algorithm

A sample by sample ADC correction would be ideal, but this is not practical for DS-50 due to different digitizer sampling rate. Previous approach by Y. Guardincerri attempts to correct

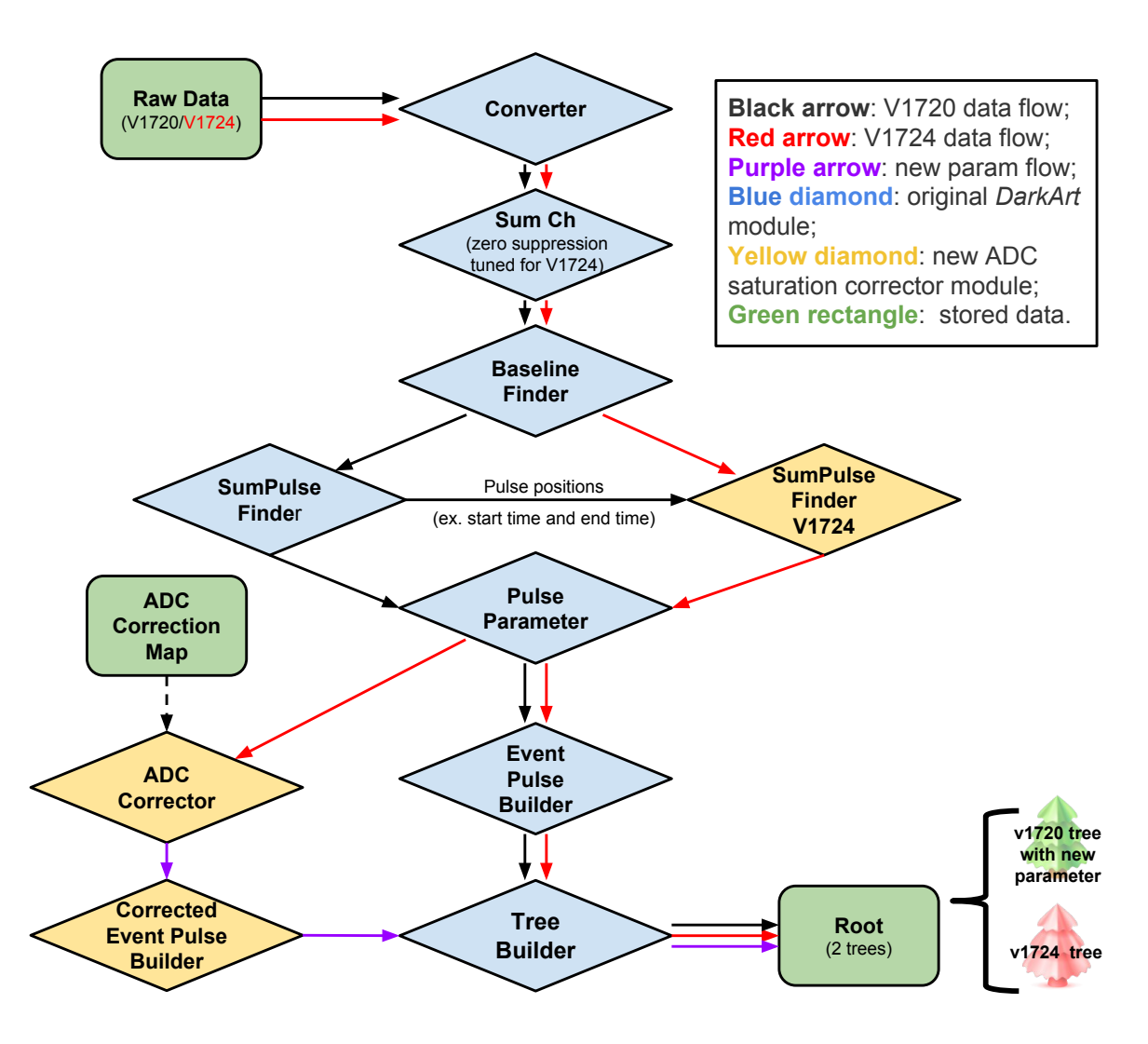


Figure A.1: An simplified DarkArt flowchart incorporating V1724 data stream. This is a simplified version to illustrate the data processing scheme with V1724 data, the actual DarkArt has many more modules.

the entire saturated waveform by re-binning two digitized waveforms. The analogy filter in front of V1724 alters the pulse shape, but since we expect the  $S_F$  for the entire pulse to stay approximately the same, we can directly make correction to saturated pulse variables, such as S1 and S2. Also since every channel is different, the ADC correction has to be done at channel level. We expect a linear correlation between two digitizers' pulse variables.

#### A.3.1 The Correction Maps

The correction map suppose to describe the variable correlation if a pulse was not saturating V1720. In this study, we use <sup>57</sup>Co calibration data to obtain this function. The choice of data set should not matter here since the correlation is a digitizer properties independent from the physics going on in the detector. First we apply the following cuts to select single scatter events whose S1 and S2 are well identified.

- All channels are alive for both ADCs (nchannel=38);
- The baseline is found for both ADCs;
- Correct trigger time.  $(-6.1\mu s < s1\_start\_time < -6\mu s)$ ;
- 2 physical pulses are identified ( $N_{\text{pulse}}$  = 2 OR s2\_echo = true);
- Vertical fiducialization  $t_{\rm drift} > 10 \mu {
  m s}$  to avoid overlaps pulses;
- Remove events triggered by S2 echo (S3) on V1720 (dt >  $1000\mu$  s);
- The first pulse is S1. ( $f_{90} > 0.05$ ). This cut removes events triggered by S2.

It's not possible to see single PE due to the low gain nature. V1724 is always disable during laser SPE calibration. For the same reason, the correlation function must be computed before SPE normalization. For the case of S2, figure A.2 shows one of 38 fitting results for an unsaturated S2 pulse. The linear fit returns two parameters,  $p_0$ ,  $p_1$ . When a S2 pulse saturate V1720 on channel i, we can compute the corrected S2 variable as the following:  $S2_{\text{corr}}^i = (S2_{\text{v1724}}^i \times p_0)/p_1$ . When a pulse is not saturated, we do not apply any correction and simply set  $S2_{\text{corr}}^i = S2_{\text{v1720}}^i$ . To get SPE normalized  $S2^{\text{total}}$ , we sum over channels:

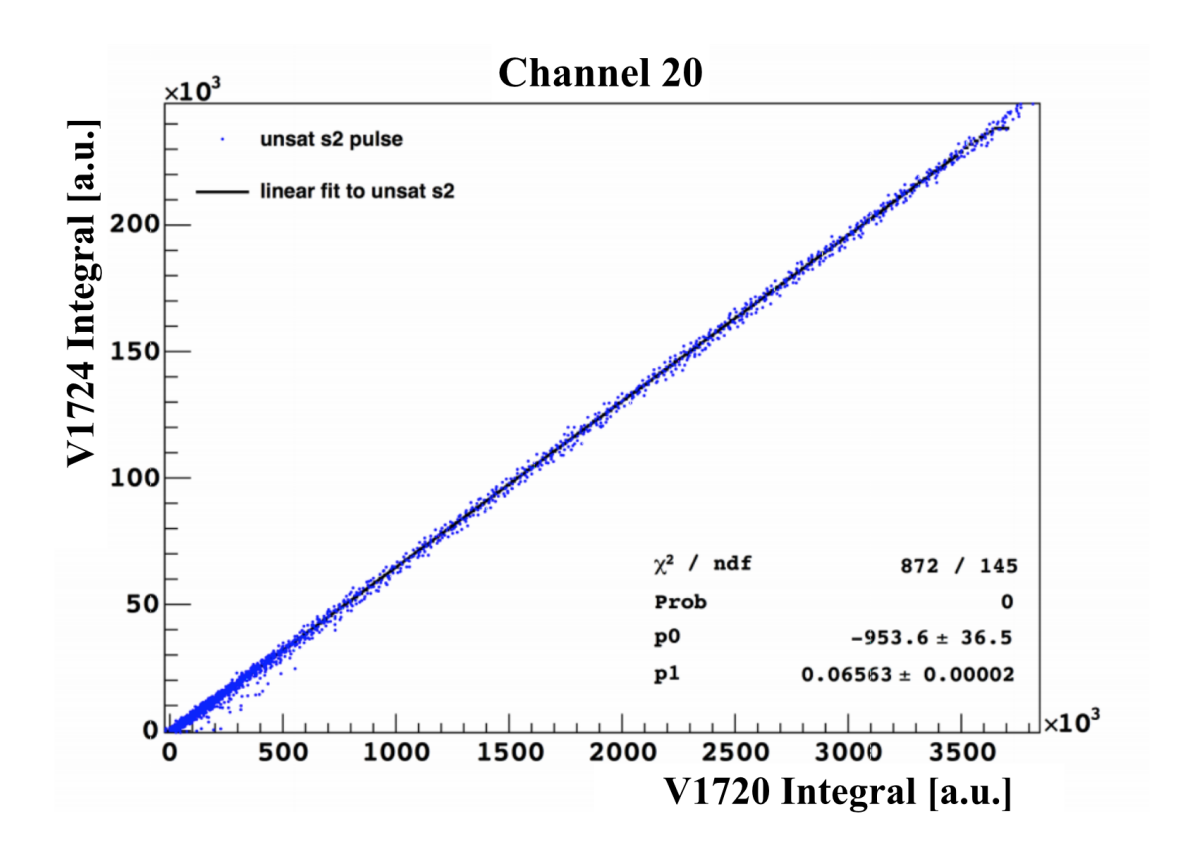


Figure A.2: An example fit on channel 20 to S2-like pulses.

 $S2_{\text{corr}}^{\text{total}} = \sum_{i=0}^{37} S2_{\text{corr}}^{i}/\text{spe}^{i}$ , where spe<sup>i</sup> is the SPE normalization factor for channel i from laser calibration. By design, if all V1720 channels are not saturated, the  $S2_{\text{corr}}^{total}$  should be identical to the original  $S2^{total}$  computed on V1720.

It was observed that S1 variables tend to return a different set of parameters  $p_0$  and  $p_1$ . We have to construct separately for S1 again to avoid possible bias, but the procedure is identical to above. Once the  $p_0$  and  $p_1$  are extracted, they are saved in in an aux file which will be loaded by a DarkArt module to make the correction. Table A.2 summarize all parameters.

Pulse information is typically in the form of pulse integral. One important characteristics between two digitizers is the relative ratio of two pulse integral. Let's define scaling factor to be  $S_F = S_{v1720}/S_{v1724}$ . Since for each ADC,  $S_x = \frac{\text{Gain}_x \times \text{Bits}_x \times \text{SampleRate}_x}{\text{InputRange}_x}$  where x can be either V1720 or V1724. According to table A.1, we have  $S_F = \frac{20\text{Gain} \times 2^{12} \times 250\text{MHz}}{2\text{V}} \times \frac{2.25V}{\text{Gain} \times 2^{14} \times 100\text{MHz}} \approx 14.1$ . This theoretically estimated scale factor should be approximately equal to  $1/p_1$  from

the fit. The average fitted  $p_1$  value for is S1 is 0.0613 and for S2 is 0.0645, which has an inverse of 16.3 and 15.5.

#### A.3.2 Correcting F90

It's a bit tricky to do correction for F90, since F90 carries pulse shape information and V1724 has received the distorted shape.

Here we assume that only S1 prompt (the first 90 ns) saturate V1720. With this assumption, it's possible to do some arithmetic to figure out what F90 supposes to be if no saturation occurred. At this point we already have the corrected S1 per channel. Let  $I_{90}^i$  be the integral over the first 90ns on channel index i, we have

$$f90_{\text{corr}}^{i} = \frac{I_{90\text{corr}}^{i}}{S1_{\text{corr}}^{i}} = \frac{I_{90}^{i} + S1_{\text{corr}}^{i} - S1^{i}}{S1_{\text{corr}}^{i}}$$
(A.1)

where the second equality use the assumption stated above. Then we sum over 38 channels with each  $f90_{\text{corr}}^i$  weighted by the corresponding  $S1_{\text{corr}}^i$ .

$$f90_{\text{corr}}^{\text{total}} = \sum_{i=0}^{37} f90_{\text{corr}}^{i} \times \frac{S1_{\text{corr}}^{i}}{S1_{\text{corr}}^{\text{total}}}$$
(A.2)

As one can verify that for an unsaturated pulse,  $f90_{\text{corr}}^{\text{total}} = f90^{\text{total}}$ .

### A.4 Validation

Validating the correction algorithm is not straight-forward. One can qualitatively look for energy peaks to see if they get sharper after correction. But quantitatively it's hard to estimate the systematics due to the correction.

As one may notice in figure A.2, the y-intercept is close to 0 but exactly equal to 0 (a typical SPE mean is at 200 a.u., so  $p_0 \approx -4.75$  PE is not so bad for a S2 pulse). When a signal height is low, we tend to lose individual spared PE on V1724 causing a slight bias

at low energy. This should be fine since saturation tend to occur at high energy. Another possible bias is that the linear correlation isn't actually linear when we extend up to much higher S2 scale. This could be caused by PMT or electronics saturation which cannot be addressed by this correction.

### A.4.1 The Alpha study

The assumption we made in A.3.2 isn't always true. For example, during  $\alpha$  study, we found that when the  $\alpha$  energy becomes so high that the first 90 ns doesn't fully contain the prompt signal. We expect the corrected F90 value to be relative flat from the energy, but instead, F90 value decreases when S1 increases. When we switch to a more appropriate f200 parameter, the fraction of light in the first 200 ns, and applied the same arithmetic correction to get  $f200_{\rm corr}^{\rm total}$ , f200 seems to be less dependent on the energy<sup>2</sup>.

<sup>&</sup>lt;sup>2</sup>If there are any energy dependent pulse shape behaviors, it may imply new micro-physics. After close inspection on  $\alpha$  event waveform, we suspect there may be some PMT saturation for those events, although no conclusive conclusion can be drew.

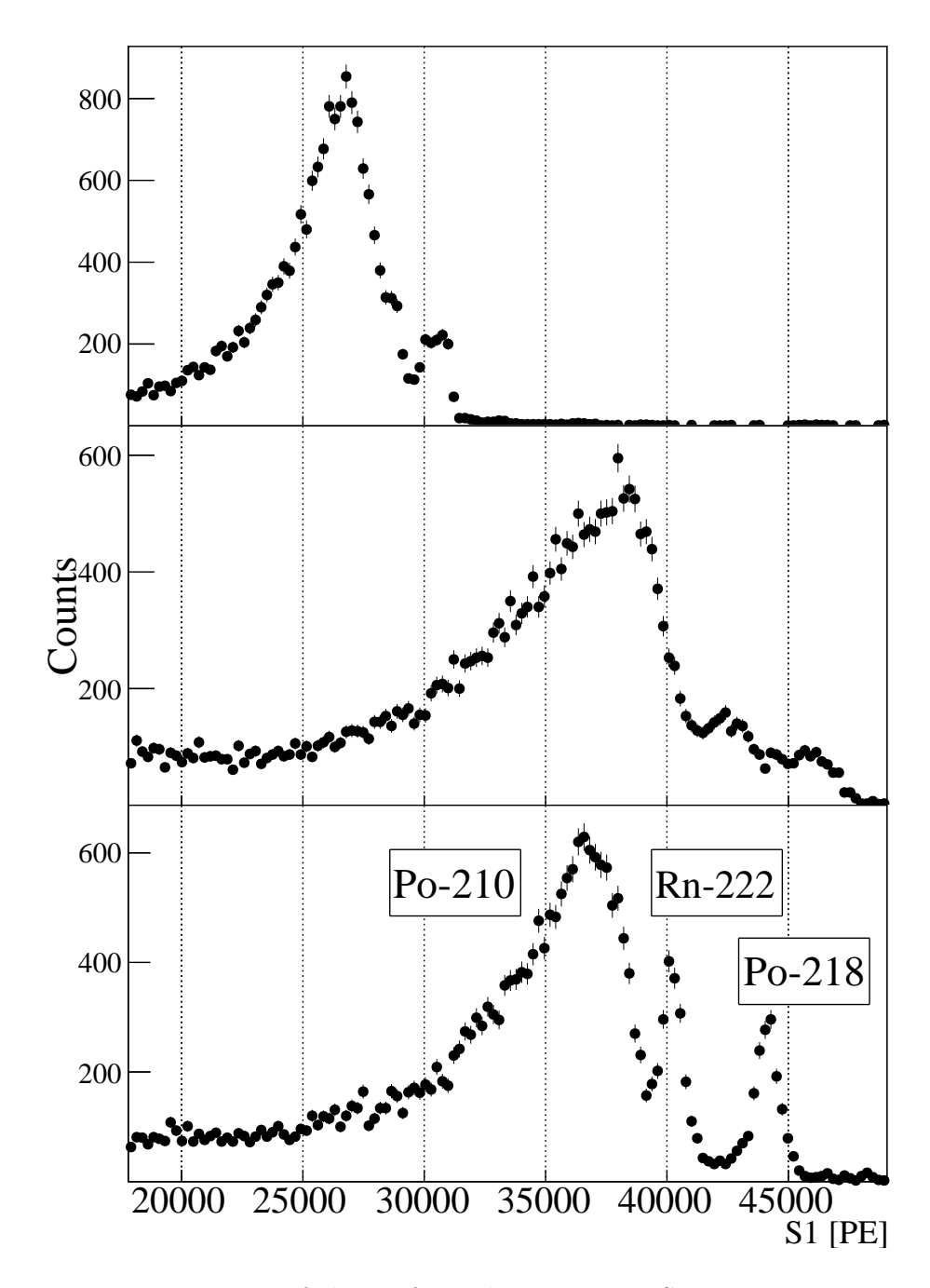


Figure A.3: Energy spectrum of the surface  $\alpha$ 's. Top: raw S1 energy spectrum of  $\alpha$  peaks before any corrections. Middle: the same spectrum after making the V1724 ADC correction. Bottom: the same spectrum after the V1724 ADC correction and the Top-Bottom Asymmetry correction. Plot from C. Stanford [64].

Table A.2: Summary of the fit parameters for all channels.

Channel	Channel S1 Correction		S2 Correction			
Index	$ p0\rangle$	p1	$\chi^2_{ t reduced}$	b0	p1	$\chi^2_{ t reduced}$
$\frac{\text{Index}}{0}$	-389.496	0.0610381	$\frac{\chi_{\text{reduced}}}{0.745327}$	-4198.39	0.0649792	$\frac{\chi_{\text{reduced}}}{0.58992}$
1	-452.717	0.0510361 $0.0580854$	1.39603	-5902.25	0.0644568	0.59948
$\frac{1}{2}$	-315.85	0.0500534 $0.0605824$	1.07594	-3222.86	0.0044508 $0.0650572$	0.39948 $0.767255$
$\frac{2}{3}$	-389.486	0.0603324 $0.060234$	0.826468	-4027.08	0.0630372 $0.0643035$	1.19286
3 4	-371.214	0.0598711	0.820408 $0.979138$	-3635.35	0.0638859	1.19280 $1.10792$
5	-384.415	0.0598711 $0.0592526$	1.07271	-4503.9	0.0038839 $0.064652$	0.98852
5 6	-392.166	0.0592520 $0.0586476$	1.65712	-4366.71	0.064032 $0.0631309$	1.21514
7	-344.592	0.0580470	1.03712 $1.41624$		0.0631309 $0.0642174$	1.21314 $1.59083$
8				-3711.26		
	-120.544	0.0653367	0.993672	-995.564	0.0662474	1.35383
9	-411.348	0.0594274	1.30638	-3356.62	0.0615116	2.79326
10	-147.947	0.0637278	0.962225	-1019.25	0.0638042	1.43924
11	-403.284	0.0583609	0.822365	-4589.75	0.0630435	1.33694
12	-425.673	0.0592398	1.11772	-4842.68	0.0640454	1.49317
13	-379.069	0.0575314	1.13312	-4465.31	0.0626178	0.761233
14	-436.183	0.0578156	0.894751	-3999	0.0604792	2.77312
15	-437.442	0.0589334	0.724552	-5753.4	0.0642676	1.18344
16	-440.834	0.0594487	1.76638	-4761.97	0.0630966	1.26134
17	-398.682	0.0594649	1.659	-4284.62	0.0632711	0.960926
18	-388.671	0.0578743	1.05527	-4531	0.0631654	1.54903
19	-147.94	0.0631643	1.23097	-1322.18	0.0644956	7.64579
20	-200.633	0.0678811	1.43189	-953.595	0.0656307	6.01409
21	-147.027	0.0626931	1.25988	-1523	0.0653954	7.62474
22	-138.445	0.0618588	0.293201	-1702.87	0.0659176	8.55826
23	-496.276	0.0639869	0.936782	-4644.06	0.0652963	22.1711
24	-207.241	0.0661481	0.775008	-1234.38	0.0657206	6.47116
25	-260.773	0.0665528	1.10975	-1416.52	0.0646643	6.87779
26	-189.626	0.0653417	0.699402	-1702.27	0.0673097	7.35547
27	-163.313	0.0622008	1.42586	-1777	0.0651532	10.0064
28	-106.54	0.0649472	0.741976	-1095.49	0.0667507	11.2071
29	-162.654	0.063747	0.814874	-1464.13	0.0661394	5.93603
30	-152.879	0.0645182	1.35467	-1195.89	0.0660707	7.46984
31	-114.94	0.0613567	1.57537	-1502.14	0.0656792	10.1531
32	-391.228	0.0598589	0.80654	-4455.09	0.0646938	28.443
33	-454.294	0.055623	0.408617	-6464.99	0.0637185	41.0844
34	-494.48	0.0574929	1.17804	-6395.1	0.0639432	39.68
35	-87.9399	0.0620328	1.68902	-1125.53	0.0653089	11.5134
36	-368.704	0.0559763	0.431489	-4914.98	0.0635128	32.4259
37	-224.91	0.0674533	1.05477	-1242.44	0.0654167	13810.3

# Appendix B

## The "Cherenkov Tail"

### B.1 The Features

When investigating the region B in plot 4.3, we discovered a stream of single PE following the main S1 pulse that extends beyond the end of DAQ window scale, as shown in the waveform plot B.1. This tail resembles the millisecond long states of TPB scintillation observed in [65]. As it turns out, a big fraction of events in region A also have this strange tail feature. If a single PE from the tail accidentally falls into the S1 late window (90 ns to 7 us), it will pull the event down from region A to region B. Therefore, we purposely include region B as a part of the pure Cherenkov selection.

Despite of the fact the Cherenkov tail resemble TPB tail, there are counter-evidence to attribute this strange feature to TPB scintillation.

- The shape of the average waveform does not match C. Stanford's measurements. A while ago, C. Stanford helped me fit the TPB function to the average waveform of events in region A+B. The fit returns a non-physical value of relaxation time. When I plotted the average waveform on top of TPB average waveform, the shape of the averaged Cherenkov tail suggests less intermediate states (microsecond scale) than TPB;
- Given prompt light in region A+B are at very low (S1< 150 PE), the size of the tail seems bigger than TPB tail. If S1= 100 PE, in average there are 24 PE in the tail (from 7  $\mu$ s to end of DAQ window);

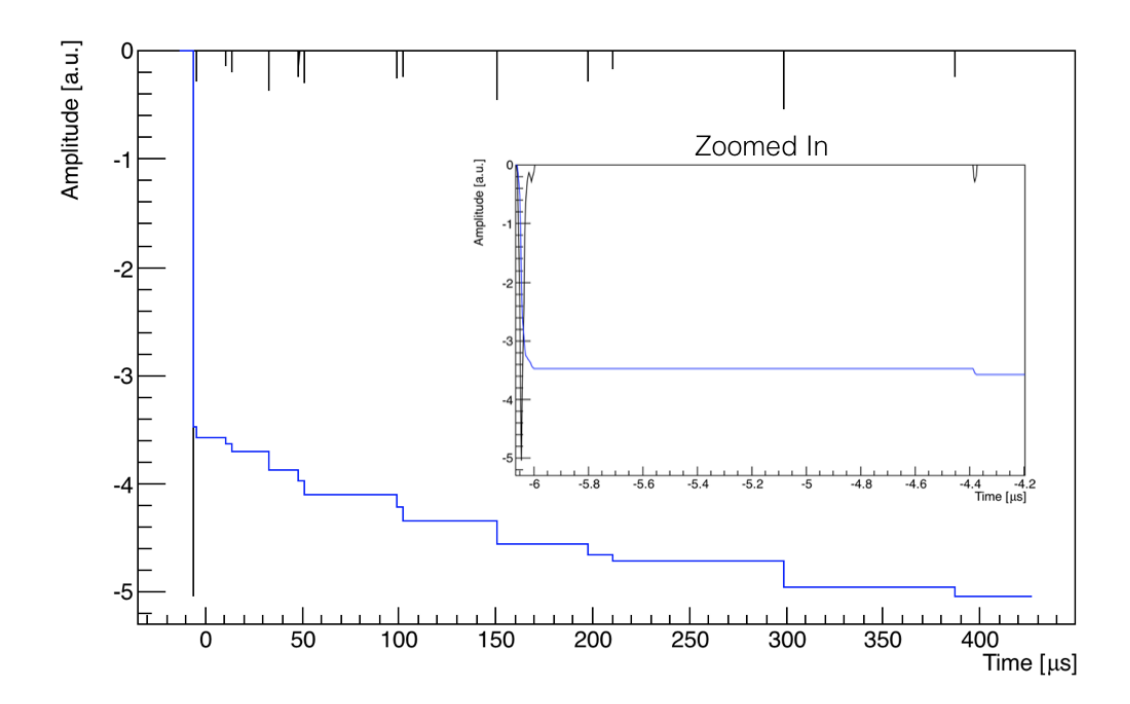


Figure B.1: The waveform of an event selected in region B to demonstrate this Cherenkov tail feature. The blue curve is the accumulated charge in arbitrary unit. Summary: run=11856, event=267, S1=22.5 PE, F90=0.967. The inserted plot is the same event zoomed in to the S1 window. As mentioned in text, this event fall into region B possibly due to one accidental PE from the tail falling in the S1 late window.

• The tail max fraction is positively correlated with the prompt max fraction (Figure B.4). The Cherenkov in PMT window typically gives high prompt channel fraction (S1pMF> 0.6), and the corresponding tail max fraction is very high as well. In addition, the tail max channel is strongly correlated to the max channel of prompt light. Assume TPB emits isotropic light, it seems unlikely to have most tail PEs concentrate in a single tube.

### B.2 The PMT Dark Noise

The average rate of dark noise of PMTs at liquid argon temperature becomes relevant during the investigation for the cause of the Cherenkov tail. Since the noise level is different from tube to tube, I did the following quick estimates for the 38 deployed PMTs in DarkSide-50 TPC.

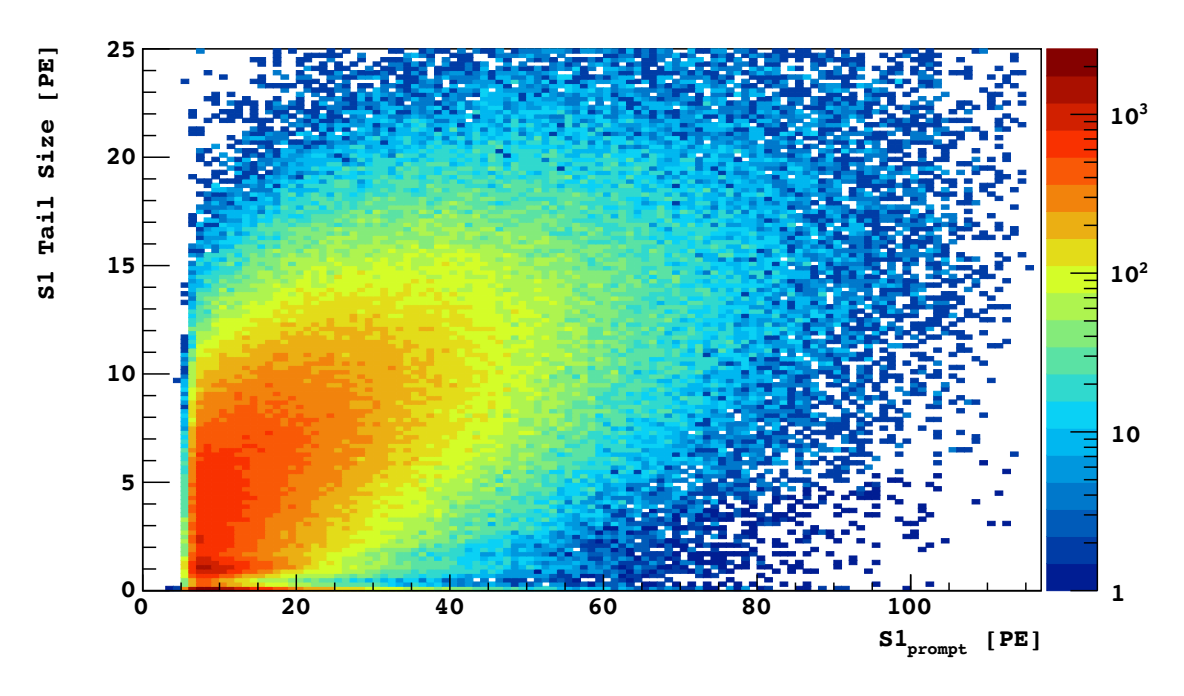


Figure B.2: Cherenkov Tail size. The tail size is correlated to the S1 pulse size. The tail is defined as the integral from the end of S1 (7  $\mu s$ ) to the end of the DAQ window.

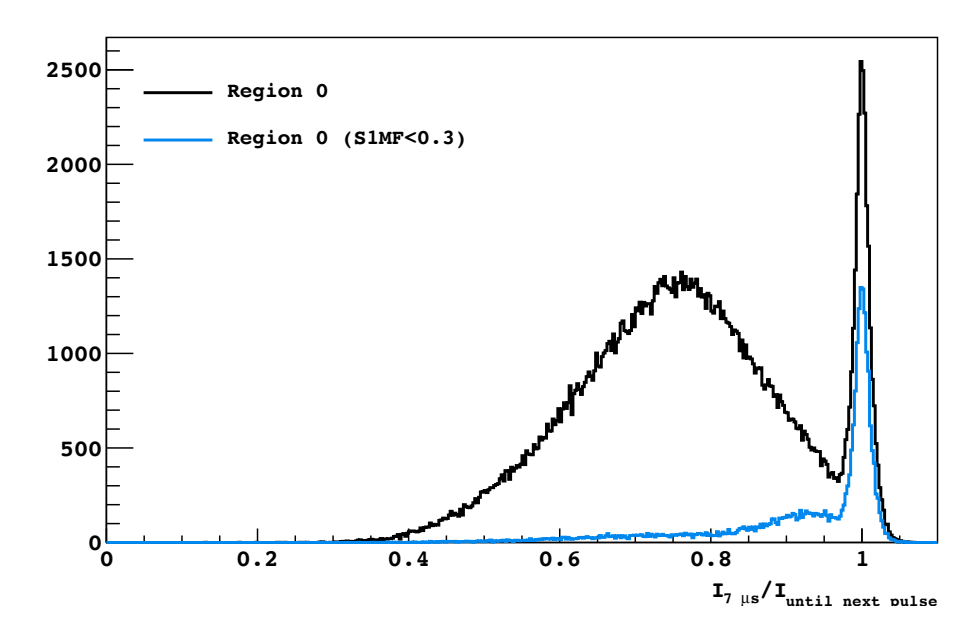


Figure B.3: Cherenkov Tail fraction. The fraction of PE are in the S1. This is the spectrum of the TPB variable for events in region A. The TPB variable is defined as the ratio between S1 (the first  $7 \mu s$ ) and the integral until the end of DAQ window (S1 + tail size).

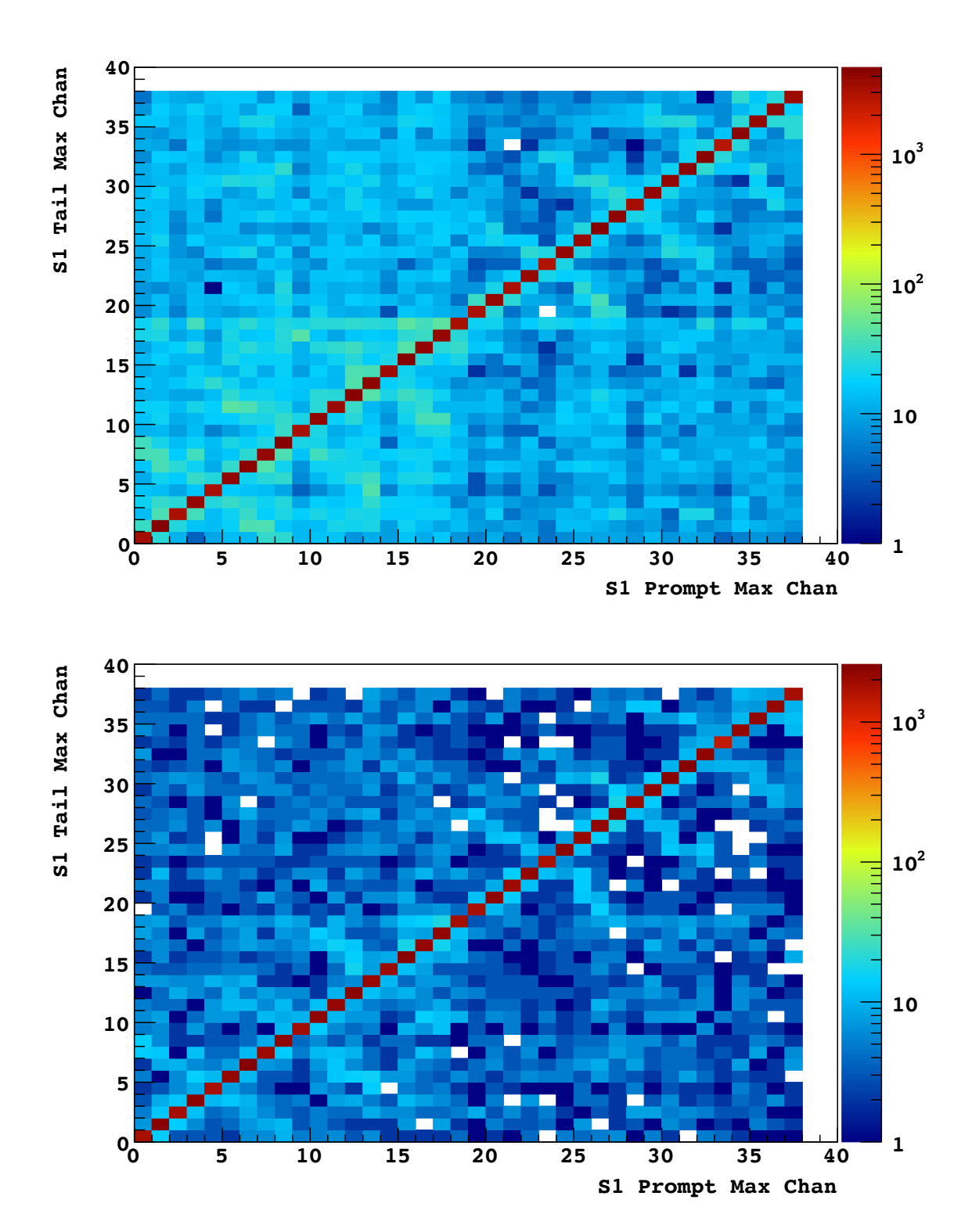


Figure B.4: Strong Correlation between the maximum channel of S1 vs the maximum channel of the tail. UAr 70-day data. Cuts: quality cuts, trigger time cut, and failing the TPB cut. Top: events in region A; Bottom: events in region B.

The WIMP search data set (SLAD v2.3.3, blinded) with the UAr target, ranged from run 15198 (March 11, 2016) to run 16369 (July 12, 2016) was used. To avoid correlation with S1 and S2 pulses, we took advantage of the random trigger which was implemented since run 15198. The analysis cuts are

- 1. Basic quality cuts (NChannels==38 && SumBaselineFound)
- 2. Trigger type cut (trigger\_type==4)
- 3. Number of pulses cut (n\_phys\_pulses==0)
- 4. Long wait cut (livetime+inhibittime > 5 ms)

The long wait cut was intended to remove events contaminated by TPB long tail. The final outcomes is not affected when the cut value changed from 5 ms to 50 ms.

Next we define several ROI time windows to integrate over. The dark rate is simply given by

$$R = N_{\rm pe}/(38 \times T \times N_{\rm ev}) \tag{B.1}$$

where  $N_{\text{pe}}$  is the ROI integral in terms of PE, T is ROI window in seconds, and  $N_{\text{ev}}$  is the number of selected events. To get  $N_{\text{pe}}$ , we fit a Gaussian function to the Single PE peak at a channel-to-channel basis, as shown in Fig B.5.

It's important to mention that we have a history of several PMT excursions. In particular PMT 18 was identified to give high rate in the range of the data set. The above analysis was repeated after we excluded the PMT 18, and the results for the average rates are  $2.1 \pm 0.17$  Hz for ROI[3] and  $2.4 \pm 0.08$  Hz for ROI[4].

In conclusion, the average dark noise at cryogenic temperature is estimated to be  $\sim 4$  Hz/PMT, and  $\sim 2$  Hz/PMT without PMT 18. Given the systematic error associated with this simple analysis is likely small, we conclude the average dark noise of the PMTs is insufficient to produce the size of Cherenkov tail.

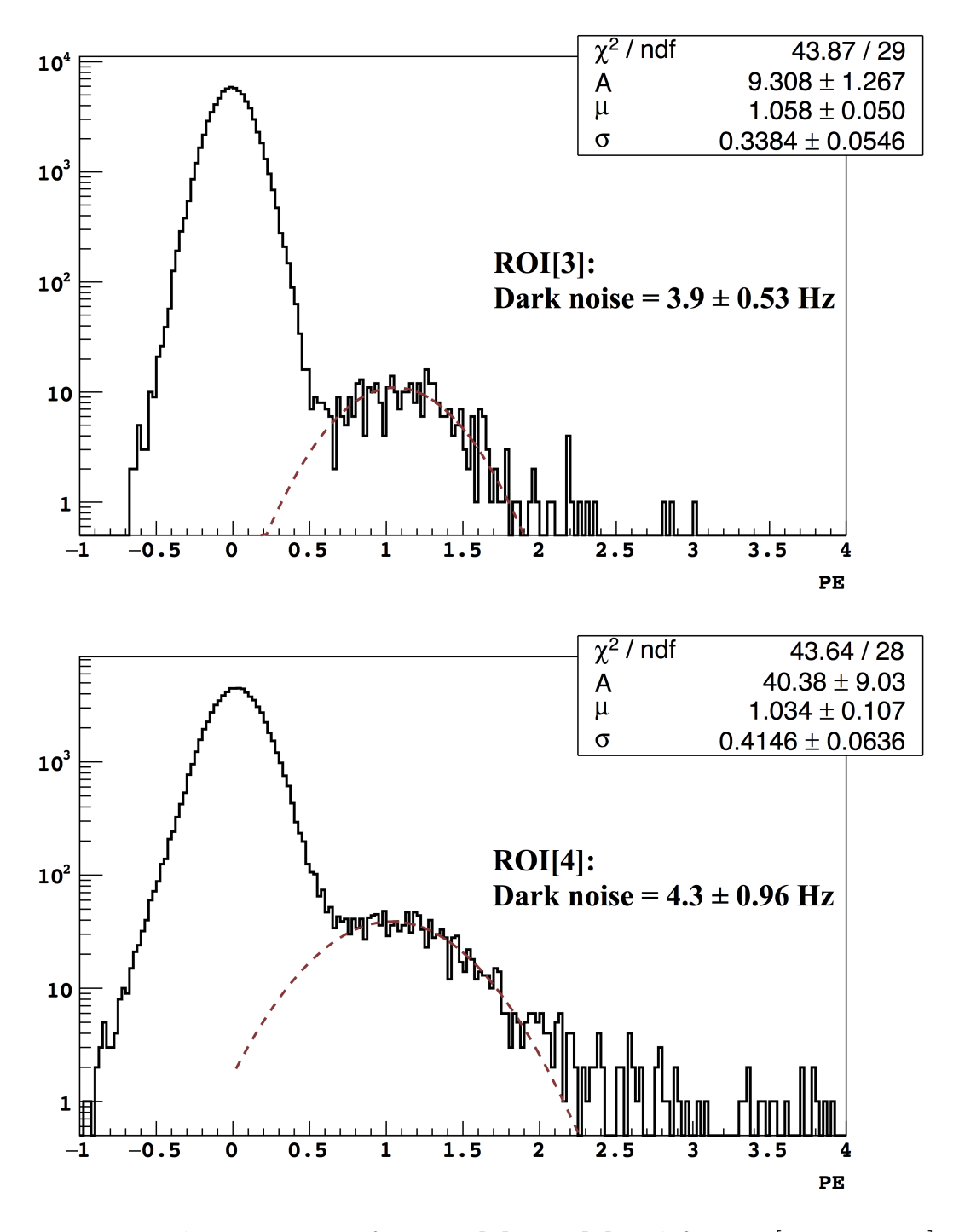


Figure B.5: Top: single PE spectrum from ROI[3]. ROI[3] is defined as [366us, 399us] with respect to the trigger time. Bottom: single PE spectrum from ROI[3]. ROI[3] is defined as [300us, 430us] with respect to the trigger time. The error in dark noise are from the fit.

# Appendix C

# Technical G4DS Implementations

### C.1 Useful features

Being able to save the creation information for every photon, such as its origin material, location, wavelength, and creation process allows us to make absolute classifications later at analysis stage. For example, a pure PTFE Cherenkov event can be distinguished from the others by requiring that all detected photons are originated in PTFE by Cherenkov process. Furthermore, being able to classify events internally allows G4DS to simulate the the optics smartly as described in Section C.2. Unfortunately, the UV absorption in wavelength shifter destroys a photon's track information, and the newly emitted photon does not know the preceding photon's origin information. To solve this problem, we create a new module DSTrackInformation.cc in G4DS to allow saving user-defined additional information associated to a track. In every physics process that create optical photons (G4Cerenkov.cc and DSLight3.cc are the only two in G4DS), we add a chunk of code recording the creation information to the class and associating the class to the track. Then in the wavelength shifter module (DSOpWLS.cc), since the wavelength shifting conversion is one to one, we simply copy over the associated information to the new tracks right before the old ones are destroyed.

This method is flexible in the sense that in the future user add more variables they want to preserve but do require some coding.

## C.2 G4DS Speed-up Scheme

There are two major implementations to speed up G4DS. One is to set a maximum energy cut off for producing S1 photons. The idea comes from that fact that our WIMP ROI is below 450 pe, so having an energy cut off above WIMP ROI is OK (my choice of this threshold is 110 keV). The default cut off threshold is arbitrarily high, but once an user specifies a threshold in the configuration file, the LAr scintillation module (DSLight3.cc) will set the number of photon to 0, if both of the following two conditions are true:

- 1. check if this particle vertex KE is greater than the threshold (DSLight3 has already excluded uncharged particle, and make sure this particle is in active LAr).
- 2. check if current particle location is at least 1 mm away from surfaces. This is done by comparing the vertex coordinates against LAr volume dimensions. It is considered away from the surfaces if:  $R_{\text{step}} < (R_{\text{max}} 1 \text{mm})$  AND  $Z_{\text{step}} < (Z_{\text{min}} 1 \text{mm})$  AND  $Z_{\text{max}} > (Z_{\text{min}} + 1 \text{mm})$ , where  $R_{\text{max}}$  is from the center of LAr to PTFE main reflector surface (not above grid),  $Z_{\text{min}}$  is from the center of LAr to the surface of cathode window, and  $Z_{\text{max}}$  is from the center of LAr to the surface of the grid.

The second condition is added to avoid a special scenario where a particle crosses the boundary between LAr and the surrounding construction material. We do want to track the scintillation photons when an energetic electron penetrate into the material potentially but only making small energy deposition in LAr. The scenario become a serious issue especially when this particle get into a Cherenkov radiator, making a potential background event. The choice of 1 mm comes from back-of-the-envelope calculation based on ESTAR data that a 3 MeV electron will at most travel 0.5 mm in LAr while depositing energy less than 110 keV.

The other implementations is what I would call Conditional Photon Tracking (CPT). Optics is slow because of the large number of photons it needs to track. But since pure LAr scintillation events are not considered a threat, we can safely improve the average simulation speed by selectively turning off photons tracking when an event does not create any Cherenkov photons. To do this, an event by event decision must be made after all the secondary particle tracking is done and before any optical photon tracking begins. Fortunately, Geant4 allows this user defined decision to intervene on a event-by-event basis, and the technique is commonly adopted by other high energy experiments to avoid simulating unwanted events.

The general algorithm goes as the following. By default, Geant4 marks all secondaries as fUrgent and pushes them into an urgent stack to be tracked first. Once the CPT option is enabled in the configuration file (default off), all optical photons will be classified as fWaiting and temporally pushed into a waiting stack until a method called NewStage() is invoked. Meanwhile a counter records the total number of Cherenkov photons. Once all secondaries in the urgent stack are done, NewStage() will check the number of Cherenkov photons and turn on a tracking flag if the counter is greater than 0. During the second round of classification, if the flag is on, the postponed photons are moved to the urgent stack for tracking. If it's off, all photons will be killed.

This CPT method speeds up G4DS by a factor of  $\sim 5$  but with a trade-off of not having pe information for pure ER events. This means we need to randomly lose 5% of pure ER events when apply the 95% S1pMF cuts to the CPT method generated MC. We have to generate two MC sets, one with CPT turned off, and the other with CPT turned on (massively produced). It's also worth mentioning that since this method is only implemented in DSStackingRDMChain.cc in G4DS, it only works for generating radioactive decays. For example, it does not work with Ar39, which uses an external spectrum based scs generator; it does not work for AmBe neutron generator (not defined as a decay), and it does not work for directly shooting primary particles in material via g4gun.

## C.3 Slim Storage Scheme

A massive MC data set requires large amount of space. An option is implemented to slim the output. When the slim option is turned on, we only save energy deposits in the following materials: LiquidArgon, GaseousArgon, PTFE, FusedSilica (diving bell cathode window), TPB, Quartz (the fused silica PMT face-plate), and BoronScintillator (LSV organic scintillator). Furthermore in rooter, if the sum of the deposited energy in the above material except BoronScintillator is 0 and the total number of photo-electron is 0, all deposits information are not saved. This is intended to skip events which only make deposition in LSV but not TPC (saving space mostly for simulating cryostat originated decays); we need TPC trigger in data anyway.

### C.4 The Instructions

The step by step instructions to set up G4DS on ds50srv01, run G4DS on Open Science Grid (OSG), and analyze the outputs on OSG were summarized at https://cdcvs.fnal.gov/redmine/projects/darkart/wiki/. Ken H. (kherner@fnal.gov) at Fermilab is an expert who can help debugging issue related to the upgrade of Fermilab computing service.

# Appendix D

# Data Stability in the 70-day

# Campaign

It is important to check the stability of the detectors to ensure the data quality. In Sec. 3.2, we presented the veto prompt time as an example. In this section, we will go over several other keys features.

## D.1 TPC Stability

#### TPC Electronic Noise

The TPC laser runs generally to have very low channel occupancy (the probability of a PMT seeing a PE per trigger) by design. As a result, we have a statistically rich pedestal in the laser PE spectrum to study the baseline fluctuation. Since the collaboration has an automatic script to analyze the laser run data and save the results into a table (dark\_art.laser\_calibration) in the DarkSide-50 database, we can easily plot the laser run related features as a function of runs.

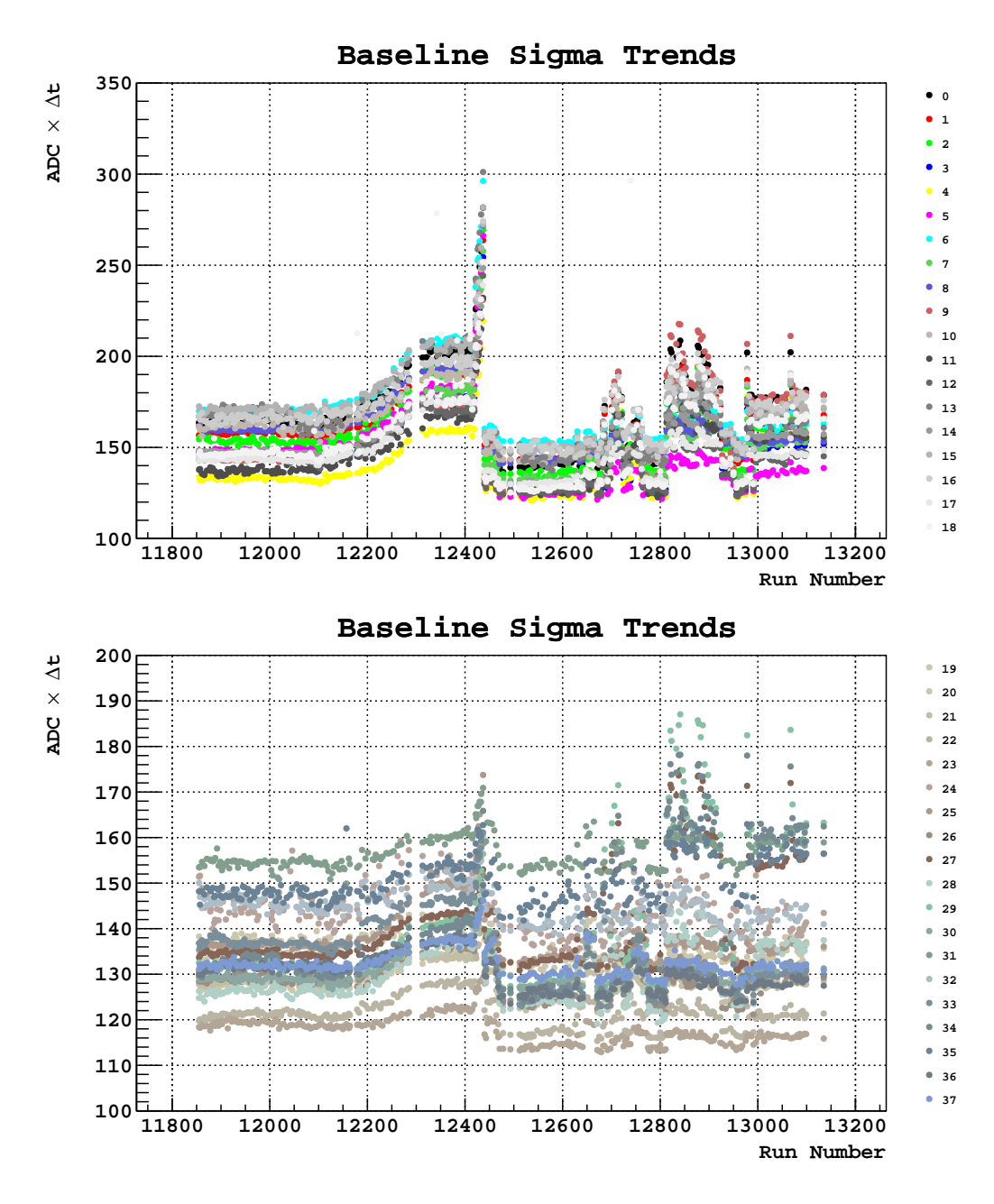


Figure D.1: TPC baseline width (sigma) of all 38 channels from the laser runs. The legend labels channel indices. Top: the bottom PMT array. Bottom: the top PMT array.

As shown in Fig. D.1, we observed an unstable behavior of suddenly increased baseline width. We decided it is safer to remove those runs from 12427 to 12436, since the scale of fluctuation is comparably large and the cause was unclear. The rest baseline seems stable.

### TPC PMT Gain

As shown in Fig. D.1 and Fig D.1, we evaluated the stability of PMT single PE response in the laser runs and observed that the gains of all PMTs had been smoothly declining. Since we took one laser run every two WIMP search runs and always use the closest laser run prior to a WIMP search run for the PE normalization, this declining trend is not a concern. As shown Fig D.1, the resolution is flat over the length of campaign.

### TPC LY

The existence of  $^{37}$ Ar isotopes in the UAr provided an option to directly monitor the TPC LY at low energy using WIMP search data.  $^{37}$ Ar undergoes electron capture with a kinematic decay energy of 2.65 keV. The approach is to fit a Gaussian plus a constant function to the peak, and use the Gaussian mean as a measure of the LY. As shown in Fig. D.1-Top, the peak does not look like a Gaussian on the left wing due to the influence of the pulse finder inefficiency (Fig. 4.25). The simple approach should be fine for the purpose of LY stability, although for the absolute LY calibration at 2.65 keV, one should take the inefficiency into account. Fig. D.1-Bottom shows the trend of TPC LY which is relatively stable. However since of  $^{37}$ Ar is only 35 days, the statistics will be a factor of  $\sim$  10 times lower toward the end of the campaign, resulting an increasing statistical error bar as the campaign progress.

### TPC Maximum Drift Time

The maximum drift time is determined by fitting an empirical tanh(x) function to the edge of drift time spectrum. The fit function is  $f(x) = p_0 + p_1 \tanh p_2(x - t_{\text{max}})$ , where we use the center of the tanh(x) as the measure of the maximum drift time in the TPC (the exact fit function is from G. Koh). The fit turns out to be very good as shown in Fig D.1-Top. We concluded a stable maximum drift time over the entire campaign (Fig. D.1-Bottom).

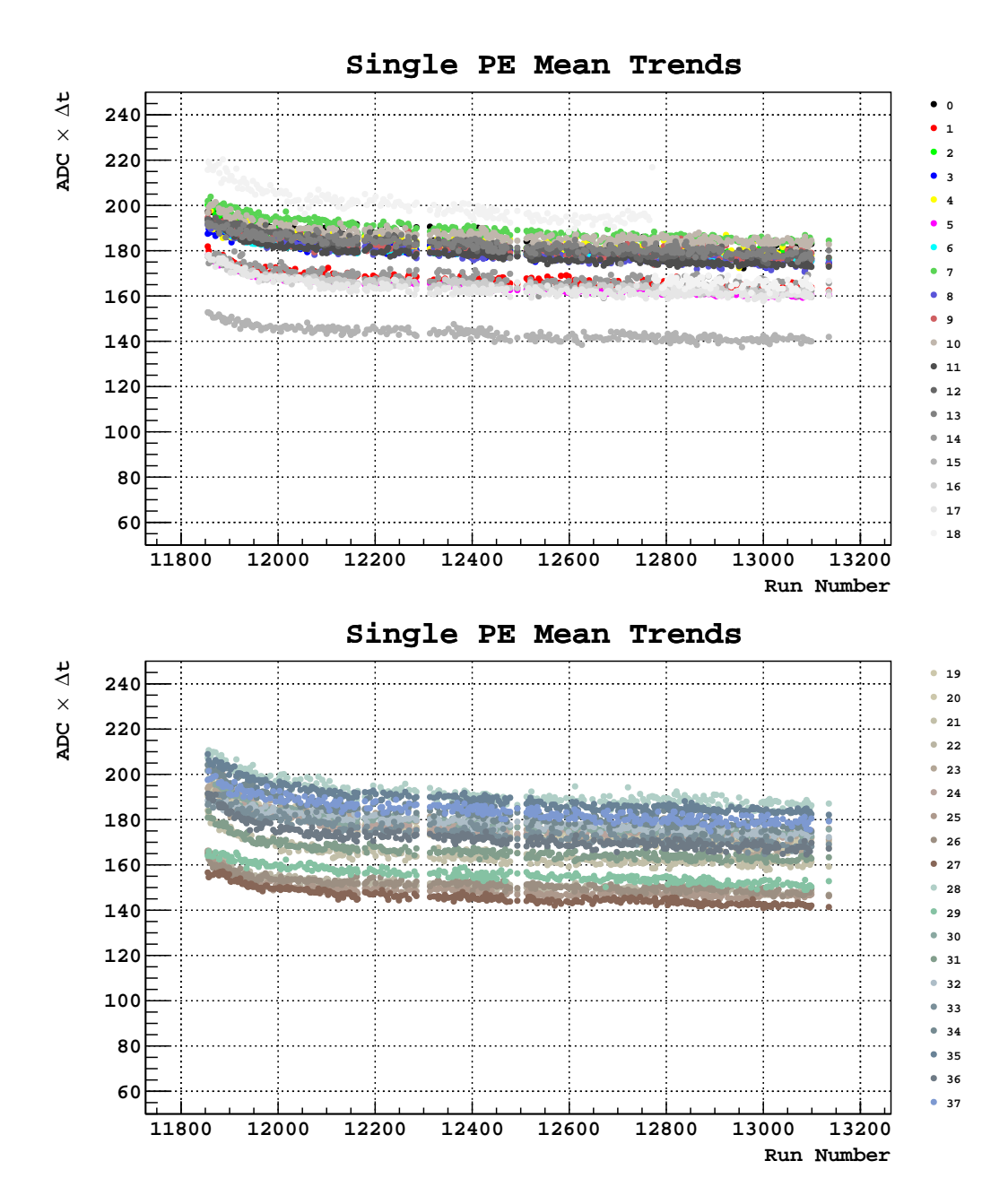


Figure D.2: TPC single PE response mean (PMT gain) of all 38 channels from the laser runs. Top: the bottom PMT array. Bottom: the top PMT array.

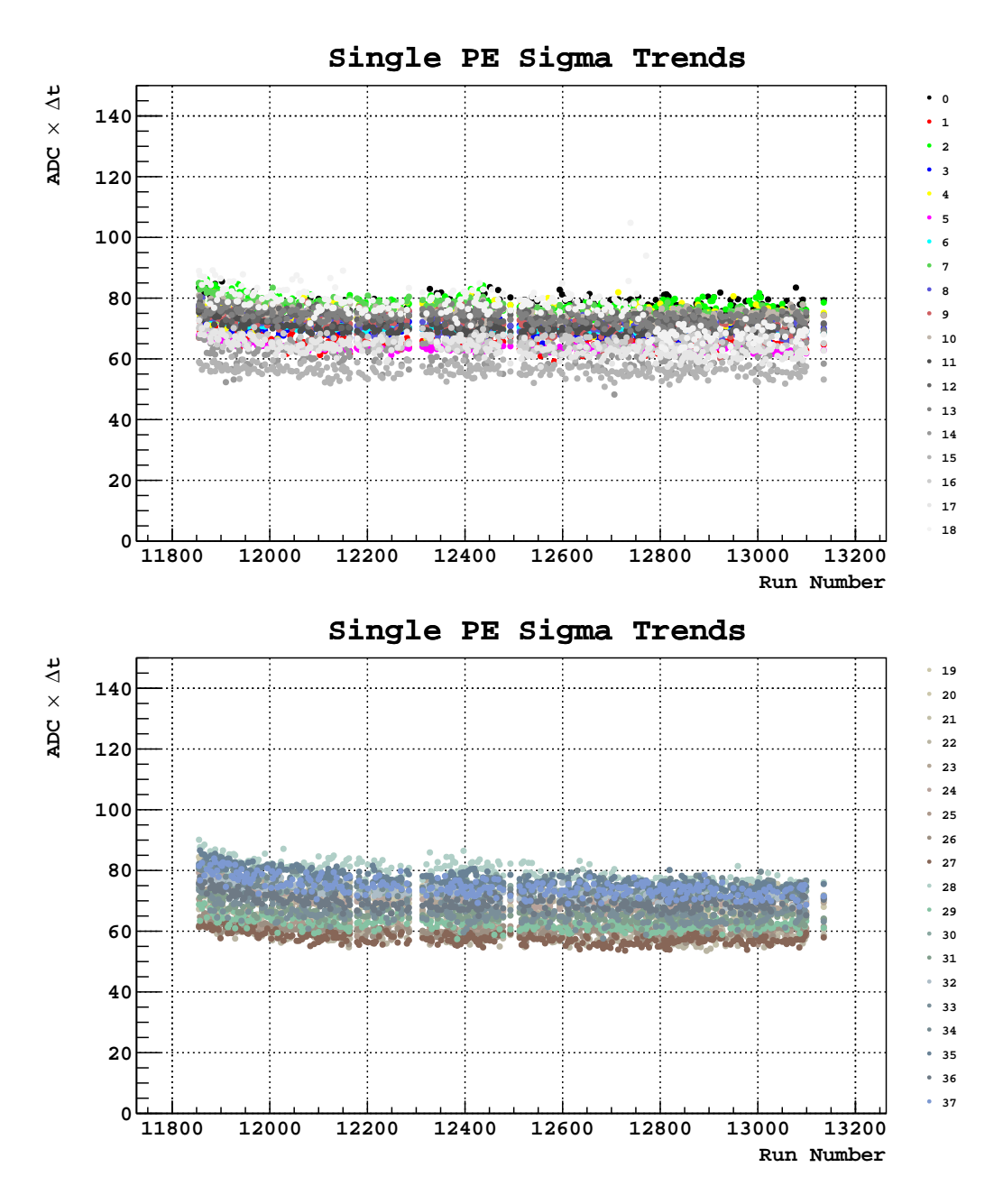


Figure D.3: TPC single PE response sigma of all 38 channels from the laser runs. Top: the bottom PMT array. Bottom: the top PMT array.

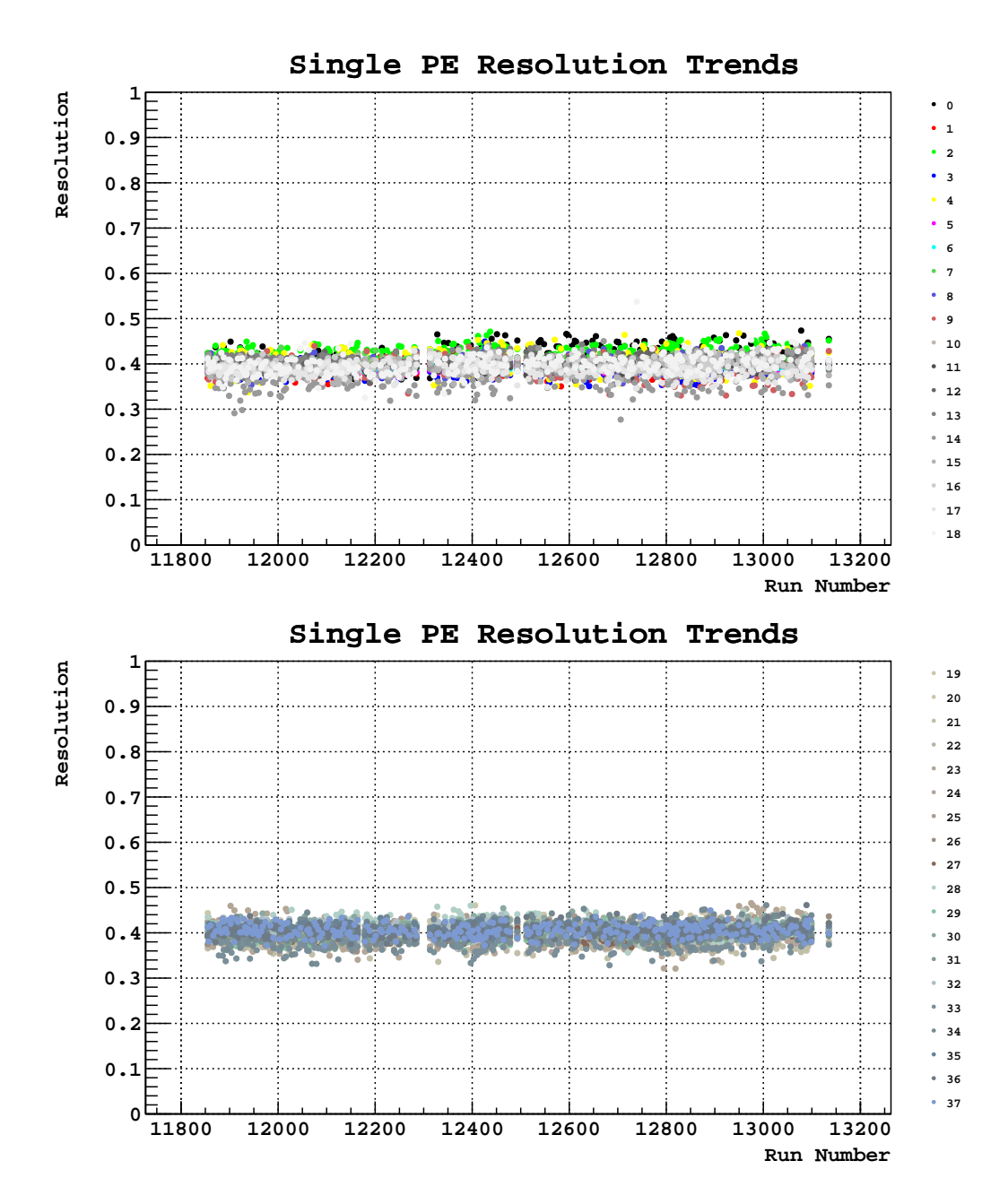


Figure D.4: TPC single PE response resolution (sigma/mean) of all 38 channels from the laser runs. Top: the bottom PMT array. Bottom: the top PMT array.

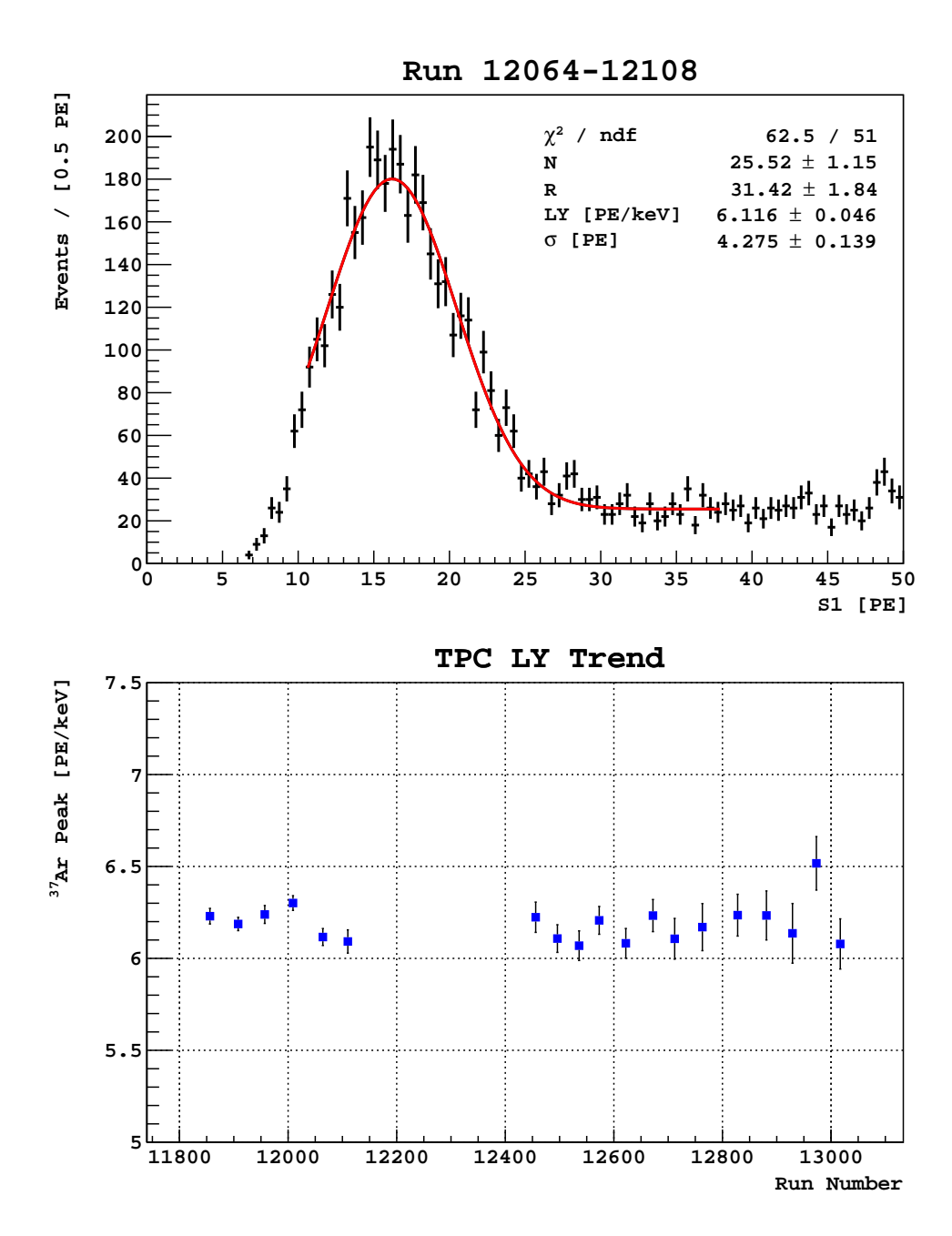


Figure D.5: Left: S1 spectrum for the group of runs from 12064 to 12108. The fit function is:  $f(x) = N(1 + \frac{R}{\sigma\sqrt{2\pi}}e^{\frac{-(x-2.65\text{-LY})^2}{2\sigma^2}})$ . Right: TPC LY stability trend from the <sup>37</sup>Ar peak as a function of run number. Each data point is a group of 30 adjunct runs.

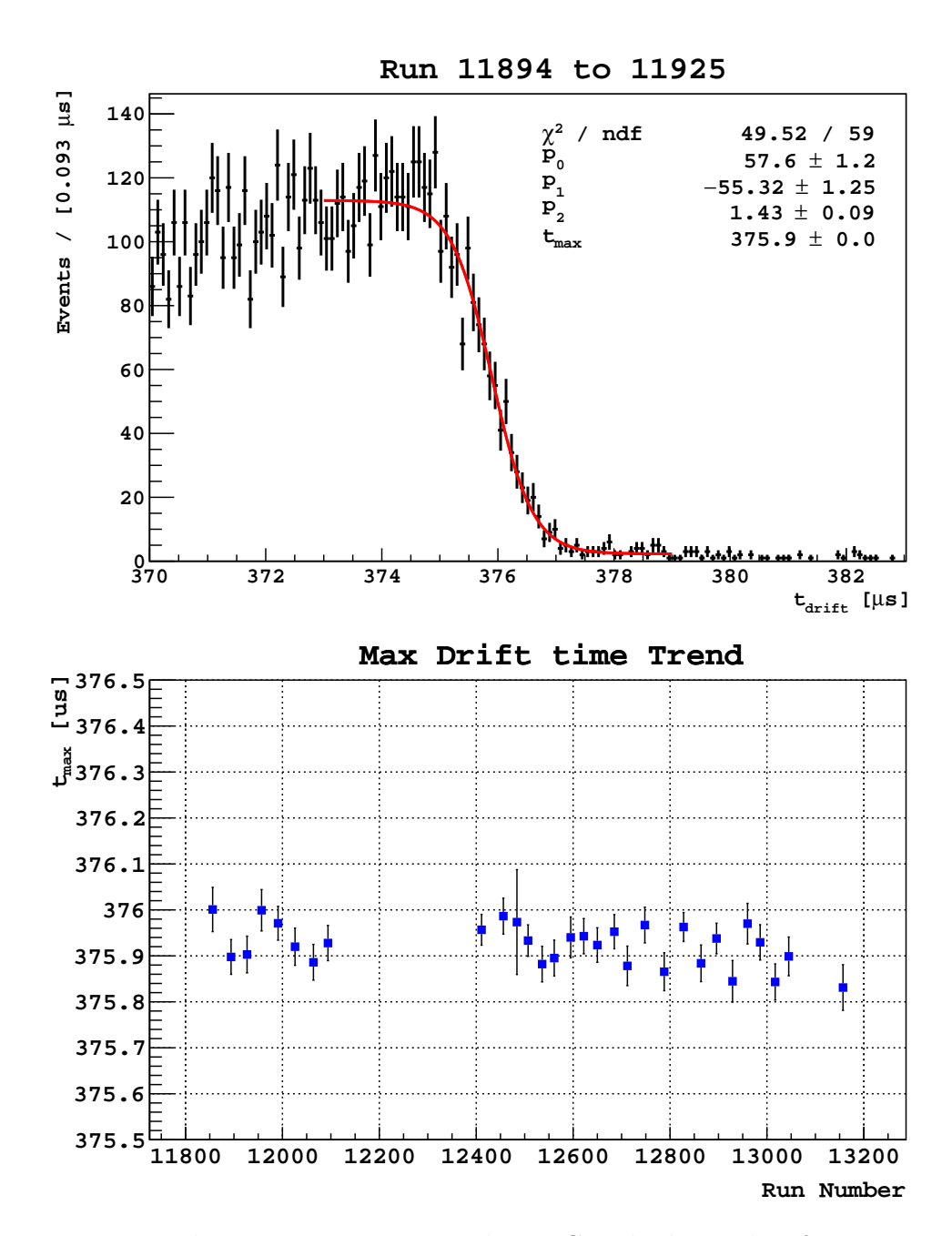


Figure D.6: Top: the  $t_{\rm drift}$  spectrum near the TPC cathode window for a group of runs from 11894 to 11925. See text for the fit function definition. Bottom: the stability trend of  $t_{\rm max}$  as a function of run number. Each data point is a group of 20 adjunct runs.

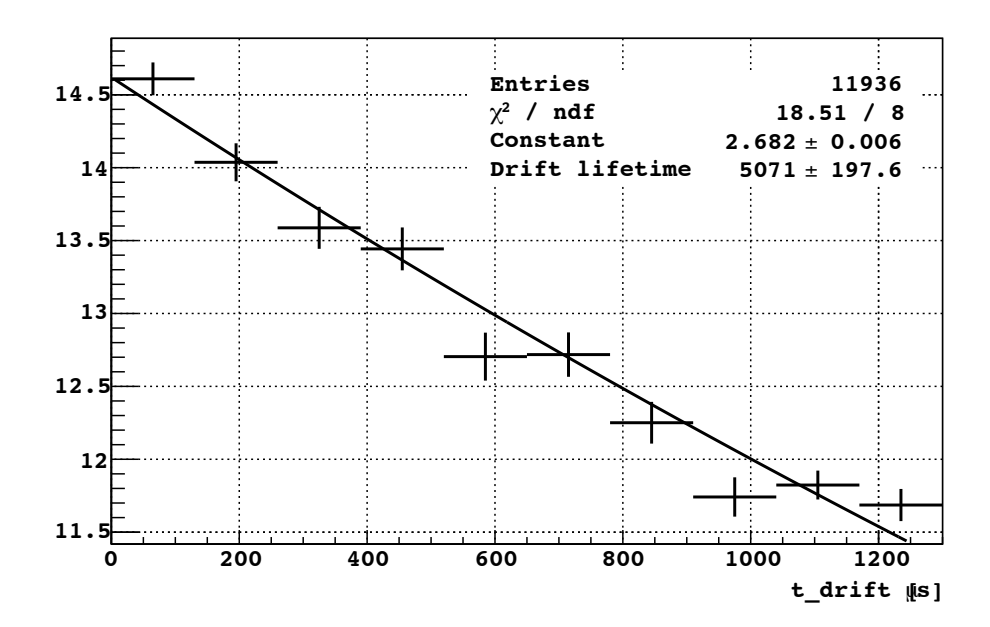


Figure D.7: Electron drift lifetime in the UAr measured at  $E_{drift}$ =50 V/cm. The special drift field runs were taken toward the end of the 70-day campaign (July 24 - July 28 2018). Plot from G. Koh.

### Electron Lifetime in the UAr

While the TPC is drifting the ionization electron toward the gas pocket, the impurity in the LAr captures some of the electrons. Due to this effect, the S2 signal size is  $t_{\rm drift}$  dependent — it is bigger toward the extraction grid and smaller toward the cathode window. The electron lifetime refers to the constant drift distance in terms of  $t_{\rm drift}$  in which an exponential fraction of the electrons survives.

In DarkSide-50 TPC, the actual lifetime is much longer than the data acquisition window as a result of using the high purity argon. Extracting the electron lifetime in standard running mode returned inaccurate estimate. However, we had took special runs with 50V/cm drift field to accurately measure electron lifetime. The analysis by G. Koh yields a  $5071 \pm 197.6 \mu s$  lifetime [22].

## D.2 LSV Stability

### LSV Electronic Noise

The pre-prompt ROI is a 300 ns wide window  $5\mu s$  prior to the prompt time. Since the pre-prompt region is dominated by electronic noises with some random coincidence, the integral spectrum is a good representation of the baseline fluctuation. Fig D.2-Top plots the spectrum RMS as a function of runs where we spotted a up rising trend near 12021. Further investigation reveals that the increase in RMS was due to an unknown origin bump at around 110 PE (Fig D.2-Bottom). It was discovered by S. Westerdale that the jumps happens right after we introduced V1724 (App A.1) to the DAQ. The RMS fell back to normal after the period of the background runs and the  $^{85}$ Kr calibration. The bump did not seem physical, and the baseline width trend seemed stable when we excluded the abnormality in the spectrum.

### LSV Light Yield

The precise estimation of the LSV LY required fitting the double peaks of <sup>60</sup>Co (1.17 MeV and 1.33 MeV) in the prompt spectrum. However, for the purpose of monitoring LY over time, it is sufficient to fit the spectrum with a simple function Gaussian plus exponential function. The Gaussian mean is used as a measure of the LSV LY. Fig. D.2 shows the stable LY trend as a function of run number.

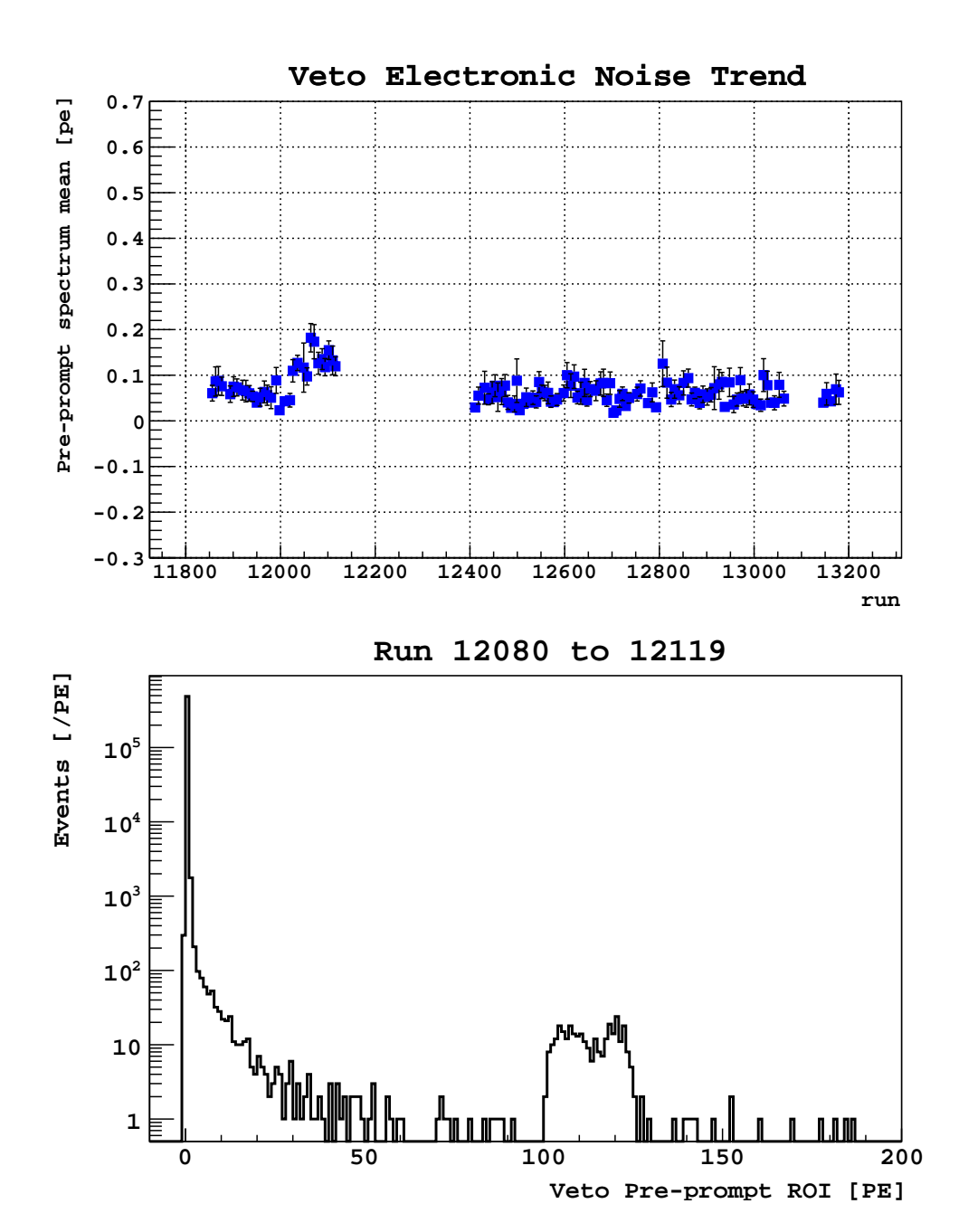


Figure D.8: Top: Veto electronic noise trend in the pre-prompt ROI. Each data point is a group of 5 adjunct runs. Bottom: An example of veto pre-prompt spectrum with a bump at 110 PE. The spectrum is largely dominated by electronic noise. The bump did not exist until run 12021 when we first introduced V1724.

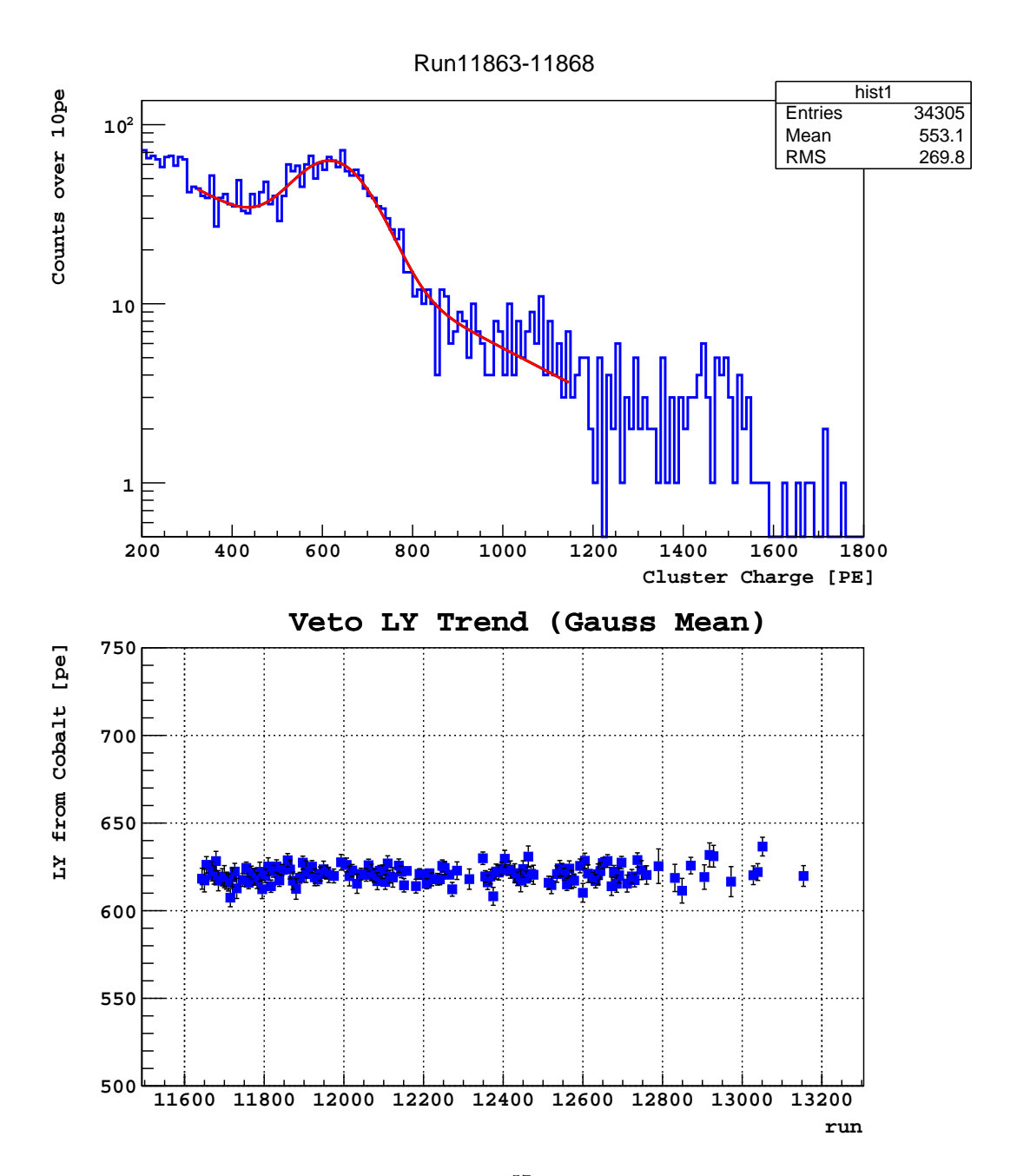


Figure D.9: Top: an example of fitting the  $^{57}$ Co peaks with a Gaussian + Exponential function. Bottom: veto mean LY trend from the  $^{57}$ Co peaks. Each data point is a group of 50 adjunct runs.

# **Bibliography**

- [1] G. Hinshaw et al. Nine-Year Wilkinson Microwave Anisotropy Probe (WMAP) Observations: Cosmological Parameter Results. *Astrophys. J. Suppl.*, 208:19, 2013.
- [2] E. Hubble and M. L. Humason. The Velocity-Distance Relation among Extra-Galactic Nebulae. APJ, 74:43, July 1931.
- [3] et.al van Dokkum. A galaxy lacking dark matter. nature, 555:629–632, March 2018.
- [4] Scott Dodelson. Modern Cosmology. Academic Press, Amsterdam, 2003.
- [5] Jonathan L. Feng. Dark Matter Candidates from Particle Physics and Methods of Detection. Ann. Rev. Astron. Astrophys., 48:495–545, 2010.
- [6] E. Aprile et al. First Dark Matter Search Results from the XENON1T Experiment. *Phys. Rev. Lett.*, 119(18):181301, 2017.
- [7] D. S. Akerib et al. Results from a search for dark matter in the complete LUX exposure. *Phys. Rev. Lett.*, 118(2):021303, 2017.
- [8] Xiangyi Cui et al. Dark Matter Results From 54-Ton-Day Exposure of PandaX-II Experiment. *Phys. Rev. Lett.*, 119(18):181302, 2017.
- [9] P. Agnes et al. DarkSide-50 532-day Dark Matter Search with Low-Radioactivity Argon. 2018.
- [10] P. A. Amaudruz et al. First results from the DEAP-3600 dark matter search with argon at SNOLAB. 2017.
- [11] J.D. Lewin and P.F. Smith. Review of mathematics, numerical factors, and corrections for dark matter experiments based on elastic nuclear recoil. *Astroparticle Physics*, 6(1):87 112, 1996.
- [12] Mark J. Reid. The distance to the center of the galaxy. Annual Review of Astronomy and Astrophysics, 31(1):345–372, 1993.
- [13] Lawrence M. Widrow, Brent Pym, and John Dubinski. Dynamical blueprints for galaxies. *The Astrophysical Journal*, 679(2):1239, 2008.
- [14] F. J. Kerr and D. Lynden-Bell. Review of galactic constants. *mnras*, 221:1023–1038, August 1986.

- [15] R. Bernabei et al. First model independent results from DAMA/LIBRA-phase2. 2018.
- [16] Spencer Chang, Graham D. Kribs, David Tucker-Smith, and Neal Weiner. Inelastic Dark Matter in Light of DAMA/LIBRA. Phys. Rev., D79:043513, 2009.
- [17] Rouven Essig, Jeremy Mardon, and Tomer Volansky. Direct detection of sub-gev dark matter. *Phys. Rev. D*, 85:076007, Apr 2012.
- [18] P. Agnes et al. Constraints on Sub-GeV Dark Matter-Electron Scattering from the DarkSide-50 Experiment. 2018.
- [19] P. Agnes et al. Low-Mass Dark Matter Search with the DarkSide-50 Experiment. 2018.
- [20] Rouven Essig, Tomer Volansky, and Tien-Tien Yu. New Constraints and Prospects for sub-GeV Dark Matter Scattering off Electrons in Xenon. *Phys. Rev.*, D96(4):043017, 2017.
- [21] P. Agnes et al. First Results from the DarkSide-50 Dark Matter Experiment at Laboratori Nazionali del Gran Sasso. *Phys. Lett.*, B743:456–466, 2015.
- [22] P. Agnes et al. Results from the first use of low radioactivity argon in a dark matter search. *Phys. Rev.*, D93(8):081101, 2016. [Addendum: Phys. Rev.D95,no.6,069901(2017)].
- [23] D. M. Mei, Z. B. Yin, L. C. Stonehill, and A. Hime. A Model of Nuclear Recoil Scintillation Efficiency in Noble Liquids. *Astropart. Phys.*, 30:12–17, 2008.
- [24] P. Agnes et al. Electroluminescence pulse shape and electron diffusion in liquid argon measured in a dual-phase TPC. Submitted to: Nucl. Instrum. Meth. A, 2018.
- [25] Jason Philip Brodsky. xy Position Reconstruction in DarkSide-50. PhD thesis, Princeton U., 2015.
- [26] Akira Hitachi, Tan Takahashi, Nobutaka Funayama, Kimiaki Masuda, Jun Kikuchi, and Tadayoshi Doke. Effect of ionization density on the time dependence of luminescence from liquid argon and xenon. *Phys. Rev.*, B27:5279–5285, 1983.
- [27] Shinzou Kubota, Masahiko Hishida, Masayo Suzuki, and Jian-zhi Ruan(Gen. Dynamical behavior of free electrons in the recombination process in liquid argon, krypton, and xenon. *Phys. Rev.*, B20(8):3486, 1979.
- [28] H. Cao et al. Measurement of scintillation and ionization yield and scintillation pulse shape from nuclear recoils in liquid argon. *Phys. Rev. D*, 91:092007, May 2015.
- [29] Brianne Rae Hackett. The DarkSide-50 Experiment: Electron Recoil Calibrations and A Global Energy Variable. PhD thesis, Hawaii U., 2017.
- [30] Luca Pagani. Direct dark matter detection with the DarkSide-50 experiment. PhD thesis, Genoa U., 2017.

- [31] G. Bellini et al. Cosmic-muon flux and annual modulation in Borexino at 3800 m water-equivalent depth. *JCAP*, 1205:015, 2012.
- [32] C. Green, J. Kowalkowski, M. Paterno, M. Fischler, L. Garren, and Q. Lu. The Art Framework. J. Phys. Conf. Ser., 396:022020, 2012.
- [33] Alden Fan. Results from the DarkSide-50 Dark Matter Experiment. PhD thesis, UCLA, 2016.
- [34] P. Agnes et al. The veto system of the DarkSide-50 experiment. JINST, 11(03):P03016, 2016.
- [35] D. V. Hinkley. On the ratio of two correlated normal random variables. *Biometrika*, 56(3):635–639, 1969.
- [36] DarkSide Collaboration. Analysis of 51-day campaign, october 2013 june 2014. DocDB 937, Analysis Note v11 (Internal access only).
- [37] V.M. Gehman, S.R. Seibert, K. Rielage, A. Hime, Y. Sun, D.-M. Mei, J. Maassen, and D. Moore. Fluorescence efficiency and visible re-emission spectrum of tetraphenyl butadiene films at extreme ultraviolet wavelengths. *Nuclear Instruments and Methods in Physics Research Section A: Accelerators, Spectrometers, Detectors and Associated Equipment*, 654(1):116 121, 2011.
- [38] Guangyong Koh. A dark matter search with DarkSide-50. PhD thesis, Princeton University, 2018.
- [39] T. Seiss. Cherenkov background in the ds-50 tpc ptfe. DarkSide Collaboration, DocDB 1240 (Internal access only).
- [40] Chris Stanford. Alphas and Surface Backgrounds in Liquid Argon Dark Matter Detectors. PhD thesis, Princeton University, 2017.
- [41] P.D. Meyers. Location of radioactivity in r11065 pmts. DarkSide Collaboration, DocDB 2231 (Internal access only).
- [42] P.D. Meyers et all. Darkside-50 500-day analysis: Background studies documentation. DarkSide Collaboration, DocDB 2105, 2105 (Internal access only).
- [43] Fred W. Billmeyer Jr. Measurements of the refractive index of films. *Journal of Applied Physics*, 18(5):431–434, 1947.
- [44] Inc. AGC Chemicals Americas. Physical properties of fluon unfilled and filled ptfe. https://www.agcchem.com/agc-certifications/finish/5-fluoropolymer-resins/15-processing-note-f12-13-physical-properties-of-unfilled-filled-ptfe.
- [45] P.D. Meyers. Ptfe properties. DarkSide Collaboration, DocDB 749 (Internal access only).

- [46] P.D. Meyers et all. Calculation of inventory of underground argon needed for ds-50. DarkSide Collaboration, DocDB 1052 (Internal access only).
- [47] C. Silva, J. Pinto da Cunha, A. Pereira, V. Chepel, M. I. Lopes, V. Solovov, and F. Neves. Reflectance of Polytetrafluoroethylene (PTFE) for Xenon Scintillation Light. J. Appl. Phys., 107:064902, 2010.
- [48] E. Shield. Teflon reflectance study. DarkSide Collaboration, DocDB 342 (Internal access only).
- [49] P.D. Meyers. Fused silica: Heraeus suprasil 312 for darkside-50. DarkSide Collaboration, DocDB 413 (Internal access only).
- [50] P.D. Meyers. Hamamatsu r11065 3-inch metal-bulb pmt specifications and quality list. DarkSide Collaboration, DocDB 42 (Internal access only).
- [51] Bo E. Sernelius. Surface Modes in Physics. WILEY-VCH, Verlag Berlin GmbH, Berlin, 2011.
- [52] DarkSide Collaboration. Website. http://palpatine.princeton.edu/darkside/internal/pictures/photopil/Disassemble\_R11065, dated 2017\_07-03 (Internal access only).
- [53] Rory Fitzpatrick. Toward an Energy Model for Electronic Recoils in DarkSide-50. PhD thesis, Princeton U., 2016.
- [54] Brianne Rae Hackett. The DarkSide-50 Experiment: Electron Recoil Calibrations and A Global Energy Variable. PhD thesis, Hawaii U., 2017.
- [55] X. Xiang M. Wada. Estimation of systematical error on s1 ly. DarkSide Collaboration, DocDB 1380 (Internal access only).
- [56] Paolo Agnes. Direct Search for Dark Matter with the DarkSide Experiment. PhD thesis, APC, Paris, 2016.
- [57] Hao Qian. Neutron Veto Efficiency of the DarkSide-50 Detector. PhD thesis, Princeton U., 2018.
- [58] Erin Elisabeth Edkins. Detailed Characterization of Nuclear Recoil Pulse Shape Discrimination in the DarkSide-50 Direct Dark Matter Experiment. PhD thesis, Hawaii U., 2017.
- [59] H. Qian. Veto cuts for 500d uar data. DarkSide Collaboration, DocDB 1657 (Internal access only).
- [60] Gary J. Feldman and Robert D. Cousins. A Unified approach to the classical statistical analysis of small signals. *Phys. Rev.*, D57:3873–3889, 1998.
- [61] T. Johnson. Cherenkov code migration. DarkSide Collaboration, DocDB 2711 (Internal access only).

- [62] C. E. Aalseth et al. DarkSide-20k: A 20 tonne two-phase LAr TPC for direct dark matter detection at LNGS. Eur. Phys. J. Plus, 133:131, 2018.
- [63] P. Agnes et al. The Electronics, Trigger and Data Acquisition System for the Liquid Argon Time Projection Chamber of the DarkSide-50 Search for Dark Matter. *JINST*, 12(12):P12011, 2017.
- [64] P. Agnes et al. Effect of Low Electric Fields on Alpha Scintillation Light Yield in Liquid Argon. *JINST*, 12(01):P01021, 2017.
- [65] Chris Stanford, Shawn Westerdale, Jingke Xu, and Frank Calaprice. Surface background suppression in liquid argon dark matter detectors using a newly discovered time component of tetraphenyl-butadiene scintillation. 2018.